Effective Dose Gradients in Lung Radiotherapy: Setting Target Margins and Monitoring Dose Deviations for Image-Guided Adaptive Strategies

by

William Kyle Foster

A thesis
presented to the University of Waterloo
in fulfillment of the
thesis requirement for the degree of
Doctor of Philosophy
in
Physics

Waterloo, Ontario, Canada, 2016

Author's Declaration

I hereby declare that I am the sole author of this thesis. This is a true copy of the thesis, including any required final revisions, as accepted by my examiners.

I understand that my thesis may be made electronically available to the public.

Abstract

Organ motion is a major source of geometric uncertainty in the delivery of external beam radiation therapy. Organ motion that occurs during the delivery of radiation therapy is referred to as intrafraction organ motion. Intrafraction motion is most predominant in the lungs due to the respiratory motion of the diaphragm and lungs. This intrafraction motion presents a substantial challenge to physicists and clinicians interested in the accurate prescription and delivery of a dose in radiation treatment.

The convolution model of target motion described in this work was used to assess the impact of respiratory motion on the delivered dose distribution. This model predicts the dose distribution that will be delivered in the presence of motion by performing a mathematical convolution between the planned dose distribution and a probability distribution describing the target motion. The model was modified from its original form to include the gradient of the probability density function, which provides additional insight into the effect of target motion. The validity of the convolution model in the context of intrafraction motion was established based on an analysis of the model assumptions as well as experimental validation of the model predictions using radiochromic film measurements. It is shown that the model makes useful predictions for a wide range of regular and irregular breathing patterns.

Breathing trace recordings acquired during four dimensional computed tomography scans of

502 unique patients were used in conjunction with the convolution model to simulate the effect of target motion using MATLAB code developed in house. The motion effect on dose coverage was simulated for each breathing trace on a range of target sizes in order to establish trends which can be used to guide margin selection. The required margins were found to have a clear dependence on the standard deviation of the probability distribution describing the target motion. A method for calculating the margin required to maintain target dose coverage is presented. A table of margin recommendations for a range of breathing patterns and target sizes is presented. The effect of motion was also simulated on clinical treatment plans including a 3-field, a 4-field and a volumetric modulated arc treatment. The clinical treatment plans demonstrate the interplay between the static dose gradients seen in a clinical setting and the loss of dose coverage due to breathing motion.

The validity of the technique is demonstrated for an extreme case of a small lung target undergoing large amplitude motion. This result represents the full use of the proposed methodology. The process demonstrates that using the margins recommended in this work will ensure target dose coverage, but that compromises will be made relative to the plan with unmodified margins. The target dose coverage comes at the expense of increased target volume and potentially increased dose to nearby organs at risk. An analytical approximation of lung target motion and static dose distributions using Gaussian functions is used to demonstrate the limit of the technique for small fields and the sensitivity of the model to its key parameters.

Acknowledgments

I owe thanks and gratitude to many people for their assistance and contributions to this work, over the course of my degree. It was a long journey that I could not have completed on my own.

First and foremost I would like to thank my co-supervisors Dr. Rob Barnett and Dr. Ernest Osei. The unending patience and belief in my abilities demonstrated by each was a constant source of reassurance throughout the process. The advice and assistance offered to me by my co-supervisors, both in regards to this thesis work and beyond, was simply invaluable.

I am extremely grateful to Dr. Stewart Gaede of the London Regional Cancer Program for generously offering the breathing data set that is used extensively in this thesis work. I would also like to thank the physicists of the Grand River Regional Cancer Centre (GRRCC): Dr. Paule Charland, Mr. Andre Fleck, Dr. Runqing Jiang, Dr. Lixin Zhan and Dr. Johnson Darko for their unwavering support and willingness to offer advice and assistance as it was required. I also owe thanks to the other staff of the Medical Physics Department at GRRCC as well: Ron Snelgrove for his detailed knowledge of the LINACs and easy accessibility, Dr. Grigor Grigorov for long discussions and support, Vanya Mathews for her administrative assistance at the hospital, and finally Denis Brochu and Marius Ogrodowczyk for custom phantom modifications.

I am also very grateful for the help of staff in the Physics and Astronomy Department of the University of Waterloo. I owe thanks to Linda Kelly for getting my program started on the

right foot and guidance dealing with the graduate school. I also have tremendous gratitude for help offered by Judy McDonnell in arranging many important dates as well as ensuring all key paperwork had been filed on my behalf. Judy was exceedingly kind and helpful to me throughout.

Finally, I would like to extend my deepest gratitude to my family for their support of me during this program. The encouragement and support offered by my parents was unwavering throughout, as it always has been. Most importantly of all I wish to thank my wife, Laura, for her incredible patience, fortitude and limitless support. At the end of the day, her love and commitment made this possible.

Dedication

For Laura and Clara.

XOXO

Table of Contents

List of Tables

List of Figures

Nomenclature

1D One Dimensional

2D Two Dimensional

3D Three Dimensional

3DCRT Three dimensional Conformal Radiation Therapy

4D Four Dimensional

4DCT Four Dimensional Computed Tomography

AAA Analytical Anisotropic Algorithm

AAPM American Association of Physicists in Medicine

ABW Additional Beam Width

AP Anterior-Posterior

CS Convolution-superposition

CT X-ray Computed Tomography Scan

CTV Clinical Tumour Volume

DIBH Deep Inspiration Breath Hold

DPI Dots Per Square Inch

DSB Double Strand Break

DVH Dose-volume Histogram

EBRT External Beam Radiation Therapy

EPID Electronic Portal Imaging Device

FWHM Full Width Half Max

GRRCC Grand River Regional Cancer Centre

GTV Gross Tumour Volume

HRR Homologous Recombination Repair

HU Hounsfield Units

ICRU International Commission on Radiation Units and Measurements

IMRT Intensity Modulated Radiation Therapy

ITV Internal Target Volume

LET Linear Energy Transfer

LINAC Medical Linear Accelerator

LKB Lyman Kutcher Burman model of NTCP

LQ Linear-Quadratic

LR Left-Right

MC Monte Carlo

MIP Maximum Intensity Projection

MLC Multi-Leaf Collimator

MLD Mean Lung Dose

MRI Magnetic Resonance Imaging

MU Monitor Unit

NHEJ Nonhomologous End Joining

NSCLC Non-Small Cell Lung Cancer

NTCP Normal Tissue Complication Probability

OAR Organ at Risk

OER Oxygen Enhancement Ratio

PDF Probability Density Function

PET Positron Emission Tomography

PFGE Pulsed-field Gel Electrophoresis

PLD Potentially Lethal Damage

PTV Planning Target Volume

QA Quality Assurance

RCL Relative Coverage Lost

RCR Relative Coverage Restored

ROI Region of Interest

RPM Realtime Position Management

RTOG Radiation Therapy Oncology Group

SAD Source-to-Axis Distance

SCLC Small Cell Lung Cancer

SI Superior-Inferior

SLD Sublethal Damage

SSB Single Strand Break

SSD Source-to-Surface Distance

TCP Tumour Control Probability

TERMA Total Energy Released in Matter

TPS Treatment Planning Software

Chapter 1

Introduction

1.1 Overview

The objective of radiotherapy is to deliver a lethal absorbed dose of radiation to the cells within a prescribed target volume containing the tumour, while sparing the surrounding healthy tissues as much as possible. Today this is achieved in radiotherapy centres using highly specialized medical imaging systems, advanced software packages for dose calculation in treatment planning systems, and medical linear accelerators (LINACs) to deliver the radiation. Each of the aspects of a radiotherapy treatment are attended to by many well trained individuals and teams.

A radiotherapy treatment is usually delivered with an external beam of high energy X-rays or electrons. When the radiation interacts with the atoms of the patient's tissue, it imparts some of its energy to those atoms. The energy that is absorbed by tissue causes chemical changes to the atoms and molecules within the irradiated cells. These chemical changes can cause biological damage which can ultimately result in the death of the cell. It is the objective of radiotherapy to cause the death of cancerous cells while sparing healthy tissues as much as possible.

The first step towards the development of a radiotherapy plan is the diagnosis of the disease. This can be accomplished with diagnostic imaging tests such as ultrasound, X-ray computed tomography (CT) scans, positron emission tomography (PET) scans [5], or multi-modality imaging such as a PET-CT scan [6]. Once the disease has been diagnosed, the development of a radiotherapy treatment plan can begin in earnest. The major steps are laid out in Figure 1.1. The process begins with careful imaging of the disease site within the patient [7]. This step involves immobilizing the patient in a position which can be reliably replicated later at the time of treatment. The imaging is typically performed using X-ray computed tomography (CT). This generates a detailed map of the patient anatomy which includes the tissue density information required for accurate dose calculation. Great care is taken during the initial simulation CT scan to position the patient in a manner which is as easily reproducible and as comfortable as possible for the patient, because the patient will be repeatedly set up in the same position for all treatment fractions.

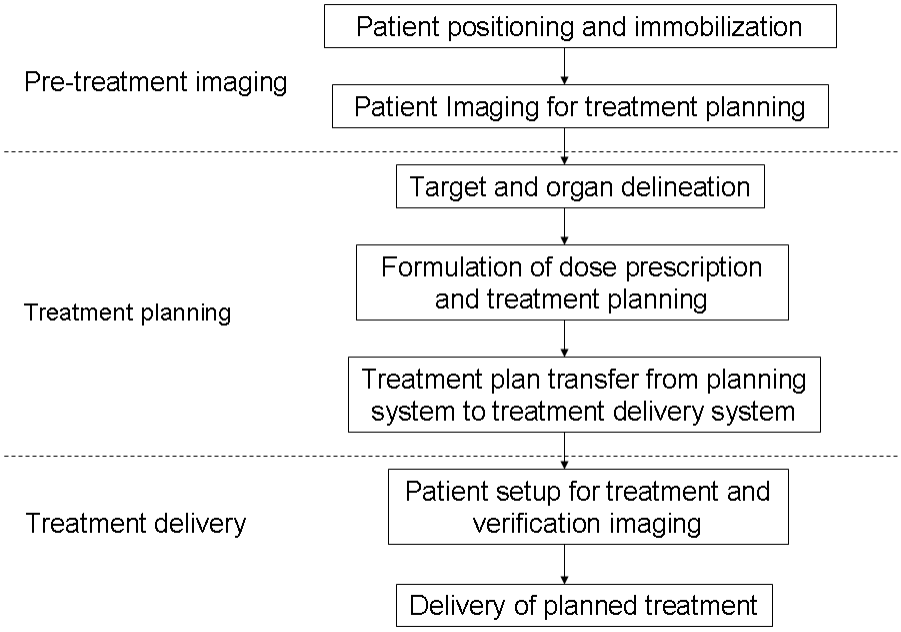

Figure 1.1: The steps involved in the development and delivery of a radiotherapy treatment plan.

After acquiring the patient image, the 3D image data is sent to the treatment planning computers. The relevant target volumes and healthy organs are then delineated on the patient image using specialized treatment planning software. After these structures have been defined within the patient, the X-ray beam angles and shapes are selected in order to deliver the prescribed dose to the target. This is a complicated procedure during which the planner is constantly trying to balance the requirement to deliver the prescribed dose to the target while sufficiently sparing the healthy tissues and organs. Great care must be taken during the treatment planning stage to account for geometric uncertainties, such that the final plan can reliably deliver the prescribed dose. These uncertainties are discussed in more detail below. Finally, the treatment plan data is

transferred to the treatment delivery system. The dosimetry of many plans is confirmed prior to delivering the treatment as part of a regular quality assurance (QA) program.

The final step is the delivery of the treatment. The delivery typically occurs over the course of several days, with the delivery of a single 'fraction' each day. In order to help ensure accurate delivery of the treatment, verification imaging of the patient setup is often acquired on the treatment unit prior to delivering the radiation. Each step in the radiotherapy treatment plays a crucial role in ensuring that the treatment is delivered as planned and, therefore, has the best chance of attaining a positive patient outcome.

1.2 Geometric Uncertainties

From a technical perspective, a key objective of a radiotherapy treatment is the geometrically accurate delivery of the prescribed radiation dose. Patient setup errors and organ motion are the two main factors that could lead to a geometric miss of the dose delivery.

Setup errors result from the difficulty of reproducing the patient's position relative to the original planning CT before each treatment fraction. Many tools are used to assist the radiation therapists with the task of reproducing the planning position of the patient on treatment day. The most common approaches seek to immobilize the patient in the treatment position. This can be accomplished using devices such as vacuum molded bags, which conform to the exterior of the patient then stay rigid for future fractions. When treating head and neck cancers, patient immobilization may be achieved using a plastic mesh mask. The mesh is pliable when heated and can be formed to the patient's face. The mask is also affixed to a frame which can be accurately positioned on the treatment unit. The positioning of a patient on the treatment unit is also guided by the use of fixed, wall mounted lasers. The patient can be aligned to the positioning lasers

using external marks on the patient. As a rule of thumb, a treatment volume will be expanded by a margin of $5\ mm$ in all directions in order to reliably accommodate setup errors.

Organ motion generally falls into two categories: *inter*fraction motion and *intra*fraction motion. Interfraction motion is organ motion that occurs in between treatment fractions. This may result from changes in organ filling or changes in patient anatomy as a result of the radiotherapy (e.g. a shrinking tumour). Interfraction motion will often manifest as change in the position of a target volume (or organ) relative to the rest of the patient anatomy. Intrafraction motion is organ motion occurring during the delivery of a fraction of a radiotherapy treatment. Intrafraction motion typically results from motion that the patient has little or no control over, such as the breathing motion of the lungs or the beating motion of the heart. The management of target motion during external beam radiation therapy (EBRT) is crucial for ensuring agreement between prescribed and delivered dose to the patient and hence successful treatment outcomes.

Of particular interest to this thesis is the large intrafraction motion of the lungs caused by respiration. Other authors have described the motion of targets in the lung due to respiratory motion [8, 9, 10]. It is generally noted that target motion in the lung is largest in the superior-inferior (SI) direction, although each patient presents with a unique motion direction and amplitude. It has also been shown that target motion resulting from patient respiration can cause the displacement of lesions in the lung by up to $2\ cm$ in some cases [11]. Organ motion of this magnitude falls well beyond the typical $5\ mm$ margin used to account for setup uncertainty, and therefore requires additional consideration in the treatment planning process.

1.3 Motion Management of Lung Targets

A report by the American Association of Physicists in Medicine (AAPM) task group TG-76 [12] highlights several different methods for managing respiratory motion, these include: motion

encompassing techniques (margin and target volume definitions), breath-hold techniques, gated treatment delivery and real time target tracking methods. Each of these methods is discussed in more detail in Chapter 3. The use of any of these techniques requires consideration of trade-offs between dose conformality, technical feasibility, demand on clinical resources and patient condition.

The least technically demanding (and therefore most widely used) of these approaches is to define treatment volumes that account for the expected motion of the target. Within this approach to motion management there are several different methods which can be used to define treatment volumes. Widely accepted motion encompassing techniques include: margin expansion [13, 2, 1], the use of an internal target volume (ITV) determined by the range of target motion [14, 15] and probabilistic approaches to volume definition [16]. Since, by definition, the expansion of treatment volumes is accompanied by an increase in normal tissue complication probability (NTCP), a balance must be struck between improving target dose coverage with larger treatment volumes and potential complications to healthy tissues.

Historically the motion of targets in lungs was studied with the use of fluoroscopic imaging [17, 18, 19, 20]. The results of these types of studies alloweed researchers to make a lot of progress in determining the extent of target motion, how external chest motion correlates with target motion within the lung and early attempts at determining necessary treatment margins to compensate for target motion. Ultimately fluoroscopic approaches fell out of favour when studying lung target motion due to difficulty of incorporating the fluoroscopic imaging data into the radiotherapy treatment process.

The increased availability of four dimensional computed tomography (4DCT) scans has increased the viability of patient-specific approaches to motion management of lung targets. 4DCT data sets provide clinicians with complete 3D images of the patient anatomy and target at several different phases of a given patient's respiratory cycle [21]. The improved contrast offered by 3D

CT images as compared to the 2D projection images of a fluoroscopic scan allows for a more detailed study of the motion. As with fluoroscopy, 4DCT allows for gathering information regarding the patient's breathing pattern [15]. A clearer picture of the target motion within the lung allows for better incorporation of the target motion into the treatment plan. However, a thorough understanding of the dosimetric impact of the organ motion must be attained before the motion information can be used clinically.

One calculation model used to predict the dosimetric impact of target motion on the delivered dose distribution is the convolution model originally proposed by Leong [22]. This model takes a planned static dose distribution (D_0) and a probability density function (PDF) describing the target location over time as its inputs. The model predicts the delivered dose distribution by performing a mathematical convolution of the inputs. The result of this convolution is a dose distribution which has been 'blurred' by the motion of the target (D_b), thereby reducing target dose coverage and increasing dose to organs at risk (OARs). The model can be written succinctly as: $D_b = D_0 \otimes PDF$. An early attempt at using the convolution model in the context of intrafraction motion was published by Lujan et. al. in 1999 [23]. The authors used fluoroscopy to determine the 1D motion of the target in order to generate the required PDF. They showed that incorporating organ motion into the treatment plan was important to maintain dose coverage and that the convolution model provided an acceptable approximation to the delivered dose distribution [23]. As reported by other authors [24], the blurring effect of target motion is predominant in regions of the dose distribution with sharp dose gradients. Since the sharp dose gradients are typically associated with field edges, selection of appropriate target margins becomes a crucial step in ensuring adequate target coverage. A predictive model such as the convolution model is a valuable tool for analyzing the impact of target motion on the delivered dose distribution.

1.4 Scope of Work

In searching for the appropriate balance it becomes clear that patient-specific approaches to target volume definition are necessary because of the wide variation in patient anatomy, disease manifestation and breathing patterns. Furthermore some lung cancer patients present highly irregular breathing patterns, characterized by large inter- or intrafraction changes to target motion amplitude or cycle frequency. These patients present unique challenges with respect to modeling and predicting the target position throughout the breathing cycle and will be less amenable to a class solution. However, by developing margin selection guidelines that can be implemented by any radiation treatment center, the benefits of a patient-specific approach can be attained. Therefore, the aims of this work are as follows:

1. to investigate the breathing patterns of radiotherapy patients using 4DCT
2. to apply a model of the dosimetric impact of lung motion on the delivered dose distributions resulting from intrafraction breathing motion
3. to experimentally verify the model predictions using radiochromic film and a dynamic anthropomorphic thorax phantom
4. to establish a set of guidelines for selecting motion compensating treatment margins on a patient-specific basis.

1.5 Outline of Thesis

The relevant photon interactions contributing to absorbed dose and radiobiological principles for EBRT of lung tumours is reviewed in Chapter 2. Chapter 3 reviews the staging and classification

of lung tumours along with treatment techniques, methods for quantifying lung target motion and the margin recipes currently available in the literature. In Chapter 4, a detailed review of the convolution model and its inputs is presented. This includes an analysis of the assumptions implicit to the model as well as an analysis of the implications of using the model in the context of intrafraction motion. Chapter 5 discusses the experimental verification of the convolution model. The procedures surrounding the use of gafchromic film and a dynamic thorax phantom are detailed. Chapter 6 discusses the details of the motion simulation study that was performed, as well as its results and interpretation. Chapter 7 contains a sensitivity analysis of the convolution model as applied to Gaussian dose profiles and motion PDFs. By using Gaussian functions as the basis of the sensitivity analysis, an analytical approach becomes feasible. Finally, Chapter 8 offers a summary and the conclusion of the study, as well as a look at some potential future work.

There are two Appendices included in this thesis as well. Appendix A details work that was presented at the Canadian Organization of Medical Physicists annual scientific meeting in 2013. This work extends the idea of the effective dose gradient due to motion and applies it to the concept of adaptive radiotherapy. The result is a proposal for a tool that would assist radiation therapists with patient setup and treatment decision making. Appendix B details the MATLAB code used to perform the simulation study that is detailed in Chapter 6.

Chapter 2

Photon Interactions, Absorbed Dose and Radiobiology

2.1 Introduction

A thorough understanding of the physical action of radiation and the subsequent chemical and biological effects has allowed for the development of radiation therapy for treating cancers. Although modern treatment centres now exist which offer radiation therapy using protons and other heavy ions, X-rays and electrons are still the most common form of radiation used in clinics today.

X-rays that enter a patient's body have a probability to interact with the tissues based mainly on the energy of the X-ray, the tissue composition and the amount of tissue in the X-ray path. X-rays that do interact with the patient's body will transfer some or all of their energy to the atoms and electrons comprising the tissue. When electrons absorb energy from the X-rays they may in turn be ejected from their orbits, thereby leaving the associated atom ionized; or a bound

electron within the atom may move to a new orbit, thereby leaving the atom in an excited state. Any ejected electrons will also travel through the tissue, interacting with other atoms and causing the ejection of more electrons from their bound states. These further interactions cause more ionizations and the process repeats until all the energy of the initial electron has been dissipated or absorbed by the tissue. The energy that is absorbed by the tissue per unit mass is referred to as the 'absorbed dose' and is measured in terms of the SI unit of Gray (Gy) [3], defined as the energy absorbed per unit mass of absorbing material (J/kg). The amount of energy absorbed by a given mass of tissue is an indirect measure of the biological damage caused to that tissue by the radiation.

The ionization of atoms in the patient's tissue is the first step in a chain of events that can ultimately lead to cell death. This chapter aims to deal with a description of photon interactions relevant to radiotherapy and the radiobiological principles at play when treating cancers. A more detailed discussion of radiotherapy for the treatment of lung cancers specifically is offered in chapter 3.

2.2 Photon Interactions

2.2.1 Linear Attenuation Coefficient

The attenuation of a photon beam entering a medium is described by the Beer-Lambert law (Equation 2.1)

$$I(x) = I_0 e^{-\mu x}. \tag{2.1}$$

In this formulation, I is the intensity of the photon beam at a depth x into the medium, I_0 is

the initial intensity of the beam and μ is the linear attenuation coefficient of the medium, often described in terms of the units cm^{-1}. The linear attenuation coefficient itself depends on the material composition and photon energy. The law can also be written in terms of the 'mass attenuation coefficient' described by

$$I(x) = I_0 e^{-(\mu/\rho)\rho x}, \tag{2.2}$$

where ρ is the density of the medium and (μ/ρ) is identified as the mass attenuation coefficient (typically expressed in units of cm^2/g). The mass attenuation coefficient describes the ability of a medium to attenuate photons independent of the material density. The quantity ρx is known as the 'mass thickness' with units usually expressed as g/cm^2. The Beer-Lambert law gives a description of the overall attenuation of a photon beam, but does not delve into the specifics of the photon interactions.

The attenuation coefficient plays a key role in X-ray CT imaging. The 3D images reconstructed from CT data are displayed in terms of the Hounsfield Units (HU) scale. The HU scale is a linear transformation of the linear attenuation coefficient scale such that pure water has a value of $0\ HU$, and air (at standard temperature and pressure) has a value of $-1000\ HU$. The HU value of a given linear attenuation coefficient [25] is determined by

$$HU = \frac{\mu - \mu_{water}}{\mu_{water} - \mu_{air}} \times 1000. \tag{2.3}$$

Since CT images are displayed in HU, the quality of a CT image can be interpreted based on the variance of the HU values within a region of the imaging subject known to have constant density. The lower the HU variance, the better the image quality. The role of CT images and the importance of their quality in context of radiotherapy treatment planning for lung cancers is discussed thoroughly in chapter 3.

2.2.2 Basic Photon Interactions

Photon interactions with matter are understood to occur through one of eight possible pathways. Those interactions are:

1. Thomson scattering (Elastic scattering)
2. Rayleigh scattering (Elastic scattering)
3. Raman Scattering (Inelastic scattering)
4. The photoelectric effect
5. Compton scattering
6. Pair production
7. Triplet production
8. Photonuclear interactions

The probability of any one of these interactions taking place depends on a myriad of parameters. The most important of the parameters are the photon energy and the atomic number (Z) of the medium. For the typical atomic number of soft tissue ($Z \simeq 7$) and the photon energies commonly used in the diagnosis and treatment of cancers, the most relevant interactions are: Rayleigh scattering, the photoelectric effect, Compton scattering and pair production. The plot in Figure 2.1 shows the mass attenuation coefficients for the relevant photon interactions with soft tissue, as adapted from Bushberg's book 'The essential physics of medical imaging' [26].

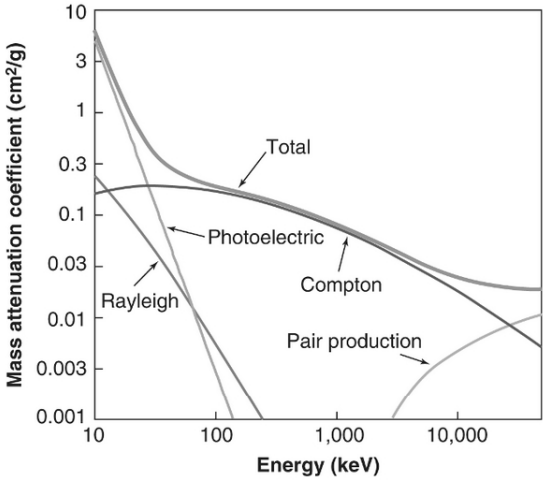

Figure 2.1: A plot of the mass attenuation coefficient versus photon energies for soft tissue ($Z \simeq 7$). The photoelectric effect, Compton scattering and pair production are the dominant processes in the diagnosis and treatment of cancers. This image appears in Bushberg's book 'The essential physics of medical imaging' [26].

Each of these interactions has a role to play in the attenuation of an X-ray photon beam. However, Rayleigh scattering is an elastic process that results in the interacting photon changing direction without imparting any energy to the medium. Therefore, Rayleigh scattering is not considered an important interaction in the context of radiotherapy. The other three dominant processes are discussed in more detail in the following sections.

2.2.3 Photoelectric Effect

In the case of photoelectric interaction, an inner shell electron of the absorbing medium completely absorbs the incoming photon [4]. The initial energy of the recoiling photoelectron (K_{pe}) is calculated by taking the difference between the incident photon energy ($h\nu$) and the work

function of the bound electron ($|W|$) as shown in Equation 2.4. The photoelectron then proceeds through the medium as a directly ionizing particle.

$$K_{pe} = h\nu - |W| \tag{2.4}$$

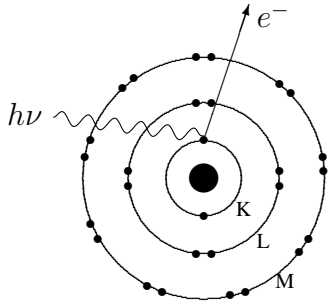

Figure 2.2: A schematic representation of a photoelectric event. Redrawn from Radiobiology for the Radiologist [3].

2.2.4 Compton Effect

In the case of a Compton scattering event, the incoming photon interacts with a loosely bound outer-shell electron of the absorbing material [4]. This electron absorbs a portion of the incoming photon's initial energy and is ejected from the atom. The law of conservation of energy can be used to determine the scattering angles of both the recoil electron and photon. The various quantities involved are related by the equations shown below, where m_0 is the rest mass of the electron and T is the energy transferred from the incoming photon to the recoil electron. The recoil electron proceeds through the material and acts as a directly ionizing particle while the recoil photon goes on to further interact with the medium.

The energy of the scattered photon is can be expressed by

$$h\nu' = \frac{h\nu}{1 + (\frac{h\nu}{m_0c^2})(1 - \cos(\phi))}. \tag{2.5}$$

The electron scattering angle is given by

$$\cot(\theta) = (1 + \frac{h\nu}{m_0 c^2})(\tan(\frac{\phi}{2})). \tag{2.6}$$

The conservation of energy dictates that

$$h\nu = h\nu' + T. \tag{2.7}$$

Compton scattering is by far the most important photon interaction in the context of radiotherapy. As seen in Figure 2.1, the likelihood of Compton scattering events dominates the other interactions in soft tissue for photon energies ranging from $\sim 80\ kV$ to $\sim 12\ MV$.

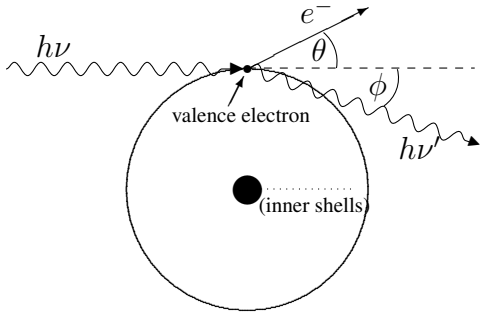

Figure 2.3: A schematic representation of a Compton scattering event. Redrawn from Radiobiology for the Radiologist [3].

2.2.5 Pair Production

Pair production can occur when a high energy photon (≥ 1.022 MeV) interacts with the nucleus of an atom. The photon is transformed into a positron and an electron. On average the energy is shared equally between the two particles. As the positron slows down in an absorber it will likely undergo an annihilation event with an electron in the absorber. The annihilation event destroys both the positron and the electron in favor of two photons headed in opposite directions with equal energy ($h\nu' = h\nu'' = m_0 c^2 = 511\ KeV$).

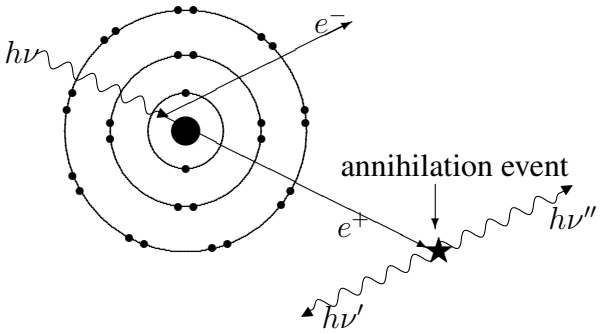

Figure 2.4: A schematic representation of a pair production and annihilation event. Redrawn from The Physics of Radiology [4].

2.3 Absorbed Dose

Each of the photon interactions described above result in the liberation of energetic electrons. As these electrons travel through a medium, they transfer their energy to the medium via Coulomb force interactions. The absorbed dose is defined as the energy transferred to an absorbing medium per unit mass of the medium. This can be described as

$$D = \frac{\Delta E}{\Delta m}. \tag{2.8}$$

The energy absorbed by a medium can cause ionizations, atomic excitations or break chemical bonds. The resulting chemical changes can disrupt biological processes and ultimately result in cell death. This sequence of events is displayed in Figure 2.5.

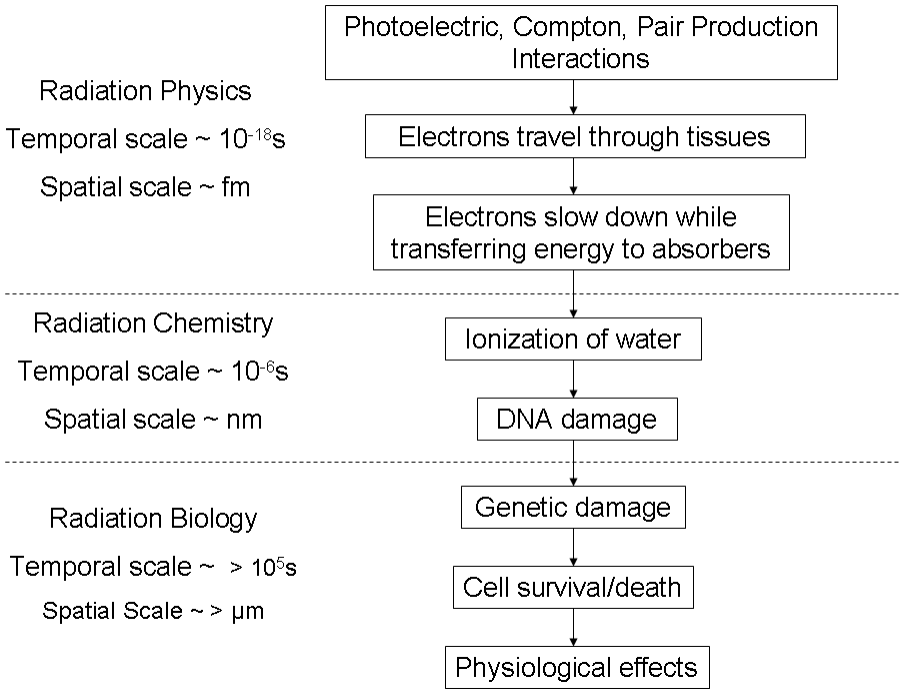

Figure 2.5: A flow chart tracking the scales and processes associated with radiation damage.

As a charged particle proceeds through the absorbing medium it will typically undergo many interactions before dissipating all of its energy and coming to rest. The absorbed dose delivered to the medium in any given volume can be determined by summing all the energy left behind by all the charged particles which passed through the volume and dividing by the mass of the medium within the given volume.

2.4 Radiobiology

Radiobiology is the study of the action of ionizing radiations on living things [3]. Shortly after the discovery of X-rays by Röntgen in 1895, the first biological effects of radiation were documented by Becquerel. He left a container of radium in his vest pocket and noticed erythema and ulceration develop on his skin roughly two weeks later. Over the course of the following century, the entire theory of radiobiology was developed by a huge number of contributors. A detailed understanding of radiobiology has allowed for the refinement of radiotherapy treatments and the exploitation of certain effects to improve treatment outcomes.

2.4.1 Mechanism of Cellular Damage

The DNA strand is the main target within a cancer cell that clinicians aim to damage with radiation therapy treatments [3]. By causing disruptions or breaks to the DNA, the cell will fail to reproduce and ultimately die, thereby limiting the growth of the cancer. The most effective form of damage to the DNA is known as a double strand break (DSB). In the case of a DSB, a disruption to each of the two phosphorus backbones of the DNA strand occurs within a distance of approximately ten base pairs from one another. A DSB is very difficult for the cell to repair and usually results in cell death. Other less lethal forms of damage are single strand breaks (SSB) and base damage. In the case of a SSB only one of the DNA backbones is disrupted. In the case of base damage, the DNA backbone remains intact but a base-pair will have been the subject of an ionization or chemical disruption. Most cells are very efficient at repairing SSBs and base damage, and these type of DNA damage do not reliably result in cell death.

DNA strand breaks can be measured using a technique known as Pulsed-field Gel Electrophoresis (PGFE) [3]. This technique separates the DNA fragments of irradiated cells by

applying a pulsed electromagnetic field which pulls the fragments through a porous gel [27]. Large DNA fragments do not travel through the gel as easily as smaller fragments under the force of the pulsed field, allowing them to be separated from one another. These experiments show that as the radiation dose delivered to the cell increase, more DNA fragments and smaller DNA fragments are produced [28].

There are two main mechanisms known to cause these breaks to the DNA strand via delivered radiation. In the first case the DNA strand is directly ionized by a charged particle. The ionized DNA strand becomes chemically reactive at the location of the ionization event and new chemical bonds can form, thereby disrupting the DNA backbone. This is the dominant mechanism of damage for radiations with high linear energy transfer (LET). The second case is known as indirect ionization. In this situation a molecule (typically a water molecule) in the surrounding medium is ionized or disrupted itself, either by direct or indirect radiation. The ionized or disrupted water molecule, known as a hydroxyl radical, is highly chemically reactive. If this reactive molecule diffuses within the vicinity of the DNA strand within its short lifetime, it will react with the DNA backbone causing a strand break.

2.4.2 Linear Energy Transfer

Linear energy transfer (LET) is the amount of energy transferred by a charged particle to the surrounding medium per unit length of path. LET is defined by the Equation below, where dE is the average energy locally imparted to the medium as it travels a distance dl [3]

$$LET = dE/dl. \tag{2.9}$$

LET is usually discussed in terms of the units $keV/\mu m$ of unit density material. It should be noted that energy imparted by a charged particle as it travels through a medium occurs at discrete

locations along the track of the particle. As such, the LET of a given particle is an average of the energy imparted to the medium over the length of the particle track. The LET of a given particle depends on the particle energy, particle charge and the density of the medium. In Table 2.1 adapted from Hall [3] the LET of various particles and energies is shown for comparison.

Radiation	LET ($keV/\mu m$)
Cobalt-60 γ-rays	0.2
250-kV X-rays	2.0
10 MeV protons	4.7
150 MeV protons	0.5
2.5 MeV α particles	166
2 GeV Fe ions (space radiation)	1000

Table 2.1: LET values for various particles and energies in water. Adapted from Radiobiology for the Radiologist [3]

Due to the dependence of LET on the particle energy, the LET varies as the particle imparts its energy to the medium along its track. In the case of high energy protons ($\geq 150\ MeV$) the LET as the particle enters water is approximately $0.5\ keV/\mu m$. As the particle loses energy the LET increases, with a sharp peak reaching approximately $100\ keV/\mu m$ at the end of the particle track. This peak is known as the Bragg peak. Although all charged particles exhibit a sharp peak in LET at the end of the track, only heavy ions show the characteristic peak in dose deposition due to a more predictable path. Light charged particles, such as electrons, travel along a torturous pathway with many changes in direction [29]. This means that the sharp dose deposition due to the Bragg peak does not occur at a predictable depth or location.

2.4.3 Linear-Quadratic Model of Cell Survival

Radiotherapy treatments are prescribed in terms of an absorbed dose, measured in Gray (Gy), to the target volume. The absorbed dose is an indirect measure of damage caused to the tissue by the energy deposited from charged particles. As the absorbed dose in a target volume increases, the likelihood of causing a SSB or a DSB increases, thereby increasing the chances of causing cell death. Radiobiological cell survival studies typically look to relate the absorbed dose to fraction of surviving cells. These cell survival studies have resulted in a model of cell survival known as the linear-quadratic (LQ) model, first proposed by Douglas and Fowler in 1976 [30]. The equation governing the LQ model is defined as

$$S = e^{-\alpha D - \beta D^2}. \tag{2.10}$$

In this formulation of the model, S is the fraction of surviving cells, D is the absorbed dose and α & β are tissue specific parameters describing the 'early' and 'late' response of the tissue to the absorbed dose. The α and β parameters of the LQ model describe the sensitivity (ease of cell killing) of a given cell line to a single fraction of low and high dose radiation respectively. α describes the initial slope (low dose region) of the survival curve, and can be interpreted as the cell's susceptibility to DNA damage from a single charged particle track. β describes the quadratic component (curvature, final slope) of the survival curve in the high dose region. β can be interpreted as the cell's susceptibility to DNA damage from two unique charged particle tracks. A sample survival curve for normal and cancerous tissue is shown in Figure 2.6. f

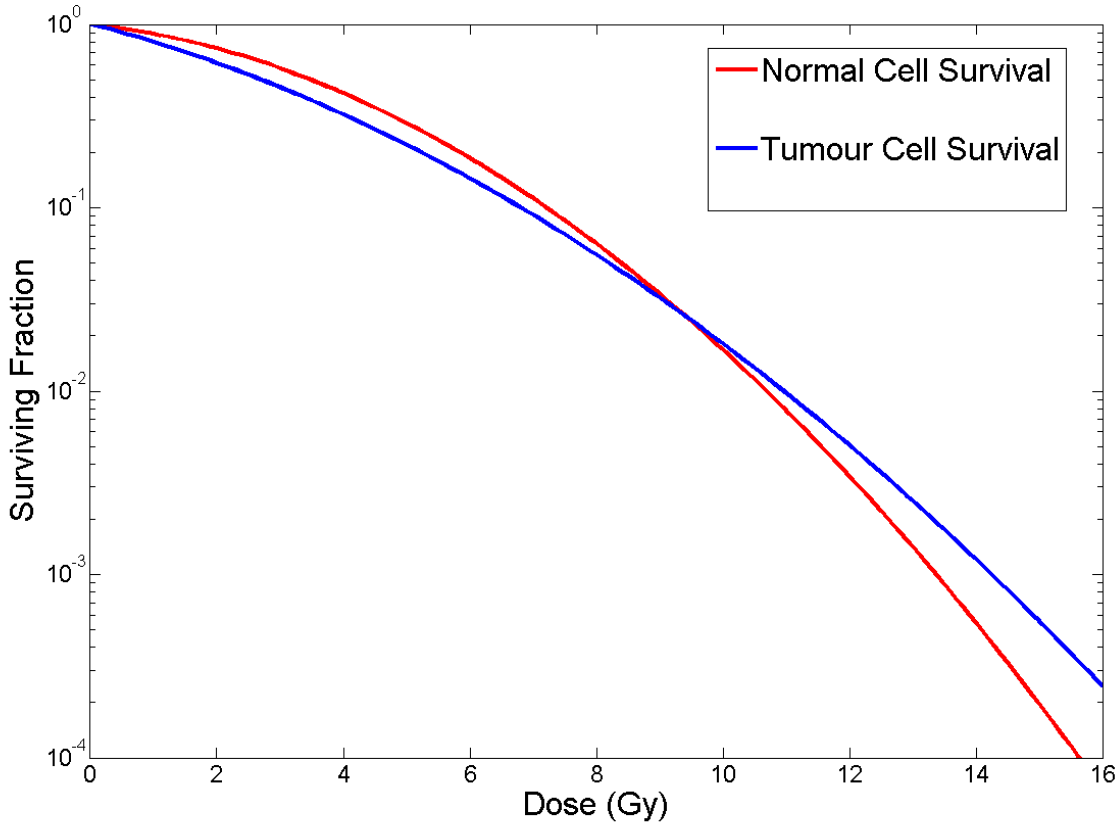

Figure 2.6: An example of normal and cancerous cell survival curves predicted by the LQ model. The normal cells have $\alpha = 0.088$ and $\beta = 0.032$ for a ratio of $\alpha/\beta = 2.75$, the cancer cells have $\alpha = 0.204$ and $\beta = 0.020$ for a ratio of $\alpha/\beta = 10.4$

The ratio α/β describes the cell's insensitivity to dose fractionation. In other words, the survival of cells with a low α/β ($\simeq 3$) is strongly dependent on the fractionation scheme. These tissues are known as 'late responding' tissues and include the lung and spinal cord [3]. On the other hand the survival of cells with a high α/β ($\simeq 10$) is weakly dependent on the fractionation

scheme. These tissues are known as 'early responding' tissues and includes skin and bone marrow cells. The therapeutic advantage in radiotherapy is attained by exploiting this difference in fractionation sensitivity and by delivering lower absorbed dose to the healthy tissue.

One feature of the LQ model that is not borne out in actual cell survival data is the continuously bending nature of the curve. In reality, the cell survival curve would have a final straight segment on a log-linear plot starting around the seventh decade of cell killing. This empirical data is not well predicted by the LQ model. However, in the range of doses typically delivered as a daily fraction in radiotherapy, the LQ model does a reasonably good job of predicting cell survival [3].

2.4.4 The Four 'R's' of Radiobiology

The effectiveness of fractionated radiotherapy can be explained by appealing to the '4 R's' of radiobiology: reoxygenation, repair, redistribution, and repopulation. Each of these concepts pertains to the cells of tissues undergoing irradiation and, along with the mechanisms for cell damage, form the basis for understanding radiobiology and cell survival in the context of radiotherapy.

Reoxygenation

The oxygenation of a cell's environment is described by the partial pressure of the oxygen content in the surrounding medium, with high oxygenation refering to a partial pressure of oxygen. The role of oxygenation in radiobiology was first investigated in detail by Mottram in the 1930's [31]. He was able to show that small tumours were more radiosensitive than large tumours due to oxygenation. Mottram also suggested fractionation in order to exploit the oxygenation effect. Later, work done by Read in the 1950's resulted in quantitative measurement of the effect

of oxygen concentration [32]. The role of oxygenation is typically understood in terms of the oxygen enhancement ratio (OER). The OER is simply the ratio of the radiation doses required to achieve the same biological outcome with the cells under hypoxic and aerated conditions [3].

The idealized understanding of the relation between oxygen concentration and radiosensitivity is shown in Figure 2.7 below. Starting from a relative radiosensitivity of 1 for the completely anoxic scenario, the radiosensitivity quickly rises in the presence of oxygen. With oxygen tension of about $3\ mm$ Hg (corresponding to about 0.5% oxygen) the radiosensitivity doubles, and at oxygen tension of $30\ mm$ Hg the relative radiosensitivity is about three times higher than the anoxic scenario. There is little gain in radiosensitivity for situations with oxygen tension higher than $30\ mm$ Hg.

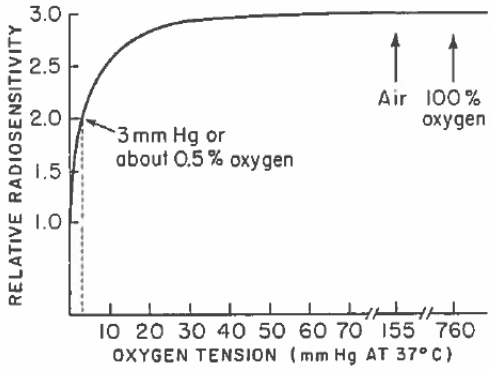

Figure 2.7: An idealized plot of the OER vs. Oxygen tension as shown in Radiobiology for the Radiologist [3]. The OER quickly increases from 1 for anoxic cells to approximately 3 when the Oxygen tension reaches about $30\ mm$ Hg. The presence of molecular Oxygen 'fixes' radiation damage, causing it to become permanent.

It is hypothesized that this increase in radiosensitivity occurs due to oxygen fixation [3]. The damage caused to DNA due to indirect action of radiation is typically easily repaired by the

cell, especially in anoxic situations. However, molecular oxygen readily reacts with the site of damage on the DNA strand, causing the damage to be permanent. Therefore, when molecular oxygen is available to react with damage to the DNA, more permanent damage to the DNA occurs, resulting in more cell death and greater radiosensitivity.

Reoxygenation is the process by which hypoxic tumour cells become oxygenated after a tumour receives a dose of radiation. This process occurs due to the usual structure of a tumour mass. The organization of cells in a tumour is haphazard (compared to healthy tissue) and therefore the transfer of nutrients throughout a larger tumour is poor. This results in 'typical' tumour structure with three layers: a layer of aerobic cells surrounding a layer of hypoxic cells which in turn surround a necrotic core at the center of the tumour. After irradiation, the aerobic cells on the exterior of the tumour will be preferentially killed due to increased radiosensitivity. As these cells die off and are removed by bodily systems, oxygen is able to penetrate deeper into the tumour, thereby reoxygenating previously hypoxic cells. When the next fraction of radiotherapy is delivered, the previously hypoxic cells will now be more radiosensitive due to reoxygenation. With repeated delivery of fractionated radiotherapy, the reoxygenation effect can be exploited to increase cell killing for an equal delivered dose.

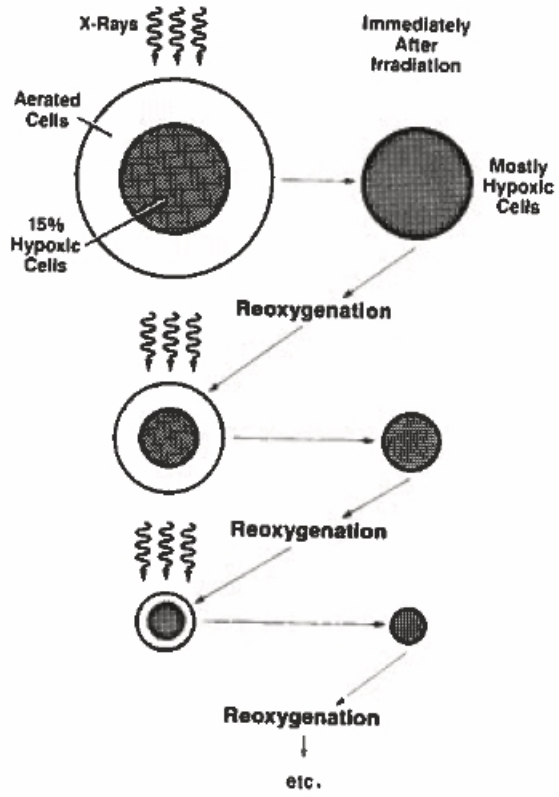

Figure 2.8: A depiction of the reoxygenation process as shown in Radiobiology for the Radiologist [3]. The oxygenated cells on the exterior of the tumour are more radiosensitive and are preferentially killed. As the previously hypoxic cells become reoxygenated, their radiosensitivity increases, making them more susceptible to radiation damage during the next treatment fraction.

Redistribution

Redistribution in the context of radiobiology refers to the distribution of cells across the various stages of the cell cycle. For mammalian cells, the cell cycle, as shown in Figure 2.9 is divided into four phases labeled: M, G_1, S, G_2. M is the 'mitosis' phase during which the cell is actively

dividing in two. S is the 'synthesis' phase during which the cell is synthesizing a replicate DNA strand. The 'G_1' and 'G_2' phases are gaps in the cell cycle during which the cell appears inactive in terms of growth and division events.

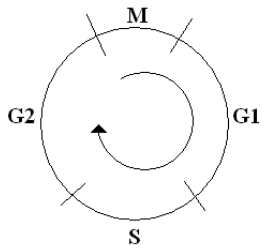

Figure 2.9: A depiction of the cell cycle adapted from Radiobiology for the Radiologist [3]. Cells progress through the cycle at different rates depending on cell type, and can become blocked in a given phase due to environmental conditions. Cells are most radiosensitive during mitosis (M) and least radiosensitive near the end of synthesis (S).

The radiosensitivity of the cell varies as it progresses through the four phases of the cell cycle. It is generally accepted that cells are most sensitive during the M phase and least sensitive close to the end S phase [3]. The increase in sensitivity during M phase is likely due to the complex and intricate process of mitosis being interrupted. The resistance shown in late S phase is likely due to the availability of the homologous recombination repair pathway, which is discussed in more detail in the following subsection.

The distribution of cells across the stages of the cell cycle is uniform for a typical population of healthy growing cells. However this uniform distribution can be disrupted by delivering a radiation dose to the cells. Cells in the radiosensitive phase of the cell cycle will be preferentially killed by a dose of radiation, resulting in the remaining cells being more heavily concentrated in

the radioresistant phases. The remaining cells will then proceed through the cell cycle, naturally redistributing themselves into more radiosensitive phases one again. This redistribution acts to sensitize the cell population to a future dose of radiation.

Repair

Radiation damage to cells can be classified in one of three categories: lethal damage, potentially lethal damage (PLD) and sublethal damage (SLD). Lethal damage is irreparable and leads directly to cell death by definition, PLD is damage that is subject to influence by the local environmental conditions the cells face after irradiation, and SLD is damage that can be reliably repaired by the cell over the course of hours under normal conditions [3].

Lethal radiation damage to cells usually takes the form of DSBs. However there are two processes by which the cell may attempt to repair a DSB, known as homologous recombination repair (HRR) and nonhomologous end joining (NHEJ) [3]. HRR is a very reliable repair mechanism that uses an undamaged DNA strand as the template for repair of the broken DNA strand. This repair pathway occurs most frequently in the late S or G_2 phase of the cell cycle. The NHEJ repair pathway for DSBs does not require an undamaged template. Instead, the repair mechanism is able to identify the broken ends of the DNA strand, prepare the ends for repair, 'bridge' the broken ends with the required base pairs and then reattach the broken ends through the process of ligation. While both pathways result in the reliable repair of DSB, they are not perfect and can occasionally lead to faulty repairs resulting in chromosomal aberrations. These aberrations may ultimately cause cell death or hereditary disease.

PLD is damage that would usually cause cell death, but may be overcome under certain local environmental conditions of the cell. The general consensus is that PLD can be repaired when the conditions for cell growth are poor [3]. In this situation, the cell will not be likely to undergo

the taxing process of mitosis. Instead the cell's resources can be put towards the necessary DNA repair. This form of damage was described by Little *et al.* [33] in an in vitro experiment. The group showed that a greater fraction of cells survive replating if they are held in a stationary state (poor growth conditions) for at least 6 hours post irradiation as compared to the fraction of cells that survive replating immediately after irradiation. It was later shown that the rate of repair and repair pathways involved in the in vitro experiment are comparable to the in vivo situation. Although the existence of PLD is widely accepted, its role in radiotherapy is not generally agreed upon [3].

SLD is damage that would usually be repaired by the cell. The repair of SLD can be observed in experiments that divide a given radiation dose into two fractions spaced apart in time. Shown in Figure 2.10 is a plot of the surviving fraction of cells versus the time interval between two equal doses of radiation adapted from Elkind *et al.* [34]. By allowing for as little as 30 minutes between irradiations, the surviving fractions is appreciably higher. After about two hours between fractions, the gain in cell survival plateaus. The increase in cell survival in the approximately two hours post irradiation is understood to be due to the repair of SLD. The hypothesis is that cell survival is decreased by compounding multiple events that would normally result in SLD on their own. Therefore, by allowing time between fractions, SLD is repaired before multiple SLD events can be accumulated in the same region of the DNA strand.

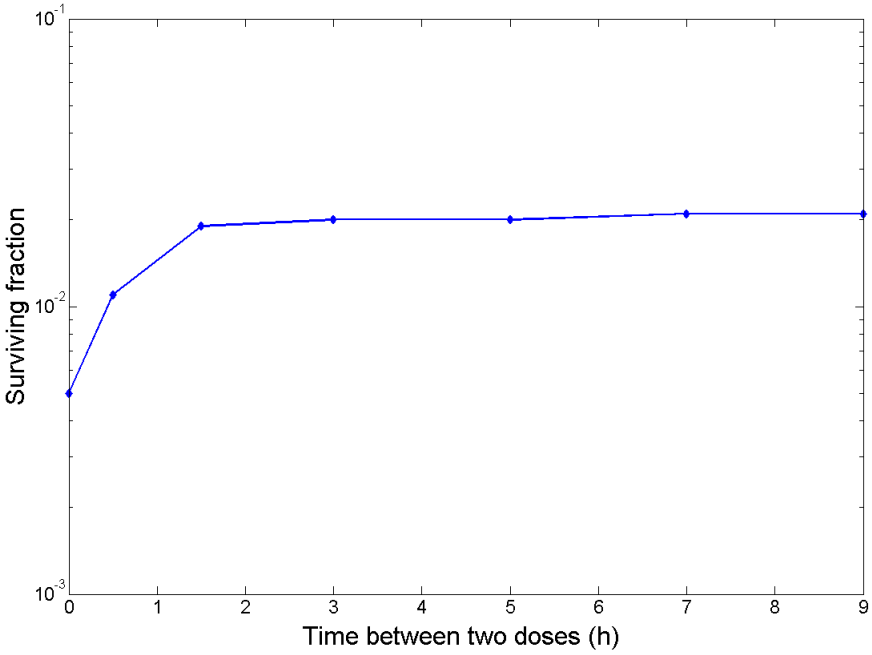

Figure 2.10: A plot of the surviving fraction of cells after two doses of radiation separated in time ($7.63\ Gy$ followed by $7.95\ Gy$). The data are adapted from the experiments performed by Elkind *et al.* [34] with Chinese hamster cells incubated at $24\ ^{\circ}C$. The surviving fraction increases rapidly when the time between doses allows for SLD repair.

Repopulation

Repopulation simply refers to the growth of new cells, whether cancerous or normal, over the course of a radiotherapy treatment. Work done by Fowler *et al.* showed that extra radiation dose is required to counteract the proliferation of new cells [35]. However, it is necessary to consider the effect of repopulation in the context of the early and late responding tissues discussed earlier. Early responding tissues in humans with a high α/β ratio are triggered to start proliferating

within a few weeks of the start of a fractionated radiotherapy regime. As a result the extra dose needed to compensate for this proliferation is not required initially, but does increase over time. On the other hand, late responding tissues will not begin proliferating within the typical $6 - 8$ week time frame of a fractionated radiotherapy regime. Therefore, as stated by Hall [3] 'prolonging overall time within the normal radiotherapy range has little sparing effect on late reactions but a large sparing effect on early reactions'. This must be balanced with the knowledge that excessive prolongation of the fractionation scheme could allow for the tumour cells to begin proliferating during the treatment.

2.4.5 Tumour Control Probability and Normal Tissue Complication Probability

Tumor Control Probability (TCP) as originally described by Munro *et al.* [36] is defined as the probability that the elimination of all tumour cells has been achieved. Webb *et al.* [37] later derived an expression for TCP based on the survival of cells exposed to a uniform dose of radiation. Where the number of surviving cells is given by the familiar LQ model (the quadratic term is omitted while considering the typical radiotherapy fraction size of $\simeq 2\ Gy$)

$$S = e^{-\alpha D}. \tag{2.11}$$

The probability of eliminating all the tumour cells is then simply given by

$$TCP = e^{-S}. \tag{2.12}$$

When the TCP is plotted as a function of dose, the resulting curve is sigmoidal in nature with increasing dose resulting in an increased probability of tumour control. However, increasing

the dose is also associated with an increase in normal tissue complication probability (NTCP). Perhaps the most popular model of NTCP was developed by Lyman [38] and expanded upon by Burman *et al.* [39]. The basis of the so-call LKB model of NTCP is an error function and four parameters defined by the following equations:

$$NTCP = \frac{1}{\sqrt{2\pi}} \int_{-\infty}^{t} e^{-t^2/2} dt, \tag{2.13}$$

$$\nu = V/V_{ref}, \tag{2.14}$$

$$t = \frac{D - TD_{50}(\nu)}{(m \times TD_{50}(\nu))}, \tag{2.15}$$

$$TD(\nu) = TD(1) \times \nu - n. \tag{2.16}$$

The parameter ν is defined as the fraction of the organ irradiated (or the proportion relative to a reference volume), D is the dose, TD_{50} is the tolerance dose resulting in a 50% complication probability, n is the parameter governing the volume dependence of the complication probability and m is the parameter governing the slope of the curve (at 50% complication probability).

It should be noted that when the NTCP is plotted as a function of dose, it is monotonically increasing [39]. Therefore any increase in dose to the healthy tissues of the patient will increase the probability of complication. Similarly, when NTCP is plotted as a function of the partial volume of the irradiated tissue, it is also monotonically increasing [39]. Therefore, any increase in the volume of normal tissue being irradiated to a given dose will also increase complication probability. These two considerations are at the heart of treatment planning. The ideal treatment

plan balances the delivery of the prescribed dose to the target volume with the volume and dose of irradiated normal tissues.

When plotted together versus the delivered dose, both the TCP and NTCP appear as sigmoidal curves separated along the dose axis. Figure 2.11 shows the plot in a hypothetical situation. A given dose will result in a given probability for NTCP and TCP. The difference in the relative responses of the tissues to a given dose is termed the 'therapeutic advantage'. The outcomes of radiotherapy treatments can be improved by increasing the therapeutic advantage. The TCP and NTCP curves can be shifted along the dose axis through several means, such as: the action of any of the 4 R's, by radiosensitizing the tumour with a chemical agent or by increasing the radioresistance of the OARs.

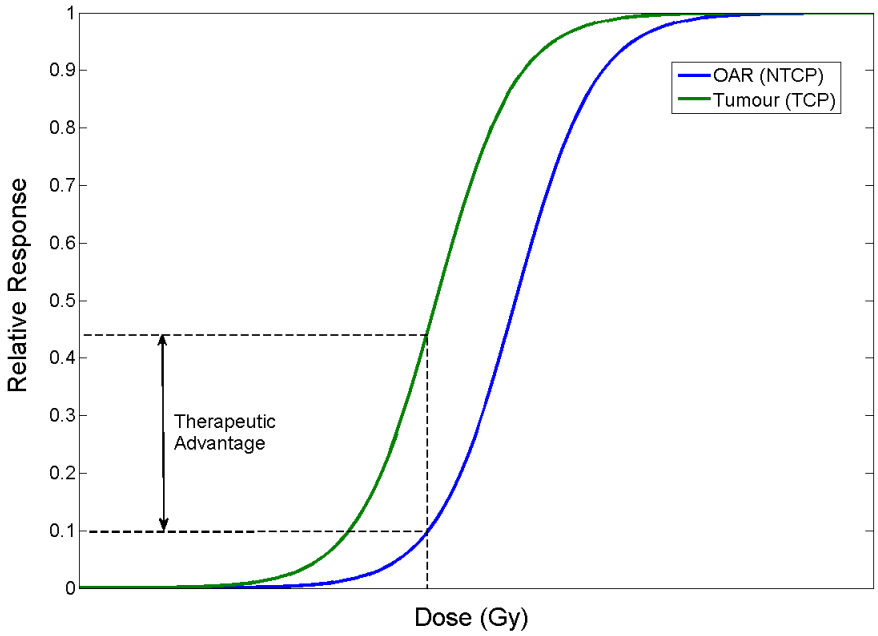

Figure 2.11: A hypothetical plot of the TCP and NTCP sigmoid curves. The difference in relative response for a given delivered dose is defined as the 'therapeutic advantage'. Radiotherapy treatment outcomes can be improved by increasing the therapeutic advantage through means such as exploiting the 4 R's, or the addition of radiosensitizing drugs.

2.5 Summary

EBRT for lung cancers is offered with X-rays in the MV energy range. These photons typically interact with human tissue via the Compton effect, however the photoelectric effect and pair production are also important photon interactions in the context of absorbed dose and radiotherapy. No matter the interaction pathway, photons act to liberate electrons from their bound states.

These free electrons are responsible for the deposition of all the energy comprising the absorbed dose to tissue. The energy absorbed by the tissue will result in ionizations to the constituent atoms and molecules of the tissue. These ionized atoms and molecules are chemically reactive. When the DNA itself is ionized, or a atom/molecule nearby the DNA is ionized, they will become chemically reactive. The result of the chemical activity can be a break in the backbone strand of the DNA molecule. In the cases where this damage is irreparable, the result is often cell death.

The study of radiobiology has allowed for the honing of radiotherapy techniques. The four 'R's' of radiobiology (Reoxygenation, Redistribution, Repair and Repopulation) form the basis of our understanding of the biological outcomes associated with the delivery of a specific dose. The study of the survival rate of cells exposed to radiation has lead to the commonly used Linear-Quadratic model of cell survival, which has often served as the basis of tumour control probabilities (TCP) and normal tissue complication probabilities (NTCP). The study and understanding of photon interactions and radiobiology forms the basis of modern radiotherapy.

Chapter 3

Review of Radiation Therapy for Lung Cancers

3.1 Introduction

Each tumour site presents with its own unique challenges for the planning and delivery of external beam radiation therapy (EBRT). Usually, the need to limit dose to the OARs in the region of a given tumour will pose the biggest challenge to delivering a high dose to the tumour. However, organ motion also presents challenges to the accurate delivery of EBRT. Although any given treatment site may be susceptible to organ motion (both interfraction and intrafraction), the respiratory motion of the lungs causes displacement of lung tumours greater than that routinely seen at any other treatment site.

The treatment of lung cancers with EBRT is also complicated by challenges with accurate dose calculation. Due to differences in tissue density between healthy lung tissue and a tumour within the lung, it is difficult to model the dose, especially in the interface region. Furthermore,

the relatively low density of lung tissue allows for increased lateral electron disequilibrium which is not typically an important consideration at other treatment sites.

Many approaches have been developed by researchers and clinicians to deal with the challenges of EBRT for lung cancers. This chapter aims to discuss lung cancer in the context of EBRT, approaches to quantifying lung target motion and approaches to accounting for that motion in treatment planning and delivery. Finally, a closer look at the margin recommendations made by other authors in the literature is provided.

3.2 Classification of Lung Cancers

Lung cancer is the leading cause of cancer death in Ontario for both men and women. Approximately 1 in 4 cancer deaths in Ontario result from lung cancer [40]. Therefore, the prevention and treatment of lung cancers is a high priority for clinicians in the provincial health system. There exists many different types of lung cancer, but they can be broadly classified into small cell lung cancer (SCLC) and non-small cell lung cancer (NSCLC) groups.

SCLC represents approximately 15% of lung cancer cases but also account for 25% of lung cancer deaths [41]. These cancers are typically much more difficult to treat due to rapid cell division and the propensity to metastasize early in the development of the disease. SCLC are most often found centrally within the lung, usually originating in the bronchi. Cigarette smoking is implicated as the cause of up to 95% of SCLC cases [42]. The treatment regime for SCLC is dependent on the stage of the disease, but will usually be a combined modality treatment of chemotherapy and radiation therapy. The metastatic potential of SCLC means that surgery is not typically offered for treatment of SCLC. Limited stage disease (confined to a single lobe of the lung) has much better survival rate than extensive disease, with a 5-year survival rate of limited

stage SCLC patients of 20%. The long term survival rates for patients diagnosed with extensive SCLC is very low, with the median survival length in the range of 8 to 10 months.

NSCLC comprises the other 85% of lung cancer cases [43]. NSCLC does not typically grow or metastasize as quickly as SCLC. As such, NSCLC is seen as more treatable and has better survival rates (5-year survival of approximately 15%). Cigarette smoking is again the most common cause of NSCLC, although environmental factors such as air pollution are implicated in up to 11% of cases in some regions [43]. Surgery is the mainstay treatment for NSCLC with complete resection and wedge resection frequently being offered. Almost 70% of patients initially present with locally advanced or metastatic disease, and for these people chemotherapy in combination with surgery is typically offered. Radiation therapy for NSCLC patients is conventionally offered in a regime of $60\ Gy$ delivered in 30 daily fractions. The Radiation Therapy Oncology Group (RTOG) performed a phase 3 trial for locally advanced, non-resectable NSCLC which resulted in local failure rates of 27%. However conventional radiation therapy alone results in a median survival of 10 months and 5-year survival rate of only 5% for this group. New radiation therapy techniques, such as stereotactic body radiation therapy for treating early stage NSCLC has shown promise, with one trial offering local control to 87.2% of patients [44].

3.3 Staging of Lung Cancers

The diagnosis and staging of lung cancer is a key step in determining the appropriate treatment regime. A computed tomography (CT) scan of the chest is most often used in the initial diagnosis of lung cancer. Additional testing, such as a complete blood cell count and electrolyte panel can be used to discriminate between SCLC and NSCLC. Since CT has limited ability to detect microscopic metastatic disease, radionuclide scans such as positron emission tomography (PET), are also being used as part of the modern diagnosis of lung cancer. PET scans allow for the

detection of the highly active cells typical of cancers and can be used to detect the metastatic activity that may be missed by a CT scan. Ultimately it is a combination of tests that leads to the diagnosis and staging of lung cancer. The stages of lung cancer are classified by TNM system, where a score is assigned to each of: T - the size and location of the tumour, N - the lymph node involvement and M - the metastatic state of the disease. The stages and TNM scores are described below as defined by the System for Staging Lung Cancer [45]. Later stage cancers have a worse prognosis.

Stage IA (T1N0M0) & IB (T2N0M0): These are the earliest stages which are commonly diagnosed. The N0 and M0 designations refer to the fact that there is no apparent lymph node involvement or metastatic spread of the disease. The T1 designation is for cancers which are $\leq 3\,cm$ in their greatest dimension. T2 tumours have at least one of the following characteristics: dimension $> 3\,cm$, limited involvement with the main bronchus, have caused a partial collapse of the lung or have caused obstructive pneumonitis. Lung cancers in stage IA and IB are most commonly treated with surgical resection. Patients in this stage who are not amenable to surgery may benefit from stereotactic radiosurgery.

Stage IIA (T1N1M0) & IIB (T2N1M0, T3N0M0): Stage II lung cancers are also most commonly treated with surgery and chemotherapy. The N1 designation denotes spread of the disease into the ipsilateral peribronchial and hilar lymph nodes. The T3 designation is for tumours of any size that are invading the structures surrounding the lung such as the: chest wall, diaphragm, pericardium. A T3 designation would also be given to a tumour causing a complete collapse of the lung.

Stage IIIA (T3N1M0, T1/2/3N2M0) & IIIB (T4N0/1/2M0, T1/2/3/4N3M0): Patients diagnosed with stage III lung cancers have poor prognosis with 5-year survival rates in the 6-9% range. The N2 designation is for mediastinal and/or subcarinal lymph node involvment while the N3 designation is for contralateral lymph node involvement. The T4 designation is for tumours

of any size that involve the critical surrounding organs such as the: heart, mediastinum, great vessels, trachea, esophagus or vertabrae. A tumour would also be classified as T4 in the case of multiple ipsilateral tumour nodules. Treatment for stage III lung cancer will typically be a combined modality approach, however in some cases the only option is for palliative treatment (often including radiation therapy) to relieve suffering.

Stage IV (Any T, Any N, M1): Any lung cancer that has metastasized to a distal region of the body (M1) is given a stage IV classification. These patients have the worst prognosis with 5-year survival of approximately 1%. Palliative treatment would be offered to these patients in most cases, as a curative approach will most likely fail.

3.4 Radiotherapy of Lung Cancers

There are many considerations that must be taken when delivering radiotherapy to any cancer site within the body, including the dose prescription and delivery technique, dose to OARs and our ability to employ accurate dose calculation algorithms. Lung cancer presents some unique challenges in these areas due to the natural radioresistance of lung cancer cells, the location of the cancer within the body relative to other organs, the physical density of lung tissue and lung motion due to respiration.

When radiotherapy is indicated for the treatment of lung cancer, the most common treatment regime being offered today is to deliver $60\ Gy$ in 30 daily fractions ($2\ Gy$ per fraction) to the treatment volume. This regime was developed and tested by the RTOG in a phase III dose escalation trial published in 1995 [46]. Ultimately this standard of care was shown to limit local failure rates to approximately 27%. However, since that time many other approaches have been tested for lung cancers at various stages. One such approach for earlier stage cancers is

known as stereotactic body radiation therapy, which delivers up to $18\ Gy$ per fraction in as few as 3 fractions [44]. In this case the authors reported high rates of local control (97.6% at 3 years), 55.8% survival at 3 years and only moderate treatment related toxicity. Different treatment regimes are routinely being tested for lung cancers of different stages, with new options becoming available as technology improves.

3.4.1 Organs at Risk

No matter what treatment regime is selected to treat a lung cancer, careful consideration must be given to the dose being delivered to the OARs. The location of the lungs within the chest put several critical structures in the vicinity of lung cancers, such as the: heart, spinal cord, and esophagus. The skin, ribs, breast (in women) and the lungs themselves are also at risk for radiation damage during treatment. The dose constraints to each of these OARs is dependent on the fractionation scheme, the toxicity endpoint, the rate at which the endpoint is met and the use of other treatment modalities. As a result many dose constraint recommendations have been published, with the data from Emami *et al.* [47], QUANTEC [48] and various RTOG protocols most commonly referenced. Table 3.1 summarizes the dose constraints to the common lung radiotherapy OARs.

OAR	Volume (%)	Dose	Toxicity Rate	Toxicity Endpoint
Heart [49]	Mean	$< 26\ Gy$	$< 15\%$	Pericarditis
Spinal cord [50]	Max	$< 50\ Gy$	0.2%	Myelopathy
Esophagus [51]	Mean	$< 34\ Gy$	$5 - 20\%$	Grade 3+ esophagitis
Lung [48]	Mean	$< 20\ Gy$	$< 20\%$	Pneumonitis
Lung [48]	V_{20}	$< 30\%$	$< 20\%$	Pneumonitis

Table 3.1: Dose constraints for various OARs common to lung EBRT. The data presented here are taken from the QUANTEC series published in 2010. These constraints represent guidelines as specific constraints depend on many patient specific factors.

Modern imaging and planning tools allow for the selection of X-ray beam angles to avoid many of these structures by providing an accurate and detailed map of the patient anatomy and its position relative to the treatment beam. As a result, major complications from radiation side effects are less frequent than in the past and the most common form of toxicity found in patients is radiation pneumonitis of the lungs [52]. Radiation pneumonitis is an early complication characterized by the development of a dry cough and shortness of breath. The late complication associated with pneumonitis is known as fibrosis. Fibrosis is a scarring of the lung tissue as a result of radiation damage. This damaged lung tissue becomes more dense, less flexible and much less effective at exchanging gases between the atmosphere and blood. Radiation pneumonitis and fibrosis leads to a further shortness of breath in patients who already typically have trouble breathing due to their condition. In 2010 a comprehensive review of radiation toxicity was published under the name QUANTEC. In considering radiation damage to the lung, the authors pointed to the mean lung dose (MLD) as the best predictor of radiation pneumonitis [48]. They recommended limiting the MLD to $\leq\ 20 - 23\ Gy$ as well as limiting the percentage of lung

volume receiving $\geq 20\ Gy$ to $\leq\ 30-35\%$ ($V_{20} \leq\ 30-35\%$).

3.4.2 Dose Calculation in Lung

Absorbed dose calculation for targets in the lung is complicated by the changes in tissue density along the path of the X-ray beam as it enters the body, travels through lung tissue and arrives at the tumour. As X-rays travel across the interface between tissues of heterogeneous density (such as the soft tissue surrounding the lungs and the low density lung tissue) the interaction probability changes. When going from higher density tissue to lower density tissue, the probability of photon interactions within the tissue drops, and as a result fewer electrons are liberated. This abrupt change in interaction probability complicates the dose calculation. As the X-rays travel from low density lung tissue into the higher density tumour mass, an abrupt change in interaction probability will again occur at the interface. Many clinical dose calculation algorithms have a difficult time modeling the dose at the interface regions due to their calculation methods. Some popular algorithms are discussed below.

During regular clinical operation, dose distributions are calculated within commercial treatment planning software (TPS). Varian's Eclipse TPS uses the Analytical Anisotropic Algorithm (AAA) which is convolution-superposition (CS) based algorithm for photon dose calculation [53]. While the fine details of the dose calculation algorithm are proprietary, the basis of the algorithm is public knowledge [54]. The CS algorithm is a model based algorithm, which means it calculates the dose directly in a model of the patient (from a CT data set). In order to calculate the dose at a given point, the CS algorithm first requires data regarding the energy fluence of the specific beam of interest. From the energy fluence and the mass attenuation coefficient provided by the CT data set, the total energy released in matter (TERMA) is calculated within the patient model. The dose calculation is then performed by taking the mathematical convolution of the

TERMA with a dose spread kernel. The dose spread kernel describes the dose distribution resulting from a narrow photon beam in water and is originally calculated using Monte Carlo (MC) methods. The result of the convolution is then superimposed with the convolutions performed at other points within the patient model to determine the final dose distribution.

The CS dose calculation algorithms are advantageous because they give reliable results under most conditions with reasonably short calculation times. However, CS algorithms have been shown to provide inaccurate results in situations with low tissue density, high energy beams and tissue inhomogeneities depending on the size of the beam and the beam energy [55]. Of particular interest to lung is the problem of lateral electron disequilibrium. Due to the low density of lung tissue, the path length of a given electron traveling through lung will be longer than that of an electron in unit density material (the basis of the CS algorithm). As a result, electrons may travel much further laterally (perpendicular to the beam direction) in lung than is actually accounted for by the dose spread kernel in the CS algorithm. Electrons which travel outside the beam profile will deposit their energy in unintended structures. This generally leads to CS algorithms underestimating dose to surrounding healthy tissue in the lung and overestimating dose in the target volume. Furthermore, since the dose spread kernel does not account for heterogeneities in the mass attenuation map of the patient, the CS model is prone to dose calculation errors at the interface of heterogeneous tissues.

In order to circumvent these issues and achieve highly accurate estimates of absorbed dose, other calculation methods must be employed, namely MC methods. MC simulations track the path and energy deposition of a huge number of virtual particles in order to determine absorbed dose in a given volume. By relying on a very large sample size of simulated particle interactions, MC simulation offers accurate dose calculations at the expense of large computing power. MC work published in 2012 [56] shows that in some extreme circumstances, electron disequilibrium can contribute to large differences (up to 20%) in the dose calculated with typical CS algorithms.

Other groups have shown that for small lung targets (stage I), commonly used dose calculation algorithms (AAA and AcurosXB) underestimate the dose by approximately 12%, while the difference is much smaller (0.8%) for stage III lung targets [57]. While MC dose calculation is generally considered the 'gold standard' for dose calculation, the slow calculation times and large computing power required have prevented MC from being used in regular clinical settings.

3.5 Quantifying Target Motion in the Lung

Treating lung cancers with EBRT is further complicated by the motion of the lungs caused by patient respiration. If conventional imaging, treatment planning and treatment delivery techniques are used, motion induced complications in the treatment process arise at each stage. Webb published a thorough review of motion effects and treatment techniques in radiation therapy [58]. In order to adequately compensate for this motion and deliver a successful treatment, a thorough understanding of the motion is required. The least invasive approach to measuring target motion in the lung is with medical imaging techniques, namely fluoroscopy, CT, and magnetic resonance imaging (MRI).

Initial attempts at quantifying target motion in the lung were performed using fluoroscopic imaging. Fluoroscopy uses continuous exposures of X-rays to generate sequential 2D digital images of the patient anatomy. While fluoroscopic images usually suffer from low contrast, the low density of healthy lung tissue (relative to other soft tissues) makes it feasible to detect and delineate lung cancers in fluoroscopic images. One early attempt at quantifying lung target motion was published by Ekberg *et al.* [18]. The authors studied the motion of lung targets using an electronic portal imaging device (EPID) to detect motion on the treatment unit. They ultimately used their data to make margin recommendations as well.

In 2003 Vedam *et al.* [20] published an article quantifying the predictability of diaphragm

motion. The authors used fluoroscopy to track the position of the diaphragm while having patients (1) breathe freely, (2) breathe with audio prompting, and (3) breathe with video prompting. The authors found that free breathing patients have diaphragm position variability similar to that of patients receiving video prompting and less variability than patients receiving audio prompting. This confirmed the earlier results of Mageras *et al.* who performed a similar study [59].

Although it is generally considered that lung target motion is greatest in the superior-inferior (SI) direction within the patient, target motion does occur in all three principal directions. Due to the 2D views provided by fluoroscopic approaches, it is impossible to measure displacements in all three directions from a single set of images. The ability to measure target displacement in 3D is one of the major advantages offered by CT and MRI patient scans. The details of 4DCT scans are discussed later in this chapter, but it is important to note some contributions made to quantifying target motion in the lung that have been made with 4D scans.

A work published by Shirato *et al.* [11] used 4DCT scans with implanted fiducial markers to detect tumour speed and location using 4DCT. The use of fiducial markers reduces uncertainty associated with delineating target volumes with low contrast images. However, implanting fiducial markers is an invasive procedure that may not be well tolerated by all patients. Bissonnette *et al.* [60] investigated interfraction and intrafraction using respiration-correlated cone beam CT (rcCBCT). They were able to assess how target motion changed during treatment by acquiring rcCBCT images before daily treatment, at the midpoint of the treatment and the end of treatment. They showed no statistical difference in tumour motion magnitude over the course of a treatment delivery of the patients studied. Shirato *et al.* studied 21 patients and were able to detect tumour displacement and speed in each of the three principal directions by using 4DCT. In a work published by Mageras *et al.* [61] the authors were able to detect the motion of lung tumours without the use of fiducial markers. The authors noted that some tumours followed a trajectory which included some hysteresis. Mageras *et al.* also derived some margin recommendations from their

study of lung target motion. Finally, a detailed work analyzing the motion of lung tumours using MRI was published by Plathow *et al.* in 2004 [62]. The authors were able to study the 3D motion of targets in each of the different lobes of the lung. Plathow *et al.* concluded that tumours in the lower lobes moved significantly more than tumours in the upper lobes. They were also able to establish the fact that regions of the lung which are involved in the disease are less mobile than the healthy regions of the lung.

Many other authors have also studied the motion of targets in the lung and have reported valuable data regarding the ranges of amplitude and direction of displacement. A summary of select published results is presented in Table 3.2. Some of the results in the summary table are divided into the region of the lung where the tumour is located. Due to the mechanics of the breathing motion, targets in the lower lobes of the lungs are more susceptible to motion.

Perhaps the most important point to note about target motion in the lung is that there is a wide range of motion presented by different patients. As can be seen in Table 3.2, there have been many studies performed, all with different values recorded for the amplitude of motion. This reinforces the need to measure and verify tumour motion in the lung on a patient-by-patient basis.

3.5.1 Breathing Traces and Correlation to Target Motion

Taking a recording of a given patient's breathing pattern is an important step toward adapting the radiotherapy treatment to their specific anatomy. This issue has been tackled by many authors using several different approaches. The most common approaches involve measuring the displacement of the exterior chest wall while the patient is in the treatment position. This can be accomplished using different technologies such as an elastic belt with embedded pressure sensor (e.g. AZ-733V Respiratory Gating System from Anzai Medical Co., Tokyo, JP) [65, 66], or with

Author & year	Direction of Target Motion		
	SI	AP	LR
Ekberg 1998 [18]	3.9 (0-12)	2.4 (0-5)	2.4 (0-5)
Engelsman 2001 [19]	(2-6) Upper lobe	-	-
	(2-9) Lower lobe	-	-
Seppenwoolde 2002 [9]	5.8	2.5	1.5
Murphy 2002 [63]	7.0 (2-15)	-	-
Sixel 2003 [10]	(0-13)	(0-5)	(0-4)
Plathow 2004 [62]	4.3 (2.6-7.1) Upper lobe	2.8 (1.2-5.1)	3.4 (1.3-5.3)
	7.2 (4.3-10.2) Middle lobe	4.3 (1.9-7.5)	4.3 (1.5-7.1)
	9.5 (4.5-16.4) Lower lobe	6.1 (2.5-9.8)	6.0 (2.9-9.8)
Shirato 2006 [11]	10.7	8.8	8.2
Liu 2007 [15]	13.4	5.9	4.0
Suh 2008 [64]	3.7 Upper lobe 8.0 Lower lobe	-	-

Table 3.2: Average (or ranges) of lung target motions reported in millimeters along the principle body directions: superior-inferior (SI), anterior-posterior (AP), left-right (LR).

an infrared marker block placed on the patient's chest and a stationary wall mounted camera. An example is the Real-time Position Management (RPM) system from Varian Medical Systems, Inc., Palo Alto, CA)[67, 68, 69] which was used to gather the breathing trace data used in this thesis work.

Varian's RPM system can be installed in a CT simulation suite to offer respiratory correlated 4DCT scans, or in treatment unit to offer gated treatments. The RPM system consists of an infrared light source and digital camera (figure 3.1), a reflective marker block (figure 3.2), hardware to allow for interfacing between the RPM system and the diagnostic/therapeutic equipment as well as the associated software [70]. The system can take recordings of the patient breathing cycle by using the camera to measure the movement of the marker block placed on the patient's chest. The RPM system samples the marker block position at a rate of $30\ Hz$ and is capable of detecting marker block excursions as small as $1\ \mu m$ as indicated by the data recorded in the output file. The RPM system interfaces with a CT scanner or treatment unit to use the breathing trace data to gate treatments in real time or to to offer respiratory correlated CT scans with retrospective data sorting.

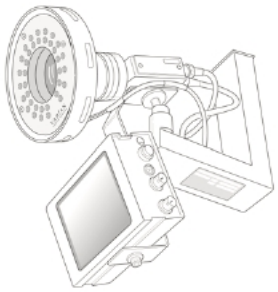

Figure 3.1: A depiction of the RPM infrared light source and camera as seen in the Varian RPM reference guide [70]. The infrared light source surrounds the camera lens. The monitor is used for patient feedback.

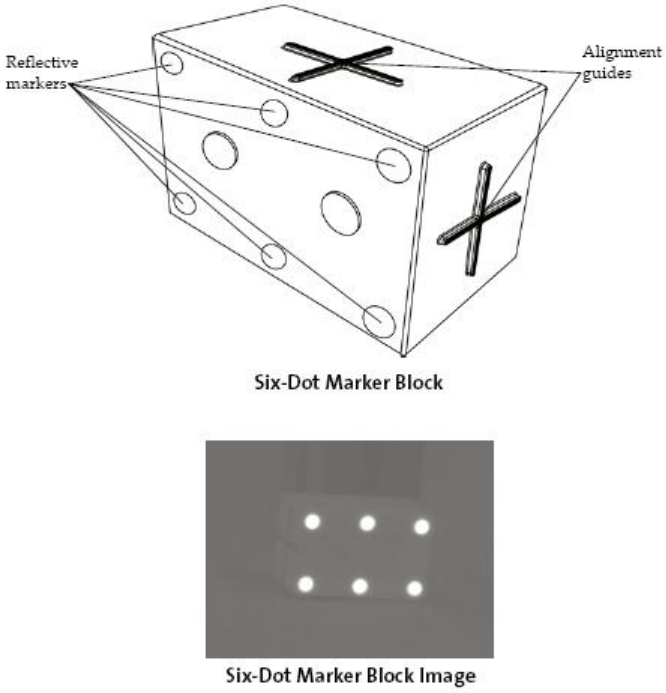

Figure 3.2: A depiction of the RPM infrared marker block as seen in the Varian RPM reference guide [70]. The markers reflect the infrared light from the camera source. In order to offer accurate measurement, the infrared signal from the reflective block must be the strongest signal in the room.

In order to provide information regarding the location of a target within the patient, any external surrogate system will rely on the correlation between the reading of the surrogate and the internal phase of the respiratory cycle. Hoisak *et al.* [8] showed that the reliability of this correlation varies from day to day among patients. The difference between the breathing phase and the target motion phase can be quantified with a phase angle difference. Redmond *et al.* [71] found average changes in the phase angle between the target motion and surrogate of 13.2% and 14.3% compared to the initial 4DCT during subsequent rescans. Redmond *et al.* also confirmed the

results of Hoisak *et al.* regarding the reliability of the correlation from day to day. Importantly, Redmond *et al.* [71] showed that the target volume excursions remained stable at subsequent rescans. Redmond *et al.* also point out that the correlation of the external surrogate to the target motion is an important issue for gated treatments, as a drift in the phase angle could easily result in a geographic miss of the delivered radiation.

The recordings generated from these methods offer insight into the patients breathing pattern in terms of the regularity of the amplitude and frequency of the breaths being taken. An example of a regular breathing trace recorded using the RPM system is shown in figure 3.3 while an irregular breathing trace is shown in figure 3.4. A patient with a regular breathing pattern will typically spend slightly more time at the full exhale phase of the breathing cycle, while irregular breathers cannot be consistently described in any broad manner.

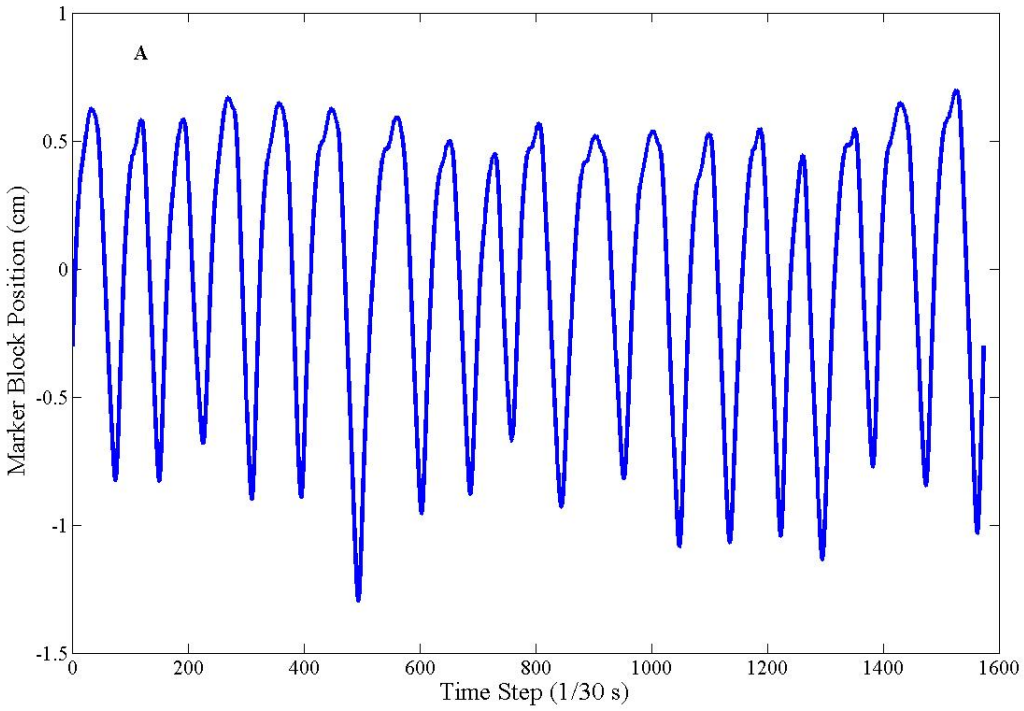

Figure 3.3: An example of a regular breathing pattern recorded with Varian's RPM system. The amplitude of the motion and the frequency of the breathing is consistent across multiple breaths.

These breathing traces offer data which can be used in many ways by clinicians. Ultimately, it is a recording of the breathing trace that allows for reconstruction of 4DCT image data sets. The breathing traces can also be used to guide clinical decision making such as treatment technique or margin selection, which will be discussed later. As can be seen in the plot of the irregular breathing pattern (3.4), it is not necessarily easy to predict future breathing motion based on a given breathing trace. This is especially true in the case of lung cancer patients who frequently have trouble with respiration due to their condition. As a result, it is important to use the breath-

ing trace with caution when involving the data in clinical decision making. Purdie *et al.* [72] described using cone beam CT images acquired at the immediately prior to treatment, and during treatment, to reduce setup error and assess intrafraction changes in tumour position.

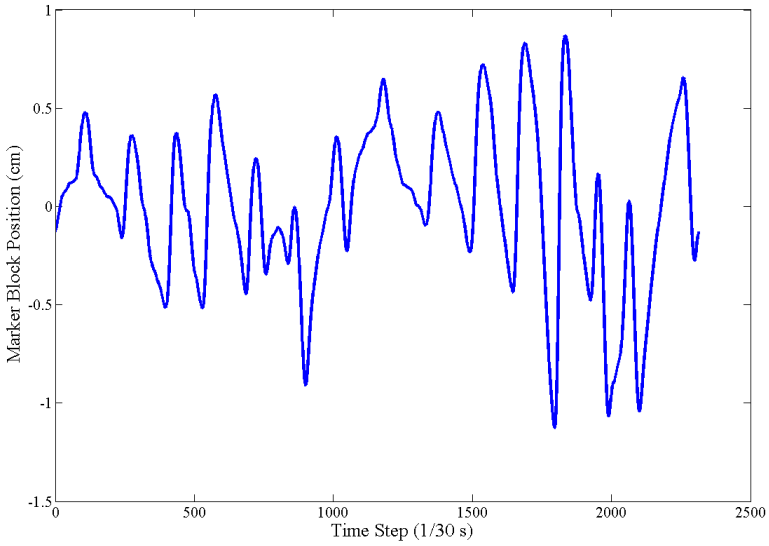

Figure 3.4: An example of an irregular breathing pattern recorded with Varian's RPM system. The amplitude of the motion and the frequency of the breathing are inconsistent across multiple breaths, while the baseline for motion can also been seen to drift.

3.5.2 Computed Tomography of Lung Cancers in Motion

Using CT imaging to determine the position of tumours is a key step in the process of delivering EBRT. In order to acquire a clear and accurate representation of the patient many trade-offs have to be made between parameters such as image resolution, absorbed dose to the patient, image noise, field of view and scan time due to the physical limitations of the system. Acquiring

CT images of the lung is further complicated by the motion of the structure during imaging. Due to the image reconstruction process used to generate 3D CT datasets, any motion which occurs during image acquisition of a conventional CT scan will cause motion artifacts in the final image. Figure 3.5 shows an example of a motion artifact at the bottom of the lung, appearing as a structure with a wavy edge. This type of artifact causes problems in the planning process because it makes delineating structures more difficult and can also compromise dose calculation, depending on the calculation algorithm being used. As a result, different approaches to imaging lung targets in motion have been developed.

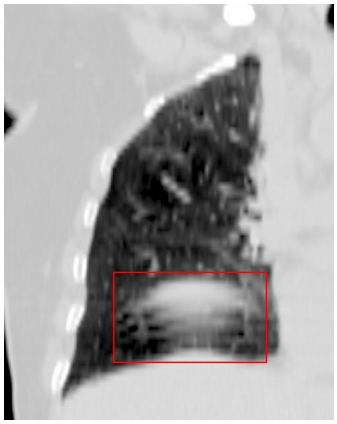

Figure 3.5: An example of a CT image artifact caused by organ motion during image acquisition. Such artifacts compromise the treatment planning process and need to be avoided.

One such approach to reducing image artifacts is known as a ‘slow scan’. By operating the CT scanner in a slow method, such that the couch position remains constant across at least one full breathing cycle, the entire range of target motion during the breathing cycle can be captured on each slice of the CT image. A slow scan can also be achieved by averaging several CT scans of the same patient together [73]. The advantage of the slow scan is that the entire range of tumour

motion is captured in the final image, although this comes at the expense of slightly increased dose to the patient and additional blurring due to motion of other structures in the image.

Breath-hold techniques can also be used during CT simulation to reduce respiratory motion artifacts. CT breath-hold techniques require the patient to hold their breath in order to reduce artifacts due to respiration. Alternatively the patient may be guided through the breathing cycle with audio or visual prompts. A work published by Hanley *et al.* [74] was one of the first to investigate breath-hold CT scans in the context of radiotherapy for the lung. The authors compared free breathing scans to breath-hold scans and found that they were able to reliably reduce the margin of uncertainty associated with the target motion by using deep inspiration breath-hold (DIBH) during CT simulation. Hanley *et al.* found that DIBH allowed for an up to 30% reduction in the volume of lung receiving $25\ Gy$ during a $75\ Gy$ treatment.

A final technique used to compensate for lung target motion is the use of maximum intensity projections (MIP). A MIP is an image (or 3D data set) comprised of the 'maximum intensity' values of several individual scans. In the case of a CT MIP, each voxel contains the maximum electron density of the corresponding voxels in the individual scans. Underberg *et al.* [75] used 3 separate CT images to generate MIPs for lung EBRT: a full inspiration, full exhalation and a midventilation scan. By combining the images into a MIP, the full range of tumour motion becomes apparent. The tumour volume as it appears on the MIP then forms the target volume on which the treatment planning is performed.

No matter the scanning technique used, the ultimate goal is to generate an image which is anatomically accurate with an acceptably low amount of noise. Image noise is quantified by determining the standard deviation of the pixel intensity of an image of a uniform subject (e.g. a cylindrical water phantom)[25]. Within a uniform region of interest (ROI) of a 2D image, the image noise can be characterized by

$$\sigma = \sqrt{\frac{1}{N-1}\sum_{i,j\epsilon ROI}(f_{i,j} - \bar{f})^2}, \tag{3.1}$$

where $f_{i,j}$ are the individual pixel intensities, N is the total number of pixels included in the sum and $\bar{f}$ is the average pixel intensity calculated by

$$\bar{f} = \frac{1}{N}\sum_{i,j\epsilon ROI} f_{i,j}. \tag{3.2}$$

The pixel intensity is simply the Hounsfield unit (HU) value associated with the given pixel. Since the HU is a rescaling of the measured linear attenuation coefficient (described in equation 2.3), the image noise is ultimately dependent on the standard deviation of the measured linear attenuation coefficients of the subject. Ford *et al.* [76] showed that for an idealized CT scanning system with isotropic voxel size, the variance in measured linear attenuation coefficient of a cylindrical object is given by

$$\sigma_\mu^2 = \frac{\pi^2}{12\Delta x^2 n_{ang} N}. \tag{3.3}$$

In this context Δx is the voxel side length, n_{ang} is the number of projection views used in the reconstruction and N is the number of photons absorbed per projection, per detector. The number of photons absorbed, N, is ultimately dependent on many parameters of the scanner design and X-ray tube operation. N is can be determined by

$$N = \frac{\Phi I \Delta t n W H \eta e^{-\mu d}}{L}, \tag{3.4}$$

where Φ is the fluence rate per unit tube current at the detector plane, I is the tube current, Δt is the exposure time per view, n is the number of detector elements per view, W is the

aperture width, H is the slice thickness, η is the quantum efficiency of the detector, μ is the linear attenuation coefficient of the subject, d is the diameter of the subject and L is the number of reconstruction bins in the image.

Given that the image noise is inversely dependent on the number of photons absorbed by the detectors (N), the best way to reduce image noise is to increase the value of N. This can be achieved by the appropriate manipulation of any of the parameters which comprise N. However, any increase in the value of N will necessarily increase the effective dose to the patient. This is the ultimate trade off for CT image quality: if you wish to reduce image noise while maintaining all other image parameters (e.g. contrast, resolution, scan time), you must increase the dose to your subject. In a clinical situation, the balance that must be struck is between acceptable image quality and dose to the patient.

4DCT for Imaging Lung Cancer

Another approach which is growing in popularity as the required technology becomes more widespread is the use of 4DCT scans. A 4D scan generates multiple (typically 8-10) complete datasets of the patient, each corresponding to a different phase of the breathing cycle. This approach offers the benefits of increased contrast (as compared to a slow scan) and the avoidance of motion artifacts in the images. The datasets may be viewed in sequential order, thus offering a short movie of the target motion due to respiration.

Modern CT hardware is required to generate a 4DCT scan. These scanners have very fast gantry speeds (on the order of 1 second per rotation) which allows the machine to acquire a complete view of the patient in less than the time required for a typical breathing cycle (on the order of 3 seconds per cycle). The acquired image views must be sorted according to when they were acquired during the breathing cycle. This is accomplished with the aide of the recorded

breathing trace. An early description of the procedure for acquiring a 4DCT scan correlated to respiratory motion was published by Ford *et al.* [77]. The images can be sorted according to the phase of the breathing trace during which they were acquired [78], or according to the amplitude (position) of a surrogate marker during the breathing cycle [79]. 4D scans come at the expense of increased dose to the patient and increased workload for the clinical resources [77]. Due to the rapid acquisition times, the individual phased images will typically have more image noise as compared to a conventional scan. However, the additional positional information gained by this method is very valuable during treatment planning.

A 4DCT is similar to a conventional CT scan in most regards. The image data is acquired and reconstructed in the same overall manner. However, in the case of 4DCT, the X-ray projection data is recorded along side the patient's breathing pattern and additional X-ray projections are acquired to use in a post-processing procedure. After acquiring the data from the scan, the X-ray projections are sorted into groups depending on which point of the breathing cycle the projection data was captured. Each of these groups of data are then used to reconstruct an image of the patient corresponding to the given portion of the breathing cycle. A typical 4DCT scan will reconstruct $8 - 10$ image data sets which can then be viewed in sequence to offer insight into the given patient's intrafraction motion. The image sorting is typically done in one of two ways: phase binning or amplitude binning.

A phase binned acquisition, as depicted in Figure 3.6, sorts the images according to the angular phase of the breathing cycle. This approach has been discussed by many authors [80, 81, 82, 83] and is the most common approach to 4DCT image reconstruction. Each full breathing cycle is divided into the desired number of segments and the projection data is grouped according to which segment it was acquired in. A full image data set is then reconstructed for each segment. This approach is ideal for a patient exhibiting a regular breathing frequency and amplitude.

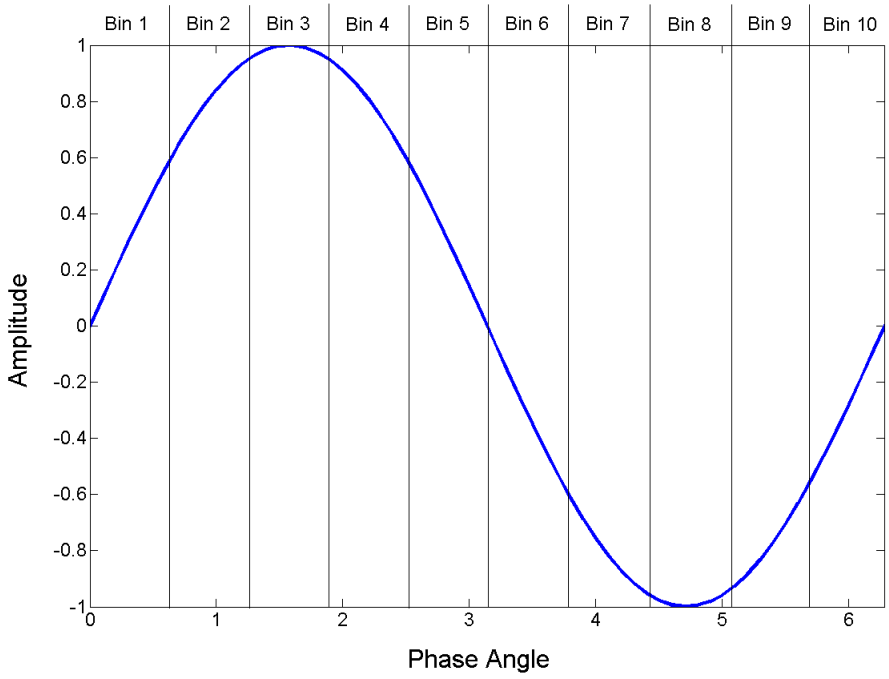

Figure 3.6: An idealized breathing trace broken into 10 phase segments for data binning prior to image reconstruction.

An amplitude binned acquisition, as depicted in Figure 3.7, sorts the images according to the amplitude of the breathing trace recorded at the time of data acquisition. Although less popular than the phase binning approach, amplitude binning has still seen widespread discussion in the literature [84, 85, 86, 87]. The entire breathing trace is divided into the desired number of amplitude segments and the projection data is grouped according to which segment it was acquired in. As before, a full image data set is reconstructed for each segment. This approach can be beneficial when the subject being imaged is exhibiting an irregular breathing pattern [87].

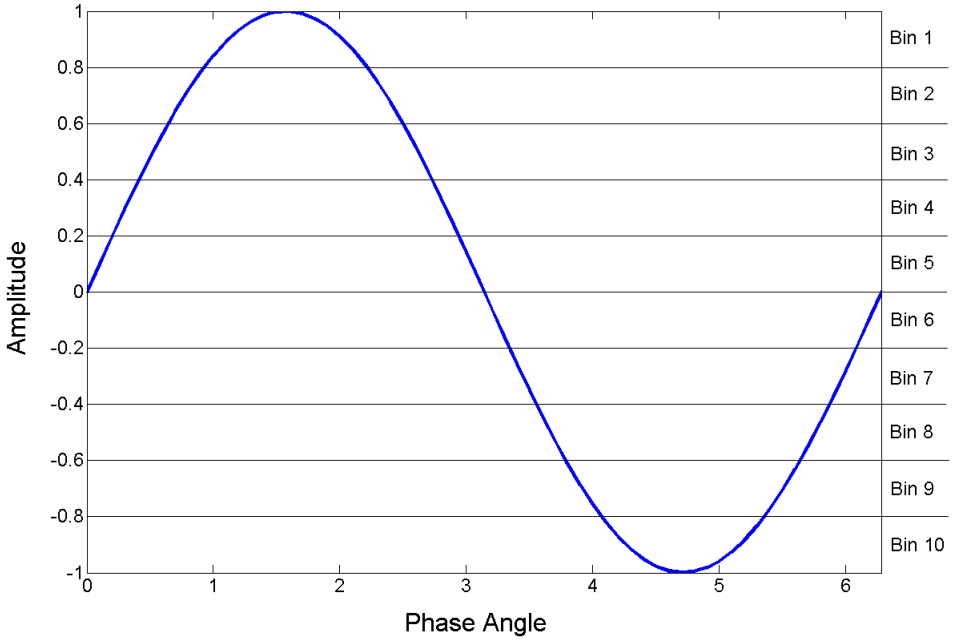

Figure 3.7: An idealized breathing trace broken into 10 amplitude segments for data binning prior to image reconstruction.

For the purposes of this work there are three particular phases of the breathing cycle which are of interest. The first is the 'peak inhalation' phase (bin 1 in the amplitude sorting scheme, bin 3 in the phase sorting scheme). During this phase the patient is just finishing the inhalation of air. In a regular breather there is typically very little pause at the moment of peak inhalation before exhalation begins. At the moment of peak inhalation the lungs reach their full capacity and any target within the lung will be at an extreme position within its motion cycle. In the most common scenario of superior-inferior motion, this corresponds to the most inferior position the target will reach. The second phase of interest is the 'peak exhalation' phase (bin 10 in the amplitude sorting scheme, bin 8 in the phase sorting scheme). During this phase the lungs are

in their natural resting state and any target within the lung will again be at an extreme position within its motion cycle. Most people will naturally pause for a moment at peak exhalation before beginning to inhale. The accumulation of this pause over the course of several breathing cycles is what contributes to the usual lobed feature of a regular breathing PDF.

The final phase of interest is the mean phase. This is the phase of the breathing cycle during which the target is at its mean position during the breathing cycle. The bin corresponding to the mean phase will depend on the given patients precise breathing trace, however it will typically fall in bin 5 or 6 of both depicted schemes. This phase is of importance because it represents the phase on which the treatment should be planned in order to confidently apply the margins ultimately recommended in this work.

The technology required to perform 4DCT imaging has only become widely available within the last 10 years. In order to acquire the image data with sufficient temporal resolution, several advances in CT technology were required. One key advancement was the introduction of the slip ring gantry. This gantry design eliminated the need for cables to transfer data between the rotating detector elements and the associated computer hardware. Without the limitations of the cables, the gantry is free to continuously rotate in the same direction. This improvement decreases the overall time required to acquire the necessary data. Along with the introduction of the slip ring came an increase in gantry rotation speed. Reducing the time per revolution of the gantry had a major impact on reducing overall scan times. Another important advancement was the introduction of helical scanning. This advancement allowed for continuous imaging of the patient as they are translated through the CT gantry. This was an important improvement because it drastically increased the duty cycle of the CT scanner, allowing for scans to be completed in as little as half the time as compared to the traditional 'step-and-shoot' approach. Finally, the use of multiple detector rows in modern CT scanners also improves the temporal resolution by allowing for complete scans of a given organ in fewer gantry rotations.

All of these technological advancements served to reduce the time required to scan a patient. The goal with 4DCT is to acquire data with sufficient temporal resolution as to be able to discern organ motion that is occurring during the data acquisition. In the case of respiratory motion, a typical breathing cycle takes between $2 - 3\ s$. It is therefore necessary to acquire a complete set of projections in less than $2\ s$ in order to have sufficient temporal resolution to detect the motion. The CT scanner in clinical use at the Grand River Regional Cancer Centre is capable of a complete gantry rotation in as little as $0.5\ s$. By combining the technological advances in CT scanner design with data binning and image reconstruction, it is possible to generate useful 4DCT images. However, it should be noted that by decreasing the exposure time with fast gantry rotations, the image quality will be degraded as per the discussion of Equations 3.1 - 3.4. This can be overcome by making the tradeoff of increased dose to the patient. The advantages of the additional information provided by a 4DCT scan must be weighed against the risks associated with this extra dose by the physician.

One of the key pieces of information provided by a 4DCT scan is the amplitude of target motion during the breathing cycle. The breathing trace data recorded by Varian's RPM system is actually the vertical position of a reflective marker block placed on the chest of a patient during the 4DCT scan [59]. While this data gives us accurate information regarding the frequency and baseline of the breathing cycle, the recorded amplitude does not correspond to the amplitude of the target motion in general. Therefore the breathing trace amplitude as recorded by the RPM system cannot be assumed equal to the amplitude of the motion of the target. In order to use the breathing trace data to generate a PDF describing the motion of the target within the patient, the amplitude of the marker block motion must be normalized to the amplitude of the target motion as revealed by the 4DCT scan. After this normalization is performed, the renormalized breathing trace can then be said to be representative of the motion of the target within the patient. This procedure was recommended by Richter *et al.*[2] in order to generate accurate 1D PDFs of target

motion and is used in this thesis.

3.6 Treating Lung Cancers in Motion

Clearly defined treatment volumes play a key role in the delivery of EBRT. The description of these volumes was standardized by the International Commission on Radiation Units and Measurements (ICRU) Reports 50 and 62 [88, 89]. These reports defined several volumes which are used to prescribe and report photon beam radiotherapy. The Gross Tumour Volume (GTV) is the main clinical target representing the bulk of the solid tumour, it is easily discernible on a CT scan. The Clinical Tumour Volume (CTV) includes the GTV and some additional surrounding volume to account for the microscopic spread of the disease which is known to occur clinically. This microscopic spread is not typically visible in CT images. The Planning Target Volume (PTV) includes the CTV and some additional surrounding volume to account for treatment uncertainties such as organ motion and setup error. ICRU Report 62 also defined an Internal Target Volume (ITV) which represents the movement of the CTV relative to other structures in the patient. The ITV was defined because target movement due to internal organ motion such as respiration or organ filling, is extremely difficult for the clinician to control. In the cases where an ITV is defined, the PTV typically surrounds the ITV to account for setup uncertainties associated with positioning the patient on the treatment unit. The treatment volumes are illustrated in Figure 3.8.

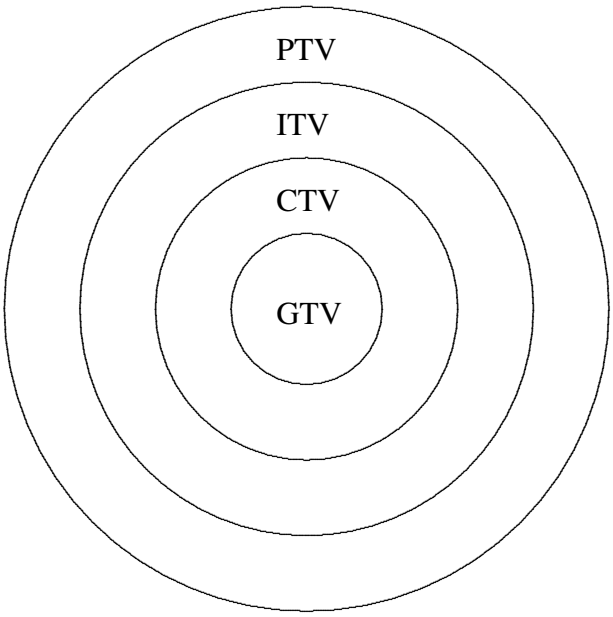

Figure 3.8: An illustration of the treatment volumes defined by ICRU Reports 50 and 62. These standardized volumes allow for consistent prescription and reporting of photon radiotherapy across clinics around the world.

There is always a trade-off to be made between the confidence that a given volume covers the intended structure, and the size of that volume. In order to minimize the NTCP associated with a given radiotherapy treatment, the treatment volumes should be kept as small as possible. However, if the treatment volumes fail to cover the intended target and the resulting treatment also fails, then the radiotherapy has not been successful and the risks associated with delivering the absorbed dose have not been balanced with the intended benefits.

3.6.1 Breath Hold Techniques

Various treatment techniques have been developed in the context of moving targets in the lung that attempt to minimize the treatment volumes while still ensuring confidence in the delivered dose coverage. One such group of approaches is known as 'breath-hold techniques'. There are many different breath-hold techniques which take advantage of different technologies while delivering the radiotherapy treatment [12]. The simplest approach involves coaching the patient to perform repeatable deep inspiration [90]. The treatment beam is only turned on when the patient's respiration is paused at the full inhale phase. A similar technique reported by Wong *et al.* in 1999 [91] used a medical device to suspend the patient breathing and achieve similar results. Finally, respiratory motion can be controlled by forcing the patient to perform only shallow breathing, thereby limiting target motion. This approach can be achieved with an abdominal compression plate. In one study, lung target motion was reduced from a range of $8-20\ mm$ to $2-11\ mm$ using this technique [92]. While breath-hold techniques have been used successfully, not all patients are amenable to their use. Lung cancer patients often have compromised respiration, and so forcing new breathing patterns onto patients can be difficult for them to achieve. The treatment planning process for breath-hold techniques starts with an evaluation of the tumour motion [92]. If the tumour motion is deemed too large (usually $> 5\ mm$ [92]) then a breath-hold technique may be indicated. In this case a free-breathing CT image is acquired along with a motion limited CT image acquired while implementing a breath-hold technique. The treatment planning is performed on the motion limited CT while the free-breathing CT image provides a reference for treatment planners. The clinical target volume is delineated on the motion limited CT, and the appropriate margins are added. At the time of treatment, verification imaging is performed to reduce any setup errors and ensure the patient is positioned as they were during the motion limited CT scan. After the patient setup is complete, the treatment is delivered. Breath hold techniques provide simple cost effective means for reducing target motion.

3.6.2 Gated Radiotherapy

Another treatment technique used to reduce the impact of lung target motion is 'gated radiotherapy'. Gated treatment takes advantage of the delivery technology to turn the treatment beams on while the target is in a specific location (the 'gate'), and off as the target leaves that location. By developing a treatment plan for the target in a specific location, the treatment volumes can be reduced. Gated treatment can be achieved by using external markers such as a camera or pressure belt [93] to determine the breathing phase. The treatment delivery is then delivered at a consistent phase of the breathing cycle. Gated treatment can also take advantage of internal markers such as an implanted fiducial marker. The position of the marker is then tracked with fluoroscopic X-ray imaging. One such study showed a reduction in target motion from $5.5 - 15.9\ mm$ during beam off time to less than $5.3\ mm$ during beam on time using this technique [94]. This level of motion reduction offers a clear advantage towards reducing treatment volumes, however they come at the expense of increased use of clinical resources, more quality assurance testing and surgical intervention in some cases. The treatment planning process for gated radiotherapy begins with a gated CT scan. This is typically accomplished by triggering the CT acquisition based on the signal of an external surrogate [12]. The image data gathered during the gated CT scan then forms the basis for the treatment plan. The target volumes are delineated on the gated CT image and the remainder of treatment is planned as usual. At the time of treatment, verification imaging needs to be performed to ensure accurate patient setup and to verify that the signal from the external surrogate is correlated to the target motion as expected. The treatment is delivered by gating the delivery beam to match the gating performed during the planning CT. Special care must be taken to ensure that the phase angle between the external surrogate signal and target motion remains consistent with the phase angle at the time of the planning CT. If there is an undetected change in the phase angle, it is possible for the treatment beam gate to be consistently triggered when the target is outside the intended treatment volume.

3.6.3 Real Time Target Tracking

The latest development in the treatment of targets in motion is that of 'real time target tracking' techniques. These techniques seek to monitor the position of the target in real time and adjust the relative position of the treatment beam such that the target continues to be irradiated throughout the motion. The target motion can be tracked using implanted fiducial markers [95], or external surrogates [96]. It has been noted that the correlation between target position and the signal from an external surrogate may not always remain constant, as a result this information may need to be updated throughout the treatment [97]. The repositioning of the treatment beam can be accomplished with conventional modern radiotherapy equipment by using the multi-leaf collimator (MLC) [98, 99] or the treatment couch [100]. Robotic radiosurgery equipment such as the CyberKnife developed by Accuray (Accuray, Sunnyvale, CA, USA) have been designed with target tracking in mind. The main obstacle to implementing real time target tracking is in balancing the additional imaging dose to the patient while still obtaining the necessary data to accurately track the target in motion. The quality assurance of such techniques also presents a difficult challenge, and as such have yet to see wide spread clinical acceptance. A method for planning real time target tracking treatments was described by Keall *et al.* [101]. This process begins with the acquisition of a 4DCT scan. The treatment is planned on each phase of the 4DCT data set. Keall accomplished this by generating a typical treatment plan on the peak inspiration phase image. The plan was then transferred to each of the other phases using automated tools within the treatment planning software to define the treatment volumes. At the time of delivery, the patient setup is verified with further imaging. During the treatment delivery, the MLC is varied dynamically such that the beam aperture follows the treatment volume that was defined on each phase of the 4DCT scan. This is accomplished with a feedback loop which includes the signal of an external surrogate used to track the target motion. As with gated treatment delivery, particular care needs to be given to the phase angle between the surrogate signal and the target

motion as seen on verification imaging before treatment delivery.

3.6.4 Motion Encompassing Techniques

The most widespread technique used to treat targets in motion are 'motion encompassing' techniques. These methods seek to define treatment volumes which encompass the motion of the target in order to ensure adequate absorbed dose is delivered. Motion encompassing techniques can be implemented at the imaging and/or treatment planning stages of radiotherapy.

At the imaging stage, motion encompassing techniques can be implemented by taking advantage of different CT scanning protocols. Researchers have developed different methods for detecting the range of motion of a given target using CT scans. As discussed earlier, slow scans allow time for a complete cycle of a given periodic target motion to be represented in each slice of a CT data set [73]. This type of image allows treatment planners to define an ITV encompassing the target motion, to which additional margins may be added to generate the final PTV. Maximum intensity projections can also be used to define the range of target motion [75]. This requires 'fusing' two CT images, one taken at maximum inhale and the other at maximum exhale phases of the breathing cycle. The fused image shows the extent of motion and can be used to define the ITV. 4DCT scans can also be used to determine the extent of target motion in order to define an ITV [15, 102]. Work by Admiraal *et al.* showed that little to no additional margin is often required when defining a PTV from an ITV [103]. It has also been shown that these approaches to defining the ITV offer favorable results in terms of reliable dose coverage as compared to adding a standard margin to each patient [104]. This emphasizes the benefits of a patient specific approach to margin selection. However, treating the entire volume represented by the extent of motion may add unnecessary dose to surrounding healthy tissue [105].

At the planning stage, there are several approaches which can be used to select treatment

margins. Probabilistic approaches to motion encompassing volumes have been developed. Perhaps the most widely known formula is that of van Herk *et al.* [13]. The van Herk formula recommends margins to retain a certain percentage of the target dose for a certain percentage of the patient population. For example, in order to retain 80% of the target dose to 90% of the population a margin of $0.4\sigma_{br}$ should be added to compensate for motion, where σ_{br} is the standard deviation of the breathing motion. In order to retain 95% of the target dose to 90% of the patient population a margin of $0.7\sigma_{br}$ is recommended [13]. This work was a seminal contribution to the ideas of margin selection as van Herk *et al.* justified their margin recipes by analyzing the motion and dose coverage of a large population of patients. By recommending margins based on the standard deviation of systematic and random errors of populations of patients, a reliable understanding of the range of required margins can be assessed. However, as this was a population based approach, these margins will not satisfy every patient. The population based recommendation will overcompensate for some patients and undercompensate for others by its nature. A patient specific approach to margin selection would still offer the best compromise between TCP and NTCP.

Other authors have attempted to compensate for variations in the breathing cycle during the planning stage. Heath *et al.* [16] took a probabilistic approach to optimizing lung treatment plans with breathing variations by optimizing an objective function which includes variations in dose due to motion and lung density changes [106]. Heath *et al.* [16] showed that dose coverage to the target volume was not improved with this approach as compared to margin-based mid ventilation compensation approaches, however some reduction in the dose to the OARs was noted. This result emphasizes the fact that typical variations in breathing patterns do not have large effect on the delivered dose distribution, as compared to the breathing motion itself.

Since motion encompassing techniques are the most widely used motion compensating treatment methods, they present the largest opportunity for improving dose delivery to targets in

motion. One of the major aims of this research thesis is to present a method for selecting treatment margins which compensate for a patient's specific breathing and target motion. By offering a patient specific approach, the optimal margin can be selected on a case by case basis to ensure that the treatment volumes are still being covered by an acceptable absorbed dose, while minimizing the additional radiation received by the surrounding healthy OARs.

3.7 Summary

Lung cancers are classified into the categories of small cell lung cancer (SCLC) and non-small cell lung cancer (NSCLC) according to the cell morphology. The vast majority of lung cancers are caused by smoking, although other environmental conditions (e.g. smog and Radon exposure) have also been implicated. Lung cancers have poor survival rates worldwide and pose a significant challenge to clinicians.

The radiotherapy of lung cancers is complicated by challenges involving calculating the dose distribution. Many dose calculation algorithms have difficulty accounting for the tissue inhomogeneity common in the lung, which can lead to dose errors. Furthermore, the motion caused by respiration poses an additional challenge to the accurate delivery of radiotherapy. Several approaches to quantifying lung target motion have been developed by researchers using tools such as fluoroscopy and 4D imaging techniques. In this thesis the images and data gathered during a 4DCT scan are used to identify the mean phase of motion. The respiratory motion can the be compensated for with additional treatment margins. This approach does come at the expense of increased dose to OARs.

Knowledge of the target motion patterns has lead to the development of several techniques for the delivery of radiotherapy to the lung. Gated radiotherapy turns the beam on only when

the target is in a specific location. Real time target tracking techniques direct the beam to follow the target as it undergoes respiratory motion. Breath hold techniques look to reduce the amount of motion by managing patient breathing and are often used in conjunction with gated delivery techniques.

Perhaps the most widely used approach to lung target motion management is with motion encompassing techniques. These approaches seek to define target volumes which will compensate for the motion of the target, either by estimating the position of the target using a probabilistic approach, or by recording the extent of target motion and irradiating the entire volume. The motion encompassing technique employed in this work seeks to add additional treatment margins based on a patients' specific breathing pattern and target volume. Since these types of approaches are most commonly used to compensate for target motion, they present a large opportunity for improving patient outcomes.

Chapter 4

The Convolution Model and its Inputs

4.1 Introduction

The convolution model employed throughout this work was originally described by Leong in 1987 [22]. At that time, the proposed use of the model was to determine the effect of random daily patient setup errors on the originally calculated dose distribution. These setup errors occur as a natural result of treatment fractionation. As patients return for their daily fractions of radiotherapy, they need to be positioned on the treatment couch each time. While much care is taken in the clinic to ensure that patient positioning is accurately reproduced each day, small variations are inevitable. The small differences in daily patient setup can manifest themselves as a displacement of the entire patient from the originally planned position, or as a shift in the relative locations of the organs within the patient. Changes in patient position or anatomy which occur on a day-to-day basis (as opposed to during treatment delivery) are categorized as 'inter-fraction motion'. Any change in patient position or anatomy from the original plan will manifest as deviations between the planned and delivered dose distributions. The original convolution

model aimed to predict the extent of the changes to the dose distribution in order to allow for the compensation of interfraction motion during treatment planning.

The convolution model has also been used to study the effect of intrafraction motion on the delivered dose distribution. An early work assessing the convolution model for intrafraction motion was published by Lujan *et al.* [23] in 1999. In that work, the authors used fluoroscopic imaging and direct simulation to investigate the use of the convolution model for intrafraction motion. The authors showed that the results of the convolution model predictions were very similar to the results of a direct simulation of the dose delivered at each phase of the breathing cycle. At the time, the authors were limited in their approach by the lack of availability of 4DCT. It is valuable to revisit the use of the convolution model for intrafraction motion in the context of this new technology.

Intrafraction motion is a serious challenge to targets in the lung and liver in particular. As a result the use of the convolution model in the context of intrafraction motion as described in the literature is focused on these two disease sites. This chapter will describe the convolution model and its inputs in detail, as well as assess the model assumptions and review the historical use of the convolution model in the literature.

4.2 The Convolution Model of Target Motion

The convolution model as originally proposed by Leong in 1987 [22] is given by the equation

$$D_b(x,y,z) = \int\int\int D_0(x-x', y-y', z-z')PDF(x',y',z')dx'dy'dz', \qquad (4.1)$$

or succinctly as

$$D_b(\vec{r}) = \int D_0(\vec{r} - \vec{r}')PDF(\vec{r}')d\vec{r}' \tag{4.2}$$

$$D_b(\vec{r}) = D_0(\vec{r}) \otimes PDF(\vec{r}). \tag{4.3}$$

$D_b(\vec{r})$ represents the resulting 'blurred' dose distribution; $D_0(\vec{r})$ is the static dose distribution (as calculated *a priori* by treatment planning software); $PDF(\vec{r})$ is a probability density function describing the position of the target over the course of all treatment fractions; and the coordinates (x, y, z) correspond to the standard body directions of left-right (LR), anterior-posterior (AP) and superior-inferior (SI), respectively. $D_0(\vec{r})$ is referred to as the 'static' dose distribution because it comes from a treatment plan that does not account for target motion. The plan is generated on a static image of the patient and assumes the patient will be static while receiving their treatment. In the context of this thesis work, the static plan would be generated on an image of the patient at a particular phase of their breathing cycle. This is the phase of the breathing cycle which has the target at its mean location. The model prediction, $D_b(\vec{r})$, is referred to as the 'blurred' dose distribution because the qualitative effect of the convolution is to spread (or blur) the static dose distribution.

The Fourier transform is commonly used to treat convolutions because the convolution operation reduces to multiplication in the Fourier space. This is described in Bracewell [107] as

$$F^{-1}\left[F(f(x))F(g(x))\right] = f(x) \otimes g(x), \tag{4.4}$$

where F is the Fourier transform

$$F(f(x)) = \int_{-\infty}^{\infty} f(x)e^{-2\pi ikx}dx, \tag{4.5}$$

and F^{-1} is the inverse Fourier transform

$$F^{-1}(f(x)) = \int_{-\infty}^{\infty} f(x)e^{2\pi ikx}dx. \tag{4.6}$$

Jiang *et al.* [24] proposed a modification to the model by first noting that the derivative of a convolution is well defined ([108]) as:

$$\nabla D_b(\vec{r}) = \nabla D_0(\vec{r}) \otimes PDF(\vec{r}) \tag{4.7}$$

$$\nabla D_b(\vec{r}) = D_0(\vec{r}) \otimes \nabla PDF(\vec{r}) \tag{4.8}$$

Therefore, given a reference point $\vec{k}\epsilon R^3$, the blurred dose can also be expressed as:

$$D_b(\vec{r}) = D_b(\vec{k}) + \int_s \nabla D_b(\vec{r})d\vec{r} \tag{4.9}$$

$$= D_b(\vec{k}) + \int_s [\nabla D_0(\vec{r}) \otimes PDF(\vec{r})]d\vec{r} \tag{4.10}$$

$$= D_b(\vec{k}) + \int_s [D_0(\vec{r}) \otimes \nabla PDF(\vec{r})]d\vec{r} \tag{4.11}$$

where s is the line from $\vec{k}$ to $\vec{r}$. In the case of a straight one dimensional dose profile with dose equal to zero (or negligibly small) at $\vec{k}$, these equations can be simplified to

$$D_b(x) = \int \frac{d}{dx} D_0(x) \otimes PDF(x)dx \tag{4.12}$$

$$D_b(x) = \int D_0(x) \otimes \frac{d}{dx} PDF(x)dx. \tag{4.13}$$

This approach of Equation 4.12 is advantageous because regions of the dose distribution with large dose gradients are most susceptible to changes due to target motion. Therefore, taking the gradient first will highlight regions of the dose distribution where the blurring effect is greatest. Jiang *et al.* [24] also showed that the model can be formulated in terms of an integral over the static dose distribution convolved with the spatial gradient of the PDF as shown in Equation 4.13, however did not pursue this line of investigation in detail.

This formulation of the convolution model described in Equation 4.13 will highlight features of the PDF which have the largest impact on the delivered dose distribution. The shape of the PDF is largely governed by the 'regularity' of the breathing pattern. For the purposes of this work, a breathing trace is considered 'regular' if it exhibits clear periodicity. A regular breathing trace will show little breath-to-breath variation in breathing frequency, breathing amplitude and baseline location (the baseline is the geometric mean location of the breathing trace). An image of the patient while they are in the baseline phase can be obtained by selecting the appropriate phase of a 4DCT scan. A regular breathing trace will tend to result in a PDF with two prominent lobes, corresponding to the peak inhalation and peak exhalation phases of the breathing cycle. This two mode shape can be seen in the PDF presented in Figure 4.2. A breathing trace is considered 'irregular' if it does not exhibit stable amplitude, frequency or baseline location. An irregular breathing trace will typically result in a PDF with a single prominent lobe and other (minor) unique features depending on the specifics of the trace. The distinction between regular and irregular breathing patterns remains qualitative due to the wide range of breathing patterns exhibited by patients. Any attempt to put a strict definition on regular versus irregular breathing will likely involve arbitrary definitions of thresholds regarding the trace parameters.

It should be noted that a property of the convolution can be used to help interpret the predictions made by this model. As described by Bracewell [107], the integral of the convolution of

two functions is equal to the product of the areas of the two functions. This can be shown as

$$\int_{-\infty}^{\infty} f(x) \otimes g(x)dx = \int_{-\infty}^{\infty} \left[\int_{-\infty}^{\infty} f(u)g(x-u)du \right] dx \tag{4.14}$$

$$= \int_{-\infty}^{\infty} f(u) \left[\int_{-\infty}^{\infty} g(x-u)dx \right] du \tag{4.15}$$

$$= \left[\int_{-\infty}^{\infty} f(u)du \right] \left[\int_{-\infty}^{\infty} g(x)dx \right]. \tag{4.16}$$

This is important in the context of this work because the area under the PDF is unity (by definition). This implies that the integral dose being delivered during intrafraction motion is equal to the integral dose delivered by the same plan to a static patient. In other words, the effect of target motion can be interpreted as a redistribution of the dose you expect to deliver to a static target.

A careful understanding of the model inputs and the associated model assumptions is required to make proper use of the convolution model. This model makes assumptions tied to each of the inputs, and these assumptions must be satisfied in order for the model to make accurate predictions. The two assumptions will be referred to as 'shift invariance' (connected to the static dose input) and 'sufficient sampling' (connected to the PDF input). A thorough analysis of these assumptions in the context of interfraction motion was published in two papers by Craig *et al.* [109, 110]. However, it is important to re-confirm the validity of these assumptions in the context of intrafraction motion.

4.2.1 Convolution Model Inputs - Static Dose Distribution and its Gradient

The static dose distribution used as a model input in this work was planned on a dynamic thorax phantom. The details pertaining to the phantom, scanning procedure and planning procedure are given in Chapter 5. Briefly: the planning followed a procedure similar to that of a patient

undergoing radiotherapy treatment. The phantom was configured with a lung equivalent insert that is designed to accept a piece of radiographic film for dose measurement. The phantom was then scanned using the department's typical thorax scanning protocol. The image of the static phantom obtained in this scan was used to generate the static dose distribution (D_0) used in the convolution model predictions. After completing the scan, the DICOM data was sent to the treatment planning computers. The treatment volumes were then defined on the phantom image data set, which included a simulated GTV, CTV and PTV. The PTV was approximately spherical in shape and had a diameter of $3.7\ cm$.

In order to generate the treatment plan, a simple three field, conformal technique was used. As well as being clinically relevant, this technique also allows for simple adjustments to be made in order to test the effect of varying field sizes and dose rates. A dose of $200\ cGy$ per fraction was selected in order to remain consistent with conventional conformal treatments of the lung. Further details on the treatment plan are provided in Chapter 5.

After completing the treatment plan including the TPS dose calculation, the static dose profile can be obtained. The Eclipse TPS offers users the ability to plot and export dose profiles along any straight line within the patient. The exported dose profile data can then be imported into other software, such as MATLAB or a spreadsheet program, for analysis. A dose profile through the plan isocentre is presented in Figure 4.1.

The use of dose gradients in this motion model as described by Equation 4.12 offers an important tool for understanding the regions of the dose distribution which will be most susceptible to changes due to target motion. The regions of the dose distribution where the gradient is small (or zero) make little (or no) contribution to the blurred distribution that we expect to deliver in the presence of motion. In practice this means that the penumbral regions (defined as the region where the dose falls from $80\% - 20\%$ of the prescribed dose) of the distribution where the magnitude of the dose gradients is largest, will be most susceptible to the blurring effect of target

motion. As a result, the outer edges of the target volume are at the highest risk of losing dose coverage as a result of target motion.

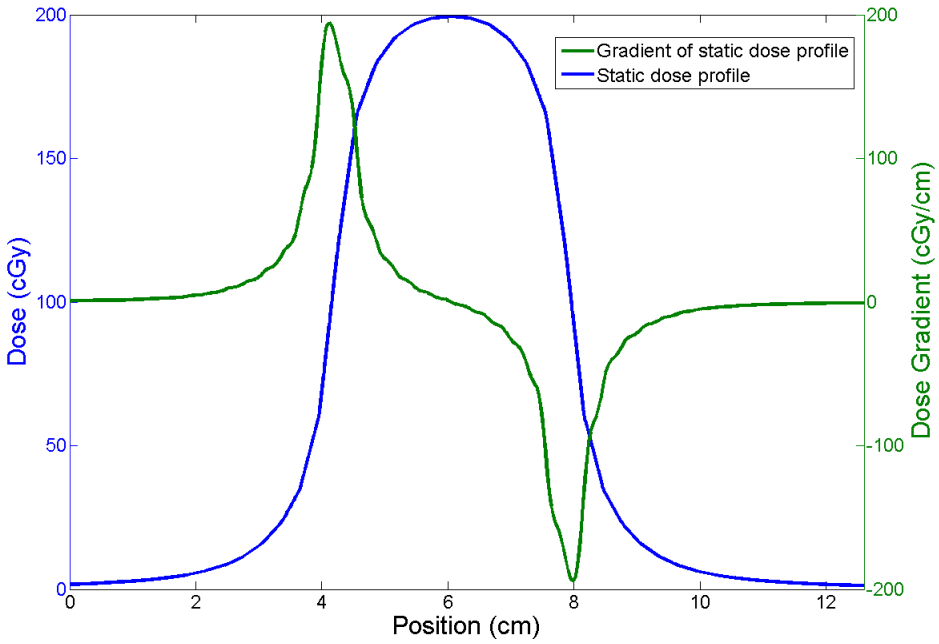

Figure 4.1: A static dose profile and its derivative taken from the treatment planned on the static phantom. The profile is taken in the SI direction starting superior to the treatment volume, along the length of the film insert.

In terms of treatment planning, the loss of dose coverage is the complication caused by target motion. An appropriate treatment plan has to balance the NTCP with the TCP. In the presence of target motion, the loss of target dose coverage represents a loss of TCP. In order to recover the TCP by increasing target margins, the treatment plan will necessarily increase NTCP. The presence of target motion makes striking the appropriate balance more difficult. In situations where the target volume is directly adjacent to an OAR, it may not be possible to safely increase

target margins in a given direction and therefore different treatment techniques may need to be considered.

Understanding what margins are necessary to retain the desired TCP for a given dose distribution and breathing pattern is one of the key motivations for this work. It is the hope that by giving clinicians tools for margin selection, decisions can quickly and easily be made regarding the balance of TCP and NTCP for a given treatment plan.

4.2.2 Convolution Model Inputs - Motional PDF and its Gradient

The PDFs used for this work were generated from 502 unique patient breathing traces. The traces were recorded at the London Regional Cancer Program (London, Ontario) using the Varian RPM system (Varian Medical Systems, Inc., Palo Alto, CA). The breathing traces were acquired during 4DCT simulation and were originally used for 4DCT image reconstruction. The PDFs were generated from each breathing trace using MATLAB (The Mathworks, Inc., Natick, MA) to create a histogram of the breathing trace recorded during 'beam on'. A PDF was then generated from the histogram using MATLAB's Kernel Smoothing Density Estimate routine (ksdensity). The resulting function was normalized such that the area under the curve was unity, as required by the definition of a PDF. A graphical depiction of this process for a regular breathing trace is provided in Figure 4.2.

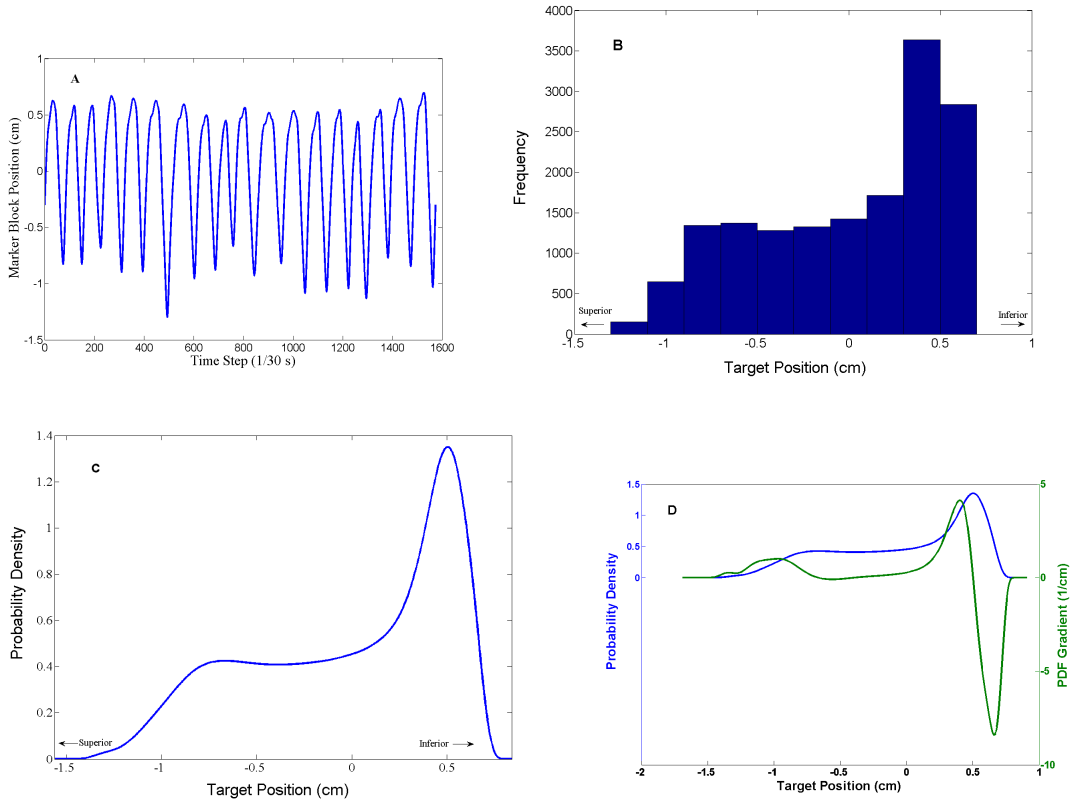

Figure 4.2: The development of a PDF from a recorded breathing trace. Figure A is the recorded breathing trace. Figure B is the associated histogram generated by binning the breathing trace data. Figure C is the final PDF generated with a MATLAB routine and normalized appropriately. Figure D shows the PDF and its gradient.

The origin of the PDF coordinate system was placed at the mean location of the recorded positions, as suggested by other authors [1, 111]. For the purposes of the analysis performed in this work, the breathing trace amplitudes as recorded by the Varian RPM system were assumed to be equal to the target motion amplitude within the patient. This was done to ensure a wide range of motion amplitudes were considered. Although the amplitude of target motion within the

patient is not equal to the amplitude of the marker block motion in general, the breathing trace amplitude can be renormalized [2] to the target motion amplitude as seen on 4DCT. A breathing trace renormalized in this way is representative of one dimensional motion of the target during breathing.

The formulation of the convolution model described by Equation 4.12 makes use of the gradient of PDF for calculating the blurred dose distribution. In the case of the regular breathing PDF depicted in Figure 4.2 the gradients with the largest magnitude surround the peak inspiration and peak expiration phases of the breathing cycle. These phases correspond to the largest displacements of target from its mean position. As a result, the largest contribution of the PDF gradient to the blurred dose distribution is seen in these regions of large displacement. This emphasizes the fact that the blurring of the delivered dose distribution is predominantly influenced by the 'most likely' position of the target during its motion. The rate of change of the PDF along a given direction can then be seen as a measure of the amount of dose blurring that is expected as a result of target motion.

4.3 The Convolution Model Assumptions

As with any physical model, certain assumptions are required to be met in order to generate accurate predictions. Work done by Craig *et al.* [109, 110] described the two main assumptions inherent to the convolution model in the context of interfraction motion: shift invariance of the dose distribution and sufficient fractionation. In order to have confidence in extending the convolution model to intrafraction motion, these model assumptions need to be analyzed in the context of intrafraction motion.

4.3.1 Assumption of Shift Invariance

The concept of shift invariance in this model is closely associated to the static dose distribution. The assumption being made is that the static dose distribution is unchanged by changes in patient anatomy. In other words, we assume the exact same dose distribution is being delivered to the patient, despite any changes to the patient's position or internal anatomy. Strictly speaking, this assumption cannot be met as the dose deposited by charged particles depends directly on the stopping power of the medium along the path they are traveling. Therefore any slight differences between the patient positioning or internal anatomy at planning time, as compared to treatment time, will result in differences between the planned and delivered dose distribution due to changes in the stopping power along the path. However, the model is still able to provide a reasonable approximation for most clinical situations where the changes in internal anatomy and position are small (due to the extreme care taken by therapists during patient setup). This allows the model to provide useful predictions even if the assumption is not strictly met.

The convolution of the static dose distribution and a motional PDF is simply a mathematical operation and therefore care must be taken when interpreting the results in a physical situation. For example, as pointed out by Craig *et al.*[109], the convolution involves shifting the dose distribution. At the surface of the patient, there is no 'dose' outside the patient to shift. Therefore additional assumptions are required when interpreting the results of the convolution model at the surface of the patient. The effect of tissue inhomogeneity must also be considered when using the convolution model for targets such as lung cancer. In the same work, Craig *et al.* showed that the additional error in dose calculated using this method due to lung equivalent inhomogeneity is approximately 1%. This level of accuracy is sufficient to proceed with confidence when using the model to analyze the motion of lung targets.

Fortunately, for small changes in patient position and internal anatomy, the resulting static

dose distribution is modified only slightly. Craig *et al.* [109] showed that the typical changes in patient positioning and anatomy that are encountered on a routine basis only result in small changes in the predicted dose distribution. Specifically, changes due to radiological path length differences were shown to be $< 0.1\%$. Although errors due to inhomogeneties of a 'few percent' were noted, these errors were localized and small compared to errors encountered due to 'inhomogeneity' at the surface of the patient. Ultimately the authors felt that the convolution model is useful in situations where dose inhomogeneities are present, especially for plans with multiple beams and targets at depth within the patient, which are used in this thesis work.

4.3.2 Assumption of Sufficient Sampling

The convolution model employs a PDF to describe the motion of the target during treatment. As described by Craig *et al.* [110], in the strict mathematical interpretation of the convolution model the assumption being made is that the dose is being delivered in an infinite number of fractions, each delivering an infinitesimal dose. In the case of interfraction motion, each daily fraction represents a single sample of the PDF describing the motion. A typical fractionated treatment plan will deliver the prescription dose over the course of approximately 30 fractions. As a result, the positions sampled by the anatomy during the delivery of this finite number of fractions may not end up being representative of the PDF used to make the predictions by the convolution model. Craig *et al.* showed that the average maximum dose error was 11% for the convolution model when the effect of finite fractions was considered. Ultimately the authors warned that the effect of finite fractions appears to have a greater impact on the delivered dose distribution than typical plan evaluation parameters.

When using the convolution model in the context of intrafraction motion the problem of sufficient sampling also must be considered. In this case, the motion of the target during beam

delivery must correspond to the motion of the target used to generate the PDF. In other words, the proportions of the positions sampled by the target while the treatment beam is on must be substantially similar to the proportions of the positions measured *a priori*. In order to test this assumption a simulation of 'beam on sampling time' was developed.

Each recorded breathing trace was analyzed to determine the minimum required time to achieve sufficient sampling. This was done empirically using the Kullback-Leibler divergence as a measure of the similarity between two probability distributions. The sufficient sampling simulation was performed by first selecting a random point in the breathing trace as the starting point. The trace was then broken into 0.1 s subsections beginning with the starting point, with the trace repeating itself as necessary. A 'sub-PDF' was then generated from each of the new trace subsections and the sub-PDF was compared to the PDF generated from the full trace using the Kullback-Leibler divergence. The goal is then to determine 'at what level of Kullback-Leibler divergence between the two PDFs are the resulting blurred distributions substantially similar to one another?'. To determine an empirical answer, each sub-PDF was also convolved against a dose profile to determine the resulting blurred distribution. To evaluate the difference in dose coverage the D_{95} metric was used. The D_{95} is the minimum dose received by 95% of the target volume. A ratio between the D_{95} of each blurred dose profile from the sub-PDF convolutions and the D_{95} of the blurred dose profile from the full PDF convolution was calculated. By relating the Kullback-Leibler divergence of each sub-PDF to the relative D_{95} offered by each sub-PDF, we can get an understanding of the sampling time required to achieve sufficient sampling.

As part of this simulation study, 42,347 sub-trace PDFs were generated and compared to their corresponding full trace PDF. An arbitrary threshold Kullback-Leibler divergence value of 1 was selected to define a sub-trace PDF as 'substantially similar' to the corresponding full trace PDF. A histogram of the relative D_{95} when the Kullback-Leibler divergence is less than 1 is presented in Figure 4.3. Of the sub-trace PDFs analyzed, 93.9% resulted in a D_{95} within 3% of

the expected value after convolution (Figure 4.3). Furthermore, 94.4% of all the patient breathing traces analyzed reached a Kullback-Leibler divergence of less than 1 within the maximum 12 seconds of sampling time used in this simulation. The minimum required sampling time to generate a sub-PDF with Kullback-Leibler divergence less than 1 when compared to the full PDF for each of the patient breathing trace is summarized in Figure 4.4. Although the vast majority of breathing traces met the Kullback-Leibler divergence threshold within 12 seconds or less, the breathing traces which are most likely to fail to meet the Kullback-Leibler divergence threshold are traces with very large standard deviation ($\geq 0.8cm$).

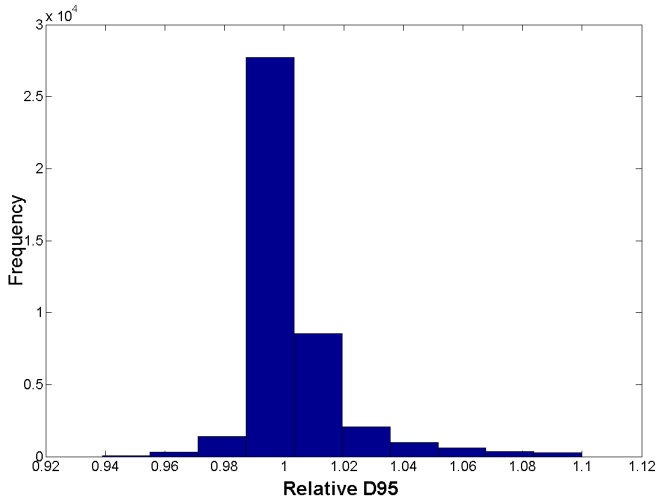

Figure 4.3: A histogram showing the distribution of relative D_{95} values when comparing sub-PDF and full PDF convolutions. All sub-PDFs included in this data had Kullback-Leibler divergence less than 1 when compared to the full trace PDF.

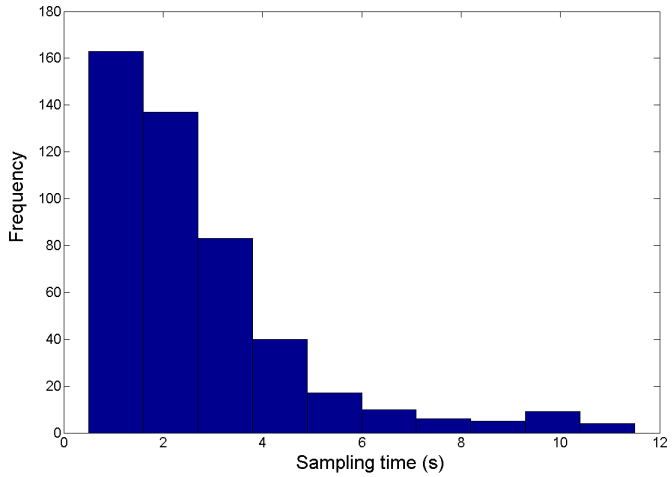

Figure 4.4: A histogram showing the distribution of sampling times required to generate a sub-PDF that has a Kullback-Leibler divergence of less than 1 when compared to the full trace PDF.

As can be seen in Figure 4.4, after six seconds of beam on time, 92.8% of the breathing traces had achieved sufficient sampling. By ten seconds of beam on time, over 99% of the breathing traces had achieved sufficient sampling. Beam on times of six seconds or greater are common for many types of radiotherapy treatments offered to lung cancer patients. In the case of a conventional 3D conformal radiation treatment (3DCRT) or four field box, the typical beam will deliver around $80 - 100$ monitor units (MU). Using the standard dose rate of $400\ MU/min$, this corresponds to a beam on time of $12 - 15\ s$. By decreasing the dose rate, additional positional sampling can be achieved in order to help ensure the sufficient sampling assumption is met. Although modern treatment technology is trending towards higher dose rates, increasing the dose rate has the effect of decreasing the reliability of the convolution model by jeopardizing the sufficient sampling assumption. Additional care must be taken when using high dose rates ($>\ 400\ MU/min$) if the convolution model is being employed. Regardless of the dose rate being

employed for treatment, sufficient beam on time must be used to ensure accurate application of the convolution model. For example, a modern flattening- filter-free (FFF) treatment beam may be operated at a dose rate of $1200\ MU/min$. To ensure sufficient sampling with a $10\ s$ beam on time, a minimum of $200\ MU$ should be delivered by the treatment beam.

The assumption of sufficient sampling may also be jeopardized in the case of an IMRT treatment. IMRT treatments have beams which are subdivided into many segments with different beam shapes. Each beam segment may account for as little as $10\ MU$, and in this case it is very likely that the sufficient sampling assumption will not be strictly met. The problem of small beam segments interacting with targets in motion is known as the 'interplay effect' and it has been analyzed by several authors [112, 113, 114]. These authors report that in most cases the interplay effect results in a negligible difference between the planned and delivered dose distributions over the course of a conventionally fractionated treatment plan. This fact makes the application of the convolution model to IMRT treatment plans possible, however special care should be taken to avoid small beam segments, and ensure that a large number (~ 30) of fractions are used, in order to satisfy the sufficient sampling criteria.

4.4 Use of the Convolution Model to Assess Interfraction and Intrafraction Motion

Interfraction Motion

The convolution model of interfraction organ motion has been employed by many researchers since being proposed. Jiang *et al.* [24] used this model extensively to describe the effect of prostate motion on intensity modulated radiation therapy (IMRT) plans. Furthermore, those authors showed that the dose gradients can be incorporated into the model in order to offer a

clearer picture of regions of the dose distribution which will be sensitive to anatomical changes. Li *et al.* [115] used the convolution model to quantify the interplay effect in prostate IMRT. The interplay effect is a term used to describe the interplay between organ motion and the delivery of beam segments during IMRT. Li *et al.* performed convolutions between the dose distributions resulting from each segment of IMRT delivery and the corresponding motion PDF of the prostate. They showed that for individual segments large discrepancy between mean target dose could arise ($> 25\%$), however over the course of a 30 fraction treatment, the differences would be negligible. Conversely, a hypofractionated treatment would be at greater risk of delivering a treatment with a large discrepancy between the mean planned and delivered dose to the target.

The convolution model was also employed by Rosu *et al.* [116] to assess changes in liver dose due to organ motion. The authors performed two convolutions: one for setup errors and one for temporal position changes. Rosu *et al.* showed that the changes in liver NTCP due to these motions ranged from $+12.0\%$ to -11.7%, and were dependent on the location of the target within the liver. In a separate investigation, Balter *et al.* [117] used the convolution model to assess the use of patient specific setup margins versus population based setup margins. They showed that population based setup margins tended to result in higher NTCP values, and thus that a patient specific approach could yield safer treatments.

The convolution model was also used to investigate random setup errors in the context of the treatment of head & neck cancers. Astreinidou *et al.* [118] used the convolution model to determine the treatment margins required to maintain the dose delivered to 95% of the treatment volume, given a certain distribution of setup uncertainties. For IMRT treatments, they found a margin of $1.5\ mm$, when the setup errors are normally distributed, with standard deviation of $2\ mm$, and a margin of $3\ mm$ for setup errors with standard deviation of $4\ mm$. Siebers *et al.* [119] used the convolution model to investigate the effect of patient setup on boost treatments for head & neck cancer patients. They found that systematic setup errors caused a greater dose dis-

crepancy then random setup errors. Therefore the dosimetric accuracy of head & neck treatments would benefit more from methods that reduce systematic errors as opposed to random errors.

In each of these cases the researchers have used to convolution model with a Gaussian PDF to assess the difference between the planned and delivered dose distribution in the presence of setup errors. They all note a loss of target dose coverage as a result of the setup errors, and each offers an approach to rectifying the loss of coverage (either by increasing the prescribed dose or by increasing the treatment margin). Interfraction target motion is an issue for every treatment site and the convolution model has been used repeatedly to assess its impact.

Intrafraction Motion

In recent years, the convolution model has been extended in order to describe the modification of the delivered dose distribution which results from organ motion occurring during treatment delivery. This type of motion is categorized as 'intrafraction motion'. One of the original publications using the convolution model to assess intrafraction motion was published by Lujan *et al.* [23]. In this study the authors compared the dose distributions that were calculated in the static case to dose distributions predicted by the convolution model, as well as to dose distributions resulting from a direct simulation of the organ motion. The authors used an asymmetric 1D PDF to describe liver motion resulting from breathing (the fact that breathing motion results in an asymmetric PDF was identified by Balter *et al.* in 1996 [120]). Lujan *et al.* had several key results in their work. First, they noted that due to the finite beam-on time during a treatment, the initial phase of the breathing cycle would influence the delivered dose distribution. However, they found that over the full course of a conventionally fractionated treatment, these phase differences would effectively cancel out. Secondly, they found that the dose distribution calculated by direct simulation of each phase of breathing (which accounts for changes in beam

pathlength) was nearly identical to the prediction made by the convolution model. Since the convolution model calculations are much simpler to perform than a direct simulation, the use of the convolution model to describe the effect of target motion is preferred.

Engelsman *et al.* [1] used the convolution model to investigate the displacement of iso-dose lines due to motion in the context of lung cancer treatment. They found little to no change in the position of iso-dose lines for target motions with amplitude less than $10\ mm$. However for motions larger than $20\ mm$ margins of $7\ mm$ or greater need to be applied, depending on the dose gradient in the region of interest. Engelsman *et al.* also showed a correlation between breathing amplitude and the standard deviation of the breathing motion. Richter *et al.* [2] also used the convolution model in the context of intrafraction lung motion. They analyzed the effect that inhomogeneous target dose distributions had on breathing motion margins. Richter *et al.* found that by increasing the prescribed dose delivered to the target volume, they could reduce the margin required to maintain a given dose to the edge of the target. This result follows intuitively from the concept of dose blurring described by the convolution model. The total dose delivered to the entire patient is not affected by target motion, however the distribution of the dose is affected. By increasing the prescribed dose, the dose blurring can be compensated for. Richter *et al.* also noted a quadratic relationship between their required margins and the standard deviation of the PDF used to describe the target motion.

An important result for the use of the convolution model for intrafraction respiratory motion was published by George *et al.* [121] in 2005. In this work, the authors assessed whether or not the total geometric error due to combined effects of interfraction motion and intrafraction diaphragm motion is normally distributed. The authors ultimately concluded that when assessing populations, the combined error can be considered normally distributed. However, when individual patient measurements are acquired, diaphragm motion (and thus respiratory motion) is not normally distributed. This is a key point because it underlines the importance of patient specific

measurements. The use of imaging on the treatment unit at the time of treatment has helped to reduce setup errors. Therefore the relative importance of addressing the patient's specific breathing motion increases.

With the use of 4DCT scans, clinicians are now able to get more detailed information about the target trajectory and periodicity than ever before. The focus of this work is to revisit the intrafraction convolution approaches employed by other authors in the context of the patient specific information available from 4DCT scans.

4.5 Example Convolutions & Analysis

In order to understand the expected results and trends that arise from the use of the convolution model, it is instructive to assess the results of some example convolutions across a range of breathing traces and target volume sizes. The first point to recognize is that although different breathing traces may all share the properties of a regular breathing trace (e.g. little or no baseline shift, consistent breathing period, consistent breathing amplitude), it is not expected that they will result in the same blurred dose profile after convolution. Instead, the spread of the PDF along the x-axis (position) has the most predominant effect on the resulting dose distribution. This spread is ultimately characterized by the PDF's standard deviation. Examples of three regular breathing traces and their corresponding PDFs are shown in Figures 4.5 and 4.6, respectively. It should be reiterated that the area under each PDF is equal to unity as required by the definition of a PDF.

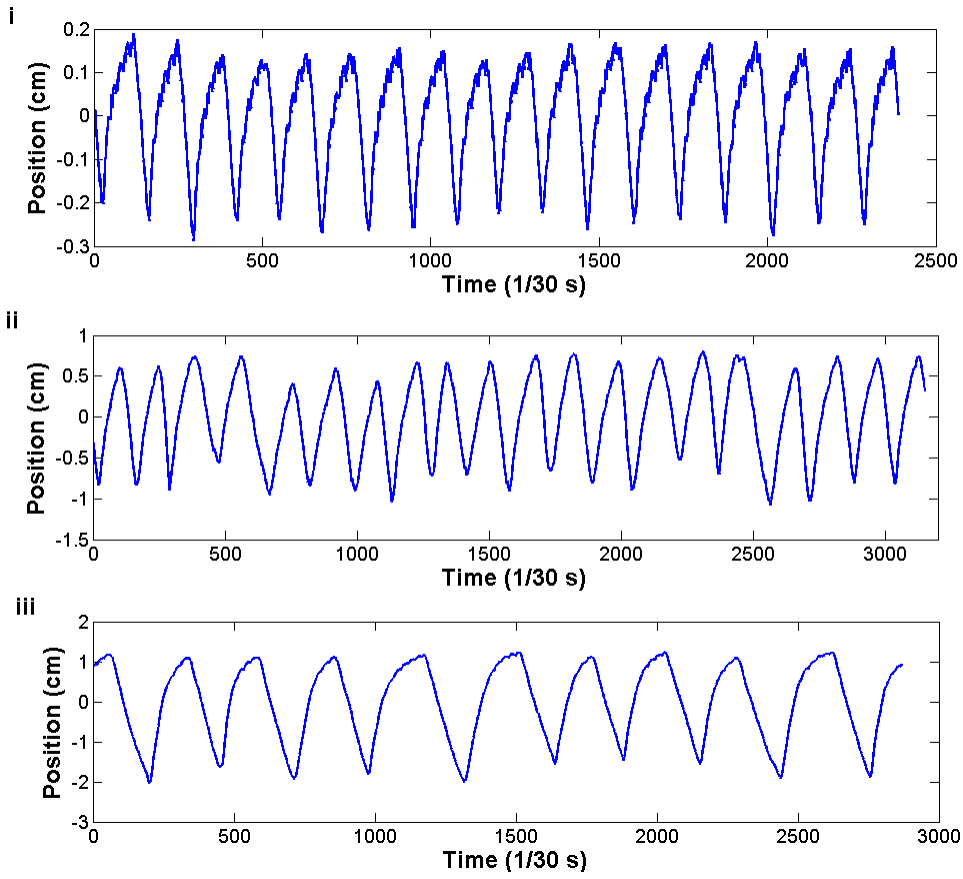

Figure 4.5: Examples of regular breathing traces. Despite being different from one another, each trace could be considered regular due to stable breathing frequency, amplitude and baseline.

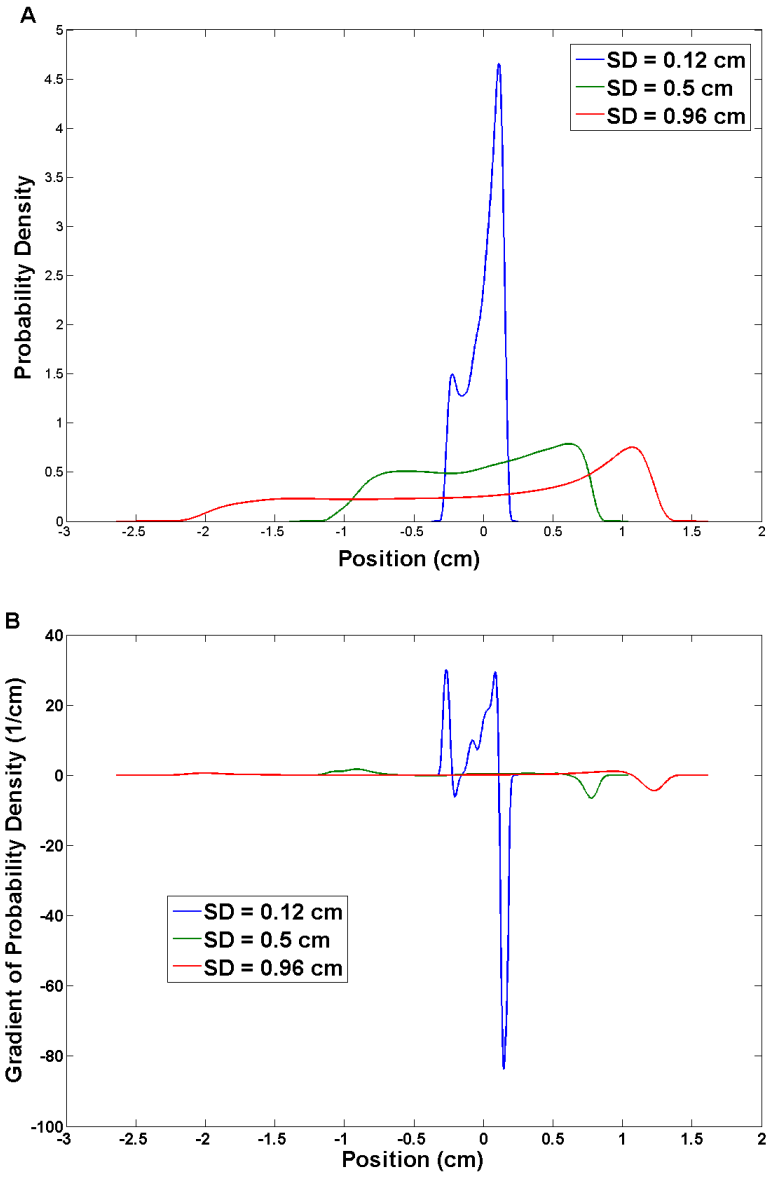

Figure 4.6: The PDFs and PDF gradients corresponding to the regular breathing traces above. Although each trace is regular in nature, the PDFs resulting from each trace are quite different in terms of standard deviation. Figure A depicts the corresponding PDFs on the same axes to contrast their shape. Figure B plots the gradients of each PDF.

The convolution of each of these PDFs with a static dose distribution ultimately reveals the effect of target motion on the delivered dose distribution. Since small targets are more susceptible to loss of dose coverage, it is important to assess the result of the convolution on a range of target sizes. These results for the three regular traces described in this section are shown in Figure 4.7.

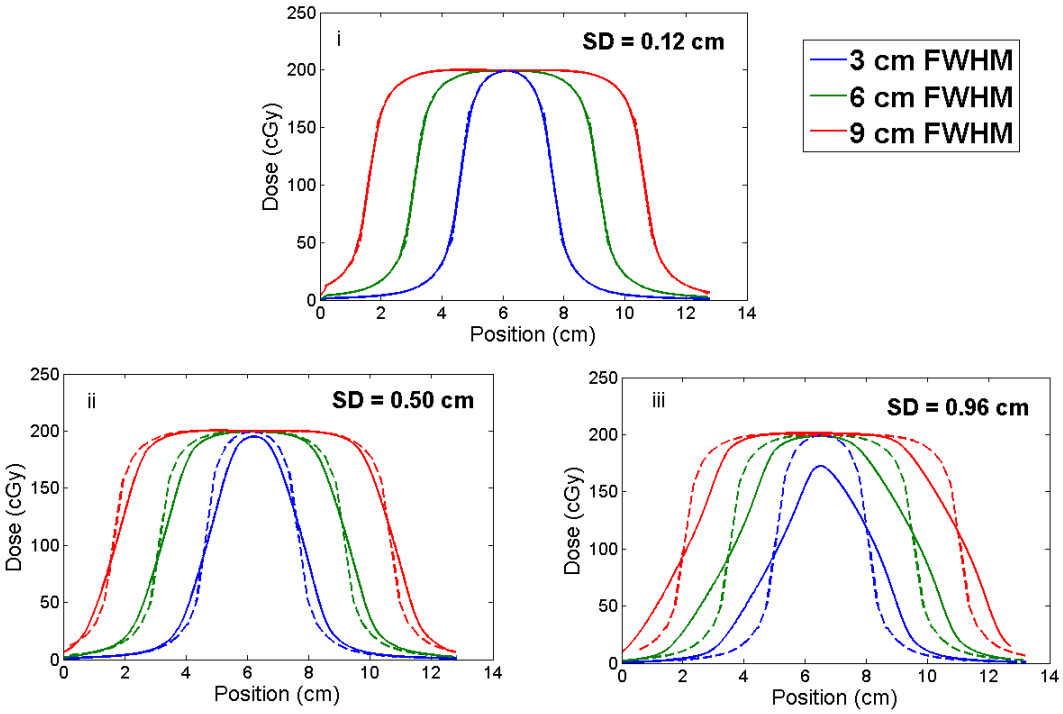

Figure 4.7: Examples of blurred dose distributions resulting from the convolution of the regular breathing trace PDFs and the dose profiles corresponding to a range of target sizes. Dashed lines are the original static profiles, solid lines are the resulting blurred distributions. The target size is characterized by the dose profile's full-width-half-max (FWHM). (i),(ii) and (iii) depict the resulting blurred distributions for the PDFs with SD of 0.12 cm, 0.5 cm and 0.96 cm respectively.

It is clear from Figure 4.7 that as the standard deviation of a given PDF increases, so does the amount of blurring in the resulting dose distribution. The susceptibility of small targets to large motion is also highlighted in Figure 4.7 (iii) where both the dose coverage and maximum dose delivered to the small target have seen a substantial drop.

The trend in the amount of blurring resulting from the convolution also holds true for irregular breathing traces. An irregular breathing trace is typically characterized by baseline shifts, inconsistent breathing period and/or inconsistent breathing amplitude. As with the regular breathing traces, a set of irregular traces are not expected to result in similar dose blurring after convolution simply based on these attributes. Again, it is seen that the spread along the x-axis (standard deviation) of the breathing trace PDF is what best predicts the resulting blurring. Examples of three irregular breathing traces and their corresponding PDFs are shown in Figure 4.8 and 4.9, respectively. As with the regular breathing PDFs, the irregular PDFs are also normalized such that the area under the curve is unity.

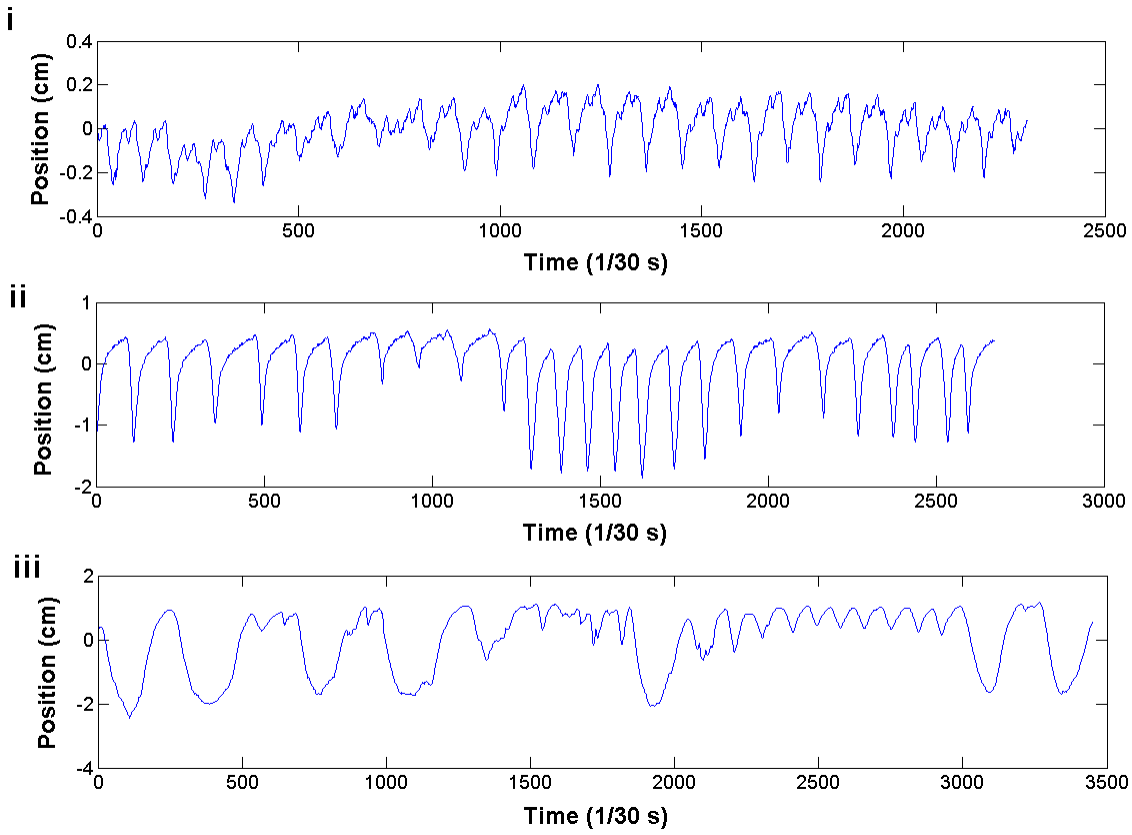

Figure 4.8: Examples of irregular breathing traces. Each trace exhibits breath-to-breath irregularities in at least one of: breathing amplitude, breathing frequency or baseline location.

Figure 4.10 shows the resulting convolutions of the irregular breathing traces with the same three target dose profiles. The clear trend of increasing blurring with increasing PDF standard deviation is again apparent in the case of the irregular breathing traces.

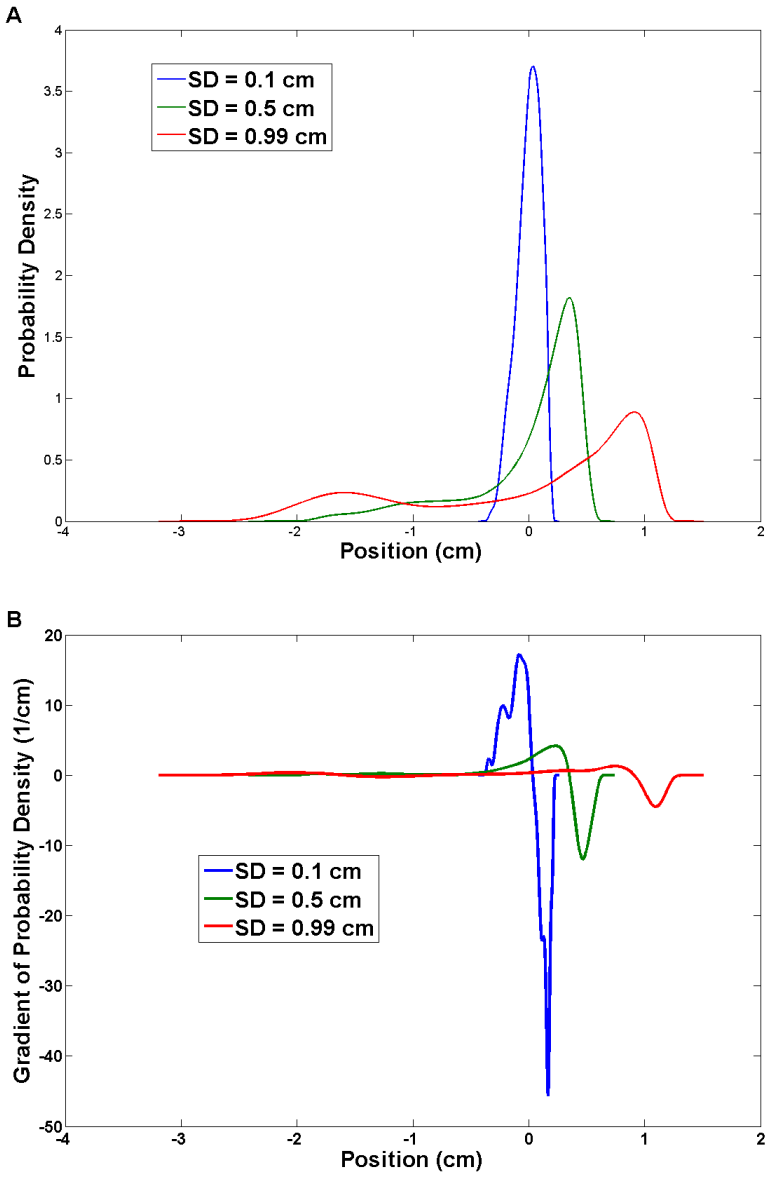

Figure 4.9: The PDFs and PDF gradients corresponding to the irregular breathing traces above. The PDFs resulting from each trace exhibit a more prominent single mode, as compared to the regular trace PDFs. Figure A depicts the corresponding PDFs on the same axes to contrast their shape. Figure B plots the gradients of each PDF.

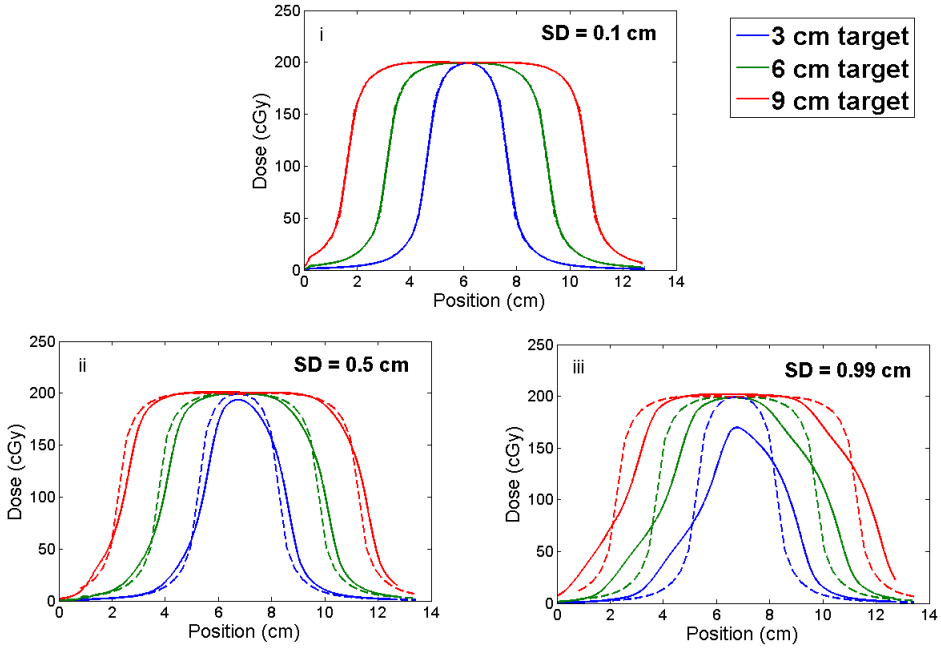

Figure 4.10: Examples of blurred dose distributions resulting from the convolution of the irregular breathing trace PDFs and the dose profiles corresponding to a range of target sizes. Dashed lines are the original static profiles, solid lines are the resulting blurred distributions. The target size is characterized by the dose profile's full-width-half-max (FWHM). (i),(ii) and (iii) depict the resulting blurred distributions for the PDFs with SD of 0.1 cm, 0.5 cm and 0.99 cm respectively.

It is also important to note the relative asymmetry of the blurred dose profiles resulting from the convolution with irregular breathing in Figure 4.10 (iii) and regular breathing in Figure 4.7 (iii). This asymmetry is best explained by looking at the gradient of the PDFs as suggested by Equation 4.13. In the case of the large standard deviation PDFs for both regular and irregular traces, we can plot the PDFs along with their derivatives, as shown in Figure 4.11.

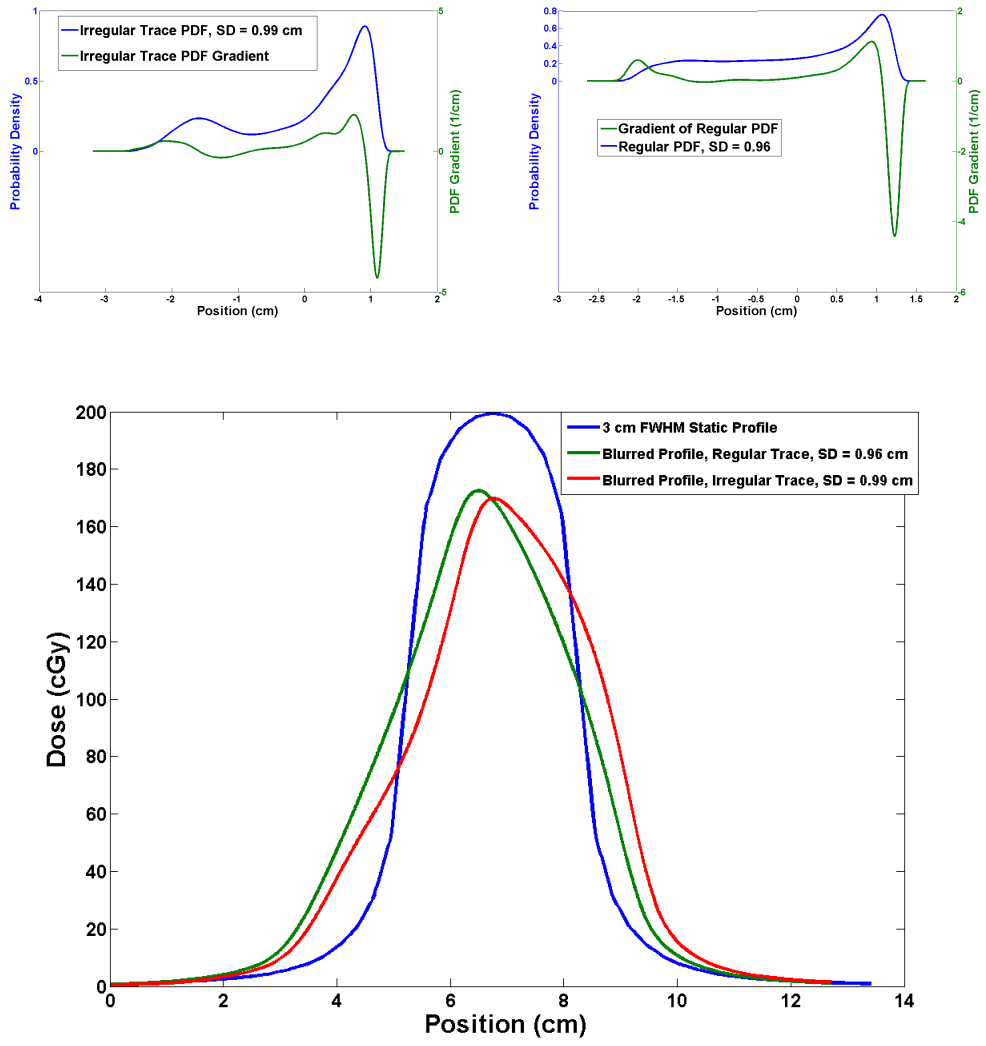

Figure 4.11: A plot of a regular and an irregular breathing trace PDF with their gradients. In these cases, the PDFs have substantial asymmetry due to the specific breathing patterns. As a result, the PDF gradients also have large asymmetry. The large asymmetry in the PDF gradient is what contributes to an asymmetric blurred dose profile.

When performing the calculation defined in Equation 4.13 it can be seen that the regions of the $\frac{d}{dx}PDF(x)$ that are equal, or nearly equal, to zero will offer little or no contribution to the resulting convolution. Correspondingly, regions of the $\frac{d}{dx}PDF(x)$ which are largest will make the largest contribution to the resulting convolution. The PDF gradient highlights these regions. In the case of Figure 4.11, a prominent asymmetry in the $\frac{d}{dx}PDF(x)$ can be seen. This feature of the PDF gradient is not being balanced by any other features of $\frac{d}{dx}PDF(x)$ and as a result, creates the asymmetry seen in the blurred profiles.

4.6 Summary

The convolution model has been used by many different researchers to assess the impact of interfraction and intrafraction organ motion on the delivered dose distribution. Jiang *et al.* [24] showed the model can be reformulated in terms of the static dose gradient, or equivalently, the PDF gradient. This approach highlights the features of the inputs which have the most prominent effect on the resulting blurred dose distribution.

The convolution model requires two inputs: a static dose distribution and a PDF describing the target motion. In this work the static dose distribution must come from a plan generated on an image of the patient with the target in its average position. The PDF describing target motion is garnered from 4DCT data. Tied to these inputs are the assumptions of shift invariance and sufficient sampling. As has been reported by other authors and investigated in this work, the model assumptions can be met to a reasonably strong degree, providing confidence in the modified dose predictions made by the convolution model.

The trends in target dose blurring that result from the convolution of PDFs and dose profiles of various sizes show the impact of the PDF standard deviation and gradient of the PDF on the

delivered dose distribution. The asymmetric nature of gradient of the breathing trace PDFs also determines asymmetric blurring of the dose distribution.

Chapter 5

Film Measurement Procedures and Results

5.1 Introduction

The convolution model of target motion described in Chapter 4 is most frequently used in the context of predicting the effect of interfraction target motion on delivered dose distributions. This type of work was done in the context of random setup errors for tumour sites such as prostate [24, 115], liver [116, 117], or head and neck [118, 119]. However, this study looks to extend the use of the convolution model to intrafraction motion. In order to have confidence that this model can be used in the context of intrafraction motion, experimental measurements must be made to verify the predictions made by the convolution model.

Radiochromic film is the dosimeter of choice for performing these verification measurements. Film offers the best combination of spatial resolution, signal to noise ratio and ease of use for this application. Additionally, film has the advantage of offering a dose measurement over a 2D region of interest. This allows the user to extract dose profiles or perform dose map comparisons with the dose predictions made by the treatment planning software. In this work there is also a

need for comparison with dose predictions made by the convolution model itself. The film measurements performed for this work were taken in a dynamic anthropomorphic thorax phantom that was programmed to perform custom breathing motions. The details of the phantom and film measurements are given in this chapter.

5.2 Radiochromic Film Handling

The radiochromic film used in this work was Gafchromic EBT2 (International Specialty Products, Wayne, NJ). This film offers several advantages over traditional radiochromic film products. Gafchromic EBT2 film requires no processing, which eliminates the need for a darkroom and the associated equipment and chemicals. Gafchromic EBT2 also has low energy dependence and reacts independently of dose rate and fractionation [122].

Gafchromic EBT2 film consists of several layers of material: a base layer ($175\ \mu m$), an active layer ($28 \pm 3\ \mu m$), an adhesive layer ($25\ \mu m$) and a laminate layer ($50\ \mu m$) as shown in Figure 5.1 [122]. The film works by undergoing chemical changes in the active layer in response to the absorbed dose. The active layer of Gafchromic EBT2 consists of diacetylene monomers oriented in the same direction. In response to the absorbed dose, the monomers react with one another to form polymers. The result of this reaction is a change in the optical properties of the film, which can then be used to assess the absorbed dose.

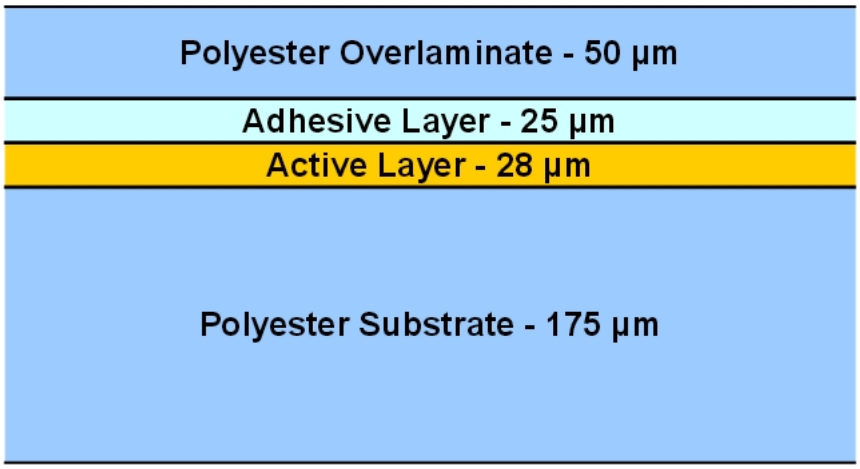

Figure 5.1: A depiction of Gafchromic EBT2 film configuration as shown in the Gafchromic EBT2 white paper published by ISP [122]. Optical density changes in the film result from polymerization reactions in the active layer.

Proper handling of the film includes several steps and considerations as detailed by the manufacturer [122], and expanded upon in the AAPM TG-55 report titled 'Radiochromic film dosimetry: Recommendations of AAPM Radiation Therapy Committee Task Group 55' [123]. These recommendations span topics regarding the handling, calibration and readout of radiochromic film. The key recommendations made by these groups are as follows:

- The film should be exposed to the minimum possible amount of ambient light. Although the manufacturer claims the film is stable in ambient light, the ultraviolet component of the light can contribute to changes in optical density of the film. Andres *et al.* [124] showed that a 6 hour exposure to (relatively intense) room lighting changed the optical density of Gafchromic EBT2 by the equivalent of a 6.1 cGy dose.

- The film should be handled by touching the sides and edges of the film with careful at-

tention paid to avoiding leaving fingerprints or other marks in the area of the film to be used for dose measurement. Any marks or fingerprints on the film will adversely affect the readout of the film.

- It is important to maintain a consistent orientation of the film for readout [124]. The monomers in the active layer are anisotropic and have a specific orientation which results in different readout values depending on the orientation of the film on the scanner bed.

- The film must be digitized at a specific time interval after irradiation due to post-exposure changes in the film. This is because the initial polymerization reaction takes place in approximately 30 ms, however slow changes continue to take place over the course of hours after exposure. Andres *et al.* showed that a minimum of 2 hours is required, post exposure, for the film to stabilize [124].

- The lot number and model number of the film should always be noted so that any variation in the manufacture of the film can be accounted for, if necessary.

- Calibration of the film should use a well-characterized, uniform radiation field.

- The calibration should be performed over the range of dose values expected to be measured experimentally.

For this work, Gafchromic EBT2 film of the same batch (lot # A02181104) was calibrated and handled according to the procedures laid out in AAPM TG-55 [123] and the recommendations of the manufacturer [122]. All the films were digitized with an Epson 10000XL flatbed scanner (US Epson, Long Beach, CA) 22 hours after irradiation. This time frame was selected to allow for the film to develop and to provide consistency in the handling procedure. Calibration and analysis of the images was performed using the RIT v1.2 software package (Radiological

Imaging Technology, Inc., Colorado Springs, CO). Careful handling and digitization of the films used for calibration and measurement allows for dose measurements near $200\ cGy$ to be acquired with a relative uncertainty of $\pm 6\%$ [125].

5.3 Radiochromic Film Calibration

Calibration of the Gafchromic EBT2 film was performed by irradiating pieces of film to a known dose and then reading the optical density of the films using a flatbed scanner. New pieces of film from the same batch (or sheet) can then be used experimentally and compared to the calibration films in order to determine dose. The film calibration was performed in a 'solid water' phantom setup as depicted in Figure 5.2. The setup has a source-to-surface distance (SSD) of $95\ cm$, source-to-axis distance (SAD) of $100\ cm$ and a field size of 10 x $10\ cm$ at isocentre. This setup mimics the absolute dose calibration geometry used by the Grand River Regional Cancer Centre (GRRCC). The LINACs at GRRCC have been calibrated such that 1 MU delivers $1\ cGy$ to the centre of the field under these setup conditions.

A single piece of film was cut into 13 squares with a side length of $5\ cm$. The films were labeled and their orientation relative to the original full sheet of film was noted. Each piece of film to be used for calibration was placed in the centre of the 10 x $10\ cm$ field (at isocentre) with $5\ cm$ of solid water on top and $10\ cm$ of solid water below to provide back scatter material. Each piece of film used for calibration was irradiated once with a predetermined number of monitor units.

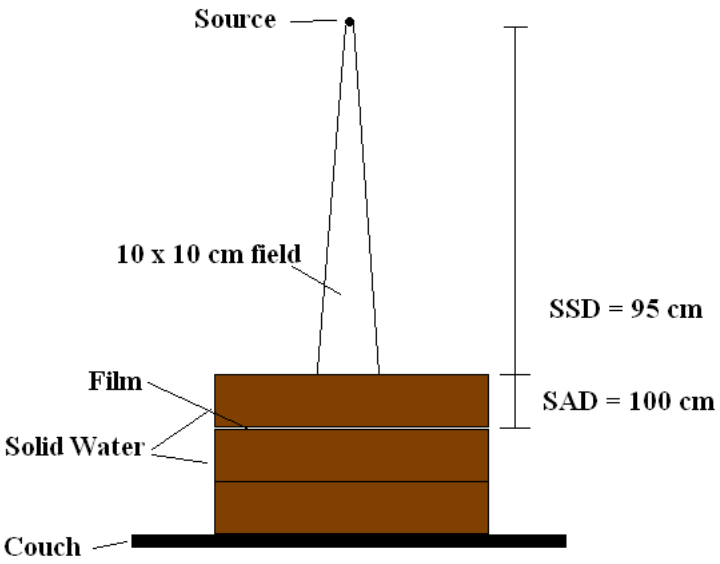

Figure 5.2: A depiction of the film calibration setup geometry. In this configuration, one monitor unit delivers one cGy of dose to the centre of the film.

The manufacturer's recommended analysis of the irradiated films is for a minimum of 13 dose points, including zero dose, to generate a reliable calibration curve. The dose points used should cover the range from zero to a value at least 25% larger than the highest dose you expect to measure with the current calibration [122]. The dose points used for this calibration were: 300, 240, 200, 160, 120, 90, 70, 50, 40, 30, 20, 10 and 0 cGy. Example calibration films scanned together to show contrast are displayed in Figure 5.3.

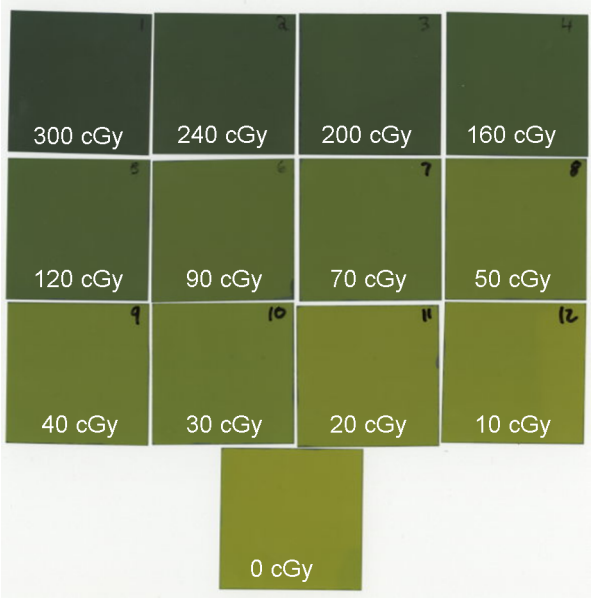

Figure 5.3: Example calibration films after irradiation. The films are shown scanned together in order to demonstrate the colour progression associated with increased dose delivered to the film.

In order to digitize the films, the scanner was first allowed to warm up. After warming the scanner, the films are scanned individually and are each placed on the same area of the scanner bed by using a template to align the film. Each film is scanned using the same settings. The scanning resolution was set to 72 DPI to balance image noise and image resolution. After all the films were scanned, each image was imported into the RIT software for analysis. The calibration curve is created by first selecting a region of interest on each calibration film. The optical density data in the region of interest is averaged to determine the optical density value which corresponds to the given dose level. The film scanner measures the amount of transmission of light through a film and converts this analog signal into digital values with a range between 0 and 65,535 A/D units, where 0 is no light being transmitted (most dense) and 65,535 indicates that the light is transmitted through air (least dense). The A/D units are used in the calibration

software to generate the calibration cure. The graph of A/D units versus dose is then created with each of the 13 data points plotted. The calibration curve was fitted to the data using a cubic spline. The calibration data is shown in Figure 5.4. The doses delivered during experimental film measurements can then be analyzed based on the calibration curve.

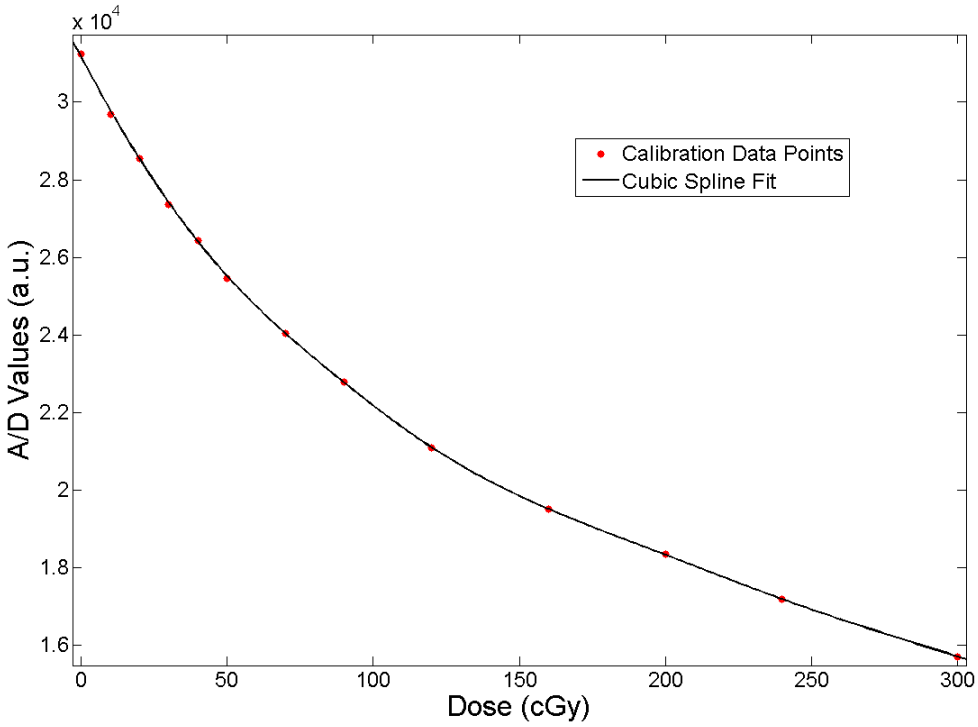

Figure 5.4: The calibration curve for Gafchromic EBT2 film used in this work. The curve consists of 13 data points and a cubic spline fit with $R^2 = 0.9999$.

5.4 Anthropomorphic Breathing Phantom Film Measurements

Description of the Phantom

In order to verify the delivery of the dose distribution calculated by Eclipse v10.1 TPS (Varian Medical Systems, Inc., Palo Alto, CA) and predicted by the convolution model, Gafchromic EBT2 film measurements were taken in an anthropomorphic breathing phantom. The CIRS Dynamic Thorax Phantom, Model 008 (Computerized Imaging Reference Systems, Inc., Norfolk, VA) used for these measurements is shown in Figure 5.5. The phantom is made of epoxy materials that are radiologically equivalent to tissue in the energy range of $50\ kV$ to $25\ MV$. It is equipped with a drive unit capable of performing target motions with sub-millimeter accuracy and reproducibility. The phantom can accommodate different dosimeters (film, MOSFET or ion chambers) depending on its configuration. The dimensions of the thorax phantom represent the 'average man' [126].

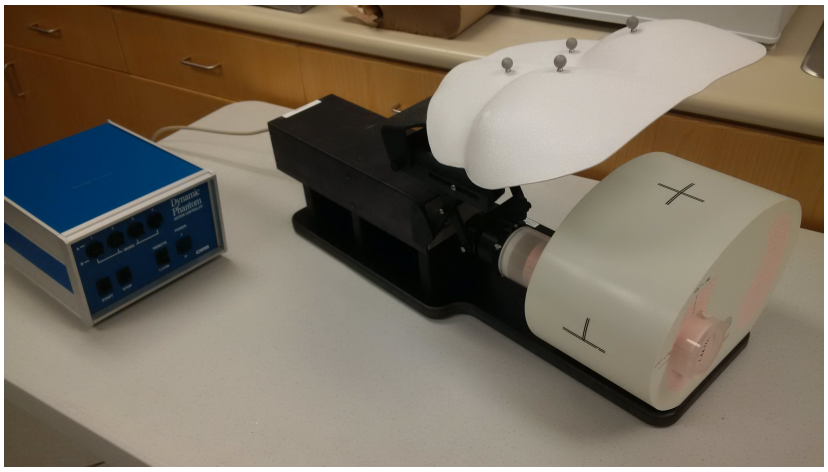

Figure 5.5: A picture of the CIRS Dynamic Thorax Phantom, Model 008. This phantom was used for all film measurements.

The phantom can be used in both static and dynamic modes. In the static mode, the phantom is at rest and no target motion is used. In dynamic mode the phantom can perform many different motions. The phantom system comes pre-programmed with several sinusoidal 'breathing patterns' to choose from. However, the phantom can also be manually programmed to replicate custom breathing patterns with one dimensional target motion. For this work, film measurements were taken in both static and dynamic modes for the verification of the delivered dose distributions.

CT Simulation of the Phantom

A CT simulation of the static phantom was acquired at the GRRCC using a Siemens SOMATOM Sensation Open scanner (Siemens AG Medical Solutions, Erlangen, Germany). This is a large bore scanner capable of complete gantry rotations as fast as $0.5\ s$. The scanner uses a proprietary STRATON X-ray tube that functions with tube current in the range of $28 - 400\ mA$ and tube voltage of $80,\ 100,\ 120$ or $140\ kV$. The scanner features $26,880$ detectors arranged in 40 rows and is capable of reconstructing images with isotropic voxels with side length as small as $0.33\ mm$ [127].

The CIRS phantom was scanned using a typical departmental chest scan protocol. The chest scan protocol used a tube voltage of $120\ kV$ and tube current of $55\ mA$. The resulting dataset is reconstructed with anisotropic voxels with axial dimensions of 0.0977 x $0.0977\ cm$ and slice thickness of $0.3\ cm$. The phantom was setup and aligned on the CT couch using the external markers affixed to the phantom and the in room lasers for reference. Figure 5.6 is a coronal slice at the plane of interest in the phantom CT data set used for treatment planning.

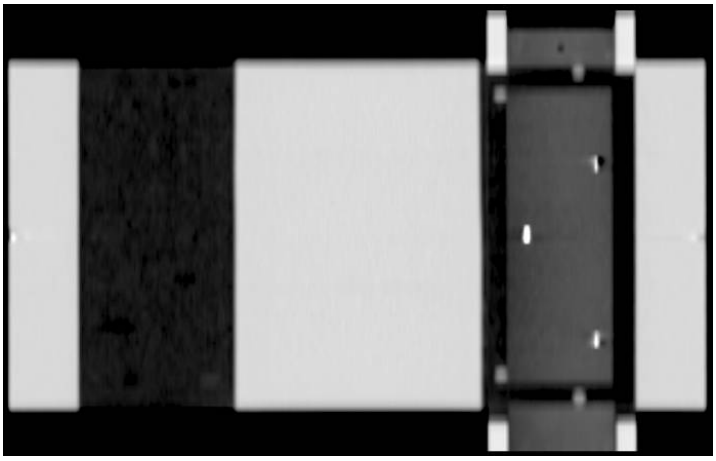

Figure 5.6: A coronal slice taken from the CT scan of the CIRS dynamic thorax phantom configured with the film insert. Note the fiducial markers which are used to align the selected dose profiles for comparison.

After completing the scan, the reconstructed images were pushed via the network from the CT scanner computers to the computers serving the TPS. From there the phantom images were imported into the TPS in order to generate the treatment plan.

Treatment Planning on the Phantom

A simple, open MLC, three field plan was generated with the Eclipse TPS. The plan parameters are displayed in Table 5.1. The beam isocentre was placed at the centre of the film insert within the phantom. The dose rate was $400\ MU/min$ for all beams and all couch angles were set to 0°. The beam angles were selected in order to avoid excessive interference from the treatment couch and the dose prescription was set to deliver 200 cGy to 99% of the PTV. The dose was calculated using Varian's AAA v.10.0.28 algorithm. The main reason for taking this approach

to the treatment plan is that simple open fields result in dose profiles with the steepest dose gradients. This makes these types of plans the most susceptible to loss of dose coverage due to target motion. The dose profiles taken from film measurements of this plan were compared to the dose profiles calculated by Eclipse at the same location inside the phantom.

	Beam 1	Beam 2	Beam 3
Gantry Angle (deg)	315	0	45
(X,Y) Jaw settings (cm)	(3.7 , 3.7)	(3.2, 3.7)	(3.6, 3.7)
MU	86.6	92.5	93.9

Table 5.1: A summary of the treatment plan parameters used to irradiate the phantom for static and dynamic film measurements. The coordinate system used is the IEC convention.

In order to compare dose profiles from the TPS dose calculations to the profiles measured on film, careful consideration must be given to geometry of the film insert. The phantom's film insert accepts rectangular pieces of film cut to dimensions of 13.5 x 4 cm. As can be seen in Figure 5.6, the phantom's film insert has pegs to allow for consistent film placement. The pegs also serve to align both halves of the film insert, and hold them together. The film insert also has fiducial markers placed within it to provide reference points on the CT images for film measurement comparisons. Comparison of the measured and calculated dose profiles was achieved by selecting a dose profile along the superior-inferior direction of the phantom through treatment plan isocentre, in the TPS. The distance from the right edge of the film to the selected dose profile was then recorded. After irradiating and digitizing the film, the measured dose profile for comparison was selected by measuring the same distance from the edge of the film, then selecting the dose profile passing through that point, parallel to the length of the film. All dose profiles originated at the superior edge of the film.

5.5 Film Measurements in the Static Phantom

The film measurements taken in the static mode were used to determine confidence in the repeatability and accuracy of the film handling and measurement procedures. These results also serve to verify the calculations made by the Eclipse TPS environment. In order to acquire the static film measurements, the CIRS phantom was setup on the treatment unit using the same configuration as at the time of CT scanning. The external markers on the phantom were aligned with the in room lasers. After aligning the phantom with the lasers the required couch shifts were applied, such that the treatment beam isocentre was at the centre of the film insert as planned. The couch shifts were predetermined by the TPS by comparing the location of the isocentre at the time of the CT simulation to the location of the beam isocentre in the treatment plan.

The dose profile resulting from a static phantom film measurement is shown in Figure 5.7. The absolute dose profiles have good agreement with the predictions made by Eclipse. In this case, 96.1% of the measured dose points are within 3% or $3\ mm$ of the corresponding dose points in the Eclipse prediction. These criteria are commonly used when assessing the level of agreement between a measured and calculated dose plane in the context of a gamma evaluation [128], and is similar to the recommendations of Van Dyk *et al.* [129] for a quality assurance threshold. The error bars represent $\pm 6\%$ of the absolute dose, which is the error level that can be expected with good handling techniques as determined by Hartmann *et al.* [125].

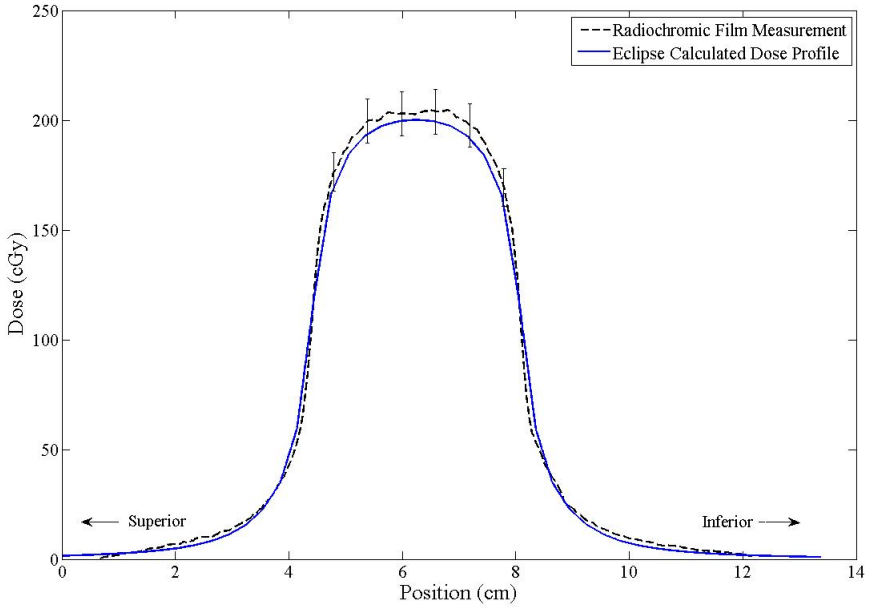

Figure 5.7: A comparison of the dose profile calculated by the Eclipse TPS and the corresponding dose profile measured on radiochromic film in the CIRS phantom in static mode.

Several such film measurements were performed over the course of this work. The resulting dose profile comparisons consistently showed good agreement between film measurement and dose calculation in Eclipse. The static dose profile measurements were an important part of refining the measurement technique and building confidence in the measurement procedure and results.

5.6 Film Measurements in the Dynamic Phantom

Film measurements were also taken with the phantom in the dynamic mode. This was achieved by programming the one dimensional motion of the phantom insert to replicate the motion of selected patient breathing traces. Programming the phantom to perform a custom motion based on a recorded breathing trace requires several steps. First, the recorded trace data needs to be manipulated and scaled such that it is geometrically centered with a maximum amplitude of 1 and minimum amplitude of -1 (arbitrary units). The manipulated trace also needs to be smoothed to remove any fine structure from the recorded trace. The smoothing step is necessary to avoid damaging the phantom motion hardware. The trace manipulation and smoothing was performed in MATLAB. The next step is to reformat the trace data such that it is readable by the motion controlling software (Motion Perfect 2.4.4, Trio Motion Technology, Freeport, PA, USA) of the CIRS phantom. The CIRS phantom can then be connected to the computer running Motion Perfect via the serial port. With the custom trace data loaded on the computer, the CIRS phantom can then be made to perform the custom motion by setting it to manual motion mode and issuing the command to start the motion. The amplitude, A, of motion performed by the phantom is defined by the user. The scaled breathing trace will then span the range $[-A, A]$ when performing the custom motion.

The film measurements taken with the phantom in the dynamic setting were used to verify the ability of the convolution model to predict the effect of intrafraction motion on the delivered dose distribution. Several patient breathing traces were used; some with regular repetitive breathing and others with highly irregular breathing patterns. With the film insert in place and the phantom set to perform the custom motion, the same three field treatment plan used for the static case was delivered to the target. The dose profiles from the films acquired in the dynamic mode were compared to the dose profile predictions made by the convolution model. Figure 5.9 and Figure

5.11 present the results of two such dynamic phantom film measurements.

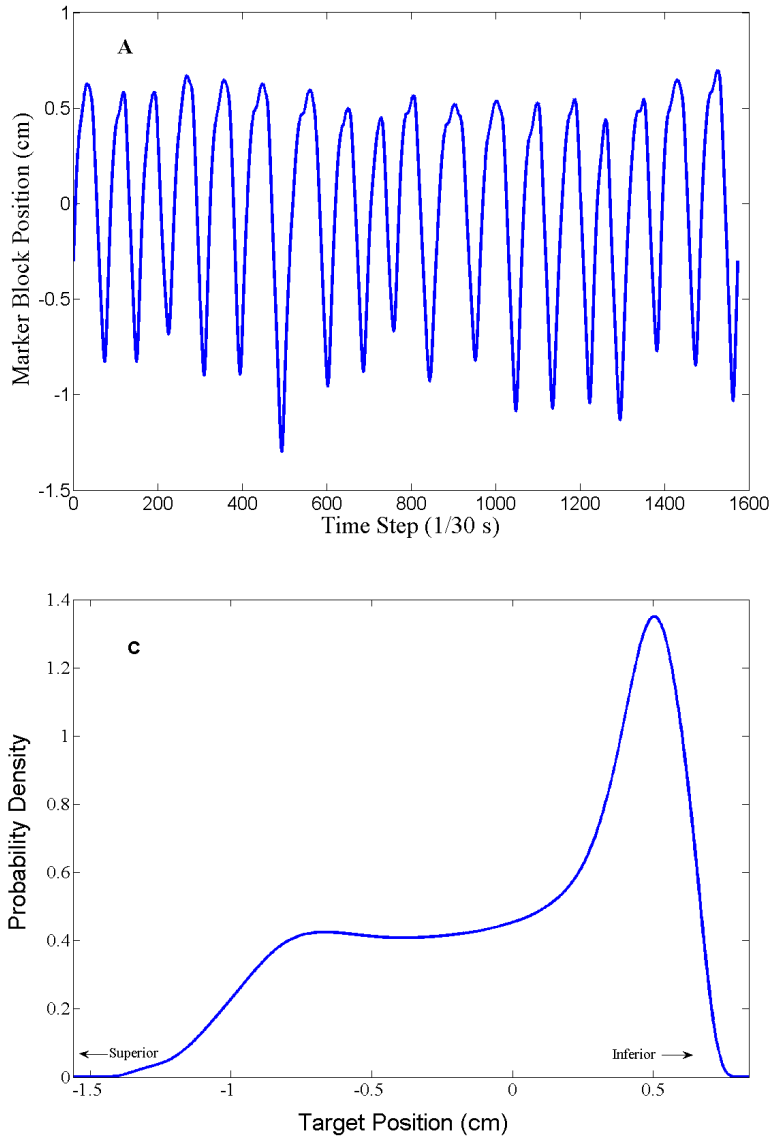

Figure 5.8: A) A regular breathing trace used to program the dynamic thorax phantom. C) The PDF generated from the trace (standard deviation of $0.52\ cm$).

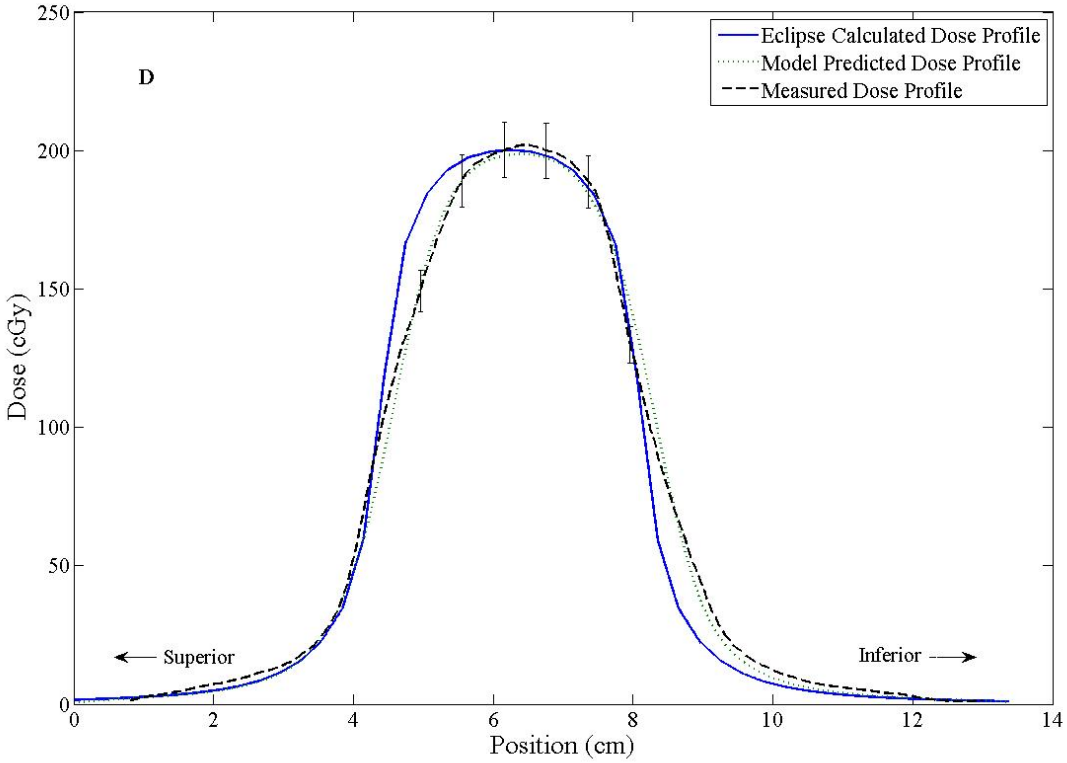

Figure 5.9: D) Dynamic mode dose profile measurements demonstrating the applicability of the convolution model for intrafraction motion in the case of regular breathing traces.

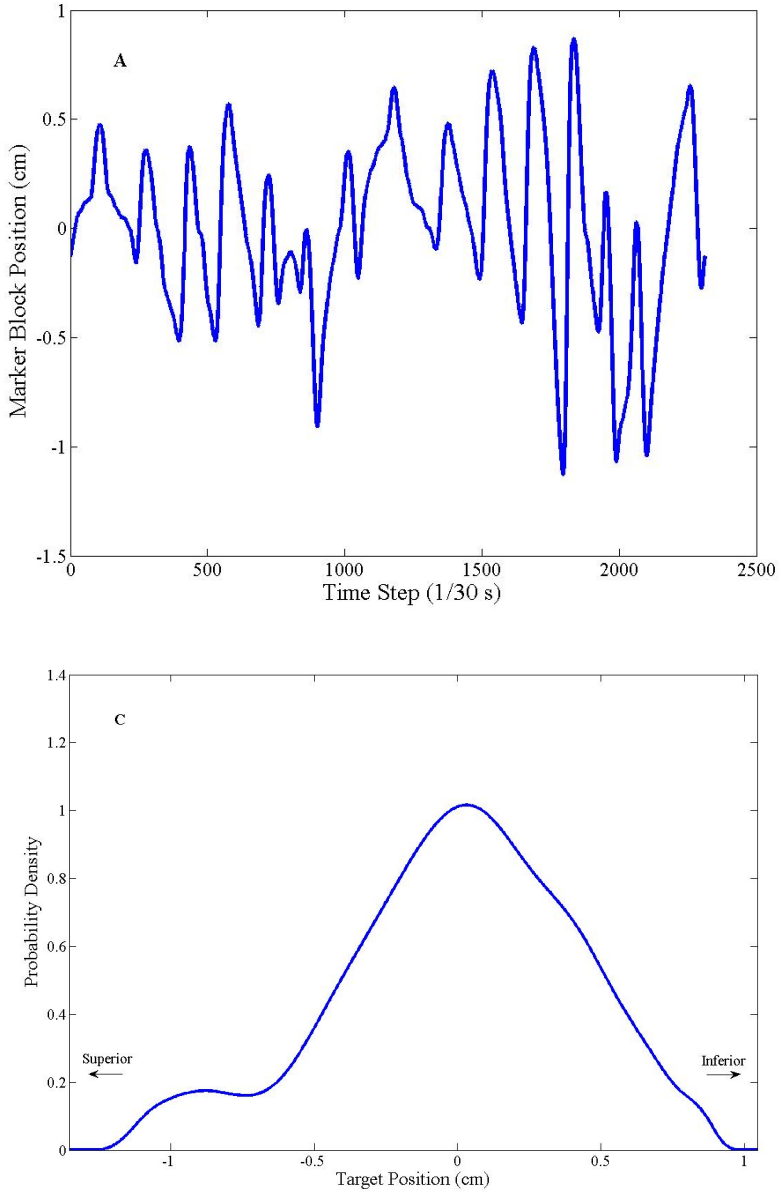

Figure 5.10: A) An irregular breathing trace used to program the dynamic thorax phantom. C) The PDF generated from the trace (standard deviation of $0.40\ cm$).

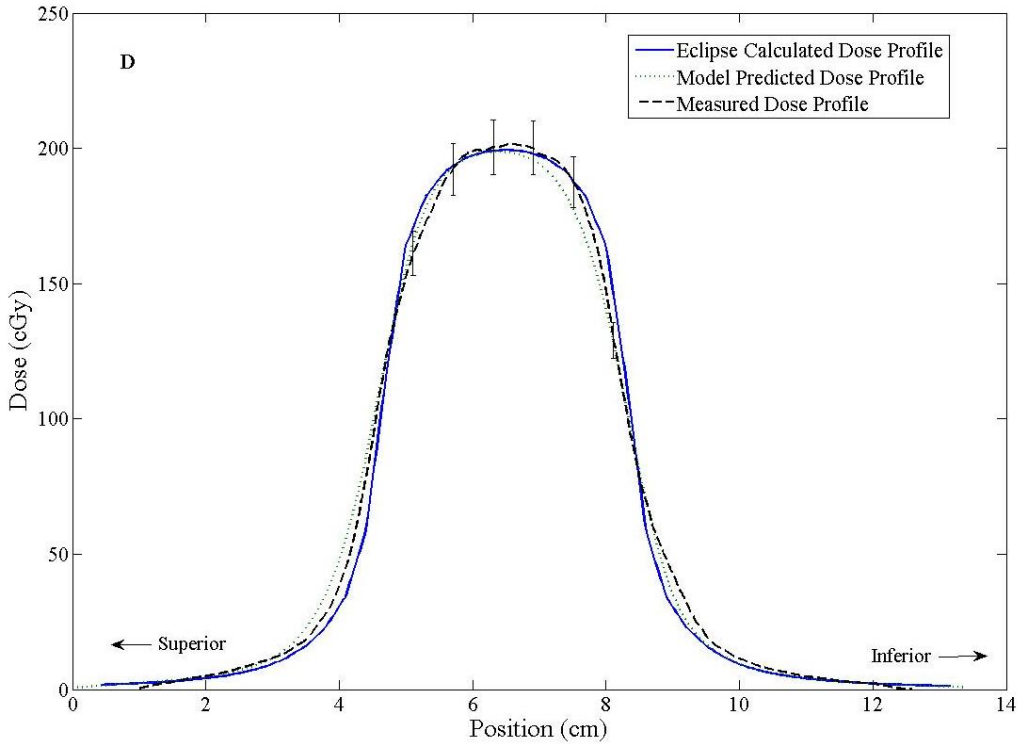

Figure 5.11: D) Dynamic mode dose profile measurements demonstrating the applicability of the convolution model for intrafraction motion for irregular breathing traces.

The selected traces were used to demonstrate that the convolution model makes valid predictions for a range of breathing patterns, including regular and irregular breathers. In the case of the regular breathing pattern (Figure 5.9), 98.9% of the measured dose points passed the 3% / 3 mm criteria, while the measurement of the irregular breathing pattern (Figure 5.11) dose distribution passed on 98% of dose points. The obvious discrepancy between the Eclipse calculation and the convolution model prediction (and corresponding film measurement) is the 'blurring' effect of target motion. Eclipse dose not account for target motion while performing the dose calculation. These results underscore the needs for target motion management.

5.7 Summary

These experimental measurements were necessary to verify the validity of the convolution model in the context of intrafraction motion, and to assess the use of the margin recommendations made in this work. The results show good agreement between the TPS calculations and film measurements taken in the static phantom, which gives confidence in the film handling and measurement procedures. The dynamic mode film measurements have good agreement with the predictions made by the convolution model for both regular and irregular breathing patterns.

These experimental results indicate that under most circumstances the convolution model makes valuable predictions regarding the effect of motion on the delivered dose distribution. The confidence developed in the accuracy of the motion model justifies larger scale simulation and analysis of the effect of breathing motion on the delivered dose distribution. The results of such an analysis could be used to identify trends in the resulting dose coverage, which could then inform intrafraction motion management strategies.

Film measurement procedures such as these could provide an effective QA procedure for measuring dose profiles with patient specific breathing patterns measured during 4DCT scans. This verification could be done on a plan-by-plan basis to provide clinicians confidence that increased margins are justified and offer an effective means for compensating for target motion.

Chapter 6

Motion Simulation Study

6.1 Introduction

Confidence in the reliability of the convolution model for intrafraction target motion has been established by performing radiochromic film measurements as described in Chapter 5. These static and dynamic mode film measurements provide the basis for further analysis on the effect of target motion by analyzing the predictions of the convolution model on a larger scale. Ultimately, one of the aims of this work is to generate margin predictions which can be used by clinicians while making treatment planning decisions. In order to accomplish this aim, we need to analyze the effect of target motion on the delivered dose distribution under a wide range of conditions. Specifically we want to analyze a variety of breathing patterns and target sizes in order to establish trends that can be used to make margin recommendations. Computational simulation of the target motion allows for the rapid data generation and analysis required to identify these trends.

The motion simulations generated in this work were performed in MATLAB using standard MATLAB routines and custom code. As discussed in chapter 4, the convolution model requires

the input of a motional PDF obtained from a 4DCT scan and a static dose profile. The motional PDFs were generated from each of 502 unique patient breathing traces. The traces used in this work were recorded from patients undergoing clinical 4DCT scans over a four year period at the London Health Sciences Centre. The static dose profiles were obtained by first generating a simple treatment plan on a CIRS Dynamic Thorax phantom (described in chapter 3) in the Eclipse treatment planning software. Static dose profiles along the appropriate directions were then exported from the treatment plan and used in the MATLAB simulation. The results of the simulation described in this chapter and film measurements described in chapter 5 were published in the Journal of Applied Clinical Medical Physics [130].

6.2 MATLAB Simulation Process

The effect of motion on the delivered dose distribution as predicted by the convolution model was simulated for each of the 502 patient breathing traces on a set of static dose profiles generated from targets ranging from 2-10 cm in diameter. An in house MATLAB program was used to perform the convolutions and analyze the dose coverage offered by the resulting blurred dose profiles. The main dose coverage metric used to assess the effect of the target motion was the D_{95}. The D_{95} is defined as the minimum dose received by 95% of the target volume. This metric is akin to a point on a dose-volume histogram (DVH) and is used to assess the quality of the dose coverage offered by a given treatment plan. Other dose coverage metrics such as the equivalent uniform dose and D_{99} were also assessed. Below is the pseudo code description of the simulation process:

- IMPORT list of static dose profile files
- FOR EACH static dose profile file:

  - compute dose coverage metrics of the static profile

- IMPORT list of breathing trace files
- FOR EACH breathing trace file:
  - extract positional data recorded during beam-on
  - compute breathing trace statistics (breathing amplitude, length of data recording)
  - generate histogram of recorded breathing trace positions
  - generate normalized PDF from histogram
  - compute PDF statistics (standard deviation, mean, skewness, kurtosis)
  - place PDF origin at the PDF mean
  - perform convolution of PDF with EACH static dose profile
  - compute dose coverage metrics of the blurred dose distribution

Having simulated the outcomes of target motion based on a wide variety of breathing traces and target sizes, the data must be analyzed to identify trends and correlations that can be used to justify margin recommendations.

6.3 PDF Statistics

It is useful to look at some descriptive statistics summarizing the breathing traces (and corresponding PDFs) used in the simulation study. Figure 6.1 shows the distribution of the total time recorded for each breathing trace. It should be noted that all traces are comprised of data recorded over a minimum of $24.5\ s$ with the median recording time of $77.9\ s$. Given that a typical breathing cycle is approximately $3\ s$, recording the breathing trace on this time scale ensures that a

minimum of 8 breathing cycles are captured during the recording period. This gives time for any breathing irregularities to manifest, which is a necessary requirement for a useful and reliable breathing trace.

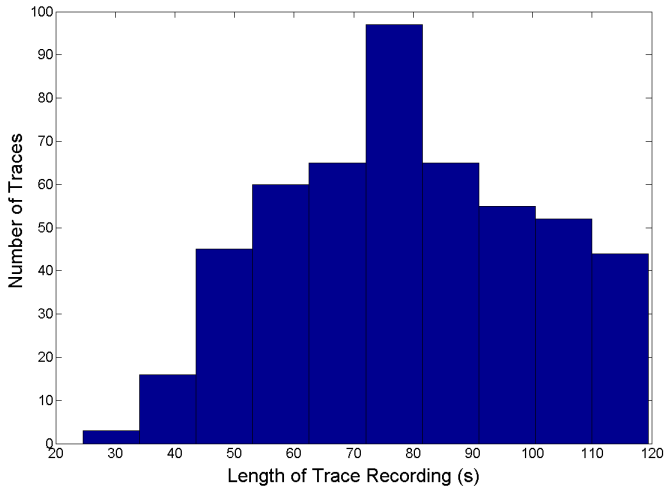

Figure 6.1: A histogram detailing the distribution of breathing trace recording times. The minimum and maximum recording time were $24.5\ s$ and $119.5\ s$ respectively. The median recording time was $77.9\ s$ and the average recording time was $78.8\ s$.

The breathing amplitude and breathing trace standard deviation are also important parameters for making margin recommendations. Figure 6.2 and Figure 6.3 display histograms of the breathing amplitude and PDF standard deviation for all the breathing traces used. The amplitude is determined by referencing the maximum displacement recorded by the marker block. The standard deviation is calculated according to

$$s = \left(\frac{1}{n-1} \sum_{i=1}^{n} (x_i - \bar{x})^2 \right)^{1/2}, \tag{6.1}$$

where s is the standard deviation, x_i are the recorded positions, $\bar{x}$ is the average position and n is the total number of data points.

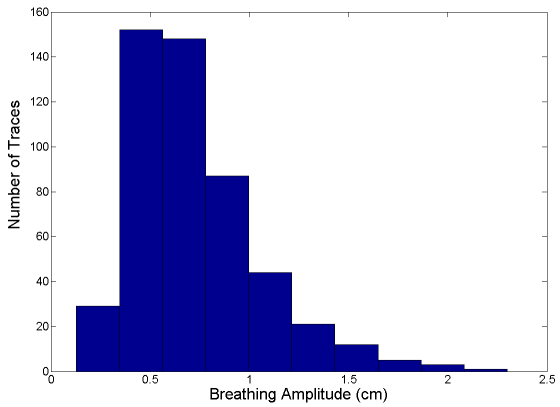

Figure 6.2: A histogram detailing the distribution of breathing trace amplitudes. The minimum and maximum amplitudes were $0.13\ cm$ and $2.30\ cm$ respectively. The median amplitude was $0.66\ cm$ and the average amplitude was $0.73\ cm$.

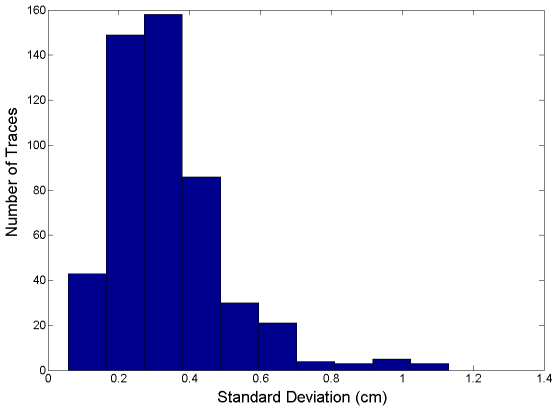

Figure 6.3: A histogram detailing the distribution of breathing trace standard deviations. The minimum and maximum standard deviations were $0.057\ cm$ and $1.13\ cm$ respectively. The median standard deviation was $0.31\ cm$ and the average standard deviation was $0.34\ cm$.

It should be noted that the positions (and amplitude) recorded for the breathing trace are in fact the positions of the marker block, used as part of Varian's RPM system, on the patient's chest. Although the breathing trace positions and amplitude recorded this way are not equal to the positions or amplitude of the target motion in general, the trace can be normalized according to the amplitude of motion determined in a 4DCT scan. Once the trace has been normalized, it is representative of the 1D motion of the target. The breathing traces used for this simulation study were not normalized in this manner (as would be required when applying the results of this work clinically), however the raw trace information provides a wide range of breathing amplitudes and trace patterns for study here.

The relationship between the PDF standard deviation and breathing amplitude is also pertinent. As can be seen in Figure 6.4 there is a clear correlation between the amplitude and standard deviation. Intuitively this is the expected result; as the amplitude of the motion increases, so too

does the standard deviation (often interpreted as the 'average distance from the average' of the data points). The slope of the best fit line is approximately 0.46 ($R^2 = 0.864$), indicating that the value of the standard deviation is approximately 46% of amplitude. This is similar to the result identified by Engelsmann *et al.* [1]. Although the amplitude accounts for a major portion of the standard deviation, higher order features of the PDF (such as skewness and kurtosis) also make contributions to the PDF standard deviation.

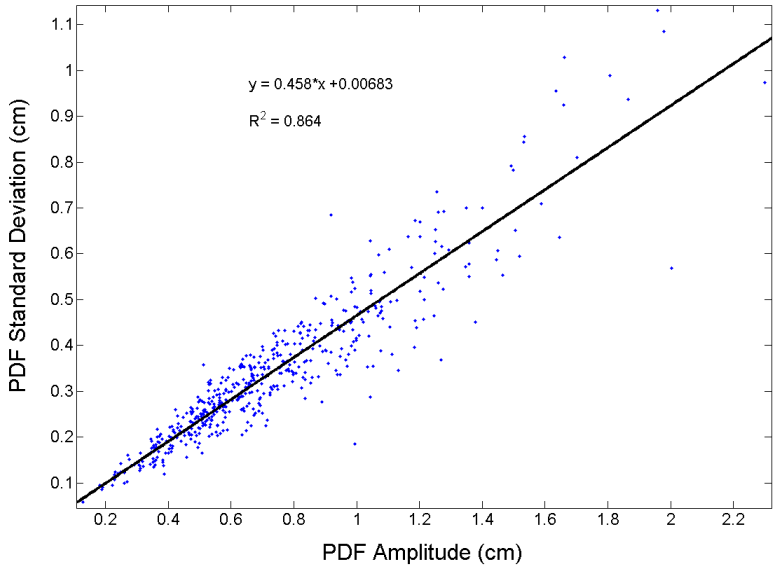

Figure 6.4: A plot showing the relationship between the PDF standard deviation and the breathing amplitude.

6.4 Target Volume Dose Coverage

In order to make margin selection recommendations, it is useful to know the loss of target coverage which is expected on case by case basis. This simulation study revealed that the loss of

target D_{95} is predictable, based on the patient's specific PDF standard deviation. Figure 6.5 demonstrates the relationship between the expected loss of target D_{95} (in terms of the ratio of the static and blurred D_{95} values) and the standard deviation of the breathing pattern. These results are in line with data presented by other authors [2, 1] regarding the predictive power of the PDF standard deviation with regards to the target dose coverage. The D_{95} was used to assess dose coverage because this metric is often used in the clinic to evaluate whether a given treatment plan offers acceptable coverage. Other dose metrics could be used in principal, the D_{95} was selected for its relevance to clinicians.

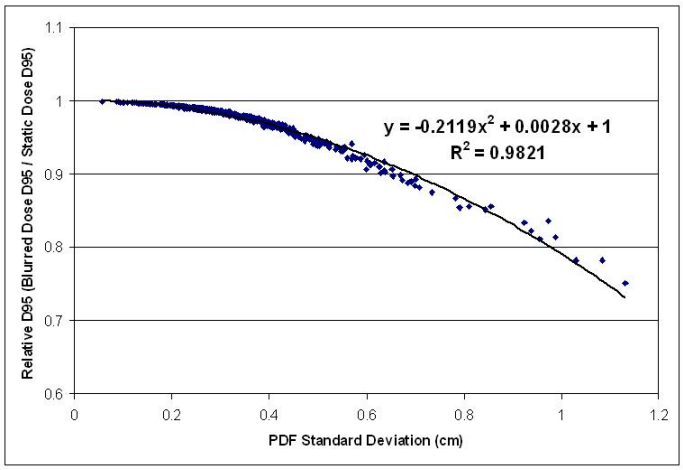

Figure 6.5: A plot of the relative D_{95} (blurred D_{95} to static D_{95}) versus PDF standard deviation. As the amount of motion increases, so t0o does the loss of target dose coverage.

The next assessment was to determine how much target D_{95} can be recovered by incrementally increasing the beam width. The incremental increase in beam width was achieved by adding the additional beam width to the center of the static dose profile, leaving the dose gradients in the penumbral regions of the profile unchanged. This approximation allowed for rapid assessment of the additional beam width required to recover the lost dose coverage.

Using MATLAB code (included in Appendix B) an iterative process was used to determine the necessary additional beam width:

- A blurred dose profile is calculated based on a static dose profile and a given PDF.
- The relative D_{95} of blurred profile is calculated.
- If the relative D_{95} is less than 1, the width of the original static dose profile is increased (as described above). If the relative dose profile is greater than or equal to 1, then the iterative process stops.
- The blurred dose profile is re-calculated based on the wider static dose profile and the same PDF.
- The relative D_{95} of the new blurred profile is calculated and the process repeats.

Once the iterative process has stopped, the additional beam width required to recover the lost D_{95} is recorded. Shown in Figure 6.6 is a plot of the additional beam width required to completely recover lost D_{95} due to dose blurring caused by target motion. The fit equation $y = 18.582x^2 + 2.234x$ describes the data set well ($R^2 = 0.984$).

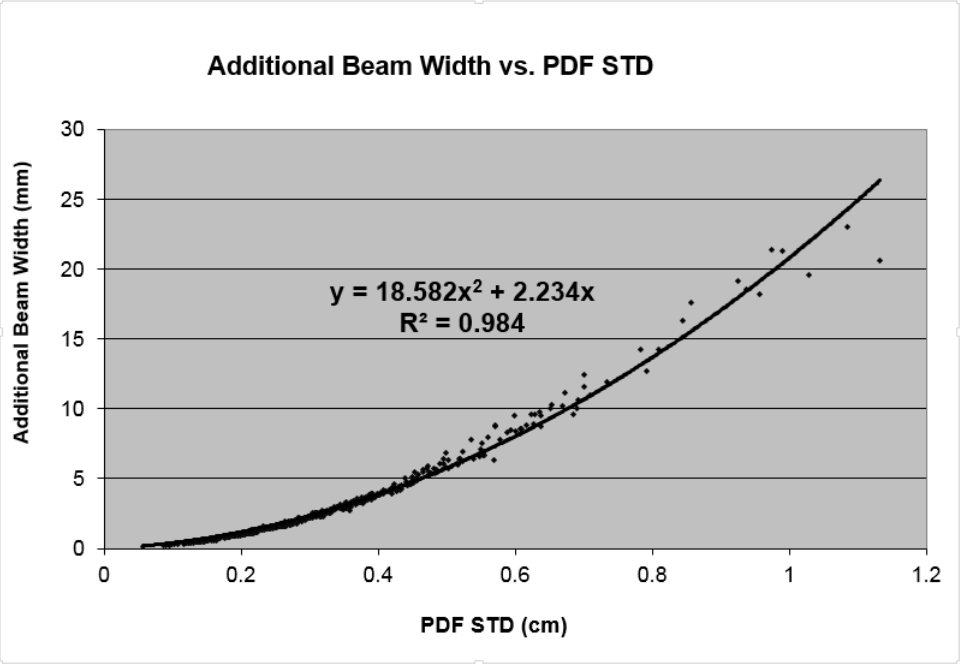

Figure 6.6: A plot of the additional beam width required in the direction of motion to compensate for loss of target D_{95} vs. PDF standard deviation. The additional beam width should be applied in the direction of motion.

For example, suppose a given patient presented with a breathing trace whose PDF has a standard deviation of $0.4\ cm$. After referencing Figure 6.6 or using the fit equation, it is determined that an additional $3.9\ mm$ of beam width is required to compensate for the target motion.

6.5 Effect of Target Size

It is necessary to consider the role of target size when trying to compensate for motion and deliver a specific D_{95} to the target. As the size of the target along the direction of motion increases, so

does the width of the dose profile (defined as the full-width-half-max [FWHM] of the profile) required to adequately cover the target. As the FWHM of the dose profile increases, the relative contribution of the penumbral region of the profile to the overall dose profile, decreases. Since the penumbral region of the profile is most predominantly affected by the convolution (compared to the central region of the profile), smaller targets will be more susceptible to loss of dose coverage due to motion as compared to larger targets.

In order to assess this effect, the relative D_{95} data resulting from the convolution of each breathing trace was analyzed over a range of target sizes. The results of this simulation study are summarized in Figure 6.7. As the FHWM of the various profiles increases, the given profile becomes less sensitive to motion in terms of loss of D_{95}. For example, the target profile with a FHWM of $2.6\ cm$ loses approximately 7% of its original D_{95} when faced with target motion of $0.4\ cm$ standard deviation. The same level of motion causes a loss of approximately 1.5% of the original D_{95} to a target profile with a FHWM of $5.1\ cm$. As the target FWHM increases beyond $5.1\ cm$, the changes in sensitivity to motion become small. This is due to the smaller relative contribution of the penumbral regions to wider profiles. As a result, the D_{95} data for targets with FWHM greater than $5.1\ cm$ begins to overlap with the data for the $5.1\ cm$ target and was therefore omitted from Figure 6.7.

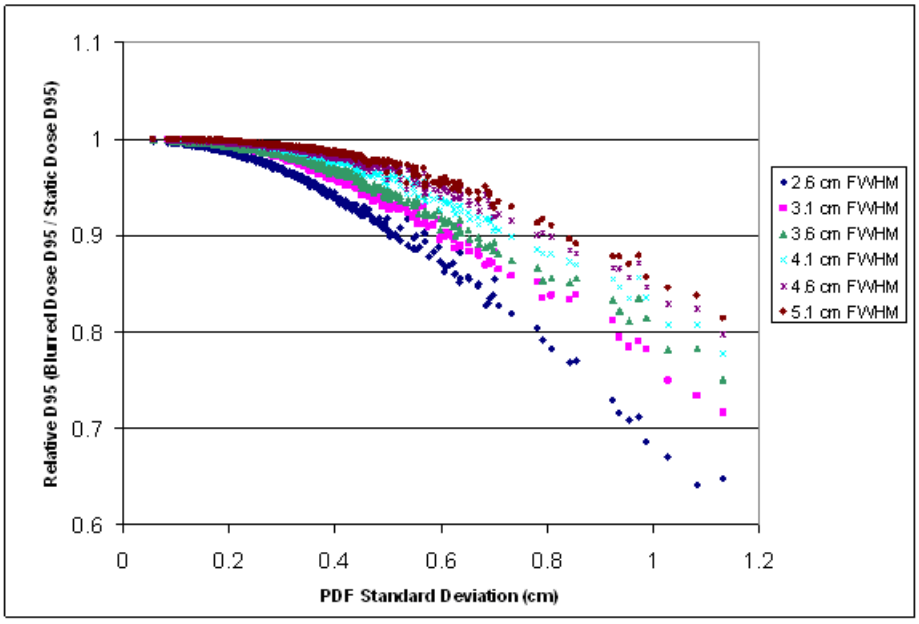

Figure 6.7: A plot of relative D_{95} versus PDF standard deviation for multiple target sizes. The sensitivity to coverage loss due to motion decreases with increasing target size. The change in sensitivity becomes small as the FWHM of the increases beyond $5.1\ cm$.

The iterative process described in the previous section was extended to static dose profiles with initial FWHM values ranging from $2.6\ cm$ to $10.1\ cm$. Shown in Figure 6.8 is a plot of the additional beam width required vs. PDF standard deviation for a range of initial static dose profile FWHM values.

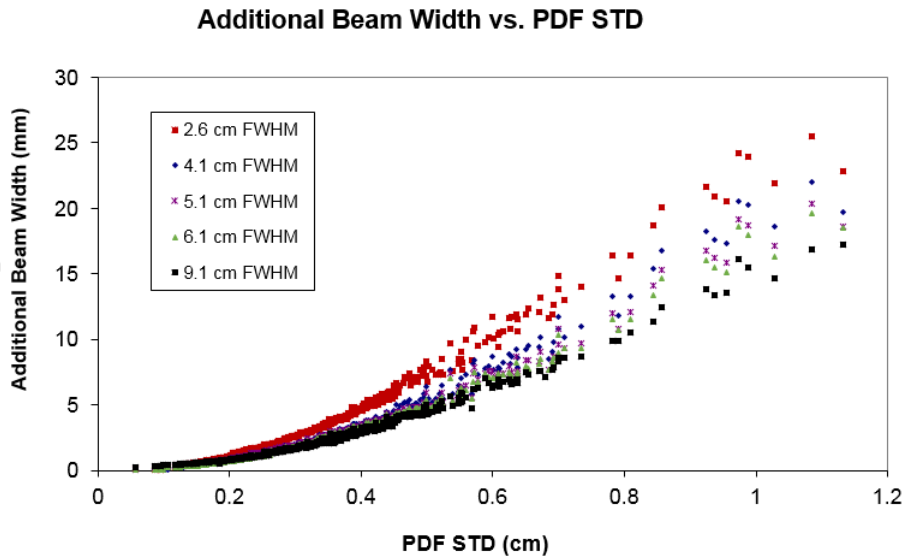

Figure 6.8: A plot of the additional beam width required in the direction of motion to compensate for loss of target D_{95} vs. PDF standard deviation. The additional beam width should be applied in the direction of motion. This plot includes the trends for several initial static dose profile FWHM values

6.6 Treatment Margin Recommendations

Treatment margin recommendations can be made by using the simulation results discussed above. The margin required to maintain the planned target D_{95} in the presence of breathing motion with a given standard deviation can be calculated by using fit equations from the data presented above. The fit equations for each of the FWHM values tested are included in Table 6.1 below, where ABW is the additional beam width required and s is the standard deviation of the PDF describing the motion.

Profile FWHM (cm)	Fit equation of ABW data	R^2 of fit
2.6	$ABW = 20.734s^2 + 3.282s$	0.9754
3.1	$ABW = 19.098s^2 + 3.574s$	0.981
3.6	$ABW = 18.582s^2 + 2.234s$	0.984
4.1	$ABW = 18.84s^2 + 1.003s$	0.9819
4.6	$ABW = 16.832s^2 + 2.051s$	0.9835
5.1	$ABW = 16.561s^2 + 1.537s$	0.9849
5.6	$ABW = 16.551s^2 + 1.201s$	0.9836
6.1	$ABW = 16.213s^2 + 1.353s$	0.9856
7.1	$ABW = 15.438s^2 + 1.427s$	0.9863
9.1	$ABW = 13.531s^2 + 1.977s$	0.9894
10.1	$ABW = 13.829s^2 + 0.5121s$	0.985

Table 6.1: A summary of equations describing the additional beam width (ABW) per unit standard deviation (s) for various target sizes.

A table of margin recommendations spanning a range of target sizes and target motions can be generated using these equations. These margin recommendations are presented in Table 6.2 below.

	PDF Standard Deviation (cm)								
Dose Profile FWHM (cm)		0.1	0.2	0.3	0.4	0.5	0.6	0.7	0.8
	2.6	0.5 (mm)	1.5	2.9	4.6	6.8	9.4	12.5	15.9
	3.1	0.5	1.5	2.8	4.5	6.6	9.0	11.9	15.1
	3.6	0.4	1.2	2.3	3.9	5.8	8.0	10.7	13.7
	4.1	0.4	1.0	2.0	3.4	5.2	7.4	9.9	12.9
	4.6	0.4	1.1	2.1	3.5	5.2	7.3	9.7	12.4
	5.1	0.3	0.9	1.8	3.1	4.7	6.7	8.9	11.5
	5.6	0.3	0.9	1.8	3.1	4.7	6.7	8.9	11.6
	6.1	0.3	0.9	1.9	3.1	4.7	6.7	8.9	11.6
	7.1	0.3	0.9	1.8	3.0	4.6	6.4	8.6	11.0
	9.1	0.3	0.9	1.8	3.0	4.4	6.1	8.0	10.2
	10.1	0.2	0.7	1.4	2.4	3.7	5.3	7.1	9.3

Table 6.2: Summary of the recommended additional margin required (mm) to compensate for a loss of target D_{95} due to target motion. As the FWHM of the dose profiles increases, the required margins decrease.

6.7 Motion Simulation with Clinical Plans

Three clinical treatment plans were also selected for motion simulation: a three field, a four field and a volumetric modulated arc therapy (VMAT) plan, all of which were used to treat patients at GRRCC. The dose profiles from these plans were convolved with the same set of breathing traces used in the phantom plan simulation. The clinical dose profiles and target definitions that were originally used in these plans were kept the same for the purposes of this simulation. The

resulting loss of target coverage in the respective PTVs was recorded in order to assess the effect of motion in clinically relevant situations.

The result of the target motion simulation on the clinical plans reinforces the notion that the proper margin selection is an effective tool in compensating for target motion. After including the modeled effect of target motion, the dose coverage still remained high for the majority of breathing patterns. As shown in Figure 6.9 it is only after the target motion becomes large (PDF standard deviation greater than $0.4\ cm$) that margins beyond what are typically applied should be considered in order to maintain target D_{95}.

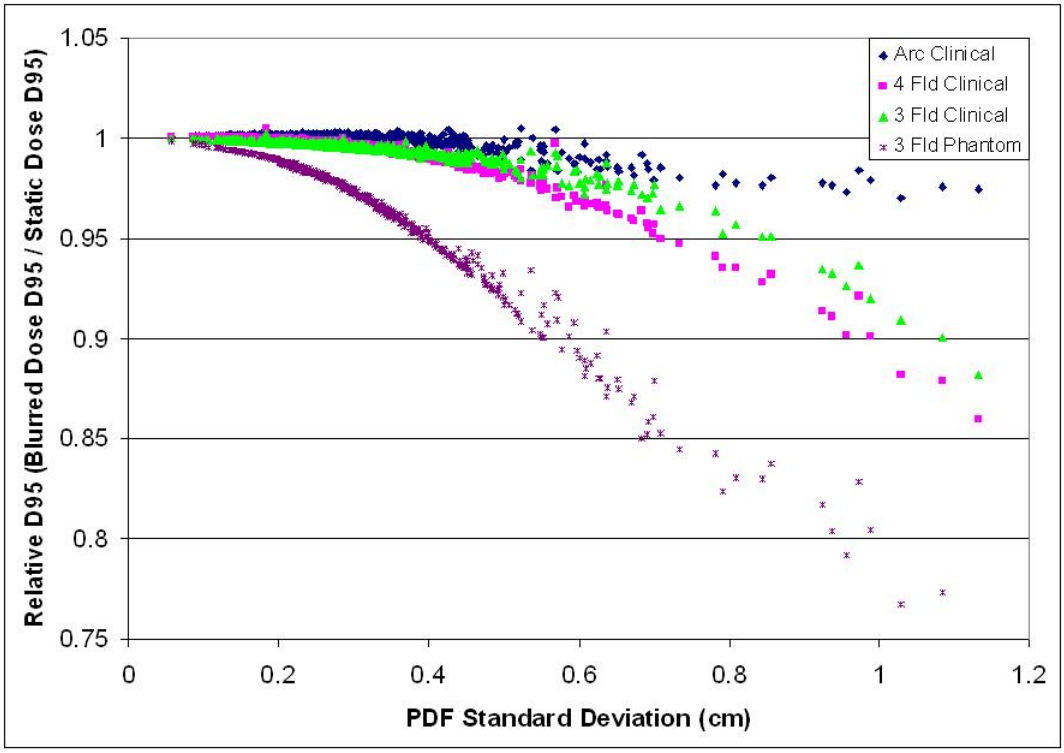

Figure 6.9: A plot of the relative D_{95} versus the PDF standard deviation for three clinical plans with the phantom data for comparison. The clinical plans with typical margins selected are robust in the face of target motion up to a PDF standard deviation of approximately $0.4\ cm$. For target motion beyond this level, additional margins would be required to maintain target D_{95}.

The clinical plans show less susceptibility to motion for two main reasons: large target size ($5\ cm$ FWHM) and softer dose gradients as compared to the dose profile from the phantom treatment plan. Since the dose gradients play an important role in the loss of coverage, it is instructive to look at the width of the penumbra in the dose profiles near the beam edge of these plans. In the cases of the clinical three field and VMAT plans, the 80%-20% penumbra was measured at $14\ mm$ (Figures 6.10 & 6.11). In the case of the four field plan, the penumbra of

the dose profile was $9\ mm$ (Figure 6.12). In each case the dose gradient was less steep than in the phantom plan, which had a penumbra of $8\ mm$. The typical clinical plan (regardless of technique) will have dose gradients which are softer than those seen in the simple three field phantom plans. As a result, the margin recommendations generated from the phantom plans can be seen as a worst case scenario, and any plan with softer dose gradients will be sufficiently compensated for by using the same margins.

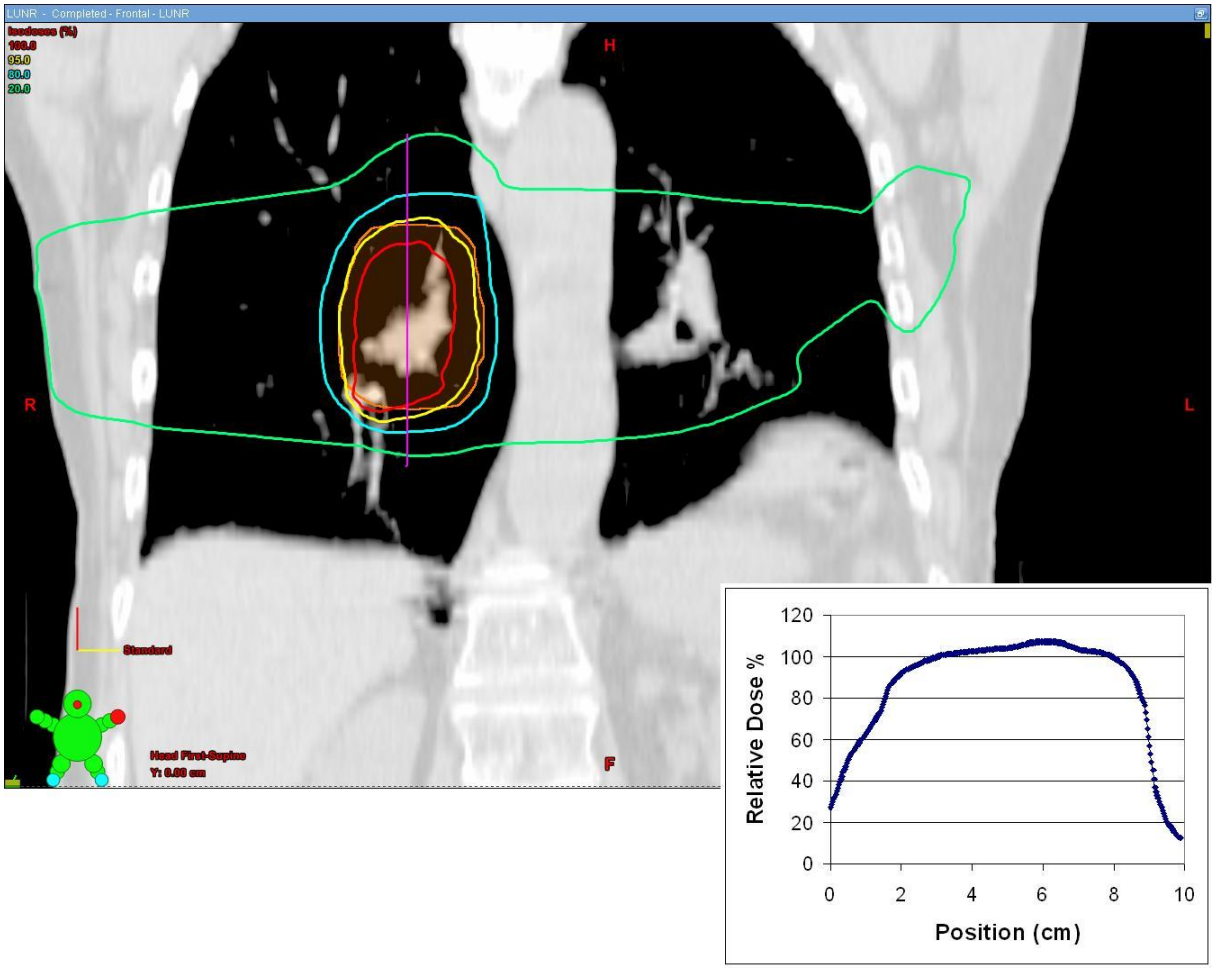

Figure 6.10: An image through the isocentre of the clinical three field treatment plan. The inset dose profile was used as the basis of the simulations of target motion in the case of the three field plan. The dose profile runs from superior to inferior through the center of the treatment volume along the vertical line indicated.

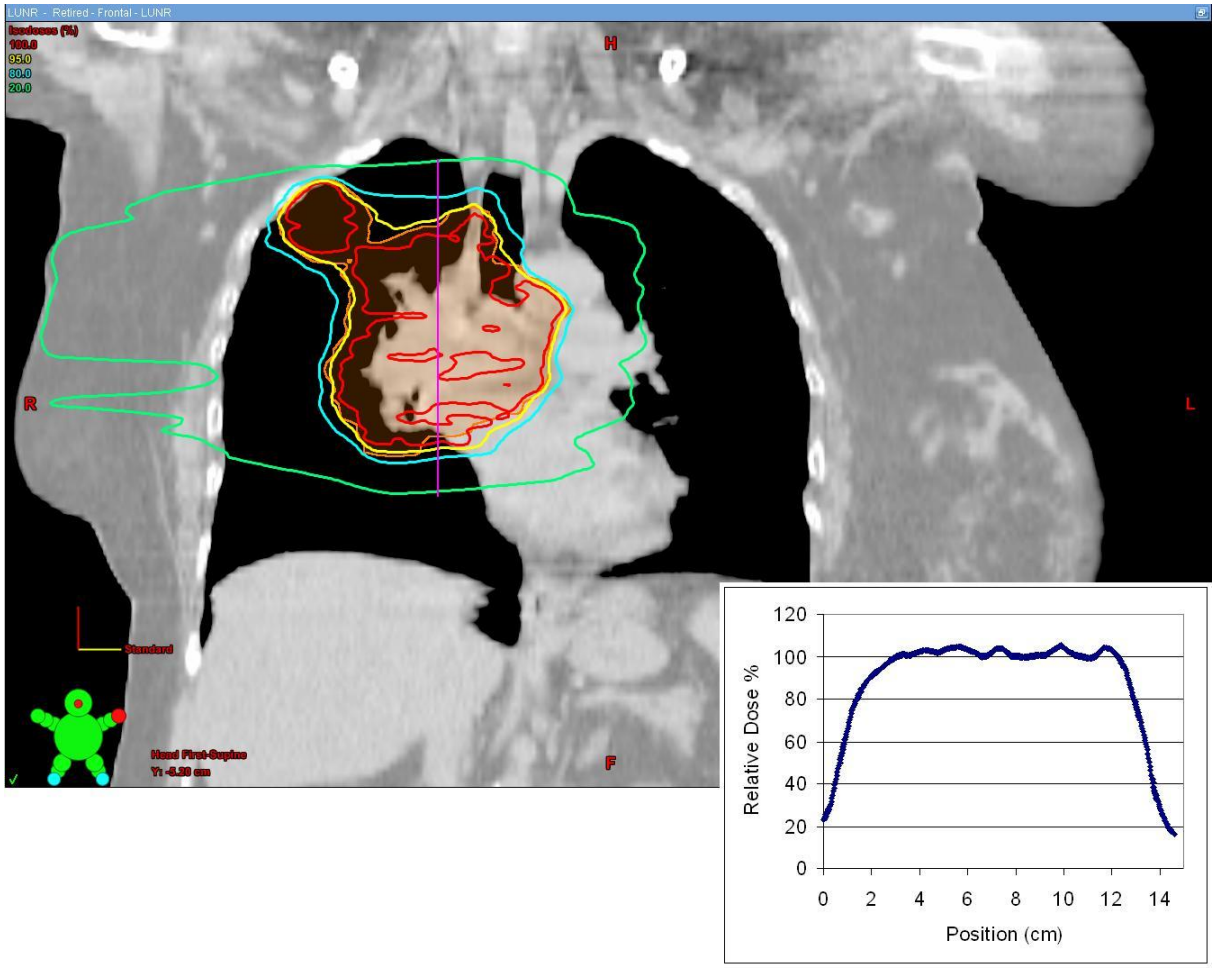

Figure 6.11: An image through the isocentre of the clinical VMAT treatment plan. This plan was comprised of two arcs. The inset dose profile was used as the basis of the simulations of target motion in the case of the VMAT plan. The dose profile runs from superior to inferior through the center of the treatment volume along the vertical line indicated.

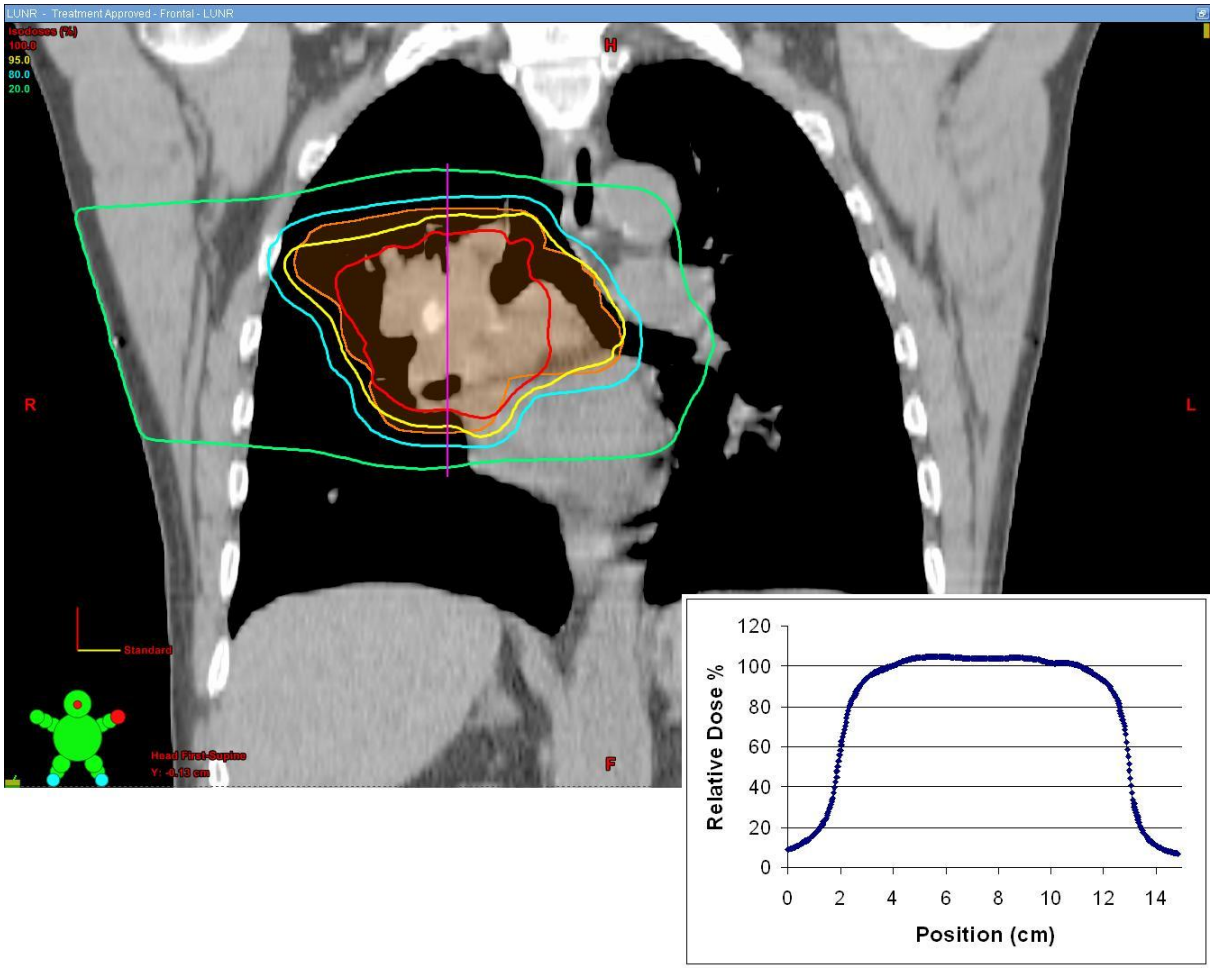

Figure 6.12: An image through the isocentre of the clinical four field treatment plan. The inset dose profile was used as the basis of the simulations of target motion in the case of the four field plan. The dose profile runs from superior to inferior through the center of the treatment volume along the vertical line indicated.

Since the size of the target plays an important role in the loss of D_{95}, it is important to consider the width of the dose profiles in these plans. The FWHM for the clinical three field,

four field and VMAT plans were measured at $8.5\ cm$, $11.1\ cm$ and $12.8\ cm$ respectively. The same trend that was identified with the study of target size can be seen in these three clinical plans as well. However, the variation in dose gradients also plays a role in the clinical results. The results of the phantom study are generated with very steep dose gradients resulting from a simple three field plan with overlapping beam edges. In practice, these phantom plan dose gradients will be as sharp as, or sharper, than what can be achieved in a clinical situation. As a result the margin recommendations of the phantom plan can be taken as a worst case scenario, and can be safely applied to a clinical plan which has equivalent or softer dose gradients.

The analysis of the clinical treatment plans reveals that they are rather robust in the face of target motion. Figure 6.9 displays the loss of target D_{95} versus the PDF standard deviation and also includes the phantom results of the $4.1\ cm$ FWHM target for comparison. Images of the dose distributions and the associated dose profiles are displayed in Figures 6.10-6.12.

The clinical plans lose very little D_{95} for target motions which have a PDF standard deviation below $0.4\ cm$. It is only after the PDF standard deviation is larger than approximately $0.4\ cm$ that the loss of target D_{95} becomes appreciable. This highlights the effectiveness of selecting appropriate margins to compensate for target motion.

6.8 Example Margin Selection

Having determined recommended field margins shown in Table 6.2, it was instructive to re-examine the dynamic phantom dose profiles measured for a small target volume and extreme standard deviation (characteristic of a stereotactic radiosurgery case with large, irregular tumor motion). A treatment plan for a small target ($2.6\ cm$ FWHM dose profile) was first generated in Eclipse. The static dose profile was extracted from the treatment plan and convolved with a

breathing trace PDF with a large standard deviation ($0.8\ cm$) to assess the impact of target motion on dose coverage. A new plan was then generated by adding the appropriate margin from Table 6.2 to the small target ($16\ mm$). The phantom was programmed to replicate the motion recorded in by the breathing trace and the new plan was then delivered to the phantom in motion. The dose coverage offered by the new plan under motion was then compared to the original static plan in order to validate the use of Table 6.2 for margin selection recommendations.

The results of this validation measurement are depicted in Figure 6.13 and summarized in Table 6.3. The D_{95} of the target PTV increases from 75.8% of the original D_{95} without motion compensation to 99.1% with motion compensation. In this case, the additional margin would play an important role in ensuring an adequate dose is delivered to the treatment volume in the presence of target motion. It should also be noted that by expanding the margins in this treatment plan, it is possible that adjacent OARs could receive an increased dose. By using the margin recommendations in Table 6.2 a clinician would be able to assess the impact of the expanded margin on OARs at the treatment planning stage.

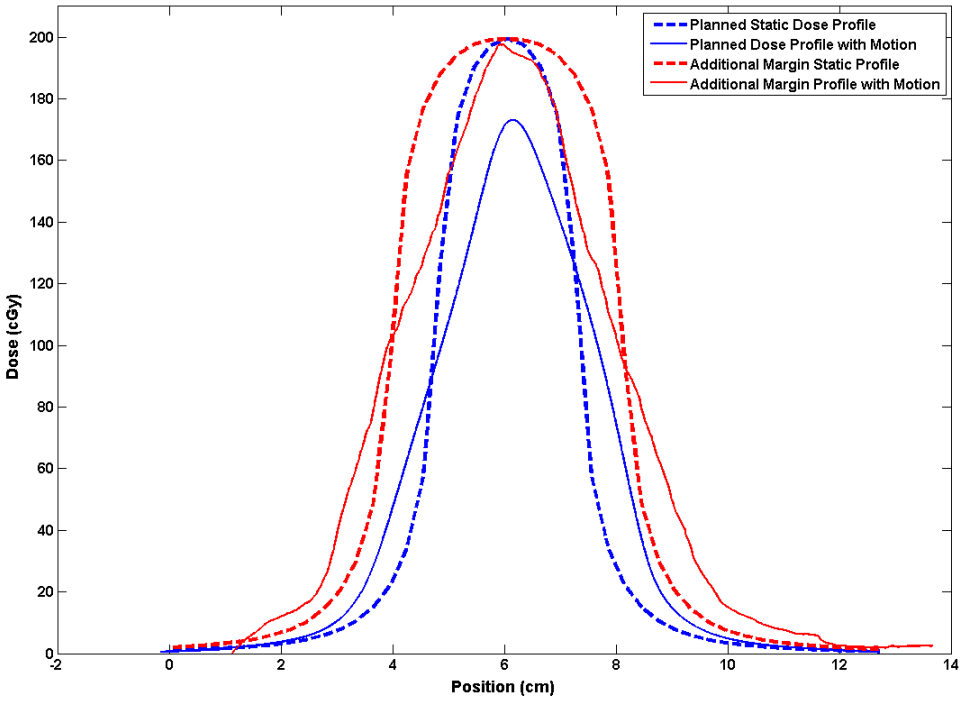

Figure 6.13: A plot of dose profiles demonstrating the margin recommendations provided in this work. The original static profile is taken from Eclipse, then convolved with the PDF. The original static plan loses dose coverage due to the target motion. When the margin recommendation from Table 6.2 is included in the plan, the target dose coverage is largely recovered when the treatment is delivered in the presence of the same target motion.

	Original Static Profile (Eclipse)	Original Profile with Motion (Eclipse, convolved)	Profile with Added Margin & Motion (film measurement)
D_{95} (cGy)	189.9	143.9	188.2
Relative D_{95} (%)	100	75.8	99.1

Table 6.3: Summary of the results of the margin selection example to demonstrate use of the margin recommendations presented in this work. The D_{95} of the PTV is largely recovered by including the margin recommended in Table 6.2.

For this type of situation the increase in field dimensions could compromise the dose to adjacent organs as seen in a treatment plan with adjusted margins. A clinical decision to use a different treatment technique, instead of simply increasing the margins, could be guided by the treatment plan with extended margins. By assessing the treatment plan with the extended margins in place, the clinician has the ability to compare other treatment options, to a treatment plan with margins that will compensate for target motion.

6.9 Comparison of Margin Recipes

Since Leong [22] proposed the idea of incorporating target motion into dose calculations via the convolution model, other authors have also assessed how the blurred dose coverage depends on the model parameters. The works of Engelsmann *et al.* [1], Richter *et al.* [2] and van Herk *et al.* [13] also identified the standard deviation of the motional PDF to be a key predictor of changes to dose coverage. Although each group used the standard deviation to make margin recommendations, the dose coverage metrics used as the basis for comparison are different in each case. The differences in margin recommendations made in this work and as compared to the above cited authors offers an interesting perspective on the trade-offs and weighting of

outcomes that must be considered clinically when applying treatment margins to accommodate for target motion.

6.9.1 Comparison with Engelsmann *et al.*

The approach detailed by Englesmann *et al.* [1] looks to assess how the position of the 95% isodose line is displaced as a result of the dose profile blurring predicted by the convolution model. In a 1D dose profile, the 95% isodose line corresponds to the point where the dose is 95% of the maximum profile dose. The location of the 95% isodose line relative to the target PTV is used clinically to assess the quality of dose coverage offered by a give treatment plan. By offering margin recommendations that look to preserve the location of the 95% isodose line, the authors are looking to ensure that the abosorbed dose received by the tissue at the border of the target volume location remains at planned level. This is in contrast to the D_{95} used in this thesis (defined as the minimum dose received by 95% of the target volume), which summarizes the dose coverage to the entire target volume. By making margin recommendations that look to preserve the target D_{95}, we look to ensure that the 95% of the target volume receives at least the same dose as originally planned, after considering target motion.

A major difference in the approach Englesmann *et al.* used to generate the margin recommendations lies in the static dose profiles used as the input to the convolution model. The authors used an analytical expression based on the sum of Error Functions (Equation 6.2) as an approximation of a one sided dose profile only.

$$D(x) = \frac{\omega_1 erf(\frac{x}{b_1}) + \omega_2 erf(\frac{x}{b_2})}{2} \bullet 100\% \tag{6.2}$$

In this context the 0% dose is located at $x = -\infty$, 50% dose at $x = 0$ and 100% dose at $x = \infty$ [1]. It should be noted that the integral dose of this profile is infinite, and as such the

analysis by Englesmann *et al.* loses the effect of conserved integral dose that is a property of the convolution model. The result is that changes to the maximum dose, and therefore the location of the 95% isodose line, that result from small targets undergoing motion is not captured by this approach. As such, Engelsmann *et al.* do not provide margins that depend on the size of the target being treated. The margins suggested by Englesmann el al. are summarized in Table 6.4 in comparison with the margins recommended in this work.

Standard Deviation (cm)	0.4	0.8	1.2
Englesmann *et al.* [1]	1 (mm)	4.5	9.5
2.6 cm FHWM	2.3	8.0	16.9*
5.6 cm FWHM	1.6	5.8	12.8*
10.1 cm FWHM	1.2	4.7	10.2*

Table 6.4: A comparison of the margin recommendations presented in this work with the recommendations of Engelsmann *et al.* [1]. The margins from this work are taken as half the ABW recommendations (total symmetric margin) for accurate comparison to Engelsmann et al (one sided dose profile). For large targets, the recommended margins are similar, but for small targets the additional margin recommended here is much larger. The values marked with an asterisk are extrapolated values based on the equations in Table 6.1.

The margins recommended by both approaches for large targets are in fact quite similar. This result is intuitive as the analytical expression of Englesmann *et al.* (Equation 6.2) describes an 'infinitely' wide static dose profile. Since this approach loses the effect of conserved integral dose, Engelsmann *et al.* are not able to properly assess the margins required for small targets. In particular the margins recommended here for a target with FWHM of $2.6\ cm$ are more than twice as large as the recommendations of Engelsmann *et al.* The effect of target size on the required target margin should not be overlooked.

6.9.2 Comparison with Richter *et al.*

Richter *et al.* [2] also used the standard deviation of the motional PDF as an important predictor in loss of dose coverage. The margins recommended by Richter *et al.* aim to preserve the absorbed dose at the border of the target volume. The approach taken by the authors was to compensate for target motion by both increasing target margin, and increasing the dose delivered to the target. They assessed the additional margin required while also delivering 105%, 125%, and 150% of the originally prescribed dose. Since increasing the dose delivered to the target also compensates for the dose spillage resulting from the blurring caused by target motion, the effect of increasing the dose to the target is to reduce the additional margin required to maintain the dose to the edge of the target volume.

The margin recommendations from Richter *et al.* are summarized with comparison to this work in Table 6.5. It can be seen in the table that the margin recommendations are similar for medium sized targets in this case. The approach of increasing the prescribed dose allows for smaller margins to offer the same level of dose coverage.

Standard Deviation (cm)	0.1	0.2	0.3	0.4	0.5	0.6	0.7
P105	0.3 (mm)	0.9	1.6	2.6	3.8	5.2	6.9
P125	0.4	0.9	1.5	2.2	3.0	4.0	5.0
P150	0.3	0.5	0.8	1.2	1.5	1.9	2.2
2.6 cm FHWM	0.5	1.5	2.9	4.6	6.8	9.4	12.5
5.6 cm FWHM	0.3	0.9	1.8	3.1	4.7	6.7	8.9
10.1 cm FWHM	0.2	0.7	1.4	2.4	3.7	5.3	7.1

Table 6.5: A comparison of the margin recommendations presented in this work (profile FWHM specified) with the recommendations of Richter *et al.* [2] using different prescribed doses (P105, P125, P150). The values for the recommended margins from Richter *et al.* were calculated using the formulas given in the paper. Although Richter *et al.* do not specify the size of the target used to generate this data, the recommendations from both approaches are similar for medium sized targets.

By increasing the prescribed dose, the authors effectively increase the integral dose in the static plan. This way, the dose spillage that results from the blurring due to target motion is partially compensated for without increasing the target margin. The potential drawback of this approach is the large increase in dose to surrounding healthy tissue that results from the increased dose prescribed to the target. In many cases the dose prescribed to the target volume is limited by the dose that will also be imparted to surrounding healthy tissues. As a result, it may not always be safe to drastically increase the prescribed dose to a target volume in order to compensate for target motion.

6.9.3 Comparison with van Herk *et al.*

In comparison with the approach detailed by van Herk et al [13], we can see that the margin recommendations presented here are similar for some situations. Although the van Herk formula makes no accounting for target size, we can compare the margin recommendations based on the van Herk *et al.* 'linear approximation of the random component for 95% dose coverage'. This is a simple formula which approximates the margin required to compensate for target motion as '0.7σ' where σ is the standard deviation of the motion. The approach of van Herk *et al.* seeks the margin that results in 95% of the prescribed dose covering the target for 90% of patients. These results are presented in Table 6.6.

Standard Deviation (cm)	0.1	0.2	0.3	0.4	0.5	0.6	0.7	0.8
van Herk Approximation	0.7 (mm)	1.4	2.1	2.8	3.5	4.2*	4.9*	5.6*
2.6 cm FHWM	0.5	1.5	2.9	4.6	6.8	9.4	12.5	15.9
5.6 cm FWHM	0.3	0.9	1.8	3.1	4.7	6.7	8.9	11.6
10.1 cm FWHM	0.2	0.7	1.4	2.4	3.7	5.3	7.1	9.30

Table 6.6: A comparison of the margin recommendations presented in this work in comparison with the commonly used van Herk recommendations. For small targets, the recommended margins are similar, but for larger targets D_{95} can be maintained with less additional margin than suggested by van Herk *et al.* Since van Herk *et al.* only claim accurate approximation of the formula used up to a standard deviation of $0.5\ cm$, the values marked with an asterisk are noted as an extrapolation.

For small targets, the margin recommendations are similar. For larger targets, the results computed in this study suggest less additional margin is required. The differences in margin recommendations likely arise due to differences in the approach to the problem. The approach of

van Herk *et al.* is to find margins that satisfy the majority of the population of patients studied. However if a patient specific approach to margin selection is taken, there is opportunity for reduced target margin for patients with larger sized targets. This can be seen in the comparison table above where patients with small target motion ($PDFSD < 0.4\ cm$) have smaller margin recommendations from this work as compared to van Herk *et al.*

6.10 Summary

Target motion was simulated for a wide range of breathing traces and target sizes in order to determine the loss of target dose coverage. Statistics describing the range of breathing traces were presented. It was shown that breathing trace amplitudes in this large data set ranged from 0.13 to $2.30\ cm$ with an average amplitude of $0.73\ cm$. The standard deviations of the PDFs in the data set ranged from 0.057 to $1.13\ cm$ with an average standard deviation of $0.34\ cm$.

A quadratic function used to describe the loss of target dose coverage in terms of the standard deviation of the PDF describing the motion of the target was found to correlate strongly with the data set ($R^2 = 0.9821$). The size of the target along the direction of motion was also found to influence the amount of coverage being lost, with larger targets being less susceptible to loss of dose coverage due to motion. The recovery of target dose coverage was also found to correlate with the PDF standard deviation, and these two trends were used to generate margin recommendations. A table of margin recommendations based on the PDF standard deviation and target size was presented in Table 6.2. These margins can be applied in a clinical situation to compensate for the reduction of the target's D_{95} due to intrafraction motion.

An example application of the use of the methodology and margin recommendation table was presented for a small target and extreme motion. This example demonstrates how the table

can be used to ensure adequate dose coverage of the target volume. The influence of the studied motions on a set of clinical treatment plans was also assessed. This assessment demonstrated the interplay between target size, dose gradient and standard deviation of the target motion.

Finally the margins recommended in this thesis were compared with published recommendations from other authors who also took advantage of the convolution model to assess the impact of target motion on target dose coverage. The margins presented here are comparable to those presented by other authors under some circumstances, however the inclusion of dependence on target size presented in this thesis offers opportunity for smaller margins for some patients, as compared to the other recommendations.

Chapter 7

Convolution Model Sensitivity Analysis

7.1 Introduction

In this thesis a convolution technique has been applied to determine the impact of intrafraction lung motion on absorbed dose. As shown previously, a patient specific lung PDF was derived from 4DCT data, and the gradient of the PDF was convolved with the static dose profile to obtain a blurred or motion-impacted dose gradient along the superior-inferior direction. The blurred dose gradient was then integrated along the superior-inferior direction to obtain the blurred dose profile. This technique was developed in Chapter 4 using Equation 4.8, expanded with clinical examples in Section 4.5, and demonstrated graphically in Figures 4.7 to 4.11. Using a dynamic, tissue equivalent phantom programmed for clinical breathing patterns and radiochromic film for dose measurement, the convolution technique described above was validated experimentally and the results were summarized in Chapter 5.

In Chapter 6, breathing patterns from 502 patients were used to simulate the effect of intrafraction motion on static dose profiles obtained from a standard treatment plan designed to

cover targets ranging from 2-10 cm in diameter. D_{95} was selected as the metric for comparing static and motion-impacted dose profiles based on clinical importance and the relative D_{95} was defined as the ratio of the blurred D_{95} to the static D_{95}. After analysis it was determined that relative D_{95} has a quadratic dependence on the standard deviation of the static dose profile and this is shown in Figures 6.5 and 6.7 and Table 6.1. A program was written in MATLAB to calculate the additional beam width (ABW applied to the static dose profile) that is required to restore the high dose region impacted by lung motion. Table 6.2 shows ABW as a function of the standard deviation of the PDF and also the FWHM of the static dose profile.

In addition to the conformal treatment plan, a 3-field, 4-field and a VMAT plan were also analyzed with the 502 patient breathing patterns to assess impact on relative D_{95} and the validity of recommended margins in Table 6.2. The results were shown in Figure 6.9 and the conclusion was that Table 6.2 is valid for conformal and more complex planning techniques including multiple beams and arcs.

In Section 6.8, the margin recommendations were tested experimentally using a treatment plan with a single beam of $FWHM = 2.6\ cm$ and the dynamic lung phantom programmed for a lung PDF with $SD = 0.8\ cm$. These parameters were chosen to simulate a Stereotactic Radiation Surgery (SRS) treatment and to test the extreme margin recommendations from Table 6.2. The results from Figure 6.13 show that D_{95} is restored with the recommended margins at the expense of lower dose spillage adjacent to the target due to a wider field. This effect is shown in Figure 7.1. The intersection points of the blurred dose profiles (with and without ABW) and the static dose profile are highlighted in the figure with ovals.

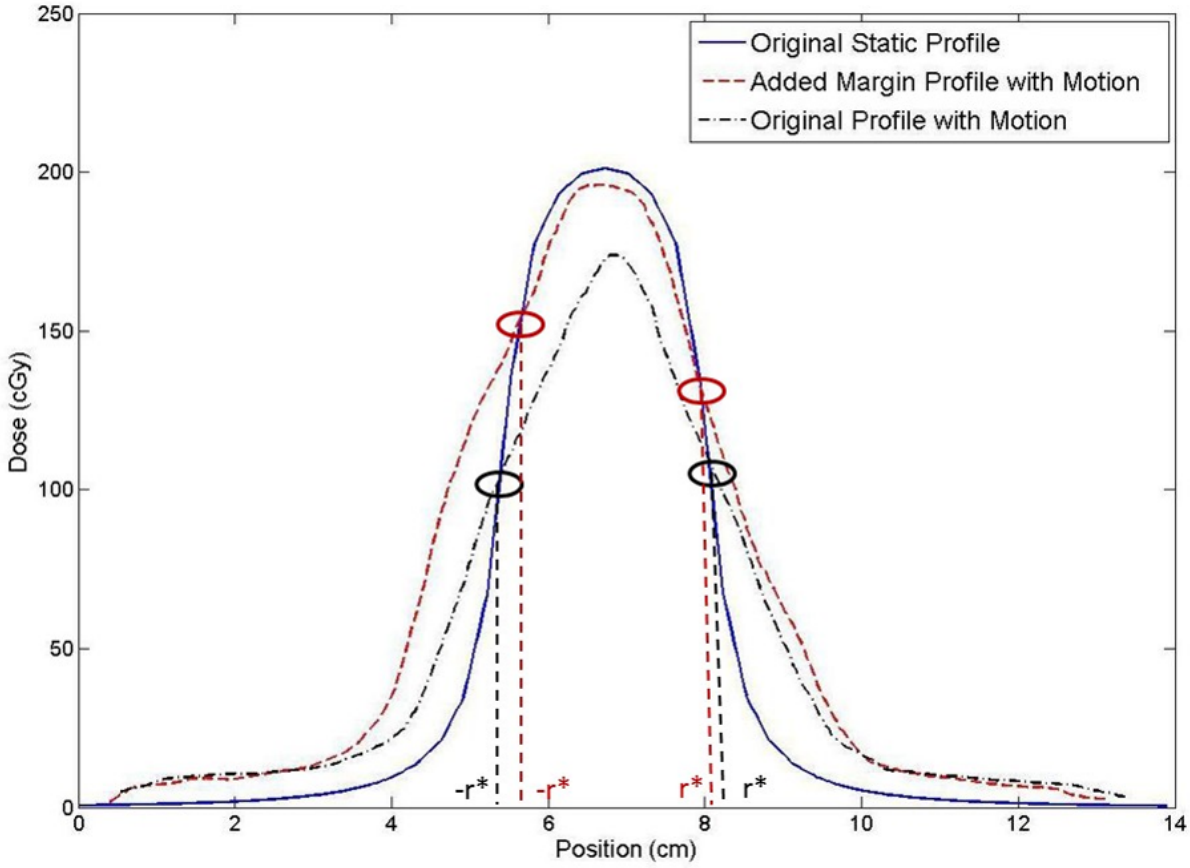

Figure 7.1: The D_{95} is restored with the additional beam width, however it comes at the expense of lower dose spillage adjacent to the target. The intersection points of the blurred dose profiles (with and without ABW) and the static dose profile are highlighted in the figure with ovals.

7.2 Factors Determining the Blurred Dose Gradient

The motivation for breaking down the convolution integral as described by Equation 4.8 is a fundamental understanding of the factors contributing to the blurred or motion-impacted dose. Furthermore, the selection of a principal direction of motion (the superior-inferior direction in this analysis) provides flexibility to construct the most relevant lung PDF and to make margin adjustments tailored to a patients breathing. As shown in Figures 4.7, 4.10, 4.11, and 6.13, the convolution-derived, blurred dose profile depends on the following parameters:

- the shape and symmetry of the PDF along *r*
- the standard deviation of the PDF
- the slopes of the leading and trailing edges of the static dose profile
- the FWHM and the shape of the plateau region of the static dose profile

In this chapter an analytical model is developed to explain how each of these parameters contributes to the blurred dose profile. In general and as shown in Figure 7.2, the leading and trailing edges of the blurred dose profile have a lower slope than the leading and trailing edges of the static dose profile, as a result of the convolution. For field sizes $< 5\ cm$, the peak height of the blurred dose profile falls below that of the static dose profile in order to conserve integral dose (also referred to as imparted energy, [4]).

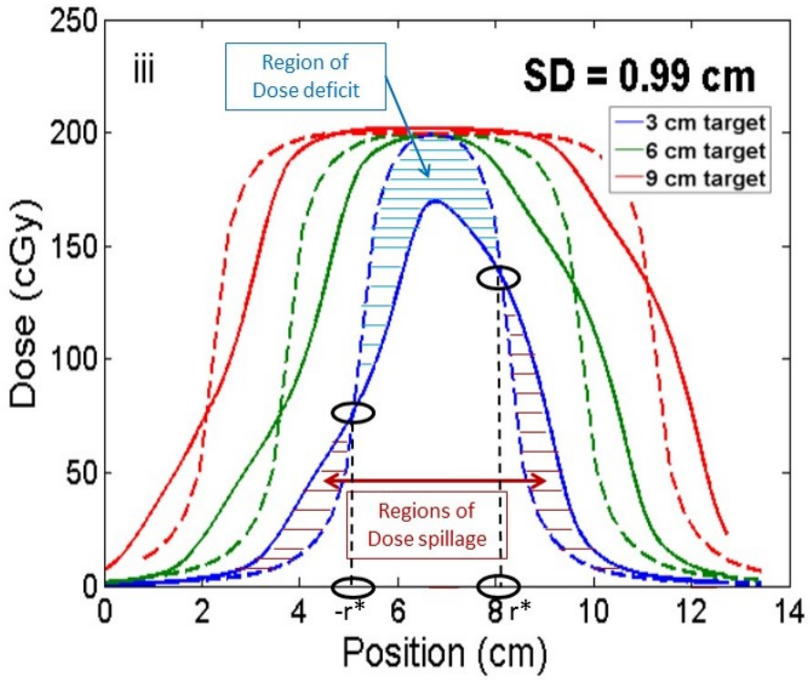

Figure 7.2: The D_{95} is restored with the addition beam width, however it comes at the expense of lower dose spillage adjacent to the target. The intersection points of the blurred dose profiles (with and without ABW) and the static dose profile are highlighted in the figure with ovals.

This is a consequence of the convolution theorem, which, applied to Equation 4.1 yields

$$\int D_b(\vec{r})dr = \int D_0(r) \otimes PDF(r)dr = \left[\int D_0(r)dr\right] \bullet \left[\int PDF(r)dr\right]. \qquad (7.1)$$

In this study the PDFs were normalized (i.e. $\int PDF(r)dr = 1$) and Equation 7.1 reduces to

$$\int D_b(r)dr = \int D_0(r)dr. \tag{7.2}$$

In Figure 7.2 the intersection points of the blurred and static dose profiles are identified with ovals and their projections on the r axis are shown as $-r^*$ and r^* relative to the static profile centered at the origin. These points are used to identify regions of under and overdose for the blurred profile relative to the static profile.

For the static dose profile,

$$\int_{-\infty}^{\infty} D_0(r)dr = \int_{-\infty}^{-r^*} D_0(r)dr + \int_{-r^*}^{r^*} D_0(r)dr + \int_{r^*}^{\infty} D_0(r)dr \tag{7.3}$$

and similarly for the blurred dose profile,

$$\int_{-\infty}^{\infty} D_b(r)dr = \int_{-\infty}^{-r^*} D_b(r)dr + \int_{-r^*}^{r^*} D_b(r)dr + \int_{r^*}^{\infty} D_b(r)dr. \tag{7.4}$$

Using Equation 7.2 and subtracting components from Equations 7.3 and 7.4,

$$\int_{-r^*}^{r^*} D_0(r) - D_b(r)dr = \int_{-\infty}^{-r^*} D_b(r) - D_0(r)dr + \int_{r^*}^{\infty} D_b(r) - D_0(r)dr \tag{7.5}$$

In words, Equation 7.5 states that the region of dose deficit shown in Figure 7.2 is equal to the sum of the regions of dose spillage arising from the convolution of the static dose profile with the PDF.

It is important to note that by adding additional margins to the static dose profile to recover the dose deficit arising from lung motion (per Table 6.2), the dose spillage regions will also expand. This means that the impact on the DVH for OARs adjacent to the target volume must be assessed carefully along with the PTV coverage as part of using this methodology.

7.3 Analytical Modeling Using Gaussian PDF Functions

Since the parameters contributing to the blurred dose gradient described in the previous section are highly patient and treatment plan specific, it is not practical to derive a comprehensive sensitivity model that applies to all cases. By employing a simpler lung PDF than observed clinically, however, it is possible to provide an analytical sensitivity analysis that explains the basic physics.

Jiang *et al.* [24] used a Gaussian PDF to describe interfraction prostate motion and previously showed the equivalence of deriving the blurred dose gradient from the convolution of a static dose profile with the gradient of a Gaussian PDF or from the convolution of the gradient of the static dose profile with a Gaussian PDF. This is shown in Figures 7.3 and 7.4 for PDF standard deviations ranging from $0.2\ cm$ to $0.8\ cm$.

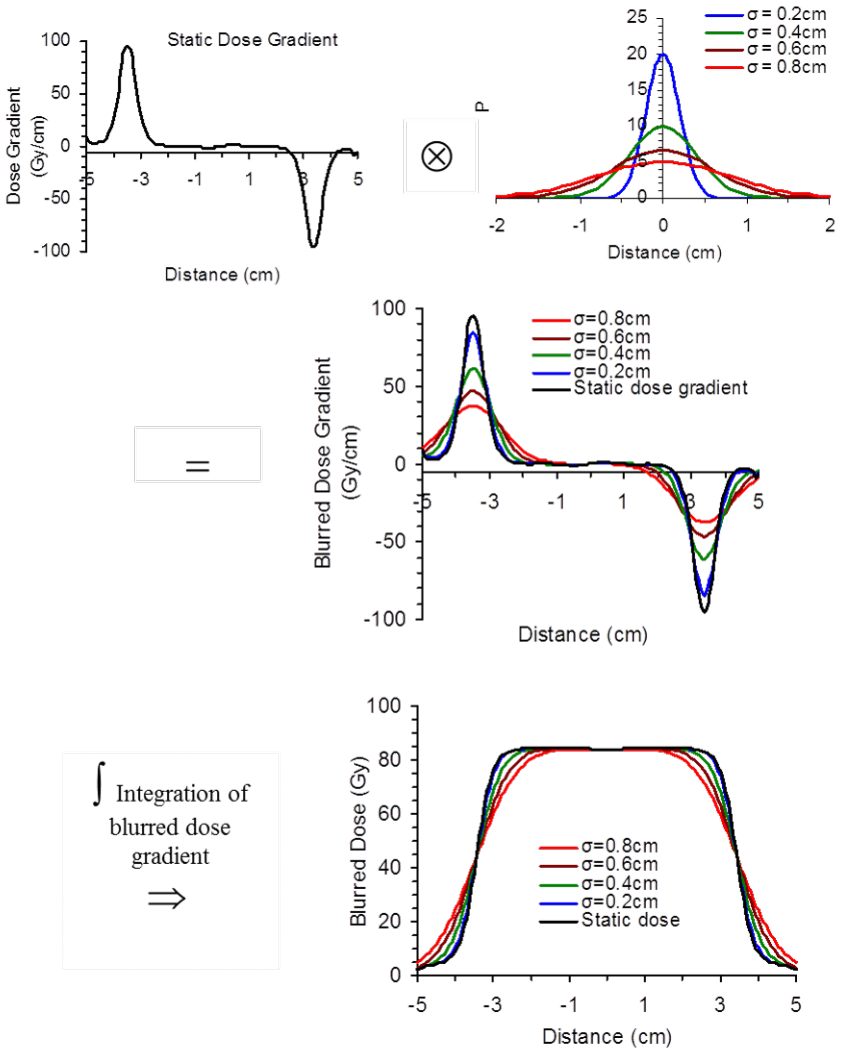

Figure 7.3: An example of Gaussian blurring applied to gradient of a static dose profile as described by Jiang *et al.* [24]. The standard deviation of the Gaussian PDF ranges from 0.2 to 0.8 cm.

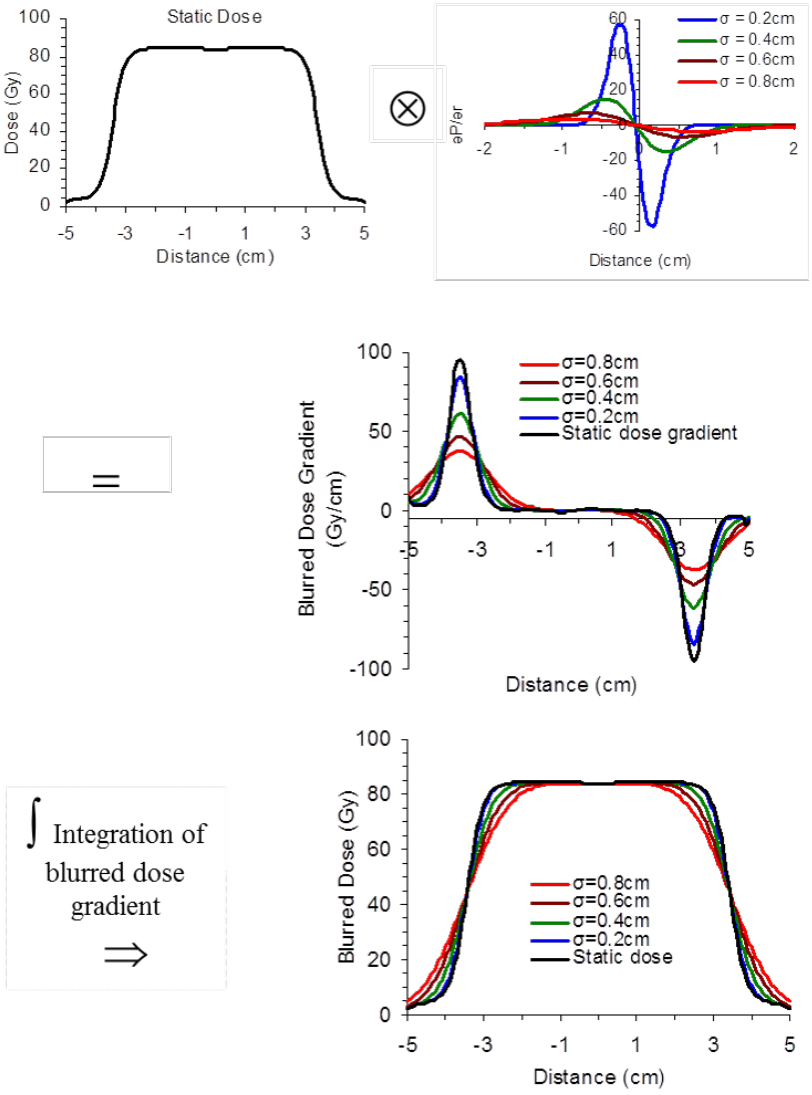

Figure 7.4: An example of blurring a static dose profile with the gradient of a Gaussian PDF as described by Jiang *et al.* [24]. The standard deviation of the Gaussian PDF ranges from 0.2 to 0.8 cm.

Due to the symmetry of both the static dose profile and the gradient of the Gaussian PDF in

this example (Figure 7.4), the blurred dose gradient is also symmetric along with the resulting blurred dose profiles.

From the analysis in Chapters 4 and 6 and preceding discussion, it is clear that the biggest impact on the static dose profile will occur for narrow beam profiles ($FWHM < 5\ cm$) and large PDF standard deviations ($> 4\ mm$). The following analysis provides a quantitative explanation for this effect using separate Gaussian functions to describe the dose profile and PDF.

A normalized uni-variate Gaussian function (centered on the origin) is described by

$$G(r) = \frac{1}{\sigma\sqrt{2\pi}} e^{-\frac{1}{2}(\frac{r}{\sigma})^2}. \tag{7.6}$$

The first partial derivative is given by

$$\frac{\partial}{\partial r} G(r) = \frac{-r}{\sigma^2} G(r) = \frac{-r}{\sigma^3\sqrt{2\pi}} e^{-\frac{1}{2}(\frac{r}{\sigma})^2}, \tag{7.7}$$

and the second partial derivative is given by

$$\frac{\partial^2}{\partial r^2} G(r) = \frac{-\sigma^2 + r^2}{\sigma^4} G(r) = \frac{-\sigma^2 + r^2}{\sigma^5\sqrt{2\pi}} e^{-\frac{1}{2}(\frac{r}{\sigma})^2}, \tag{7.8}$$

which will be zero when $r = \pm\sigma$.

When $r = \pm\sigma$ the slope of $G(r)$ will be maximized (designated by MS)

$$G^{MS} = \left[\frac{\partial}{\partial r} G(r)\right]_{r=\sigma} = -\frac{e^{-\frac{1}{2}}}{\sigma^2\sqrt{2\pi}}. \tag{7.9}$$

When $r = 0$, $G(r)$ will be have maximum peak height (designated by PH)

$$G^{PH} = G(0) = \frac{1}{\sigma\sqrt{2\pi}}. \tag{7.10}$$

The convolution of two normalized Gaussian functions

$$G_1(r) = \frac{1}{\sigma_1\sqrt{2\pi}} e^{-\frac{1}{2}(\frac{r}{\sigma_1})^2} \tag{7.11}$$

and

$$G_2(r) = \frac{1}{\sigma_2\sqrt{2\pi}} e^{-\frac{1}{2}(\frac{r}{\sigma_2})^2} \tag{7.12}$$

is given by

$$G_3(r) = G_1(r) \otimes G_2(r) = \frac{1}{\sigma_3\sqrt{2\pi}} e^{-\frac{1}{2}(\frac{r}{\sigma_3})^2}, \tag{7.13}$$

where

$$\sigma_3 = \sqrt{\sigma_1^2 + \sigma_2^2}. \tag{7.14}$$

Using Equations 7.6 to 7.14, let $G_1(r)$ represent the normalized lung PDF obtained from 4DCT and $G_2(r)$ represent the dose profile along the direction of relevant lung motion, *r*. Because $G_2(r)$ was defined as a normalized Gaussian, it needs to be scaled by $\sigma_2\sqrt{2\pi}$ so that the height of the dose profile is unity (i.e. 100% or 1.0). This axis can also be scaled by absolute dose with units of Gy. The net result is a scaled convolution Gaussian described by

$$G_4(r) = \sigma_2\sqrt{2\pi} G_3(r), \tag{7.15}$$

and the maximum slope of $G_4(r)$ when $r = \sigma_3$ is given by

$$G_4^{MS} = \left[\frac{\partial}{\partial r} G_4(r)\right]_{r=\sigma_3} = \frac{-\sigma_2}{\sigma_3^2} e^{-\frac{1}{2}} = \frac{-\sigma_2}{\sigma_1^2 + \sigma_2^2} e^{-\frac{1}{2}}. \tag{7.16}$$

The maximum height of $G_4(r)$ when $r = 0$ is given by

$$G_4^{PH} = G_4(0) = \frac{\sigma_2}{\sigma_3} = \frac{\sigma_2}{\sqrt{\sigma_1^2 + \sigma_2^2}} = \frac{1}{\sqrt{1 + \left(\frac{\sigma_1}{\sigma_2}\right)^2}}. \tag{7.17}$$

For the description of $G_2(r)$, (i.e. the static dose profile), both the FWHM and σ_2 are relevant physical parameters. For a Gaussian function, these are related by

$$FWHM = 2\sigma_2\sqrt{2ln2}, \tag{7.18}$$

or

$$\sigma_2 = \frac{FWHM}{2\sqrt{2ln2}}. \tag{7.19}$$

From the clinical data analyzed in this thesis, the relevant range of PDF standard deviations for lung patients was from $0.1\ cm$ to $0.8\ cm$ and the FWHM of the beam profile was varied from $2.6\ cm$ to $10.1\ cm$. Similar parameters were used in a spreadsheet with Equations 7.6 to 7.19 to generate data shown in Figures 7.5 to 7.13 and Table 7.2. Figures 7.14 to 7.16 were generated from MATLAB and show static dose profiles of $1\ cm$ and $5\ cm$ FWHM respectively convolved with Gaussian lung PDFs with standard deviations ranging from $0.1\ cm$ to $1.0\ cm$. The MATLAB analysis included Gaussian and rectangular static dose profiles.

7.4 Analysis of Gaussian Convolution Model

The most important results from the analysis are shown in Figures 7.5 and 7.6. Figure 7.5 shows that the maximum height of the blurred dose profile varies as $\frac{1}{\sigma_3}$ and Figure 7.6 shows that the maximum slope of the blurred dose profile varies as $\frac{1}{\sigma_3^2}$. The relative dependencies of both the maximum height and maximum slope on σ_1 and σ_2 (or FWHM) are largely determined from Equation 7.14 (i.e. $\sigma_3^2 = \sigma_1^2 + \sigma_2^2$) as explained in the previous section.

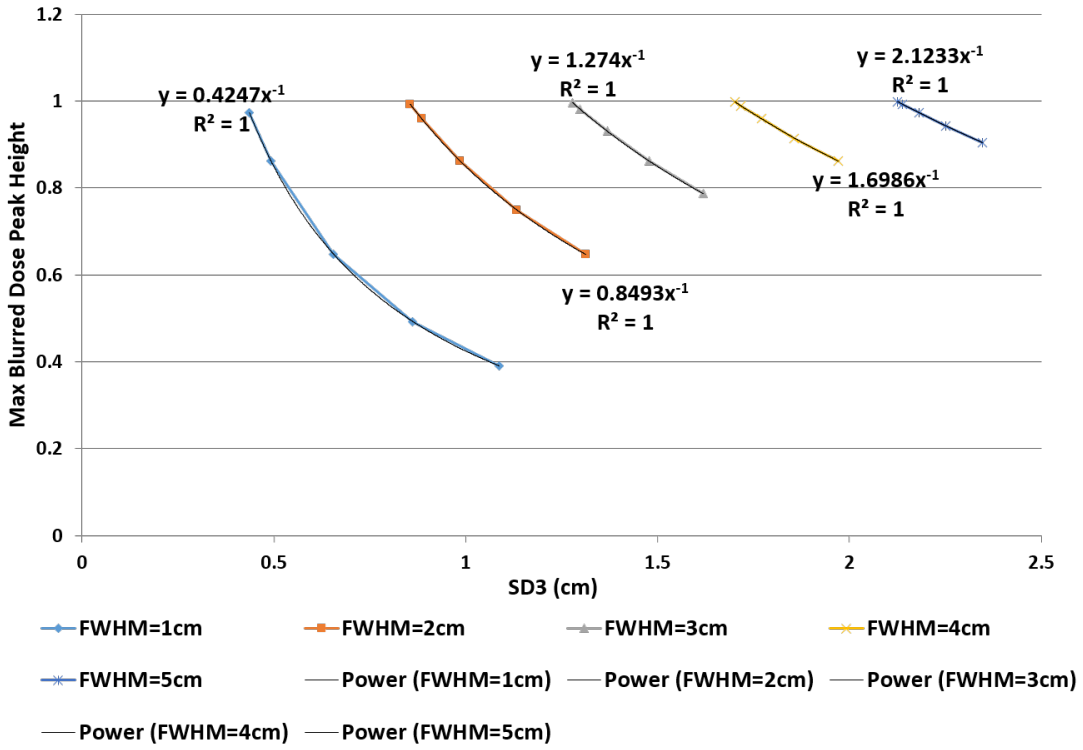

Figure 7.5: The plot of maximum blurred dose peak height versus the standard deviation of the blurred dose profile for several static dose profile FWHM values. The PDF standard deviation ranges from $0.1\ cm$ to $1.0\ cm$. As the combined standard deviation (SD3) increases, the peak height of the blurred dose profile decreases. As the FWHM of the static dose profile increases, the sensitivity of the peak height to SD3 decreases.

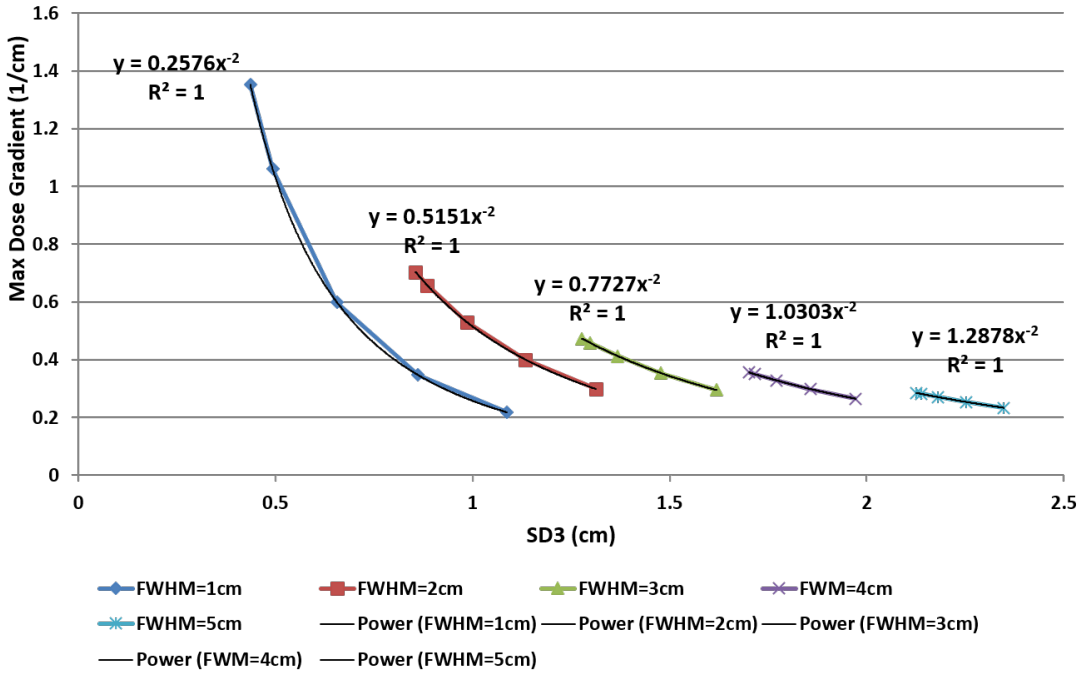

Figure 7.6: The plot of maximum blurred dose gradient versus the standard deviation of the blurred dose profile for several static dose profile FWHM values. The PDF standard deviation ranges from $0.1\ cm$ to $1.0\ cm$. As the combined standard deviation (SD3) increases, the maximum dose gradient of the blurred dose profile decreases. As the FWHM of the static dose profile increases, the sensitivity of the the maximum dose gradient to SD3 decreases.

The simultaneous $\frac{1}{\sigma}$ and $\frac{1}{\sigma^2}$ dependencies of the maximum height and maximum slope of the blurred dose profile respectively, reflect conservation of integral dose as shown previously in Equation 7.2 (i.e. $\int D_b(r)dr = \int D_0(r)dr$). Stated in words, the standard deviation (σ_3) of the blurred dose profile will expand relative to the standard deviation (σ_2) of the static dose profile due to lung motion characterized by the standard deviation (σ_1) of the PDF. This expansion is given by Equation 7.18 (i.e. $FWHM = 2\sigma_2\sqrt{2ln2}$). As σ_1 increases for a given static dose

profile FWHM, the maximum height of the blurred dose profile will decrease and the maximum slope will also decrease such that the area under the blurred dose profile remains constant and equal to $\int D_b(r)dr$.

The same functional relationship between reduced peak height and reduced slope can be derived by using a right triangle for the blurred dose profile as shown below. This example is a simplification of the Gaussian model and is only provided for clarity.

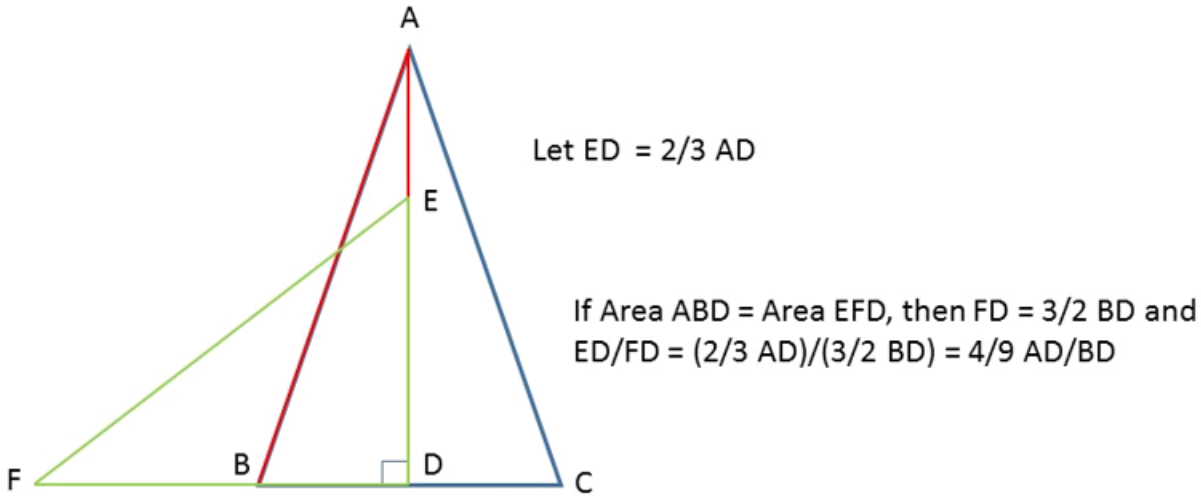

Figure 7.7: A simplification of the Gaussian convolution model depicting the relation between reduced peak height and reduced maximum slope for constant area.

In this example the static dose half profile is given by right triangle ABD and the blurred dose half profile by right triangle EFD. As the peak height of the blurred dose profile is reduced (arbitrarily) by $2/3$, the base must be expand by $3/2$ in order for the area of the triangles to be

equal. For that situation, the slope of triangle EFD (relative to base FD) is given by ED/FD which is equal to $\left(\frac{2}{3}\right)^2$ or $\frac{4}{9}$ AD/BD which is the slope of the original static profile (relative to base BD).

The maximum blurred dose peak height curves in Figure 7.5 were generated from Equation 7.17. Each of the curves correspond to a different static dose FWHM ranging from $1.0\ cm$ to $5.0\ cm$ as shown in the legend. For each FWHM, the PDF standard deviation (σ_1) was varied from $0.1\ cm$ to $1.0\ cm$. Power regression data fits were added to provide graphical verification of the numeric analysis. As shown in Figure 7.5 the R values for each of the power regression data fits are equal to 1 and the coefficients are the σ_2 values that were calculated from integer FWHM values using Equation 7.19.

The abscissa for both Figures 7.5 and 7.6 is labeled *SD3* and corresponds to σ_3 in the equations. For each of the curves in Figures 7.5 and 7.6, the range of applicable σ_3 values decreases as determined from Equation 7.14. The applicable σ_3 range is defined as $\sigma_3|_{\sigma_1=0.1\ cm}^{\sigma_1=1.0\ cm}$ and is calculated for each of the σ_2 values corresponding to the integer static dose FWHM values. For Figures 7.5 and 7.6, the applicable range of σ_3 decreases from $0.65\ cm$ at $FWHM = 1.0\ cm$ to $0.22\ cm$ at $FWHM = 5.0\ cm$.

Although the maximum height of the blurred dose profile for a given static FWHM decreases as $\frac{1}{\sigma_3}$, the maximum peak height for constant σ_1 increases as FWHM increases from $1.0\ cm$ to $5.0\ cm$. From Equation 7.17, the maximum peak height is given by $\left(\sqrt{1+\left(\frac{\sigma_1}{\sigma_2}\right)^2}\right)^{-1}$ and the limit as $\sigma_2 \to \infty = 1$.

This trend can be seen from Figure 7.5 and is described using the smallest and largest values of σ_1. For $\sigma_1 = 0.1\ cm$ (lowest clinical PDF standard deviation studied), the maximum peak height varies from 0.973 for $FWHM = 1.0\ cm$ to 0.999 for $FWHM = 5.0\ cm$. For σ_1 = 1.0 cm (highest clinical PDF SD studied), the maximum peak height varies from 0.391 for $FWHM = 1.0\ cm$ to 0.905 for $FWHM = 5.0\ cm$. The explanation for the relatively large drop in maximum

peak height for FWHM values of $1\ cm$ and $2\ cm$ is due to conservation of integral dose from the convolution theorem explained previously (Equation 7.2). As the static dose profile FWHM decreases to small values (e.g. $1\ cm$ needed for SRS), and as the patients breathing becomes more erratic (higher PDF standard deviation), the peak height drops below unity in addition to an increase in the maximum slope in order to conserve the area under the blurred dose profile. The drop in maximum peak dose height for static dose $FWHM < 2.5\ cm$ is discussed in more detail in Section 5.

In Figure 7.6, the data for the maximum gradient of the blurred dose profile was generated from Equation 7.6 using the same range of values for FWHM and σ_1 as used to generate the maximum peak height. Power regression data fits were also added to provide graphical verification of the numeric analysis. Shown in Figure 7.6, the R values for each of the power regression fits are equal to 1 and the coefficients are the σ_2 values that were calculated from integer FWHM values multiplied by $e^{-0.5} = 0.607$.

In contrast to the behavior of the maximum peak height, the maximum dose gradient for a given static FWHM decreases as $\frac{1}{\sigma_3^2}$, and the value of the maximum gradient for constant σ_1 generally decreases with increasing FWHM. An exception to this trend occurs for $\sigma_1 \geq 0.75\ cm$ as FWHM increases from $1.0\ cm$ to $2.0\ cm$. For this situation as shown in Figure 7.6, there is a small increase in the maximum blurred dose gradient which is again due to conservation of integral dose. For the large drop in maximum peak height for $FWHM = 1\ cm$ and large σ_1, there is also a large decrease in the maximum dose gradient. As the FWHM increases from $1.0\ cm$ to $2.0\ cm$ at large σ_1 the maximum peak height increases and the maximum dose gradient must increase slightly to conserve integral dose.

Derivatives of the blurred dose profiles are shown in Figures 7.8 and 7.9 for static dose FWHM values of $2.6\ cm$ and $5.1\ cm$. For both figures the derivatives are shown for σ_1 values of 0.2, 0.5 and $0.8\ cm$.

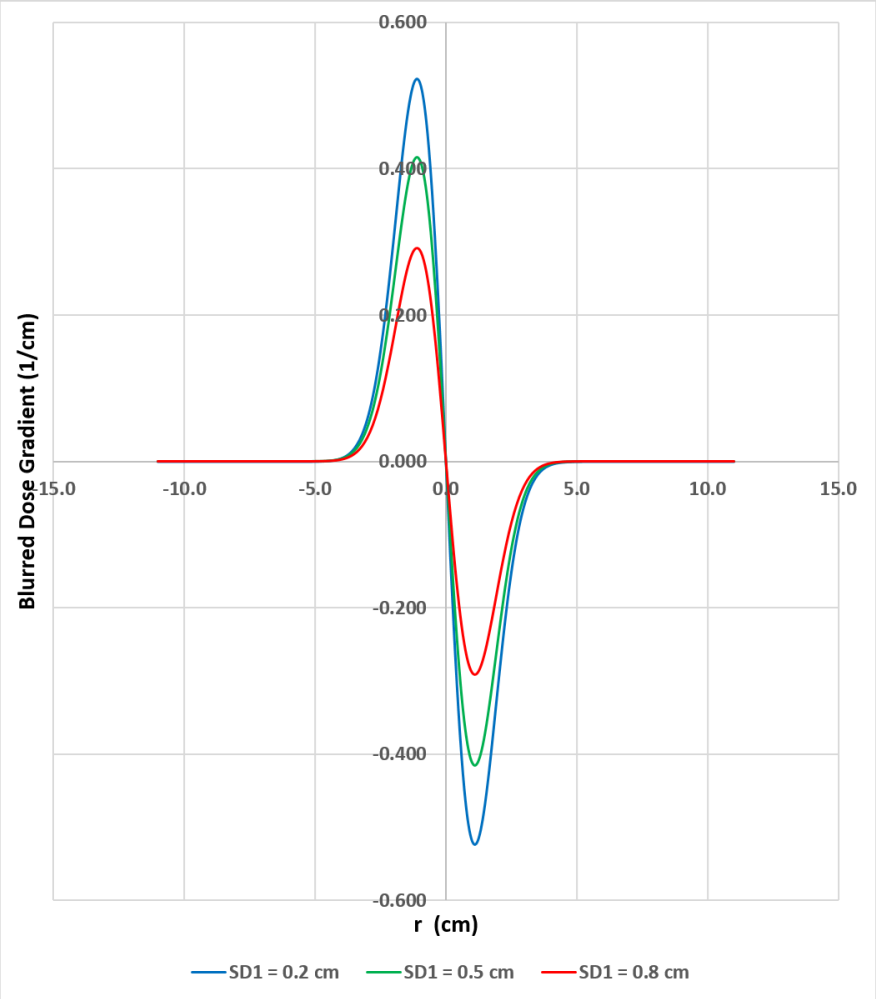

Figure 7.8: The derivatives of the blurred Gaussian dose profiles generated from a static Gaussian dose profile with FWHM of $2.6\ cm$ and PDF standard deviations of $0.2\ cm$, $0.5\ cm$ and $0.8\ cm$.

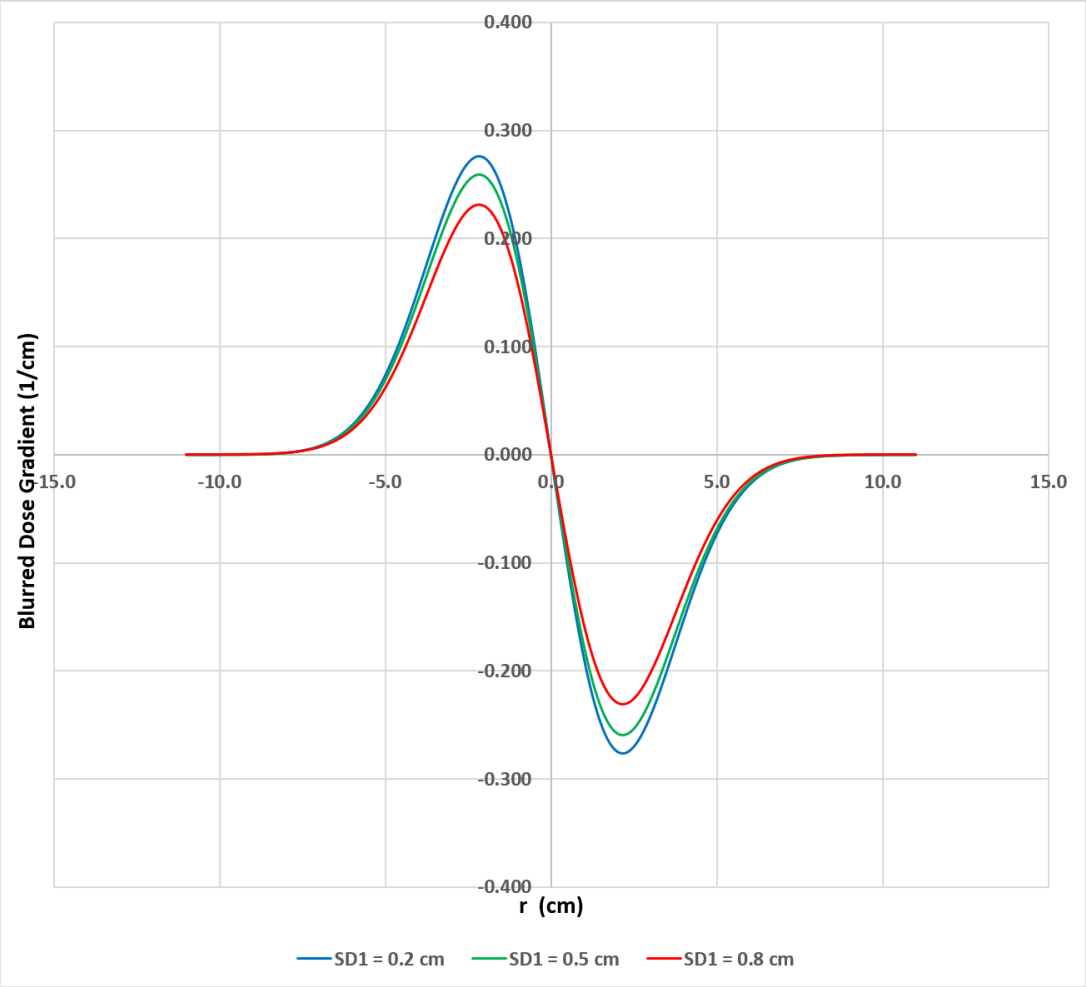

Figure 7.9: The derivatives of the blurred Gaussian dose profiles generated from a static Gaussian dose profile with FWHM of $5.1\ cm$ and PDF standard deviations of $0.2\ cm$, $0.5\ cm$ and $0.8\ cm$.

For the Gaussian convolution model presented in this chapter the blurred dose profiles were derived analytically to provide a parametric sensitivity analysis. This is in contrast to the methodology used in the thesis where the derivatives of the lung PDF were first convolved with the static dose profile to obtain the blurred dose gradient and then integrated along the superior-inferior (r)

direction as described before. As shown in Figures 7.8 and 7.9, the derivatives of the blurred dose distribution are symmetric, and, due to the peaked nature of the Gaussian static dose profile, the transition of the derivatives from positive to negative is continuous through the origin with the separation of the positive and negative peaks defining the blurred dose FWHM. For the Gaussian convolution model there is no flat spot between the peaks of the blurred dose gradient as shown in Figures 7.3 and 7.4 for a more flat static dose profile.

7.5 Table 6.2 Revisited

Table 6.2 in this thesis describes recommended margins to be applied to the static dose FWHM in order to recover D_{95} that is lost due to lung motion quantified by the PDF standard deviation. The table lists the ABW required as a function of FWHM and SD and is based on the quadratic polynomial data fits shown in Table 6.1. The parametric boundaries of the Table 6.2 are $2.6\ cm \leq FWHM \leq 10.1\ cm$ and $0.1\ cm \leq SD \leq 0.8\ cm$.

The recommended ABW data in Table 6.2 were plotted in Figure 7.10 as a function of the FWHM of the static dose profile. Power regression data fits were added showing that the recommended ABW varies approximately as $\frac{1}{\sqrt{FWHM}}$ (for fixed PDF standard deviation). This graph was used to extend the experimental data to $FWHM < 2.5\ cm$. The power regression equations are tabulated in Table 7.1.

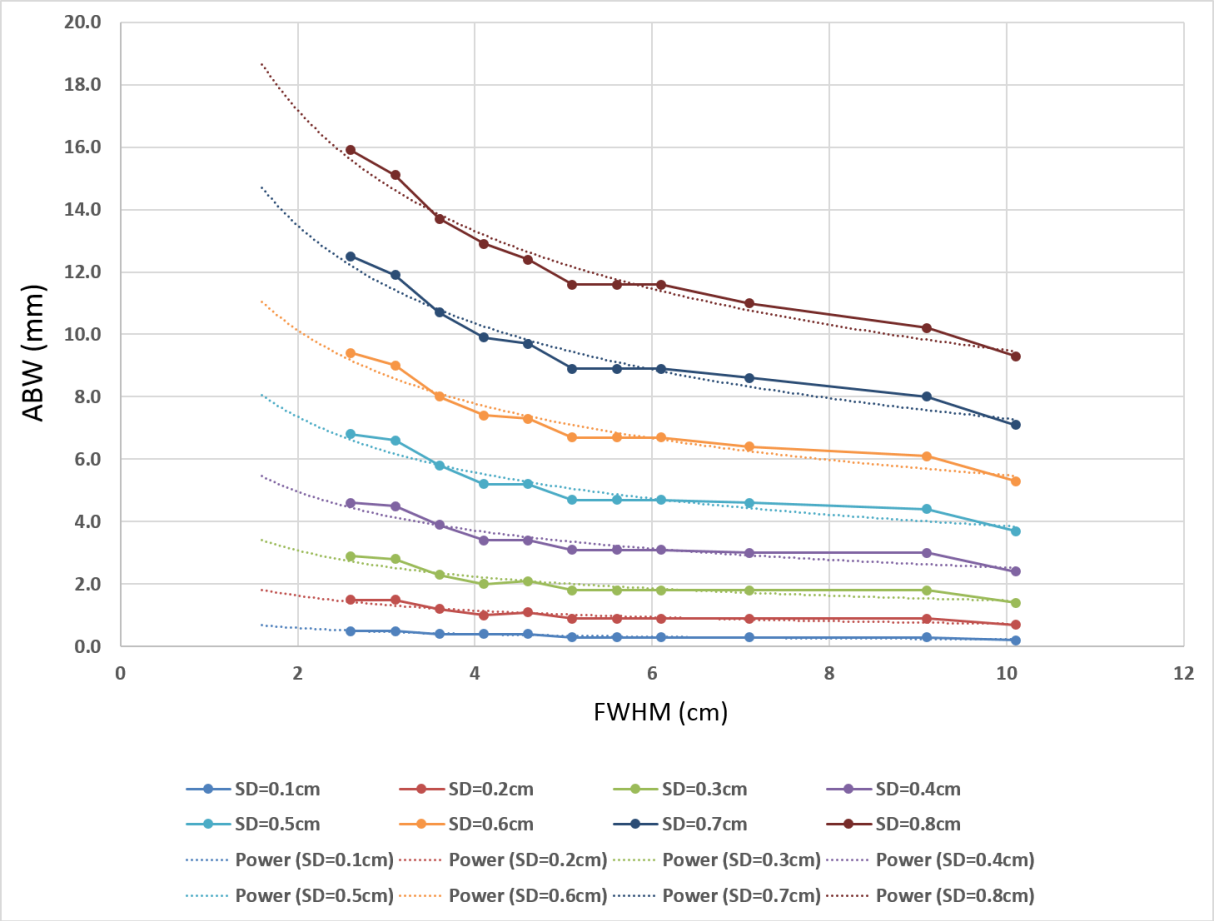

Figure 7.10: Plots of the recommended additional beam width from Table 6.2 as a function of static profile FWHM for a range of fixed PDF standard deviations. The data presented here was used to extend the experimental data to $FWHM < 2.5\ cm$. In general, as the FWHM of the static profile increases, the required additional beam width decreases for a given PDF standard deviation.

The analytical convolution model presented in this chapter provides a reasonable benchmark for testing the recommended margins in Table 6.2. For this investigation, the analytically simu-

PDF SD (cm)	Fit equation of ABW data (mm) vs FWHM (cm)	R^2 of fit
0.1	$ABW = 0.8903x^{-0.584}$	0.8511
0.2	$ABW = 2.3039x^{-0.5}$	0.8339
0.3	$ABW = 4.2274x^{-0.458}$	0.8438
0.4	$ABW = 6.6367x^{-0.419}$	0.8810
0.5	$ABW = 9.7082x^{-0.4}$	0.9157
0.6	$ABW = 13.197x^{-0.381}$	0.9463
0.7	$ABW = 17.563x^{-0.381}$	0.9547
0.8	$ABW = 22.181x^{-0.369}$	0.9717

Table 7.1: A summary of equations describing the additional beam width (mm) versus FWHM (cm) of the static Gaussian dose profiles for fixed PDF standard deviation.

lated blurred dose profile was computed using FWHM values for $G_2(r)$ and σ_1 values for $G_1(r)$ from Table 6.2 and compared with Equation 7.13 evaluated with the recommended margins applied to $G_2(r)$. The results are shown in Table 7.2 and graphically in Figures 7.11 and 7.12.

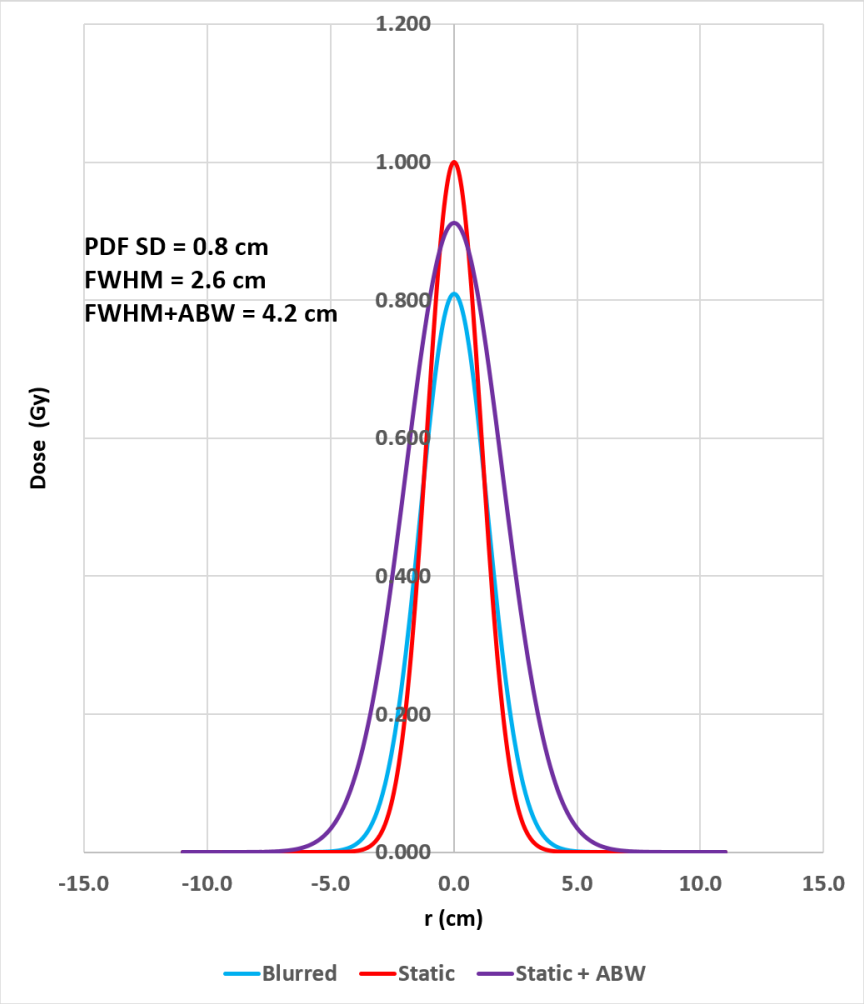

Figure 7.11: Analytically simulated static, blurred and ABW blurred dose profiles. The original static profile had $FHWM = 2.6\ cm$. The ABW recommended in this case is $1.6\ cm$. The loss of dose coverage and the dose recovered by the ABW shown here is summarized in Table 7.2

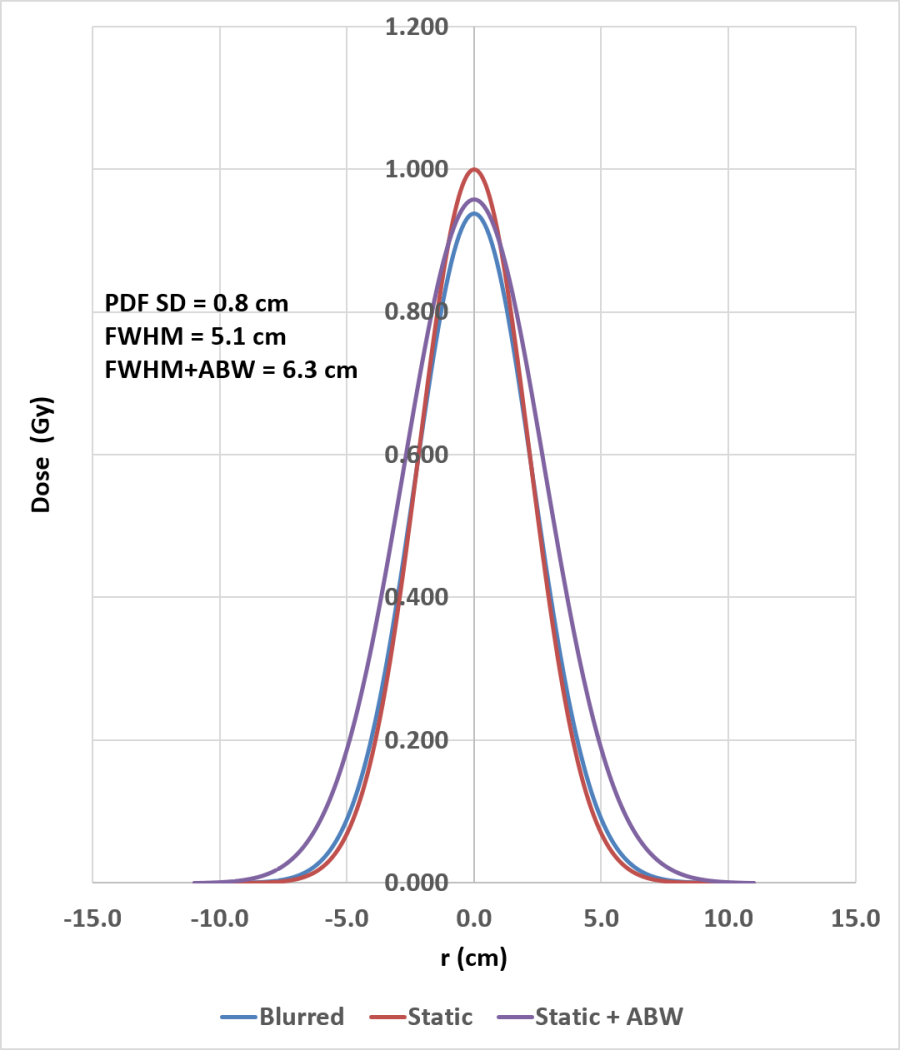

Figure 7.12: Analytically simulated static, blurred and ABW blurred dose profiles. The original static profile had FHWM $= 5.1\ cm$. The ABW recommended in this case is $0.8\ cm$. The loss of dose coverage and the dose recovered by the ABW shown here is summarized in Table 7.2

In the context of the analytical model presented, D_{95} has limited practicality and was replaced with the dose deficit defined in Equation 7.5 and shown in Figure 7.2. To calculate the dose deficit

using Equation 7.5, the intersection points r^* and r^* were derived as follows.

By equating the motion-modified dose profile $G_4(r) = \sigma_2\sqrt{2\pi}G_3(r)$ with the scaled static dose profile $G_2(r) = \frac{1}{\sigma_2\sqrt{2\pi}}e^{-\frac{1}{2}\left(\frac{r}{\sigma_2}\right)^2} \bullet \sigma_2\sqrt{2\pi}$ the intersection points are given by

$$\frac{\sigma_2}{\sigma_3}e^{-\frac{1}{2}\left(\frac{r^*}{\sigma_3}\right)^2} = e^{-\frac{1}{2}\left(\frac{r^*}{\sigma_2}\right)^2}. \tag{7.20}$$

Solving for r^* gives

$$r^* = \pm\sigma_1\sigma_2\sqrt{\frac{2(ln\sigma_3 - ln\sigma_2)}{\sigma_3^2 - \sigma_2^2}}. \tag{7.21}$$

When Table 6.2 is applied to $G_2(r)$ such that $FWHM = FWHM + ABW$, the intersection points of $G_2(r)$ and $G_{3ABW}(r)$ are given by

$$r^* = \pm\sigma_1\sigma_2\sqrt{\frac{2(ln\sigma_3 - ln\sigma_{2ABW})}{\sigma_3^2 - \sigma_2^2}}, \tag{7.22}$$

where $G_{3ABW}(r)$ and σ_{2ABW} include ABW from Table 6.2.

For clarity in Table 7.2, r* is calculated from Equation 7.21 was labeled $r1^*$ and r^* calculated from Equation 7.22 was labeled $r2^*$. The initial deficit integral dose resulting from lung motion was derived from

$$A1_{deficit} = \int_{-r1^*}^{r1^*} D_o(r) - D_{b,ABW}(r)dr, \tag{7.23}$$

and residual deficit integral dose determined with recommended ABW from Table 6.2 was derived from

$$A2_{deficit} = \int_{-r2^*}^{r2^*} D_o(r) - D_{b,ABW}(r)dr, \tag{7.24}$$

where $D_{b,ABW}$ is the blurred dose with ABW.

Since the integral dose from Equation 7.23 includes the residual integral dose from Equation 7.24, the recovered dose from using the static dose profile with ABW was calculated using

$$RecoveredIntegralDose = 1 - \left(\frac{A1_{deficit}}{A2_{deficit}}\right). \tag{7.25}$$

The results and parametric details are shown in Table 7.2.

FWHM (cm)	FWHM + ABW	σ_1 (cm)	$r1^*$ (cm)	$r2^*$ (cm)	$G_2(r1^*)$ (Gy)	$G_2(r2^*)$ (Gy)	$G_3(0)$ (Gy)	$G_{3,ABW}(0)$ (Gy)	$A1_{deficit}$ (Gy cm)	$A2_{deficit}$ (Gy cm)	Dose Recovery $\left(1-\frac{A2}{A1}\right)$
1.0	1.23	0.2	0.446	0.241	0.576	0.851	0.905	0.934	0.152	0.016	0.895
1.0	1.97	0.5	0.520	0.261	0.473	0.828	0.647	0.858	0.258	0.037	0.857
1.0	3.22	0.8	0.592	0.239	0.379	0.853	0.469	0.863	0.362	0.033	0.910
2.6	2.75	0.2	1.113	0.518	0.601	0.896	0.984	0.986	0.344	0.007	0.978
2.6	3.28	0.5	1.156	0.577	0.578	0.872	0.911	0.941	0.408	0.034	0.917
2.6	4.19	0.8	1.222	0.575	0.542	0.873	0.810	0.912	0.513	0.051	0.901
3.6	3.72	0.2	1.535	0.689	0.604	0.903	0.992	0.992	0.472	0.005	0.988
3.6	4.18	0.5	1.568	0.755	0.591	0.885	0.950	0.963	0.520	0.028	0.946
3.6	4.97	0.8	1.622	0.761	0.570	0.883	0.886	0.935	0.614	0.049	0.920
5.1	5.19	0.2	2.70	0.954	0.605	0.908	0.996	0.996	0.665	0.004	0.994
5.1	5.57	0.5	2.194	1.019	0.599	0.895	0.974	0.978	0.698	0.022	0.968
5.1	6.25	0.8	2.235	1.023	0.587	0.894	0.938	0.957	0.782	0.044	0.944
10.1	10.17	0.2	4.291	1.578	0.606	0.935	0.999	0.999	1.414	0.002	0.999
10.1	10.47	0.5	4.304	1.689	0.604	0.925	0.993	0.994	1.408	0.011	0.992
10.1	11.03	0.8	4.326	1.690	0.601	0.925	0.983	0.986	1.463	0.024	0.984

Table 7.2: A summary of the parametric analysis of the Gaussian convolution model. The legend is on the next page.

- FWHM of the static dose profile
- FWHM + ABW added to static profile (per Table 6.2)
- SD1 is for static dose profile
- $r1^*$ is the intersection of blurred dose profile with static dose profile
- $r2^*$ is the intersection of blurred static profile including ABW with static dose profile
- $G_2(r1^*)$ is the value of static dose profile at $r1^*$
- $G_2(r2^*)$ is the value of static dose profile at $r2^*$
- $G_3(0)$ is max height of blurred dose profile at $r = 0$
- $G_{3,ABW}(0)$ is max height of blurred dose profile including ABW at $r = 0$
- $A1_{deficit}$ is integral dose lost due to target motion
- $A2_{deficit}$ is the integral dose lost to target motion after the field size has been increased per Table 6.2
- Dose Recovery $= 1 - \frac{A2_{deficit}}{A1_{deficit}}$

When ABW from Table 6.2 motion is recovered within an average of $96\% \pm 2.5\%$ for $0.1\ cm \leq \sigma_1 \leq 0.8\ cm$ lung PDF and $2.6\ cm \leq FWHM \leq 10.1\ cm$ static dose profile. This indicates that the ABW recommendations from Table 6.2, applied to the analytical Gaussian convolution model, provide very good general recovery of the dose deficit resulting from organ motion within the σ_1 and FWHM parameters specified. For static dose profiles with FWHM values less than $2.5\ cm$ however (i.e. outside of the clinical parametric boundaries of Table 6.2), dose recovery may not be practical using an ABW technique. As demonstrated previously, this

is due to a significant decrease in blurred dose maximum peak height and softer maximum dose gradients arising from convolution of small static dose FWHM and large PDF SD. This extreme is shown in Figures 7.13 to 7.15. In Figure 7.13, the ABW for $FWHM = 1.0\ cm$ was extrapolated from a power regression data fit shown in Figure 7.10. From Table 7.2, the recovered integral dose for $PDFSD = 0.8\ cm$ is 0.91 which would be a problem clinically. Figures 7.14 and 7.15 show MATLAB simulations for small FWHM and large PDF standard deviations. In Figure 7.15, the simulation is calculated for a rectangular dose pulse which is an ideal extreme provided for comparison. A more clinical stereotactic static dose profile would be a cross between the Gaussian and rectangular profiles.

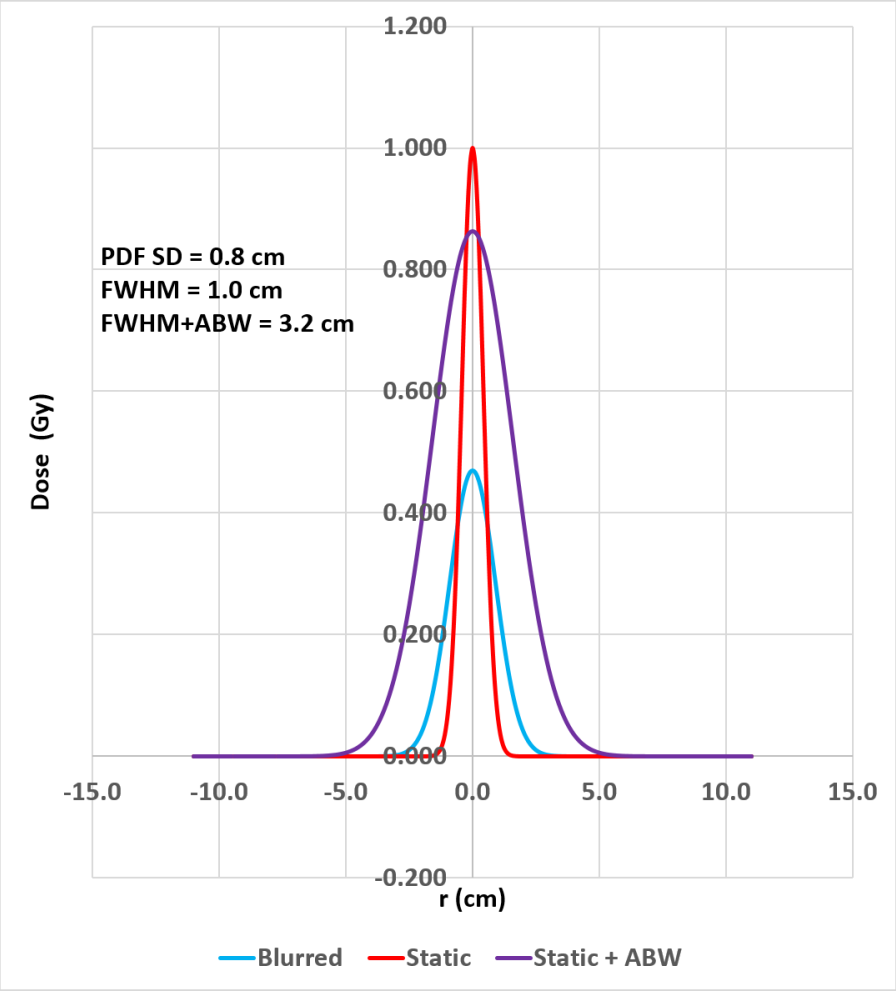

Figure 7.13: The effect of large target motion on a static Gaussian profile with FWHM of $1\ cm$. This small target is particularly susceptible to loss of dose coverage as shown by the blurred dose profile. The ABW recommendation derived from Figure 7.10 (or Table 7.1) is still insufficient to restore full dose coverage for this small field and large motion

.

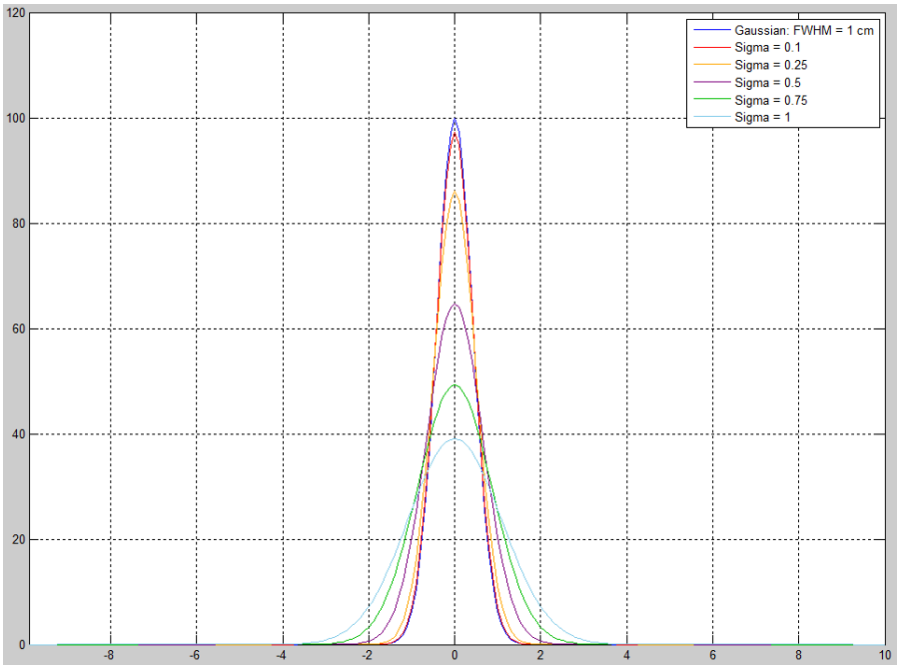

Figure 7.14: The effect of varying levels of target motion, represented by several PDF standard deviations, on a small field. As the amount of motion increases the dose coverage loss, represented by the blurred dose profile, increases. The low dose spillage becomes an important concern for small fields and large motion that may occur in the case of an SRS treatment technique.

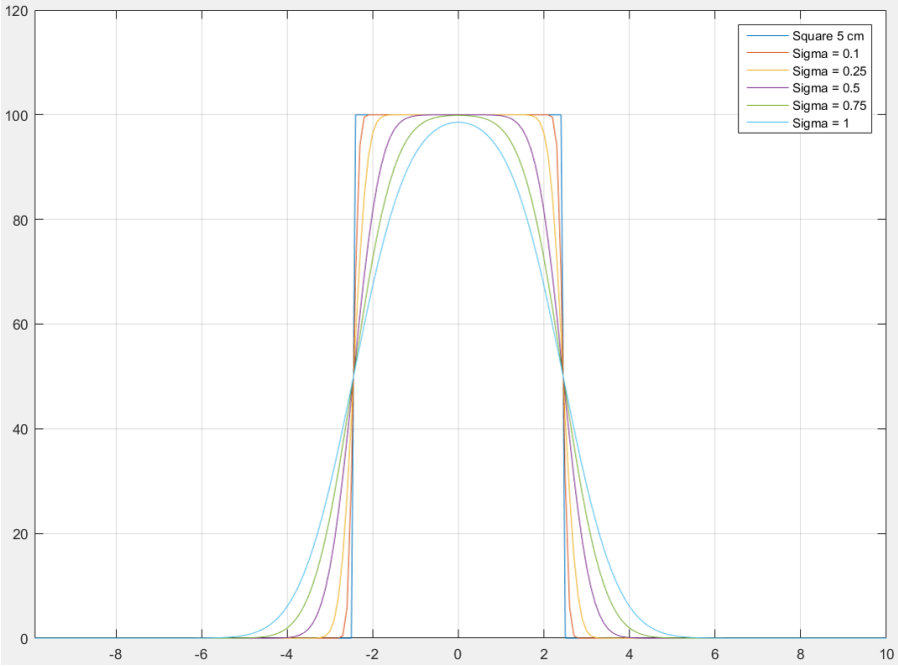

Figure 7.15: The effect of varying levels of target motion, represented by several PDF standard deviations, on an idealized square field. As the amount of motion increases, the dose coverage offered by the blurred dose profile continues to decrease.

For static dose FWHM values less than $2.5\ cm$ and PDF standard deviation values greater than $0.4\ cm$, an alternative methodology for recovering D_{95} would be to individually measure the loss in static peak dose height using individual patient data (static FWHM, PDF standard deviation) and increase the dose prescription by the reciprocal of the relative peak height. This needs to be done very carefully however with accurate small-field dosimetry using a dynamic phantom and implemented with precision IGRT based quality assurance. The important point to be raised in this section is that the recommended margins in Table 6.2 should not be used outside of the stated parametric boundaries particularly for static dose profile FWHM values less than

$2.5\ cm$.

For static dose FWHM values greater than $2.5\ cm$ and with flatter plateau regions as shown in Figures 7.3 and 7.4, convolution with a PDF SD results mainly in a reduction of the dose gradients at the leading and trailing edges, again conserving integral dose as described earlier. This is shown in Figure 7.15 from a MATLAB simulation of a rectangular static dose profile with $FWHM = 5.0\ cm$. In this example the peak dose height does not start decreasing below 1.0 until the $PDFSD = 1.0\ cm$. Figure 7.16 shows the equivalent Gaussian static dose profile where the maximum peak height starts decreasing for $PDFSD = 0.5\ cm$ due to the more peaked central region. This comparison indicates that the Gaussian model, although very useful for developing this sensitivity analysis, is more relevant clinically to SRS static dose profiles.

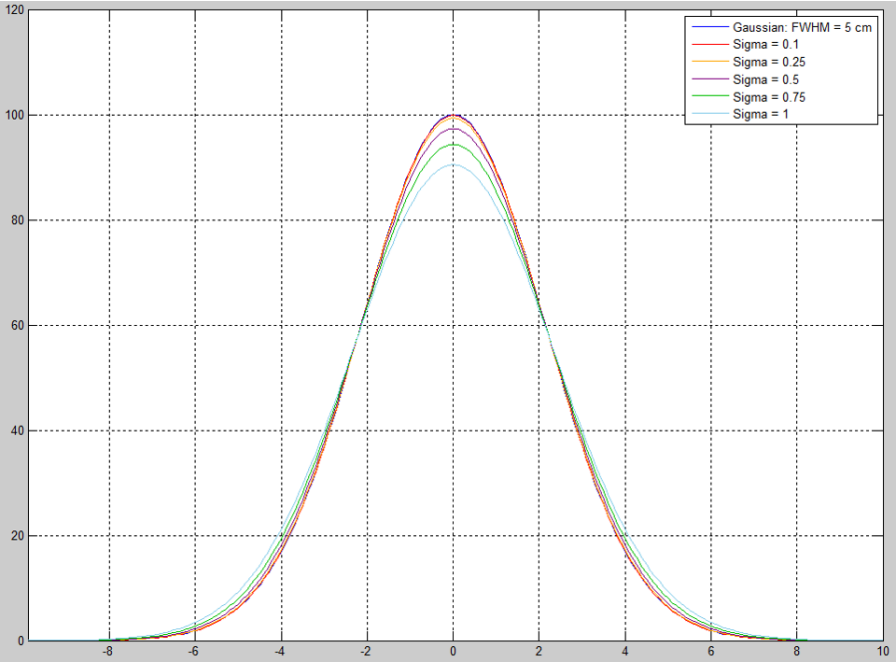

Figure 7.16: The effect of varying levels of target motion, represented by several PDF standard deviations, on an idealized square field. As the amount of motion increases, the dose coverage offered by the blurred dose profile continues to decrease. Due to the peaked nature of the Gaussian profile, the maximum peak height begins to decrease with PDF standard deviation of $0.5\ cm$, as compared to $1\ cm$ for the equivalent square profile.

7.6 Summary

In this chapter a sensitivity analysis was presented of the convolution methodology used in this thesis. Using a scaled Gaussian function for the static dose profile

$$G_2(r) = \frac{1}{\sigma_2\sqrt{2\pi}} e^{-\frac{1}{2}(\frac{r}{\sigma_2})^2} \bullet \sigma_2\sqrt{2\pi}, \tag{7.26}$$

with a maximum peak height of 1.0, and a normalized Gaussian lung PDF with $SD = \sigma_1$

$$G_1(r) = \frac{1}{\sigma_1\sqrt{2\pi}} e^{-\frac{1}{2}(\frac{r}{\sigma_1})^2}. \tag{7.27}$$

The blurred dose profile was determined from the convolution of $G_1(r)$ and $G_2(r)$ and analyzed parametrically. The analytical solution of the blurred dose profile is also a Gaussian, and was derived as

$$G_4(r) = G_2(r) \otimes G_1(r) = \frac{\sigma_2}{\sigma_3} e^{-\frac{1}{2}\left(\frac{r}{\sigma_3}\right)^2}, \tag{7.28}$$

with

$$\sigma_3 = \sqrt{\sigma_1^2 + \sigma_2^2}. \tag{7.29}$$

Summarizing the important results in this chapter;

1. the modified or blurred dose profile is given by the Gaussian function $G_4(r)$ with standard deviation $\sigma_3 = \sqrt{\sigma_1^2 + \sigma_2^2}$
2. the FWHM of the modified dose profile is given by $FWHM = 2\sqrt{2ln2}\sigma_3$
3. simultaneously
   (a) the peak height of $G_4(r)$ varies as $\frac{1}{\sigma_3}$ and

(b) the maximum slope of $G_4(r)$ varies as $\frac{1}{\sigma_3^2}$ such that the integral dose is conserved via $\int G_4(r)dr = \int G_2(r)dr$

4. generally, and governed by conservation of integral dose,

   (a) the peak height of $G_4(r)$, or a given dose profile will decrease with increasing σ_1

   (b) the maximum slope of $G_4(r)$, for a given dose profile, will decrease with increasing σ_1

   (c) the maximum peak height of $G_4(r)$, for a given σ_1, will increase with increasing FWHM of $G_2(r)$

   (d) the max slope of $G_4(r)$, for a given σ_1, will decrease with increasing FWHM of $G_2(r)$

5. additional beam width recommendations from Table 6.2 work reasonably well with the analytical Gaussian blurred dose model. When the ABW is applied to the static dose profile for a "'model-specific"' PDF standard deviation and dose profile FWHM values, the integral dose lost due to lung motion is recovered within an average of $96\% \pm 2.5\%$ for $0.1\ cm \leq \sigma_1 \leq 0.8\ cm$ lung PDF standard deviation and $2.6\ cm \leq FHWM \leq 10.1\ cm$ static dose profiles.

6. Table 6.2 should not be used clinically for static dose profiles and PDF standard deviations outside of the parameter boundaries specified in item 5 above. For static dose $FWHM < 2.5\ cm$, a patient-specific dosimetry workup should be performed to determine an estimate for the loss of integral dose due to lung motion and an optimum strategy for providing recovery.

Chapter 8

Conclusions

8.1 Discussion

Organ motion during the course of EBRT is a major source of geometric uncertainty in the delivery of the prescribed radiation dose. Organ motion that occurs between fractions during a radiotherapy treatment is known as interfraction motion. Organ motion that occurs during treatment delivery is known as intrafraction motion. Both interfraction and intrafraction motion need to be accounted for in order to accurately deliver the prescribed dose and achieve the best patient outcomes. While interfraction motion can be effectively accounted for with daily imaging on the treatment unit; compensating for intrafraction motion presents a larger challenge.

Addressing intrafraction motion continues to be a major concern for researchers and clinicians. Many approaches have been detailed in the literature, such as: breath-hold techniques, gated radiotherapy, real time target tracking and motion encompassing techniques. While each of these approaches has its advantages and disadvantages, motion encompassing techniques are the most widely used due to the ease of implementation. Motion encompassing techniques seek to

define a treatment volume which sufficiently covers the volume represented by the target motion. There have also been several approaches to motion encompassing techniques described in the literature and each one seeks to balance the need to deliver sufficient dose to the target volume while minimizing the dose to the surrounding OARs.

In this work, a motion encompassing technique to compensate for intrafraction lung motion was developed. This technique is based on the convolution model of target motion. The convolution model seeks to describe the effect of target motion on the delivered dose distribution by convolving a planned static dose distribution and a probability distribution describing the target motion. The convolution model was employed in the context of modern 4DCT equipment, which offers new tools for assessing the impact of target motion. By generating the PDF from 4DCT data and using the gradient of the PDF to obtain the blurred dose profiles, the effect of target motion can be compensated for directly within the treatment planning environment.

The validity of the convolution model in the context of intrafraction motion was assessed with radiochromic film measurements in a dynamic thorax phantom. This experimental validation used regular and irregular breathing patterns recorded from patients as the source of the motion pattern. After experimentally establishing the validity of the model, the model was employed as part of a large simulation study to search for trends that can be used to guide treatment margin selection to compensate for target motion in the lung.

The simulation study consisted of the analysis of the effect of 502 different patient breathing patterns on targets ranging in diameter from $2.6\ cm$ to $10.1\ cm$. An analysis of the dose coverage resulting from the convolution model predictions lead to margin recommendations which seek to maintain the minimum dose received by 95% of the target volume (D_{95}). The margin recommendations, as defined in Chapter 6, are based on the standard deviation of the target motion about its mean position, and the diameter of the target volume.

A sensitivity analysis of the convolution model as applied to Gaussian dose profiles and Gaussian breathing motion PDFs was presented. The sensitivity analysis of Gaussian functions allows for an analytical approach to assess the effect of varying model parameters on the model output. The analytical sensitivity analysis showed that the results derived in Chapter 6 have limitations that need to be respected in extreme cases (small targets with large motion).

8.2 Summary of Key Results

The effect of target motion was investigated based on the breathing patterns recorded from 502 unique patients. The key results can be are summarized below:

- The two major assumptions of the convolution model are generally met when the model is used in the context of intrafraction lung motion. The assumption of shift invariance was considered in the context of intrafraction motion and meets the requirements as discussed by other authors. The assumption of sufficient sampling in the context of intrafraction motion was also assessed. Ultimately, sufficient sampling will be met for the vast majority of cases given $10\ s$ of beam on time. This was established with an empirical study of patient breathing traces as well as a review of the convolution model limitations in the literature.

- The accuracy of the convolution model predictions in the context of intrafraction lung motion was established with radiochromic film measurements in a dynamic thorax phantom. For both regular and irregular type breathing patterns, the convolution model makes predictions accurate to within the 6% margin of error expected with good film handling techniques.

- Breathing trace amplitudes used in this study ranged from 0.13 to $2.30\ cm$ with an average amplitude of $0.73\ cm$.

- Breathing trace PDF standard deviations used in this study ranged from 0.057 to $1.13\ cm$ with an average standard deviation of $0.34\ cm$.

- A reasonably strong correlation ($R^2 = 0.864$) was found between breathing trace amplitude and standard deviation, indicating that the amplitude of the motion is the most important factor in determining the breathing trace standard deviation.

- The loss of target dose coverage (D_{95}) is well described by a quadratic function of the breathing trace standard deviation. This relation indicates that loss of target D_{95} is negligible for breathing patterns with a standard deviation of less than $0.2\ cm$ for all target sizes ($< 1\%$ loss of target D_{95}). In general, the loss of target D_{95} begins to become appreciable for targets undergoing motion with a standard deviation of $0.4\ cm$ or greater.

- The additional margin required to maintain target D_{95} can be computed by iteratively increasing the beam width in the direction of motion, and computing the new relative D_{95} of the blurred profile in each instance. A table of margin recommendations derived from this simulation was presented in Chapter 6.

- Since the target D_{95} is a relative quantity dependent on the size of the target volume, the role of target size in selecting these margins cannot be ignored. The results presented in the margin recommendation table indicate that little to no extra margin is required for many combinations of target size and level of motion.

- Target size plays an important role in loss of dose coverage. For targets with a FWHM of $5\ cm$ or greater, additional margin is only required for very large target motion (with standard deviation $\geq 0.4\ cm$. For targets smaller than $5\ cm$, more care must be taken to

account for target motion. Small targets with large motion are by far the most susceptible to loss of target dose coverage due to motion.

- The margin recommendations presented here can also be used to assess the trade off between target dose coverage and dose to OARs. If the margins recommended here would cause unacceptable dose to an OAR, then the clinician can use that information do decided whether the current treatment technique will be suitable.

- When the convolution model is applied to Gaussian PDFs and dose profiles, the results presented in this thesis hold except for extreme cases of small targets with large motion.

8.3 Conclusion

Intrafraction target motion during external beam radiation therapy is a large source of geometric uncertainty which has an impact on dose delivery. While technological advancements promise new approaches to compensating for intrafraction motion, the most reliable and easiest to implement of these approaches are the motion encompassing techniques. These techniques seek to define an appropriate treatment margin to ensure the target volume receives the prescribed dose. The expansion of treatment margins always comes at the cost of increased dose to OARs, and so finding optimal margins is an important step in offering a successful radiotherapy treatment. Offering patient specific recommendations for treatment margin selection allows for a fine balance to be struck between ensuring sufficient target dose and minimizing dose to the surrounding OARs.

Intrafraction motion has the effect of 'blurring' the planned dose distribution causing a loss of dose coverage to the target volume and increased dose to surrounding OARs upon treatment delivery. The convolution model was found to accurately predict the loss of target dose coverage

due to the blurring of intrafraction motion. By assessing the loss of dose coverage in relation to parameters of a given patient's specific breathing, it was found that the standard deviation of the breathing trace PDF is a useful predictor of the loss of dose coverage. For target motions with a standard deviation $\geq 0.4\ cm$ care should be taken to apply additional treatment margins as described in Table 6.2.

The size of the target volume is an important factor when considering loss of dose coverage. Small targets ($< 5\ cm$) are most susceptible to a loss of dose coverage, while large targets ($> 5\,cm$) are more robust in the face of intrafraction motion. Finally, the gradient of the patient's breathing trace PDF offered insights into the blurring effect caused by the motion. The rate of change of the PDF along the direction of motion highlights the features of the patient's breathing trace that will make the largest impact on the blurred dose distribution. While the PDF standard deviation predicts the dominant blurring effect, the gradient of the PDF can offer insight into asymmetries resulting from asymmetric breathing.

The results of this work further emphasize the need for patient specific approaches to margin selection. The interplay between target size, dose gradients, PDF standard deviation, location of the disease relative to OARs and treatment technique leaves no room for general solutions. The margin recommendations made in this work can be used to help guide treatment planning decisions by revealing the additional margin required to compensate for a given patient's specific breathing motion and target volume. By applying the margin at the treatment planning stage, the impact on OARs for that patient's disease site can be assessed. This type of patient specific approach can help ensure the patient receives the optimal treatment, and hence the best opportunity for a successful treatment outcome.

8.4 Suggestions for Future Work

This line of research could be carried on through one of several veins of future work:

- The same approach to a motion encompassing technique could be applied to other cancer sites susceptible to intrafraction target motion, such as the liver.
- The applicability of the model to segmented IMRT or volumetric modulated arc therapy techniques could be assessed.
- Extending the work towards optimizing treatment margin selection based on radiobiological considerations instead of purely physical (geometrical) considerations.
- Using the model predictions to adjust margins based on daily measured breathing patterns. This could perhaps be extended to real time margin adjustments.

Bibliography

[1] M. Engelsmann, G. C. Sharp, T. Bortfeld, R. Onimaru, and H. Shirato. How much margin reduction is possible through gating or breath hold? *Physics in Medicine and Biology*, 50(3):477–490, FEB 2005.

[2] Anne Richter, Kurt Baier, Juergen Meyer, Juergen Wilbert, Thomas Krieger, Michael Flentje, and Matthias Guckenberger. Influence of increased target dose inhomogeneity on margins for breathing motion compensation in conformal stereotactic body radiotherapy. *BMC Medical Physics*, 8:5, DEC 2008.

[3] Eric J. Hall. *Radiobiology for the radiologist*. Philadelphia : Wolters Kluwer Health/Lippincott Williams & Wilkins, Philadelphia, 7th edition, 2012.

[4] Harold E. Johns and John R. Cunningham. *The Physics of Radiology*. Charles C. Thomas, 1983, Springfield, Ill., U.S.A., 1983.

[5] Kazuhiro Yasufuku, Takahiro Nakajima, Ken Motoori, Yasuo Sekine, Kiyoshi Shibuya, Kenzo Hiroshima, and Takehiko Fujisawa. Comparison of endobronchial ultrasound, positron emission tomography, and CT for lymph node staging of lung cancer. *Chest*, 130(3):710–718, SEP 2006. PT: J; TC: 211; UT: WOS:000240585600018.

[6] T. Beyer, DW Townsend, T. Brun, PE Kinahan, M. Charron, R. Roddy, J. Jerin, J. Young, L. Byars, and R. Nutt. A combined PET/CT scanner for clinical oncology. *Journal of Nuclear Medicine*, 41(8):1369–1379, AUG 2000.

[7] G.C. Bentel. *Radiation Therapy Planning*. McGraw Hill, 2nd edition, 1996.

[8] JDP Hoisak, KE Sixel, R. Tirona, PCF Cheung, and JP Pignol. Correlation of lung tumor motion with external surrogate indicators of respiration. *International Journal of Radiation Oncology Biology Physics*, 60(4):1298–1306, NOV 2004.

[9] Y. Seppenwoolde, H. Shirato, K. Kitamura, S. Shimizu, M. van Herk, JV Lebesque, and K. Miyasaka. Precise and real-time measurement of 3D tumor motion in lung due to breathing and heartbeat, measured during radiotherapy. *International Journal of Radiation Oncology Biology Physics*, 53(4):822–834, JUL 2002.

[10] Katharina E. Sixel, Mark Ruschin, Romeo Tirona, and Patrick C. F. Cheung. Digital fluoroscopy to quantify lung tumor motion: Potential for patient-specific planning target volumes. *International Journal of Radiation Oncology Biology Physics*, 57(3):717–723, 2003.

[11] H. Shirato, K. Suzuki, G. C. Sharp, K. Fujita, R. Onimaru, M. Fujino, N. Kato, Y. Osaka, R. Kinoshita, H. Taguchi, S. Onodera, and K. Miyasaka. Speed and amplitude of lung tumor motion precisely detected in four-dimensional setup and in real-time tumor-tracking radiotherapy. *International Journal of Radiation Oncology Biology Physics*, 64(4):1229–1236, 2006.

[12] Paul J. Keall, Gig S. Mageras, James M. Balter, Richard S. Emery, Kenneth M. Forster, Steve B. Jiang, Jeffrey M. Kapatoes, Daniel A. Low, Martin J. Murphy, Brad R. Murray, Chester R. Ramsey, Marcel B. Van Herk, S. S. Vedam, John W. Wong, and Ellen Yorke.

The management of respiratory motion in radiation oncology report of AAPM Task Group 76. *Medical Physics*, 33(10):3874–3900, OCT 2006.

[13] Marcel van Herk, Peter Remeijer, Coen Rasch, and Joos V. Lebesque. The probability of correct target dosage: Dose-population histograms for deriving treatment margins in radiotherapy. *International Journal of Radiation Oncology Biology Physics*, 47(4):1121–1135, 2000.

[14] JY Jin, M. Ajlouni, Q. Chen, FF Yin, and B. Movsas. A technique of using gated-CT images to determine internal target volume (ITV) for fractionated stereotactic lung radiotherapy. *Radiotherapy and Oncology*, 78(2):177–184, FEB 2006.

[15] H. H. Liu, Peter Balter, Teresa Tutt, Bum Choi, Joy Zhang, Catherine Wang, Melinda Chi, Dershan Luo, Tinsu Pan, Sandeep Hunjan, George Starkschall, Isaac Rosen, Karl Prado, Zhongxing Liao, Joe Chang, Ritsuko Komaki, James D. Cox, Radhe Mohan, and Lei Dong. Assessing respiration-induced tumor motion and internal target volume using four-dimensional computed tomography for radiotherapy of lung cancer. *International Journal of Radiation Oncology Biology Physics*, 68(2):531–540, JUN 2007.

[16] Emily Heath, Jan Unkelbach, and Uwe Oelfke. Incorporating uncertainties in respiratory motion into 4D treatment plan optimization. *Medical Physics*, 36(7):3059–3071, JUL 2009.

[17] H. D. Kubo and B. C. Hill. Respiration gated radiotherapy treatment: A technical study. *Physics in Medicine and Biology*, 41(1):83–91, JAN 1996.

[18] L. Ekberg, O. Holmberg, L. Wittgren, G. Bjelkengren, and T. Landberg. What margins should be added to the clinical target volume in radiotherapy treatment planning for lung cancer? *Radiotherapy and Oncology*, 48(1):71–77, JUL 1998.

[19] M. Engelsmann, E. M. F. Damen, K. De Jaeger, K. M. van Ingen, and B. J. Mijnheer. The effect of breathing and set-up errors on the cumulative dose to a lung tumor. *Radiotherapy and Oncology*, 60(1):95–105, JUL 2001.

[20] S. S. Vedam, V. R. Kini, P. J. Keall, V. Ramakrishnan, H. Mostafavi, and R. Mohan. Quantifying the predictability of diaphragm motion during respiration with a noninvasive external marker. *Medical Physics*, 30(4):505–513, APR 2003.

[21] E. Rietzel, G. T. Y. Chen, N. C. Choi, and C. G. Willet. Four-dimensional image-based treatment planning: Target volume segmentation and dose calculation in the presence of respiratory motion. *International Journal of Radiation Oncology Biology Physics*, 61(5):1535–1550, APR 2005.

[22] J. Leong. Implementation of random positioning error in computerized radiation treatment planning systems as a result of fractionation. *Physics in Medicine and Biology*, 32(3):327–334, MAR 1987.

[23] A. E. Lujan, E. W. Larsen, J. M. Balter, and R. K. Ten Haken. A method for incorporating organ motion due to breathing into 3D dose calculations. *Medical Physics*, 26(5):715–720, MAY 1999.

[24] Runqing Jiang, Rob B. Barnett, James C. L. Chow, and Jeff Z. Y. Chen. The use of spatial dose gradients and probability density function to evaluate the effect of internal organ motion for prostate IMRT treatment planning. *Physics in Medicine and Biology*, 52(5):1469–1484, MAR 2007.

[25] Jiang Hsieh. *Computed tomography principles, design, artifacts, and recent advances /.* Bellingham, Wash. (1000 20th St. Bellingham WA 98225-6705 USA) : SPIE, c2009, 2nd edition, 2009.

[26] Jerrold T. Bushberg. *The essential physics of medical imaging*. Philadelphia : Lippincott Williams & Wilkins, Philadelphia, 2nd edition, 2002.

[27] Nicholas Denko, Amato Giaccia, Bruce Peters, and Thomas D. Stamato. An asymmetric field inversion gel electrophoresis method for the separation of large DNA molecules. *Analytical Biochemistry*, 178(1):172–176, APR 1989.

[28] Thomas D. Stamato and Nicholas Denko. Asymmetric field inversion gel electrophoresis: A new method for detecting DNA double-strand breaks in mammalian cells. *Radiation research*, 121(2):196–205, FEB 1990.

[29] E. B. Podgorak. *Radiation physics for medical physicists*. Heidelberg : Springer, c2010, 2nd edition, 2010.

[30] B. G. Douglas and J. F. Fowler. The effect of multiple small doses of x-rays on skin reactions in the mouse and a basic interpretation. *Radiation Research*, 66(2):401–426, May 1976.

[31] J. C. Mottram. A factor of importance in the radio sensitivity of tumours. *The British Journal of Radiology*, 9(105):606–614, 1936.

[32] John Read. The effect of ionizing radiations on the broad bean root, part X. *The British Journal of Radiology*, 25(290):89–99, 1952.

[33] J. B. Little, G. M. Hahn, E. Frindel, and M. Tubiana. Repair of potentially lethal radiation-damage in-vitro and in-vivo. *Radiology*, 106(3):689–694, 1973.

[34] M. M. Elkind, Suttongi.H, W. B. Moses, T. Alescio, and R. W. Swain. Radiation response of mammalian cells crown in culture .V. Temperature dependence of repair of x-ray damage in surviving cells (aerobic and hypoxic). *Radiation research*, 25(2):359–376, 1965.

[35] J. F. Fowler. Fractionated radiation therapy after strandqvist. *Acta Radiologica Oncology*, 23(4):209–216, 1984.

[36] T. R. Munro and C. W. Gilbert. The relation between tumour lethal doses and the radiosensitivity of tumour cells. *British Journal of Radiology*, 34(400):246–251, 1961.

[37] S. Webb and A. E. Nahum. A model for calculating tumor-control probability in radiotherapy including the effects of inhomogeneous distributions of dose and clonogenic cell-density. *Physics in Medicine and Biology*, 38(6):653–666, JUN 1993.

[38] J. T. Lyman. Complication probability as assessed from dose volume histograms. *Radiation research*, 104(2):S13–S19, 1985 1985.

[39] C. Burman, G. J. Kutcher, B. Emami, and M. Goitein. Fitting of normal tissue tolerance data to an analytic function. *International journal of radiation oncology, biology, physics*, 21(1):123–135, MAY 1991.

[40] Canadian Cancer Society; 2013 Canadian Cancer Society's Advisory Committee on Cancer Statistics. Toronto. Canadian cancer statistics 2013.

[41] Taimur Sher, Grace K. Dy, and Alex A. Adjei. Small cell lung cancer. *Mayo Clinic Proceedings*, 83(3):355–367, MAR 2008.

[42] G. Otterson, A. Lin, and F. Kay. Genetic etiology of lung cancer. *Oncology (Williston Park, N.Y.)*, 6(9):97–104, 107; Discussion 108, 111–2, SEP 1992.

[43] Julian R. Molina, Piii G. Yang, Stephen D. Cassivi, Steven E. Schild, and Alex A. Adjei. Non-small cell lung cancer: Epidemiology, risk factors, treatment, and survivorship. *Mayo Clinic Proceedings*, 83(5):584–594, MAY 2008.

[44] Robert Timmerman, Rebecca Paulus, James Galvin, Jeffrey Michalski, William Straube, Jeffrey Bradley, Achilles Fakiris, Andrea Bezjak, Gregory Videtic, David Johnstone, Jack Fowler, Elizabeth Gore, and Hak Choy. Stereotactic body radiation therapy for inoperable early stage lung cancer. *Journal of the American Medical Association*, 303(11):1070–1076, MAR 2010.

[45] CF Mountain. Revisions in the international system for staging lung cancer. *Chest*, 111(6):1710–1717, 1997.

[46] W. T. Sause, C. Scott, S. Taylor, D. Johnson, R. Livingston, R. Komaki, B. Emami, W. J. Curran, R. W. Byhardt, A. T. Turrisi, A. R. Dar, and J. D. Cox. Radiation-Therapy-Oncology-Group (RTOG)-88-08 and Eastern-Cooperative-Oncology-Group (ECOG)-4588 - preliminary-results of a phase-III trial in regionally advanced, unresectable non-small-cell lung-cancer. *Journal of the National Cancer Institute*, 87(3):198–205, FEB 1995.

[47] B. Emami, J. Lyman, A. Brown, L. Coia, M. Goitein, J. E. Munzenrider, B. Shank, L. J. Solin, and M. Wesson. Tolerance of normal tissue to therapeutic irradiation. *International Journal of Radiation Oncology Biology Physics*, 21(1):109–122, MAY 1991.

[48] Lawrence B. Marks, Soren M. Bentzen, Joseph O. Deasy, Feng-Ming Kong, Jeffrey D. Bradley, Ivan S. Vogelius, Issam El Naqa, Jessica L. Hubbs, Joos V. Lebesque, Robert D. Timmerman, Mary K. Martel, and Andrew Jackson. Radiation dose-volume effects in the lung. *International Journal of Radiation Oncology Biology Physics*, 76(3):S70–S76, 2010.

[49] Giovanna Gagliardi, Louis S. Constine, Vitali Moiseenko, Candace Correa, Lori J. Pierce, Aaron M. Allen, and Lawrence B. Marks. Radiation dose-volume effects in the heart. *International Journal of Radiation Oncology Biology Physics*, 76(3):S77–S85, 2010.

[50] John P. Kirkpatrick, Albert J. van der Kogel, and Timothy E. Schultheiss. Radiation dose-volume effects in the spinal cord. *International Journal of Radiation Oncology Biology Physics*, 76(3):S42–S49, 2010.

[51] Maria Werner-Wasik, Ellen Yorke, Joseph Deasy, Jiho Nam, and Lawrence B. Marks. Radiation dose-volume effects in the esophagus. *International Journal of Radiation Oncology Biology Physics*, 76(3):S86–S93, 2010.

[52] Paiman Ghafoori, Lawrence B. Marks, Zeljko Vujaskovic, and Christopher R. Kelsey. Radiation-induced lung injury - assessment, management, and prevention. *Oncology-New York*, 22(1):37–47, JAN 2008.

[53] Karen Breitman, Satyapal Rathee, Chris Newcomb, Brad Murray, Don Robinson, Colin Field, Heather Warkentin, Sherry Connors, Marc MacKenzie, Peter Dunscombe, and Gino Fallone. Experimental validation of the Eclipse AAA algorithm. *Journal of Applied Clinical Medical Physics*, 8(2):76–92, 2007.

[54] N. Childress, E. Stevens, D. Eklund, and M. Zhang. Mobius3D white paper: Dose calculation algorithm.

[55] James C. L. Chow, Michael K. K. Leung, and Jake Van Dyk. Variations of lung density and geometry on inhomogeneity correction algorithms: A Monte Carlo dosimetric evaluation. *Medical Physics*, 36(8):3619–3630, AUG 2009.

[56] Brandon Disher, George Hajdok, Stewart Gaede, and Jerry J. Battista. An in-depth Monte Carlo study of lateral electron disequilibrium for small fields in ultra-low density lung:

implications for modern radiation therapy. *Physics in Medicine and Biology*, 57(6):1543–1559, MAR 2012.

[57] Petra S. Kroon, Sandra Hol, and Marion Essers. Dosimetric accuracy and clinical quality of Acuros XB and AAA dose calculation algorithm for stereotactic and conventional lung volumetric modulated arc therapy plans. *Radiation Oncology*, 8:149, JUN 2013.

[58] S. Webb. Motion effects in (intensity modulated) radiation therapy: a review. *Physics in Medicine and Biology*, 51(13):R403–R425, JUL 2006.

[59] G. S. Mageras, E. Yorke, K. Rosenzweig, L. Braban, E. Keatley, E. Ford, S. A. Leibel, and C. C. Ling. Fluoroscopic evaluation of diaphragmatic motion reduction with a respiratory gated radiotherapy system. *Journal of Applied Clinical Medical Physics*, 2(4):191–200, 2001.

[60] Jean-Pierre Bissonnette, Kevin N. Franks, Thomas G. Purdie, Douglas J. Moseley, Jan-Jakob Sonke, David A. Jaffray, Laura A. Dawson, and Andrea Bezjak. Quantifying interfraction and intrafraction tumor motion in lung stereotactic body radiotherapy using respiration-correlated cone beam computed tomography. *International Journal of Radiation Oncology Biology Physics*, 75(3):688–695, NOV 2009. PT: J; TC: 44; UT: WOS:000270573100008.

[61] G. S. Mageras, A. Pevsner, E. D. Yorke, K. E. Rosenzweig, E. C. Ford, A. Hertanto, S. M. Larson, D. M. Lovelock, Y. E. Erdi, S. A. Nehmeh, J. L. Humm, and C. C. Ling. Measurement of lung tumor motion using respiration-correlated CT. *International Journal of Radiation Oncology Biology Physics*, 60(3):933–941, 2004.

[62] C. Plathow, S. Ley, C. Fink, M. Puderbach, W. Hosch, A. Schmahl, J. Debus, and H. U. Kauczor. Analysis of intrathoracic tumor mobility during whole breathing cycle by dy-

namic MRI. *International Journal of Radiation Oncology Biology Physics*, 59(4):952–959, JUL 2004.

[63] M. J. Murphy, D. Martin, R. Whyte, J. Hai, C. Ozhasoglu, and Q. T. Le. The effectiveness of breath-holding to stabilize lung and pancreas tumors during radiosurgery. *International Journal of Radiation Oncology Biology Physics*, 53(2):475–482, JUN 2002.

[64] Yelin Suh, Sonja Dieterich, Byungchul Cho, and Paul J. Keall. An analysis of thoracic and abdominal tumour motion for stereotactic body radiotherapy patients. *Physics in Medicine and Biology*, 53(13):3623–3640, JUL 2008.

[65] Keiichi Nakagawa, Akihiro Haga, Satoshi Kida, Yoshitaka Masutani, Hideomi Yamashita, Wataru Takahashi, Akira Sakumi, Naoya Saotome, Takashi Shiraki, Kuni Ohtomo, Yoshio Iwai, and Kiyoshi Yoda. 4D registration and 4D verification of lung tumor position for stereotactic volumetric modulated arc therapy using respiratory-correlated cone-beam CT. *Journal of Radiation Research*, 54(1):152–156, JAN 2013.

[66] Lars Dietrich, Siri Jetter, Thomas Tuecking, Simeon Nill, and Uwe Oelfke. Linac-integrated 4D cone beam CT: first experimental results. *Physics in Medicine and Biology*, 51(11):2939–2952, JUN 2006.

[67] T. Pan, TY Lee, E. Rietzel, and GTY Chen. 4D-CT imaging of a volume influenced by respiratory motion on multi-slice CT. *Medical Physics*, 31(2):333–340, FEB 2004.

[68] Vijay R. Kini, Subrahmanya S. Vedam, Paul J. Keall, Sumukh Patil, Clayton Chen, and Radhe Mohan. Patient training in respiratory-gated radiotherapy. *Medical Dosimetry: Official Journal of the American Association of Medical Dosimetrists*, 28(1):7–11, 2003.

[69] Stine S. Korreman, Trine Juhler-Nottrup, and Arthur L. Boyer. Respiratory gated beam delivery cannot facilitate margin reduction, unless combined with respiratory correlated image guidance. *Radiotherapy and Oncology*, 86(1):61–68, JAN 2008.

[70] CA; 2007 Varian Medical Systems Inc., Palo Alto. RPM respiratory gating system reference guide.

[71] Kristin J. Redmond, Danny Y. Song, Jana L. Fox, Jessica Zhou, C. N. Rosenzweig, and Eric Ford. Respiratory motion changes of lung tumors over the course of radiation therapy based on respiration-correlated four-dimensional computed tomography scans. *International Journal of Radiation Oncology, Biology, Physics*, 75(5):1605–1612, DEC 2009.

[72] Thomas G. Purdie, Jean-Pierre Bissonnette, Kevin Franks, Andrea Bezjak, David Payne, Fanny Sie, Michael B. Sharpe, and David A. Jaffray. Cone-beam computed tomography for on-line image guidance of lung stereotactic radiotherapy: Localization, verification, and intrafraction tumor position. *International Journal of Radiation Oncology Biology Physics*, 68(1):243–252, MAY 1 2007 2007. PT: J; TC: 125; UT: WOS:000246046000033.

[73] F. J. Lagerwaard, J. R. V. de Koste, M. R. J. Nijssen-Visser, R. H. Schuchhard-Schipper, S. S. Oei, A. Munne, and S. Senan. Multiple 'slow' CT scans for incorporating lung tumor mobility in radiotherapy planning. *International Journal of Radiation Oncology Biology Physics*, 51(4):932–937, NOV 2001.

[74] J. Hanley, M. M. Debois, D. Mah, G. S. Mageras, A. Raben, K. Rosenzweig, B. Mychalczak, L. H. Schwartz, P. J. Gloeggler, W. Lutz, C. C. Ling, S. A. Leibel, Z. Fuks, and G. J. Kutcher. Deep inspiration breath-hold technique for lung tumors: The potential value of

target immobilization and reduced lung density in dose escalation. *International Journal of Radiation Oncology Biology Physics*, 45(3):603–611, OCT 1999.

[75] R. W. M. Underberg, F. J. Lagerwaard, B. J. Slotman, J. P. Cuijpers, and S. Senan. Use of maximum intensity projections (MIP) for target volume generation in 4DCT scans for lung cancer. *International Journal of Radiation Oncology Biology Physics*, 63(1):253–260, SEP 2005.

[76] N. L. Ford, M. M. Thornton, and D. W. Holdsworth. Fundamental image quality limits for microcomputed tomography in small animals. *Medical physics*, 30(11):2869–2877, NOV 2003.

[77] E. C. Ford, G. S. Mageras, E. Yorke, and C. C. Ling. Respiration-correlated spiral CT: A method of measuring respiratory-induced anatomic motion for radiation treatment planning. *Medical Physics*, 30(1):88–97, JAN 2003.

[78] E. Rietzel, TS Pan, and GTY Chen. Four-dimensional computed tomography: Image formation and clinical protocol. *Medical Physics*, 32(4):874–889, APR 2005.

[79] X. A. Li, C. Stepaniak, and E. Gore. Technical and dosimetric aspects of respiratory gating using a pressure-sensor motion monitoring system. *Medical Physics*, 33(1):145–154, JAN 2006.

[80] Matthias Guckenberger, Juergen Wilbert, Thomas Krieger, Anne Richter, Kurt Baier, and Michael Flentje. Mid-ventilation concept for mobile pulmonary tumors: Internal tumor trajectory versus selective reconstruction of four-dimensional computed tomography frames based on external breathing motion. *International Journal of Radiation Oncology Biology Physics*, 74(2):602–609, JUN 2009.

[81] Joseph P. Santoro, Ellen Yorke, Karyn A. Goodman, and Gig S. Mageras. From phase-based to displacement-based gating: A software tool to facilitate respiration-gated radiation treatment. *Journal of Applied Clinical Medical Physics*, 10(4):132–141, 2009.

[82] A. F. Abdelnour, S. A. Nehmeh, T. Pan, J. L. Humm, P. Vernon, H. Schoder, K. E. Rosenzweig, G. S. Mageras, E. Yorke, S. M. Larson, and Y. E. Erdi. Phase and amplitude binning for 4D-CT imaging. *Physics in Medicine and Biology*, 52(12):3515–3529, JUN 2007.

[83] E. Rietzel and G. T. Y. Chen. Improving retrospective sorting of 4D computed tomography data. *Medical Physics*, 33(2):377–379, FEB 2006.

[84] Hua Li, Camille Noel, Jose Garcia-Ramirez, Daniel Low, Jeffrey Bradley, Clifford Robinson, Sasa Mutic, and Parag Parikh. Clinical evaluations of an amplitude-based binning algorithm for 4DCT reconstruction in radiation therapy. *Medical physics*, 39(2):922–932, FEB 2012.

[85] Jeffrey R. Olsen, Wei Lu, James P. Hubenschmidt, Michelle M. Nystrom, Paul Klahr, Jeffrey D. Bradley, Daniel A. Low, and Parag J. Parikh. Effect of novel amplitude/phase binning algorithm on commercial four-dimensional computed tomography quality. *International Journal of Radiation Oncology Biology Physics*, 70(1):243–252, JAN 2008.

[86] Wei Lu, Parag J. Parikh, James P. Hubenschmidt, Jeffrey D. Bradley, and Daniel A. Low. A comparison between amplitude sorting and phase-angle sorting using external respiratory measurement for 4D CT. *Medical Physics*, 33(8):2964–2974, AUG 2006.

[87] Nicole M. Wink, Christoph Panknin, and Timothy D. Solberg. Phase versus amplitude sorting of 4D-CT data. *Journal of Applied Clinical Medical Physics*, 7(1):77–85, 2006.

[88] ICRU Report 50. International commission on radiation units and measurements. Bethesda, MD, 1993.

[89] ICRU Report 62. International commission on radiation units and measurements. Bethesda, MD, 1999.

[90] D. Mah, J. Hanley, K. E. Rosenzweig, E. Yorke, L. Braban, C. C. Ling, S. A. Leibel, and G. Mageras. Technical aspects of the deep inspiration breath-hold technique in the treatment of thoracic cancer. *International Journal of Radiation Oncology Biology Physics*, 48(4):1175–1185, NOV 2000.

[91] J. W. Wong, M. B. Sharpe, D. A. Jaffray, J. M. Robertson, J. S. Stromberg, V. R. Kini, and A. A. Martinez. The use of active breathing control (ABC) to minimize breathing motion during radiation therapy. *International Journal of Radiation Oncology Biology Physics*, 39(2):164–164, 1997.

[92] Y. Negoro, Y. Nagata, T. Aoki, T. Mizowaki, N. Araki, K. Takayama, M. Kokubo, S. Yano, S. Koga, K. Sasai, Y. Shibamoto, and M. Hiraoka. The effectiveness of an immobilization device in conformal radiotherapy for lung tumor: Reduction of respiratory tumor movement and evaluation of the daily setup accuracy. *International Journal of Radiation Oncology Biology Physics*, 50(4):889–898, JUL 2001.

[93] H. D. Kubo, P. M. Len, S. Minohara, and H. Mostafavi. Breathing-synchronized radiotherapy program at the University of California Davis Cancer Center. *Medical Physics*, 27(2):346–353, FEB 2000.

[94] S. Shimizu, H. Shirato, S. Ogura, H. Akita-Dosaka, K. Kitamura, T. Nishioka, K. Kagei, M. Nishimura, and K. Miyasaka. Detection of lung tumor movement in real-time tumor-

tracking radiotherapy. *International Journal of Radiation Oncology Biology Physics*, 51(2):304–310, OCT 2001.

[95] Q. S. Chen, M. S. Weinhous, F. C. Deibel, J. P. Ciezki, and R. M. Macklis. Fluoroscopic study of tumor motion due to breathing: Facilitating precise radiation therapy for lung cancer patients. *Medical Physics*, 28(9):1850–1856, SEP 2001.

[96] S. Ahn, B. Yi, Y. Suh, J. Kim, S. Lee, S. Shin, S. Shin, and E. Choi. A feasibility study on the prediction of tumour location in the lung from skin motion. *British Journal of Radiology*, 77(919):588–596, JUL 2004.

[97] A. Schweikard, G. Glosser, M. Bodduluri, M. J. Murphy, and J. R. Adler. Robotic motion compensation for respiratory movement during radiosurgery. *Computer Aided Surgery*, 5(4):263–77, 2000.

[98] T. Neicu, H. Shirato, Y. Seppenwoolde, and S. B. Jiang. Synchronized moving aperture radiation therapy (SMART): Average tumour trajectory for lung patients. *Physics in Medicine and Biology*, 48(5):587–598, MAR 2003.

[99] P. J. Keall, V. R. Kini, S. S. Vedam, and R. Mohan. Motion adaptive x-ray therapy: A feasibility study. *Physics in Medicine and Biology*, 46(1):1–10, JAN 2001.

[100] W. D. D'Souza, S. A. Naqvi, and C. X. Yu. Real-time intra-fraction-motion tracking using the treatment couch: a feasibility study. *Physics in Medicine and Biology*, 50(17):4021–4033, SEP 2005.

[101] PJ Keall, S. Joshi, SS Vedam, JV Siebers, VR Kini, and R. Mohan. Four-dimensional radiotherapy planning for DMLC-based respiratory motion tracking. *Medical Physics*, 32(4):942–951, APR 2005.

[102] R. W. M. Underberg, F. J. Lagerwaard, J. P. Cuijpers, B. J. Slotman, J. R. V. de Koste, and S. Senan. Four-dimensional CT scans for treatment planning in stereotactic radiotherapy for stage I lung cancer. *International Journal of Radiation Oncology Biology Physics*, 60(4):1283–1290, NOV 2004.

[103] Marjan A. Admiraal, Danny Schuring, and Coen W. Hurkmans. Dose calculations accounting for breathing motion in stereotactic lung radiotherapy based on 4D-CT and the internal target volume. *Radiotherapy and Oncology*, 86(1):55–60, JAN 2008.

[104] Stuart S. C. Burnett, Katharina E. Sixel, Patrick C. F. Cheung, and Jeremy D. P. Hoisak. A study of tumor motion management in the conformal radiotherapy of lung cancer. *Radiotherapy and Oncology*, 86(1):77–85, JAN 2008.

[105] Johan P. Cuijpers, Wilko F. A. R. Verbakel, Ben J. Slotman, and Suresh Senan. A novel simple approach for incorporation of respiratory motion in stereotactic treatments of lung tumors. *Radiotherapy and Oncology*, 97(3):443–448, DEC 2010.

[106] J. Unkelbach and U. Oelfke. Inclusion of organ movements in IMRT treatment planning via inverse planning based on probability distributions. *Physics in Medicine and Biology*, 49(17):4005–4029, SEP 2004.

[107] Ronald N. (. N. Bracewell. *The Fourier transform and its applications*. Boston : McGraw Hill, Boston, 3rd edition, 2000. ID: vtug3194985; Includes bibliographical references and index.

[108] 1922 Arfken, George B. (. B. *Mathematical methods for physicists*. Elsevier; Elsevier Academic Press, Boston; Amsterdam ; Burlington, MA, 6th ed. / george b. arfken, hans j. weber. edition, 2005. ID: dedupmrg405584022; Includes bibliographical references and index.

[109] T. Craig, J. Battista, and J. Van Dyk. Limitations of a convolution method for modeling geometric uncertainties in radiation therapy. I. The effect of shift invariance. *Medical Physics*, 30(8):2001–2011, AUG 2003.

[110] T. Craig, J. Battista, and J. Van Dyk. Limitations of a convolution method for modeling geometric uncertainties in radiation therapy. II. The effect of a finite number of fractions. *Medical Physics*, 30(8):2012–2020, AUG 2003.

[111] Jochem W. H. Wolthaus, Christoph Schneider, Jan-Jakob Sonke, Marcel van Herk, Jose S. A. Belderbos, Maddalena M. G. Rossi, Joos V. Lebesque, and Eugene M. F. Damen. Mid-ventilation CT scan construction from four-dimensional respiration-correlated CT scans for radiotherapy planning of lung cancer patients. *International Journal of Radiation Oncology Biology Physics*, 65(5):1560–1571, AUG 2006.

[112] T. Bortfeld, K. Jokivarsi, M. Goitein, J. Kung, and S. B. Jiang. Effects of intra-fraction motion on IMRT dose delivery: statistical analysis and simulation. *Physics in Medicine and Biology*, 47(13):2203–2220, JUL 2002.

[113] C. X. Yu, D. A. Jaffray, and J. W. Wong. The effects of intra-fraction organ motion on the delivery of dynamic intensity modulation. *Physics in Medicine and Biology*, 43(1):91–104, JAN 1998.

[114] C. S. Chui, E. Yorke, and L. Hong. The effects of intra-fraction organ motion on the delivery of intensity-modulated field with a multileaf collimator. *Medical Physics*, 30(7):1736–1746, JUL 2003.

[115] Haisen S. Li, Indrin J. Chetty, and Timothy D. Solberg. Quantifying the interplay effect in prostate IMRT delivery using a convolution-based method. *Medical Physics*, 35(5):1703–1710, MAY 2008.

[116] M. Rosu, L. A. Dawson, J. M. Balter, D. L. McShan, T. S. Lawrence, and R. K. T. Haken. Alterations in normal liver doses due to organ motion. *International Journal of Radiation Oncology Biology Physics*, 57(5):1472–1479, DEC 2003.

[117] J. M. Balter, K. K. Brock, K. L. Lam, D. Tatro, L. A. Dawson, D. McShan, and R. K. Ten Haken. Evaluating the influence of setup uncertainties on treatment planning for focal liver tumors. *International Journal of Radiation Oncology Biology Physics*, 63(2):610–614, OCT 2005.

[118] E. Astreinidou, A. Bel, CPJ Raaijmakers, CHJ Terhaard, and JJW Lagendijk. Adequate margins for random setup uncertainties in head-and-neck IMRT. *International Journal of Radiation Oncology Biology Physics*, 61(3):938–944, MAR 2005.

[119] J. V. Siebers, P. J. Keall, Q. W. Wu, J. F. Williamson, and R. K. Schmidt-Ullrich. Effect of patient setup errors on simultaneously integrated boost head and neck IMRT treatment plans. *International Journal of Radiation Oncology Biology Physics*, 63(2):422–433, OCT 2005.

[120] J. M. Balter, R. K. TenHaken, T. S. Lawrence, K. L. Lam, and J. M. Robertson. Uncertainties in CT-based radiation therapy treatment planning associated with patient breathing. *International Journal of Radiation Oncology Biology Physics*, 36(1):167–174, AUG 1996.

[121] R. George, P. J. Keall, V. R. Kini, S. S. Vedam, V. Ramakrishnan, and R. Mohan. Is the diaphragm motion probability density function normally distributed? *Medical Physics*, 32(2):396–404, FEB 2005.

[122] NJ; 2010 International Specialty Products, Wayne. GafChromic EBT2 self developing film for radiotherapy dosimetry.

[123] A. Niroomand-Rad, CR Blackwell, BM Coursey, KP Gall, JM Galvin, WL McLaughlin, AS Meigooni, R. Nath, JE Rodgers, and CG Soares. Radiochromic film dosimetry: Recommendations of AAPM Radiation Therapy Committee Task Group 55. *Medical Physics*, 25(11):2093–2115, NOV 1998.

[124] C. Andres, A. del Castillo, R. Tortosa, D. Alonso, and R. Barquero. A comprehensive study of the gafchromic EBT2 radiochromic film. a comparison with EBT. *Medical Physics*, 37(12):6271–6278, DEC 2010.

[125] Bernadette Hartmann, Maria Martisikova, and Oliver Jaekel. Technical note: Homogeneity of Gafchromic (R) EBT2 film. *Medical Physics*, 37(4):1753–1756, APR 2010.

[126] VA; 2013 Computerized Imaging Reference System Inc., Norfolk. Dynamic phantoms user guide.

[127] Germany; 2005 Siemens AG Medical Solutions, Erlang. SOMATOM sensation open data sheet.

[128] D. A. Low, W. B. Harms, S. Mutic, and J. A. Purdy. A technique for the quantitative evaluation of dose distributions. *Medical Physics*, 25(5):656–661, MAY 1998.

[129] J. V. Dyk, R. B. Barnett, J. E. Cygler, and P. C. Shragge. Commissioning and quality assurance of treatment planning computers. *International Journal of Radiation Oncology Biology Physics*, 26(2):261–273, MAY 1993.

[130] W. K. Foster, Ernest Osei, and Rob Barnett. Margin selection to compensate for loss of target dose coverage due to target motion during external-beam radiation therapy of the lung. *Journal of Applied Clinical Medical Physics*, 16(1):139–158, 2015.

[131] T. F. Cootes and C. J. Taylor. Statistical models of appearance for medical image analysis and computer vision. *Medical Imaging: Image Processing, Pts 1-3*, 2(27):236–248, 2001.

[132] Angelo Mencarelli, Simon R. van Kranen, Olga Hamming-Vrieze, Suzanne van Beek, Coenraad R. N. Rasch, Marcel van Herk, and Jan-Jakob Sonke. Deformable image registration for adaptive radiation therapy of head and neck cancer: Accuracy and precision in the presence of tumor changes. *International Journal of Radiation Oncology Biology Physics*, 90(3):680–687, NOV 2014. PT: J; TC: 2; UT: WOS:000342355400029.

[133] Hualiang Zhong, Jinkoo Kim, and Indrin J. Chetty. Analysis of deformable image registration accuracy using computational modeling. *Medical Physics*, 37(3):970–979, MAR 2010. PT: J; UT: WOS:000275160300003.

[134] U. J. Yeo, M. L. Taylor, J. R. Supple, R. L. Smith, L. Dunn, T. Kron, and R. D. Franich. Is it sensible to ”deform” dose? 3d experimental validation of dose-warping. *Medical Physics*, 39(8):5065–5072, AUG 2012. PT: J; UT: WOS:000307917600045.

Appendix A

Using Planned Dose Gradients and IGRT-based Tissue Displacement Vectors for Calculation of Cumulative Radiotherapy Dose

A.1 Introduction

Previous emphasis in this thesis has been on the calculation of absorbed dose using the convolution of the gradient of the probability density function for lung (free breathing) and a static dose profile obtained from the planned dose distribution. As shown, this is an effective methodology for determining the change in the static dose profile due to patient-specific lung motion and provides a framework for selection of appropriate margins to ensure that the radiation oncologist's dose prescription is met. In this chapter/appendix, a methodology is presented for calculating

the cumulative dose during radiation therapy taking into account day-to-day tissue differences (target and organs at risk) as determined from regular (e.g. daily) CBCT images. Inter-fraction changes in the position or shape of organs can cause geometric misses of the target or overexposure of critical organs during external beam dose delivery. However, not all organ motion is necessarily cause for alarm as target volumes may move into high dose regions, while organs at risk (OARs) may move away into safer lower dose regions. Target or OAR motion is alarming only when the motion will ultimately result in large negative or positive changes in the planned dose to those structures, respectively. There are several methods for assessing the differences between the treatment day dose distribution and the originally planned dose distribution, such as a dose difference mapping with gamma analysis [128].

The focus of this work is to present an alternative technique, taking advantage of dose gradient and tissue displacement vector information to highlight regions of a treatment plan where dose variations will occur due to tissue displacements. The aim was to develop a software tool which would help radiation therapists identify situations where emerging changes in patient anatomy require: (1) no action (2) repositioning the patient, or (3) re-planning the treatment with adaptive modification of the dose distribution.

A.2 Dose Exchange Alarm for Optimal Patient Setup

By comparing the CT image obtained on the treatment day to the original CT-simulation image, it is possible to calculate and display a vector (i.e. quiver) plot describing the displacement of any tissue voxel. In-house code has been used to generate a tissue displacement map from contours of the day and planning contours, using a thin-plate spline technique [131]. The deformation vector map can then be used to assess the direction and severity of the tissue displacements relative to dose gradients in the original planned dose distribution (i.e. no need to calculate the dose of the

day). An example dose gradient map is show in Figure A.1, and an example quiver plot of tissue deformation vectors is shown in Figure A.2.

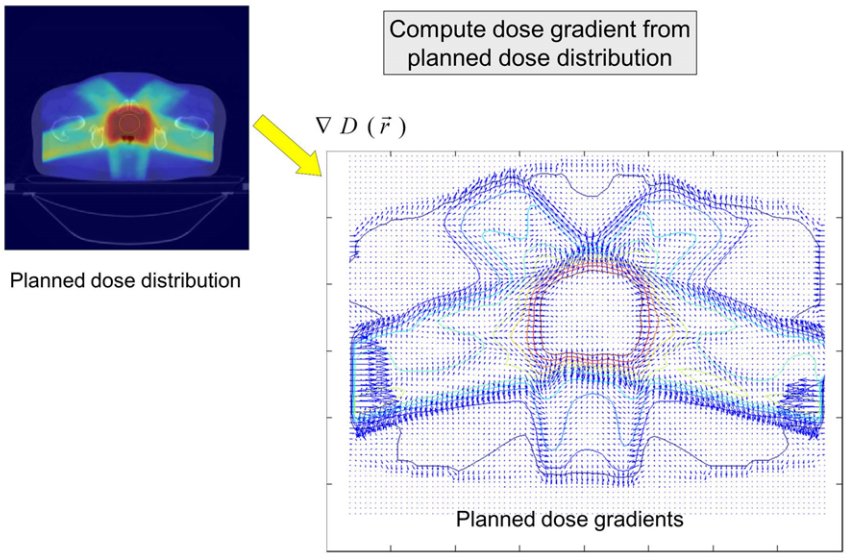

Figure A.1: An example dose gradient map calculated from a 2D dose map. Tissue movement through regions of large dose gradient is cause for concern when setting up a patient.

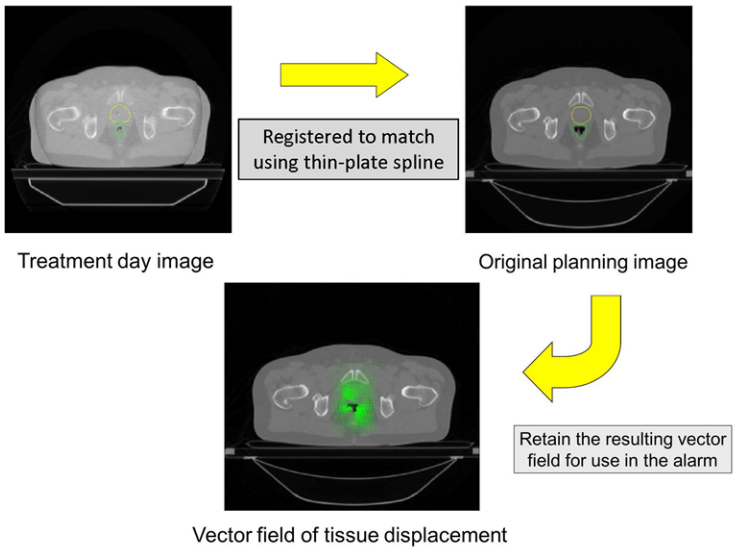

Figure A.2: An example deformation vector quiver plot overlaid on an image of the original anatomy. The vector field is used an an input to the Dose Exchange Alarm value calculation.

A.2.1 Definition of the Dose Exchange Alarm

The dose exchange alarm (DEA) requires two inputs: the tissue displacement vectors and the planned dose gradient vectors computed using the planned dose distribution. The DEA is calculated by taking the dot product between the tissue displacement vectors and the dose gradient vectors. The resulting map is interpreted as a differential dose due to the movement of tissues as defined by the quiver plot of tissue displacement. The overall information provided by the DEA map can be summarized and scored using the equation:

$$DEA = \sqrt{\sum_{ijk\,\epsilon\,ROI} (a_{ijk}\vec{\nabla}D_{ijk} \cdot \vec{ds}_{ijk} - \bar{A})^2} \tag{A.1}$$

$$DEA = \sqrt{\sum_{ijk\,\epsilon\,ROI} (A_{ijk} - \bar{A})^2} \tag{A.2}$$

In this formulation, each voxel in the region of interest (ROI) is given an 'i, j, k' index. The rest of the quantities are defined as follows:

- a_{ijk} are weighting coefficients corresponding to target tissue or organs at risk. These should be consistent with priority weights used during treatment planning.
- $\vec{\nabla}D_{ijk}$ is the dose gradient map computed at each voxel.
- $\vec{ds}_{ijk}$ are the voxel displacement vectors determined from image guidance.
- $\bar{A}$ is the simple average value of a_{ijk} over the region of interest.

A.3 Discussion

By minimizing the value of *DEA*, the necessary patient setup shifts that optimize the weighted dose matching (as opposed to anatomy matching) can be determined and applied just prior to dose delivery. This approach is analogous to minimizing the work done by charges that are moved within an electric field.

$$DEA_{opt} \mapsto f(\delta x, \delta y, \delta z, \delta\theta, \delta\phi) \tag{A.3}$$

$$MIN(DEA) = f(\delta x^\star, \delta y^\star, \delta z^\star, \delta\theta^\star, \delta\phi^\star),\ \bar{A} = 0 \tag{A.4}$$

The *DEA* value alerts the therapist to either large tissue excursions through small dose gradients, or short tissue excursions through large dose gradients. This will help identify differences in patient setup or anatomy which result in potentially critical changes in the dose delivered to prescribed targets or OARs based on tissue movement through the planned dose landscape.

The workflow chart in Figure A.3 summarizes how the alarm tool would be used prior to delivering a daily fraction. The patient has their initial setup, followed by image guidance to correct any major shifts. The *DEA* is then computed to assess internal tissue deformation. Minimizing the *DEA* as a function of rigid-body transformations produces an optimal set of patient setup shifts.

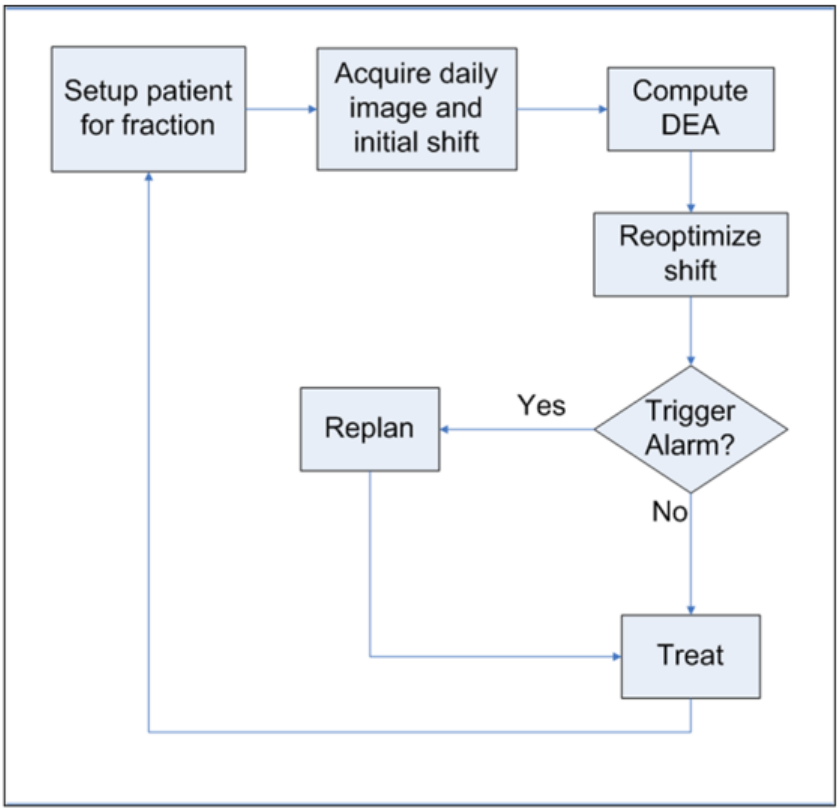

Figure A.3: An example workflow chart describing the use of the DEA during the delivery of a single fraction of a radiotherapy treatment.

Finally, the therapists apply the secondary shifts and rotations resulting from the optimization and DEA_{opt} is compared to the relevant re-planning threshold value for the given treatment site.

It should be noted that in general the DEA_{opt} will not be equal to zero and that the minimum value of the DEA will change on a daily basis in accordance with the current state of the patient anatomy. This is described with an example shown in Figure A.4.

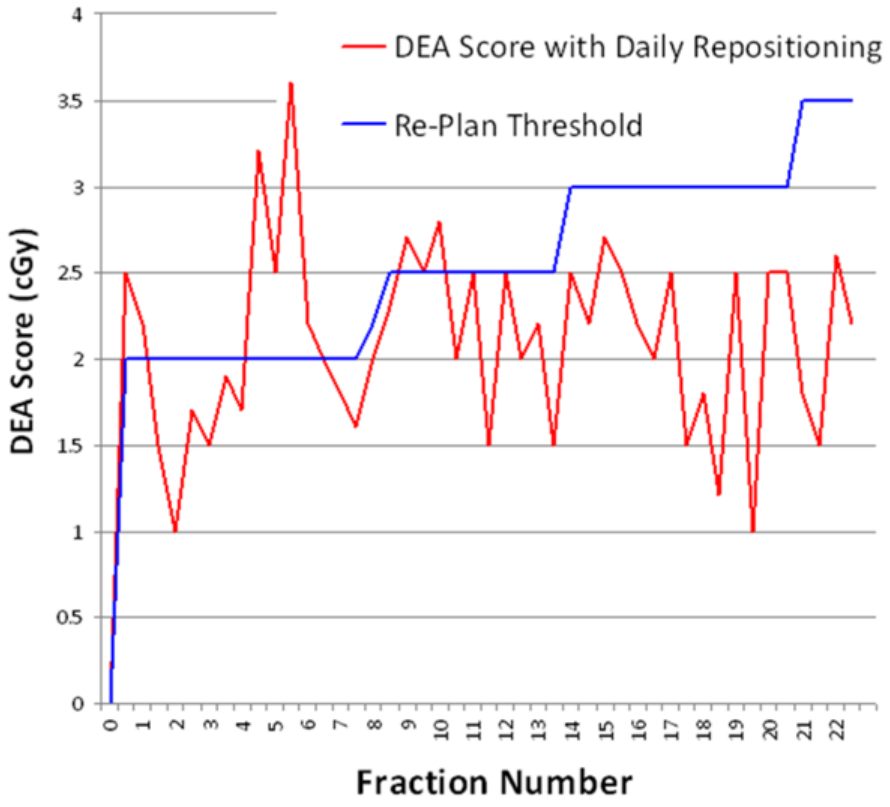

Figure A.4: A schematic plot of the optimized *DEA* values over the course of several fractions of a radiotherapy treatment. The optimized *DEA* will not be zero in general. The re-planning threshold varies throughout the treatment. In this example three optimized *DEA* violations of the threshold were permitted before triggering a re-plan at fraction 7.

The decision to re-plan a treatment would need to consider several factors, such as: the treatment site, the treatment objectives, the severity of the mismatch between the fractional dose distribution and the planned dose distribution, and the proportion of the full treatment prescription remaining to be delivered.

A.3.1 The Role of Deformable Image Registration

The DEA technique relies on a set of vector fields generated by an image registration algorithm. Basic image registration algorithms seek to register the image by applying simple shifts and rotations to images. These algorithms are known as rigid-registration algorithms. Deformable image registration (DIR) adds a layer of complexity to the image registration algorithm by also allowing for deformations of the image as well as the standard rigid registration shifts. While DIR algorithms show promise for more accurate image registration, much work is still to be done validating their results. Tissue displacement vector fields generated by accurate DIR would provide the best basis for the DEA.

Mencarelli et al. [132] compared a b-spline-based DIR algorithm with a rigid-registration algorithm on sets of planning CT data sets and CBCT data sets of patients acquired at a later date. They reported poor precision for the DIR results in tumour tissue in particular. Mencarelli et al. caution the use of DIR for monitoring tumour changes in adaptive procedures.

Zhong et al. [133] compared the performance of two DIR algorithms (Demons and b-spline) using phantom images of different body sites. Their results suggest that the accuracy of both algorithms was highly sensitive to the DIR parameter selection at each site. Therefor DIR results need to be closely scrutinized on a case by base basis.

Yeo et al. [134] assessed the accuracy of dose-warping based on the results of DIR by comparing to measurements made in a deformable dosimetric gel phantom. They reported very good agreement between DIR dose-warping and measured dose for simple open filed plans and small magnitude deformations. The agreement was markedly worse for more complex treatment plans and large deformations. The authors suggest that the DIR dose-warping is feasible, but that results should be carefully scrutinized before clinical application.

In each case, the authors find that DIR can offer accurate results under the right set of con-

ditions. However, in many practical cases the combination of conditions (e.g. body site, DIR parameter selection, magnitude of deformation) make the reliability of DIR results suspect. This is currently a major hurdle to the routine clinical use of DIR, with many research groups around the world focused on the problem. As DIR algorithms are refined, their potential for use in the DEA improves.

A.4 Future Work

Ultimately the DEA approach could provide an on-line alarm display to be employed by radiation therapists at the treatment unit. The therapists would be able to easily identify whether or not the current patient setup or anatomy warrants further setup adjustment or call for adaptive dose re-planning.

This appendix provides a proof-of-concept methodology for calculation of cumulative dose using IGRT data and dose gradients obtained from the original treatment plan. The limitations of the methodology include the simplicity of the dot product computation (first order calculation) and the accuracy of the displacement vectors determined form voxel-to-voxel DIR. Based on recent literature, generating reliable results from DIR algorithms still poses a large challenge. Additional work is in progress, in conjunction with researchers at the London Health Sciences Center to derive a site-specific constrained registration algorithm that will provide more accurate displacement vector solutions.

Future work also includes using this alarm as part of multi-fraction treatment simulations in order to determine the tumour site-specific threshold values for the DEA. These simulations could also be used to assess the ability of the weighted dose matching to steer the cumulative dose distribution towards convergence to the prescribed treatment objectives. More computer programming work is also necessary to extend this 2D proof of principle to 3D.

Appendix B

MATLAB Code

Included in this appendix is the MATLAB code used to process the dose profiles and breathing traces analyzed in this thesis. The code is available from the author as an electronic .m file or packaged as a stand-alone application with a graphical user interface.

B.1 MATLAB code

```
%%%%%Start a timer to measure the total time of simulation%%%%%
t1=tic;

%%%%%Create Output File with Headings%%%%%
write=fopen('STDvsMargin_70mm.txt','a');
fprintf(write,'%s\t %s\t %s\t %s\t %s\t %s\r','Filename','PDF STD','DoseProf1D90','DoseProf1D95','DoseProf1D99','margin');
fclose all;

%%%%%Import The List of Static Dose Profiles%%%%%
proflisting=dir('C:\Documents and Settings\stkfoste\Desktop\redo\doseprof');

%%%%%%%
%This loop performs the following actions on each static dose profile:
%- extracts the dose profile data from the txt file (assumes Eclipse export format)
%- interpolates dose points for finer detail after convolution
%- detects the 95% dose point inferiorly and superiorly and sets them as
%PTV boundaries
%%%%%%%
for kk=3:size(proflisting,1)
    %Save the profile name in a structure
    profname.(strcat('a',num2str(kk)))=strrep(proflisting(kk,1).name,'.txt','');
    %Import file data into a dummy variable (doseprofa)
```

```
23      doseprofa=importdata(strcat('C:\Documents and ...
            Settings\stkfoste\Desktop\redo\doseprof\',proflisting(kk,1).name),'\t',8);
24
25      %Save the dose and position data in seperate vectors, stored in a
26      %structure
27      doseprof.(profname.(strcat('a',num2str(kk)))).origdist=doseprofa.data(:,1);
28      doseprof.(profname.(strcat('a',num2str(kk)))).origdose=doseprofa.data(:,2);
29
30      %Generate and save the interpolation grid based on the imported position data
31      doseprofdisttrans=min(doseprof.(profname.(strcat('a',num2str(kk)))).origdist):0.001:max(doseprof.(profname.%LINE BREAK
32  (strcat('a',num2str(kk)))).origdist);
33      doseprof.(profname.(strcat('a',num2str(kk)))).dist=doseprofdisttrans';
34
35      %Interpolate the dose data and save the spatial sampling rate
36      doseprof.(profname.(strcat('a',num2str(kk)))).dose=interp1(doseprof.(profname.(strcat('a',num2str(kk)))).%LINE BREAK
37  origdist,doseprof.(profname.(strcat('a',num2str(kk)))).origdose,doseprof.(profname.(strcat('a',num2str(kk)))).dist);
38      doseprofstepsize=mean(diff(doseprof.(profname.(strcat('a',num2str(kk)))).dist));
39
40      %Detect the center of the dose profile (location of the center of the dose data)
41      traceCenter=round(size(doseprof.(profname.(strcat('a',num2str(kk)))).dose,1)/2);
42
43      %Set the maximum dose. This variable used to find PTV edges.
44      %Swap the comment on the two lines below to use a fixed dMax, or
45      %the maximum dose detected in the profile.
46      dMax=200;
47      %dMax=max(doseprof.(profname.(strcat('a',num2str(kk)))).dose)
48
49      %Determine and save the location of the PTV edges
50      dynPTVinf=dsearchn(doseprof.(profname.(strcat('a',num2str(kk)))).dose(1:traceCenter),dMax*0.90);
51      dynPTVsup=dsearchn(doseprof.(profname.(strcat('a',num2str(kk)))).dose(traceCenter:end),dMax*0.90)+traceCenter;
52      doseprof.(profname.(strcat('a',num2str(kk)))).PTVinf=dynPTVinf;
53      doseprof.(profname.(strcat('a',num2str(kk)))).PTVsup=dynPTVsup;
54
55      %%%%%Optional Profile Plotting Output%%%%%
56      % figure
57      % plot(doseprof.(profname.(strcat('a',num2str(kk)))).dist,doseprof.(profname.(strcat('a',num2str(kk)))).dose);
58  end
59
60  %%%%%Import List of Breathing Traces%%%%%
61  %listing=dir('C:\Documents and Settings\stkfoste\Desktop\redo\traces');
62  listing=dir('C:\Documents and Settings\stkfoste\My Documents\MATLAB\Organized Traces\Processed');
63  %%%%%Start the progress bar%%%%%
64  hh=waitbar(0,'Please Wait...');
65
66  %%%%%This is the main loop%%%%%
67  %%%%%
68  %This loop performs the following:
69  %- Import a breathing trace file (.vxp file - from Varian's RPM system)
70  %- Extract the portion of the breathing trace recorded during 'beam on'
71  %- Generate a PDF using the 'beam on' position data
72  %- Convolve the PDF against each imported static dose profile
73  %- Calculate the D95 of the static and blurred dose profiles
74  %- Save pertinent data in a structure
75  %%%%%
76  for m=3:size(listing,1)
77  %for m=3:5
78
79      %Read the breathing trace .vxp file, save data in a dummy variable (filedata)
80      mm=listing(m,1).name;
81      file=strcat('C:\Documents and Settings\stkfoste\My Documents\MATLAB\Organized Traces\Processed\',mm);
82      qwe=fopen(file);
83      filedata=textscan(qwe,'%f %f %f %d %d %c %d', 'HeaderLines', 10, 'Delimiter',',');
84      fclose(qwe);
85
86      %Save a vector with the recorded marker block position from imported data
87      btrac=filedata{1,1,1};
88
89      %Save a vector with the recorded beam on flag from imoported data
90      beamon=filedata{1,5,1};
91
92      %Set loop counter to 1 (k)
93      k=1;
94
95      %Instantiate empty vector for saving recorded positions during 'beam on'
96      btraca=zeros(5000,1);
97
98      %Loop through filedata, saving only positions recorded during 'beam on' in
99      %a dummy variable (btraca)
```

```
    for n=1:size(beamon)
        if beamon(n,1)<=0
        else
           btraca(k,1)=btrac(n,1);
           k=k+1;
        end
    end

    %Save pertinent portion of dummy variable in usefule variable (btrace)
    btrace=btraca(1:(k-1),1);

    %Determine the geometric center of the breathing trace
    btracecent=(max(btrace)-min(btrace))/2;

    %Center the breathing trace
    btracecentered=btrace-(ones(size(btrace,1),1)*(max(btrace)-abs(btracecent)));
    %plot(btracecentered)
    %Calculate some breathing trace statistics
    pdfmean=mean(btracecentered);
    pdfstd=std(btracecentered);
    % pdfmean=mean(btracecentered);
    % pdfstd=std(btracecentered);
    % pdfkurt=kurtosis(btracecentered);
    % pdfamp=max(btracecentered);
    % pdfskew=skewness(btracecentered);
    % pdfmaxloc=btracecentrange(1,dsearchn(normpdfa,max(normpdfa)));
    % pdfmax=normpdfa(dsearchn(normpdfa,max(normpdfa)),1);
    % diffnormpdf=diff(normpdfa);
    % diffpdfamp=max(diffnormpdf);
    % diffpdfmean=mean(abs(diffnormpdf));
    % diffpdfstd=std(diffnormpdf);
    % diffpdfkurt=kurtosis(diffnormpdf);
    % diffpdfskew=skewness(diffnormpdf);
    % diffpdfmaxgrad=max(abs(diffnormpdf));
    % diffpdfmaxgradind=dsearchn(diffnormpdf,diffpdfmaxgrad);
    % diffpdfmaxgradloc=btracecentrange(1,diffpdfmaxgradind);

    %Save a vector of position data slightly longer than the range of
    %positions covered by the breathing trace, used to help fit the PDF
    btracecentrange=min(btracecentered)*1.3:doseprofstepsize:max(btracecentered)*1.3;

    %Generate the PDF and normalize the area under the curve
    pdf = ksdensity(btracecentered,btracecentrange,'support',[min(btracecentrange) max(btracecentrange)],'width',0.2);
    normpdfa = pdnorm(btracecentrange',pdf');

    %Save pertinent data in a structure (beamo)
    filename=strrep(mm,'.vxp','');
    beamo.(strcat('a',filename)).PDFmean=pdfmean;
    beamo.(strcat('a',filename)).PDFstd=pdfstd;
    beamo.(strcat('a',filename)).FullPDF=normpdfa;
    beamo.(strcat('a',filename)).PDFdist=btracecentrange;

    %%%%%Optional PDF Plotting Output%%%%%
    %figure
    %plot(btracecentrange,normpdfa);

    %%%%%Convolution sub-loop%%%%%
    %%%%%
    %This loop performs the following:
    %- Convolves the PDF against each imported breathing trace
    %- Aligns convolved profile to static profile by shifting according to
    %PDF mean (Linear shift-invariance property of the convolution)
    %- Calculates the D95 of the static and blurred profiles
    %- Saves pertinent data to a structure (beamo)
    %%%%%
    pdfdataarray = [pdfstd];
    for gg=3:size(proflisting,1)

        %Perform convolution
        pdconv=conv(doseprof.(profname.(strcat('a',num2str(gg)))).dose,normpdfa','same');

        %Determine original static profile plot area for normalization purposes
        doseprofarea=getplotarea(doseprof.(profname.(strcat('a',num2str(gg)))).dist,doseprof.(profname.%LINE BREAK
(strcat('a',num2str(gg)))).dose);

        %Create a vector of position data for the convolved profile,
        %shifted by the PDF mean
        convdistend=(size(pdconv,1)-1)*doseprofstepsize;
```

```
178         convdist1=(0:doseprofstepsize:convdistend)';
179         convdist=convdist1-ones(size(convdist1,1),1)*pdfmean;
180
181         %Determine the plot area of the blurred profile for normalization
182         %purposes
183         convprofarea=getplotarea(convdist,pdconv);
184         %convprofarea=getplotarea(doseprof.(profname.(strcat('a',num2str(gg)))).dist,pdconv);
185         arearatio=doseprofarea/convprofarea;
186
187         %Save the static and blurred dose profiles and corresponding
188         %positional data in the beamo structure
189         beamo.(strcat('a',filename)).(profname.(strcat('a',num2str(gg)))).convprofile=pdconv*arearatio;
190         beamo.(strcat('a',filename)).(profname.(strcat('a',num2str(gg)))).convposition=convdist;
191         beamo.(strcat('a',filename)).(profname.(strcat('a',num2str(gg)))).staticprofile=doseprof.%LINE BREAK
(profname.(strcat('a',num2str(gg)))).dose;
193         beamo.(strcat('a',filename)).(profname.(strcat('a',num2str(gg)))).staticposition=doseprof.%LINE BREAK
(profname.(strcat('a',num2str(gg)))).dist;
195
196         %%%%%Optional Blurred and Static Profile Plotting Output%%%%%
197         % figure
198         % plot(beamo.(strcat('a',filename)).(profname.(strcat('a',num2str(gg)))).staticdist,beamo.%LINE BREAK
(strcat('a',filename)).(profname.(strcat('a',num2str(gg)))).staticprofile, 'color', 'black');
200         % hold all
201         % plot(convdist,beamo.(strcat('a',filename)).(profname.(strcat('a',num2str(gg)))).convprofile,'color','red')
202         % hold off
203
204         %Calculate and save the D90, D95 & D99 of the static profile. This is done by
205         %numerically ordering all dose values within the PTV and selecting
206         %the value at the 95th percentile.
207         origPTVinf=doseprof.(profname.(strcat('a',num2str(gg)))).PTVinf;
208         origPTVsup=doseprof.(profname.(strcat('a',num2str(gg)))).PTVsup;
209         origtargetdose=doseprof.(profname.(strcat('a',num2str(gg)))).dose(origPTVinf:origPTVsup,1);
210         npercent=round(size(origtargetdose,1)*0.1);
211         nfpercent=round(size(origtargetdose,1)*0.05);
212         nnpercent=round(size(origtargetdose,1)*0.01);
213         orderOTD=sort(origtargetdose);
214         origD90=orderOTD(npercent,1);
215         origD95=orderOTD(nfpercent,1);
216         origD99=orderOTD(nnpercent,1);
217         beamo.(strcat('a',filename)).(profname.(strcat('a',num2str(gg)))).staticD90=origD90;
218         beamo.(strcat('a',filename)).(profname.(strcat('a',num2str(gg)))).staticD95=origD95;
219         beamo.(strcat('a',filename)).(profname.(strcat('a',num2str(gg)))).staticD99=origD99;
220
221         %Calculate and save the D90, D95 & D99 of the blurred profile. This is done by
222         %numerically ordering all dose values within the PTV and selecting
223         %the value at the 95th percentile.
224         convPTVinf=origPTVinf+round(pdfmean/doseprofstepsize);
225         convPTVinfvalue=convdist(convPTVinf,1);
226         convPTVsup=origPTVsup+round(pdfmean/doseprofstepsize);
227         convPTVsupvalue=convdist(convPTVsup,1);
228         convtargetdose=beamo.(strcat('a',filename)).(profname.(strcat('a',num2str(gg)))).%LINE BREAK
convprofile(convPTVinf:convPTVsup,1);
230         convnpercent=round(size(convtargetdose,1)*0.1);
231         convnfpercent=round(size(convtargetdose,1)*0.05);
232         convnnpercent=round(size(convtargetdose,1)*0.01);
233         orderCTD=sort(convtargetdose);
234         convD90=orderCTD(convnpercent,1);
235         convD95=orderCTD(convnfpercent,1);
236         convD99=orderCTD(convnnpercent,1);
237         beamo.(strcat('a',filename)).(profname.(strcat('a',num2str(gg)))).convD90=convD90;
238         beamo.(strcat('a',filename)).(profname.(strcat('a',num2str(gg)))).convD95=convD95;
239         beamo.(strcat('a',filename)).(profname.(strcat('a',num2str(gg)))).convD99=convD99;
240
241         %Calculate and save the relative D90, D95 & D99
242         relD90=convD90/origD90;
243         relD95=convD95/origD95;
244         relD99=convD99/origD99;
245         beamo.(strcat('a',filename)).(profname.(strcat('a',num2str(gg)))).relD90=relD90;
246         beamo.(strcat('a',filename)).(profname.(strcat('a',num2str(gg)))).relD95=relD95;
247         beamo.(strcat('a',filename)).(profname.(strcat('a',num2str(gg)))).relD99=relD99;
248         pdfdataarray=cat(2,pdfdataarray, relD90);
249         pdfdataarray=cat(2, pdfdataarray, relD95);
250         pdfdataarray=cat(2, pdfdataarray, relD99);
251         %%%%%Optional Blurred and Static PTV Profile Plotting Output%%%%%
252         % figure
253         % plot(origtargetdose,'color','black')
254         % hold all
255         % plot(convtargetdose,'color','red')
```

```
% hold off

%%%%%%%%%%%%%%%%%%%%%%%%%%%%%%%%%%%%%%%%%%%%%%%%%%%%%%%%%%%%%%%%%%%%%%%
%%%%%Set the value of various variables used in the following
%%%%%'while' loop%%%%%

doseprofdose=doseprof.(profname.(strcat('a',num2str(kk)))).dose;
traceCenter=round(size(doseprofdose,1)/2);
newRelD95 = relD95;
p=1;
inc=p*10;
origdist=doseprof.(profname.(strcat('a',num2str(kk)))).origdist;
doseprofdist=doseprof.(profname.(strcat('a',num2str(kk)))).dist;
convprogression=[newRelD95];
%%%%%
%This loop performs the following:
%- Incrementally increases the beam width by adding additional dose
%points to the centre of the dose profile (this is called the
%recommended profile)
%- Convolves the recommended profile with the PDF
%- Calculates the D95 of the blurred recommended profile
%- If the convolved D95 is less than the original D95, the loop repeats
%with a larger increment added to the orignal profile
%- Saves pertinent data to a structure (beamo)
%%%%%
while newRelD95 < 0.9999
    %Set the incremental increase in profile width
    inc=p*10;

    %Add this increment to the middle of the original profile
    recProfinf=doseprofdose(1:traceCenter);
    recProfAdded=ones(inc,1)*doseprofdose(traceCenter,1);
    recProfsup=doseprofdose(traceCenter:end);
    recProf=cat(1,recProfinf,recProfAdded,recProfsup);

    %Generate a vector of positions for the recommended profile and
    %center it
    recProfAddedDisttrans=max(origdist):doseprofstepsize:(max(origdist)+(inc*doseprofstepsize));
    recProfAddedDist=recProfAddedDisttrans';
    recProfDista=cat(1,doseprofdist,recProfAddedDist);
    recProfDist=recProfDista-ones(size(recProfDista,1),1)*(inc/2)*doseprofstepsize;


    %Perform the convolution of the recommended profile with the
    %PDF
    Newpdconv=conv(recProf,normpdfa','same');

    %Determine original static profile plot area for normalization purposes
    Newdoseprofarea=getplotarea(recProfDist,recProf);

    %Create a vector of position data for the convolved recommended profile,
    %shifted by the PDF mean
    convdistenda=(size(Newpdconv,1)-1)*doseprofstepsize;
    convdist1a=(0:doseprofstepsize:convdistenda)';
    convdista=convdist1a-ones(size(convdist1a,1),1)*(pdfmean+((inc/2)*doseprofstepsize));

    %Determine the plot area of the blurred profile for normalization
    %purposes
    Newconvprofarea=getplotarea(convdista,Newpdconv);
    arearatio=Newdoseprofarea/Newconvprofarea;
    Newconvprofile=Newpdconv*arearatio;

    %%%%%Optional plotting of the static and blurred recommended
    %%%%%profiles
    %figure
    %plot(convdista,Newconvprofile,'color','green','DisplayName','Recommended Blurred Profile')
    %plot(recProfDist,recProf,'color','blue','DisplayName','Recommended Static Profile')

    %Calculate the D95 of the recommended blurred profile
    NewconvPTVinf=dsearchn(convdista(1:(traceCenter+(inc/2))),convPTVinfvalue);
    NewconvPTVsup=dsearchn(convdista((traceCenter+(inc/2)):end),convPTVsupvalue)+(traceCenter+(inc/2));
    Newconvtargetdose=Newconvprofile(NewconvPTVinf:NewconvPTVsup,1);
    Newconvnfpercent=round(size(Newconvtargetdose,1)*0.05);
    NeworderCTD=sort(Newconvtargetdose);
    NewconvD95=NeworderCTD(Newconvnfpercent,1);

    %Update the value of the variable to be checked by the 'while' loop
    newRelD95=NewconvD95/origD95
```

```
334
335             %Update the counter for incremental increase in dose profile
336             %width. Large increments when the relative D95 is far from 1
337             %speed up the simulation
338             if newRelD95 <0.9
339                 p=p+75
340             elseif newRelD95 <0.95
341                 p=p+50
342             elseif newRelD95 <0.98
343                 p=p+20
344             elseif newRelD95 <0.99
345                 p=p+10
346             elseif newRelD95 <0.992
347                 p=p+5
348             else
349                 p=p+1
350             end
351            % p=p+1
352         end
353
354         %Calculate the recommended margin based on the final increment
355         margin=inc*doseprofstepsize*10;
356
357         %Save margin information to write to output file
358         pdfdataarray=cat(2, pdfdataarray, margin);
359
360         %Save the recommended static and blurred profiles and their
361         %associated position data
362         beamo.(strcat('a',filename)).(profname.(strcat('a',num2str(gg)))).recprofile=recProf;
363         beamo.(strcat('a',filename)).(profname.(strcat('a',num2str(gg)))).recposition=recProfDist;
364         beamo.(strcat('a',filename)).(profname.(strcat('a',num2str(gg)))).recoConvprofile=Newconvprofile;
365         beamo.(strcat('a',filename)).(profname.(strcat('a',num2str(gg)))).recoConvposition=convdista;
366     end
367
368 %%%%%Save output data in a .txt file for export%%%%%
369 ffb=fopen('STDvsMargin_70mm.txt','a');
370 fprintf(ffb,'%s\t %g\t %g\t %g\t %g\t %g\r',filename, pdfdataarray);
371 fclose all;
372
373 %%%%%Update the progress bar
374 waitbar(m / (size(listing,1)))
375 end
376
377 %%%%%Close the progress bar
378 close(hh)
379
380 %%%%%Output total simulation time
381 toc(t1)
```